JAERI-M
92-039

INDC(JPN)-158/L

PROCEEDINGS OF THE SPECIALISTS' MEETING ON HIGH ENERGY NUCLEAR DATA

October 3-4, 1991, JAERI Tokai

March 1992

(Ed.) Tokio FUKAHORI

日本原子力研究所
Japan Atomic Energy Research Institute

JAERI-Mレポートは，日本原子力研究所が不定期に公刊している研究報告書です。
入手の問合わせは，日本原子力研究所技術情報部情報資料課（〒319-11茨城県那珂郡東海村）あて，お申しこしください。なお，このほかに財団法人原子力弘済会資料センター（〒319-11茨城県那珂郡東海村日本原子力研究所内）で複写による実費頒布をおこなっております。

JAERI-M reports are issued irregularly.
Inquiries about availability of the reports should be addressed to Information Division Department of Technical Information, Japan Atomic Energy Research Institute, Tokai-mura, Naka-gun, Ibaraki-ken 319-11, Japan.

編集兼発行　日本原子力研究所
印　　刷　いばらき印刷㈱

JAERI-M 92-039

Proceedings of the Specialists' Meeting on High Energy Nuclear Data October 3-4, 1991, JAERI Tokai

(Ed.) Tokio FUKAHORI

Japanese Nuclear Data Committee
and
Nuclear Data Center
Japan Atomic Energy Research Institute
Tokai-mura, Naka-gun, Ibaraki-ken

(Received February 17, 1992)

This report consists of the Proceedings of the Specialists' Meeting on High Energy Nuclear Data. The meeting was held on October 3-4, 1991, at the Tokai Research Establishment, Japan Atomic Energy Research Institute with the participation of forty-odd specialists, who were the evaluators, theorists, experimentalists and users of high energy nuclear data including the members of the Japanese Nuclear Data Committee.

The need of the nuclear data in the high energy region up to a few GeV was stressed in the meeting for many applications, such as spallation neutron sources for radioactive waste treatment, accelerator shielding design, medical isotope production, radiation therapy, the effects of space radiation on astronauts and their equipments, and the cosmic history of meteorites and other galactic substances. Although the neutron

---

Program Committee

Takashi NAKAMURA (Chairman)	(Tohoku University)
Yoshitomo UWAMINO	(Tokyo University)
Norio KISHIDA	(CRC Research Institute Inc.)
Yutaka NAKAJIMA	(Japan Atomic Energy Research Institute)
Satoshi CHIBA	(Japan Atomic Energy Research Institute)
Hiroshi TAKADA	(Japan Atomic Energy Research Institute)
Tokio FUKAHORI	(Japan Atomic Energy Research Institute)

nuclear data below 20 MeV have been well evaluated for fission and fusion reactor applications, the nuclear data in the high energy region have never been prepared in Japan.

With the view of producing an evaluated high energy nuclear data file, theoretical models and codes, available and necessary measurements, needs of nuclear data, and various applications were reviewed and discussed. The consensus, that the wide collaboration was necessary to produce the evaluated file and should be established, has been obtained.

Keywords: Proceedings, Nuclear Data, High Energy, Evaluation, Experiment, Applicative Review, Theoretical Review

JAERI－M 92－039

高エネルギー核データ専門家会議報文集

1991年10月３～４日，東海研究所

日本原子力研究所東海研究所
シグマ研究委員会・核データセンター
（編）　深　堀　智　生

（1992年２月17日受理）

本報文集は，高エネルギー核データ専門家会議の報文を収録したものである。専門家会議は，1991年10月３日と４日の両日日本原子力研究所東海研究所において40数名の専門家の出席のもとに開催された。出席した専門家は，高エネルギー核データの評価者，理論的研究者，実験者，利用者及びシグマ委員会委員であった。

数GeV までの入射エネルギーにおける高エネルギー核データは，放射性廃棄物処理のためのスポレーション中性子源，加速器の遮蔽設計，医療用放射性同位体製造，放射線治療，宇宙空間での宇宙飛行士や装置への影響の研究，宇宙物理学などの多岐にわたる分野から必要とされている。しかし，核分裂炉や核融合炉のための20MeV 以下の中性子に対する核データのように整備が進んでいるとは言い難く，その緒についたばかりというのが現状である。

本専門家会議では，高エネルギー核データの評価済ファイルを整備するという観点に立って，理論モデルや理論計算コード，既存もしくは必要な実験データ，利用者からの核データの要求及び応用分野の紹介などが報告・討議された。多くの討論の結果，評価済高エネルギー核データファイル作成のためには広範な協力が必要であり，その体制作りを行うべきであるとの合意が得られた。

東海研究所：〒319-11　茨城県那珂郡東海村白方字白根２－４

高エネルギー核データ専門家会議プログラム委員会

中村　尚司（委員長）	（東北大学）
上蓑　義明	（東京大学）
岸田　則生	（ＣＲＣ総合研究所㈱）
中島　　豊	（日本原子力研究所）
千葉　　敏	（日本原子力研究所）
高田　　弘	（日本原子力研究所）
深堀　智生	（日本原子力研究所）

Contents

目　　次

1.1 Measurement of Radioactive Nuclides Produced by Spallation Neutrons

Hiroshi Takada
Japan Atomic Energy Research Institute
Tokai-mura, Naka-gun, Ibaraki, 319-11, Japan

Abstract: An integral experiment was performed to study the transport of the spallation neutrons in a lead assembly irradiated with 500 MeV protons. Spatial distributions of induced radioactive nuclides were obtained in the lead assembly using various activation samples. Measured data were compared with the results of the nucleon-meson transport code.

1.Introduction

It is a current interest to transmute long-lived radioactive wastes, especially, trans-uranic nuclides to reduced their own hazard potentials. In the OMEGA(Options for Making Extra Gains from Actinides and fission products) project promoted by Science and Technology Agency of Japan, the use of accelerator driven spallation neutron source and subcritical blanket[1] is one of options for the transmutation system. The accelerator driven transmutation system is based on the similar concepts[2] of the fuel breeding system proposed in 1970s.

In the transmutation system, neutron yields and neutron spectrum are important factors which decide the performances of the system. From the viewpoint of target design, therefore, it is necessary to understand the transport of high energy neutrons in the target materials. Some experiments[3-7] have been carried out with thick targets and several hundreds of MeV protons to investigate the leakage neutron spectrum, the neutron yield and the nuclide production.

We performed integral experiment with lead assembly to study the transport of the spallation neutrons in the assembly more detail than previous experiments. Several kinds of activation samples were inserted into the assembly and were irradiated with 500 MeV protons. The number of induced nuclides was obtained by γ-ray measurement.

Preliminary calculation was also performed using the nucleon meson transport code NMTC/JAERI[8] which is based on the intranuclear cascade evaporation (INCE) model[9]. The calculated results

were compared with the experimental ones.

2.Experimental Procedure

In the experiment, the lead assembly was irradiated in the beam dump room of the 500 MeV booster proton synchrotron facility of National Laboratory for High Energy Physics. Figure 1 shows the cross section of the lead assembly. The size of the assembly was 60 cm in diameter and 100 cm in length. The 500 MeV protons were injected into the assembly through the hole of 16 cm in diameter and 20 cm in length.

The activation samples were inserted into the lead assembly along the beam axis at the position of 0, 3, 6, 10, 15, 20 and 25 cm. The purities of the samples were as follows: Al(99.999%), Fe(99.99%), Ni(99.9%), Cu(99,99%), Au(99.999%) and Pb(99.99%). The size of the sample was 6 mm in diameter and 10 mm in length, respectively.

The lead assembly was irradiated with 6.3×10^{14} to 3.3×10^{15} protons. The number of the protons was monitored by the pick up coil, the activation foil of Al and the faraday cup. After 30 hours cooling, γ-ray measurement was started with a Ge-detector (relative efficiency of 20% to 3"x3" NaI). The measured data were taken on the computer by 4k channels and were analyzed by the program BOB(10). The reaction rate was calculated by the following relation:

$$Y_{jexp} = \frac{\lambda_j I_j}{P N \varepsilon_j \eta \delta (1-e^{-\lambda_j Tr}) e^{-\lambda_j Tc} (1-e^{-\lambda_j Tm})}, \quad (1)$$

where j : jth produced nuclide,
λ_j : the decay constant,
I_j the peak area,
P the number of protons,
N the number of atoms in an activation sample,
ε_j the peak efficiency of the Ge-detector,
η the number of photons emmited per decay,
δ the self-absorption for photons in an activation sample,
Tr the irradiation time,
Tc the cooling time and
Tm the measuring time.

The peak efficiency ε_j was determined by the calibrated gamma sources of ^{22}Na, ^{60}Co, ^{137}Cs and ^{152}Eu. The self absorption for photons in an activation samples δ was calculated by Monte Carlo method assuming that the photons were produced uniformly in the sample. The uncertainties for the decay constant and the number of photon per decay were not included in this estimation. Table 1 summarizes the errors with respect to the γ-ray measurement.

3. Nucleon Transport Calculation

Preliminary calculation was performed to compare the results with the experimental ones. The nucleon flux in the lead assembly was calculated by the Monte Carlo code NMTC/JAERI neglecting the existence of the activation samples in the lead assembly. The cut off energy was 15 MeV. The reaction rate $Y_j cal$ was evaluated as follows:

$$Y_j cal = \sum \int_{Eth}^{500} \sigma^i{}_j(E)\phi^i{}_j(E)dE \quad , \qquad (2)$$

where i stands for proton or neutron, $\sigma^i{}_j(E)$ is the production cross section for the nuclides j, $\phi^i{}_j(E)$ the flux of nucleon i and Eth the threshold energy.

As for the activation cross section, the experimental data[11,12] were employed for proton induced reaction. For neutron induced reaction, on the other hand, the calculated values were employed because of lack of the experimental neutron induced activation cross sections above 20 MeV. We evaluated the cross section using NMTC/JAERI.

Figure 2 and 3 shows excitation functions for $^{nat}Ni(p,x)^{56}Ni$, and $^{nat}Ni(p,x)^{54}Mn$ reactions, respectively. One can see the differences in magnitude of 2 to 3 factors between the results. The discrepancies are caused by some crude approximation taken in the INCE model. Therefore the calculated neutron induced cross sections may include the errors as same magnitude as the one seen in Figure 2 and 3.

4. Results and Discussions

In this experiment, we identified the nuclide whose half life is beyond 10 hour. Main identified nuclides were summarized in Table 2

for Al, Fe, Ni and Cu.

Figure 4 shows the spatial distribution of ^{206}Bi produced in lead samples. The distributions imply that the proton induced reactions were induced only on the vicinity of the axis. Since the range of the 500 MeV proton is 20 cm in the lead, it is seemed that the secondary protons induced ^{206}Bi in deep position. On the axis, distribution does not show the rapid decrease as is seen in the results at r= 3 cm. This fact means that the high energy protons were transported forword direction predominantly.

Figure 5 shows the reaction rate of ^{48}V in nickel sample, which is apart 10 in mass number from the target nucleus. It is reqired beyond 30 MeV for the ^{48}V production in nickel. On the beam axis, ^{48}V was mainly produced by proton induced reaction. As is seen in Figure 4, the contribution of protons is small at the deep position from the axis. Therefore the spatial distribution corresponds for the traces of the high energy neutrons.

Figure 6. shows the spatial distribution of ^{57}Ni produced in nickel samples. Since the protons was incident on the surface at 20 cm in depth, the reaction rate shows the greatest value at the position and decrease exponentially. It should be noticed that the production of ^{57}Ni was observed at the position of r= 25 cm. Because the Q-value of the ^{57}Ni production is 12.4 MeV, it is indicated that the fast neutrons were transported to the periphery of the lead assembly

In Figure.7, calculated results are compared with the experimental ones for ^{56}Ni produced in nickel samples. The Q-value of the reaction is -22.5 MeV. The error bars imply the uncertaintis of the statistics in the Monte Carlo calculation. One can see that the calculated results represented the shape of the longitudinal distribution well for the results of r=3 to 10 cm from the lead assembly axis. On the axis, the calculated results agree well with the experimental ones at the depth between 20 cm and 40 cm where the proton induced reaction was dominant. However, significant discrepancy is seen between the results as the depth increases. Considering the difference of the results is much larger than the magnitude of the error bar, some systematic error may be included in the results.

As mentioned in section 2, the discrepancies seem to be caused by the errors included in the calculated cross section. it is also necessary to investigate accuracy of the calculated neutron spectrum in the lead

assembly. In addition, the existence of the activation samples was not taken into account in the calculation so that the calculated flux might include the errors ascribed to the perturbation effect that the high energy nucleons penetrate more easily in the activation samples on the axis than surrounding lead.

Therefore, further investigation should be required from the experimental and the calculational aspects to compare the results in detail.

Acknowledgement

This work was carried out under the contract for the use of the booster synchrotron facility of National Laboratory for High Energy Physics. The authors wish to thank the staffs of National Laboratory for High Energy Physics for their support and encouragement.

References

(1) TAKIZUKA, T., et al.: Proc. 5th Int. Conf. Emerging Nucl. Energy Systems. (Karlsruhe, 1988)
(2) For example, GRAND, P., KOUTS,H.J., Eds.: BNL-50838 (1978)
(3) ARAKITA, Y., et al.: Nucl. Instr and Meth. **164,** 225 (1979)
(4) VASIL'KOV, R. G., et al.: Atomnaya Energiya **44**, 329 (1978)
(5) CIERJACKS, S. S., et al.: Jul-Conf-45, 215 (1981)
(6) RAUPP, F. et al.: Jul Conf-45, 333 (1981)
(7) RUSSEL, G. G.: Jul-Conf-45, 621 (1981)
(8) NAKAHARA, Y. and TSUTSUI. T.: JAERI-M 82-198 (1982) (in Japanese).
(9) BERTINI, H. W.: Phys. Rev. **131**, 1801(1963).
(10) BABA, H.: JAERI-M 7017 (1977).
(11) MICHEL, R., WEIGEL, H. and HERR, W.: Z. Phys. **A286,** 393 (1973).
(12) MICHEL, R. and STUCK, R.: J. Geophys. Res. **89**, B673 (1984).

Table 1 Estimated experimental errors.

Items	Estimated errors (%)
1. Number of protons	10
2. Statistics of peak area	< 1 to 50
3. Peak efficiency	2.0 to 4.0
4. Number atoms in the Ni sample	< 0.5
5. Time for irradiation, cooling and measuring	< 0.5

Table 2. Identified Nuclides in the samples of Al, Fe, Ni and Cu.

Samples	Identified Nuclides
Al	^{7}Be, ^{22}Na, ^{24}Na
Fe	^{42}K, ^{43}K, ^{44m}Sc, ^{46}Sc, ^{48}V, ^{48}Cr, ^{51}Cr, ^{52}Mn, ^{54}Mn, ^{56}Co
Ni	^{42}K, ^{43}K, ^{44m}Sc, ^{46}Sc, ^{48}V, ^{48}Cr, ^{51}Cr, ^{52}Mn, ^{54}Mn, ^{52}Fe, ^{59}Fe, ^{55}Co, ^{56}Co, ^{57}Co, ^{58}Co, ^{56}Ni, ^{57}Ni
Cu	^{42}K, ^{43}K, ^{44m}Sc, ^{46}Sc, ^{48}V, ^{48}Cr, ^{51}Cr, ^{52}Mn, ^{54}Mn, ^{59}Fe, ^{55}Co, ^{56}Co, ^{57}Co, ^{58}Co, ^{56}Ni, ^{57}Ni, ^{62}Zn, ^{65}Zn

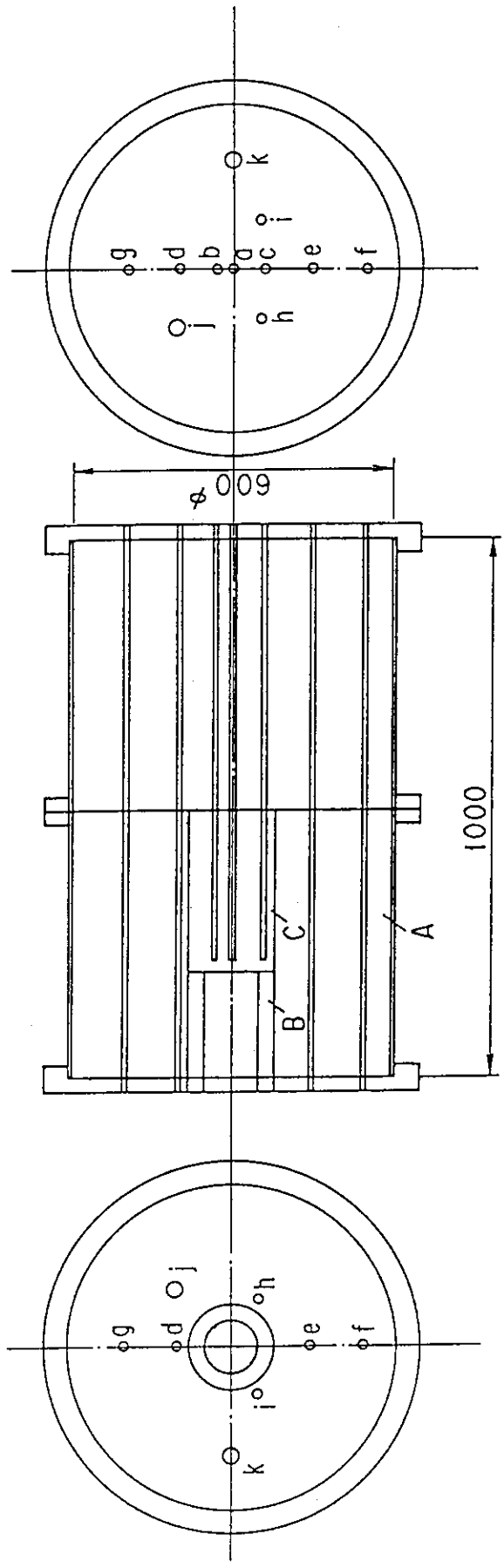

Figure 1. Cross sectional view of the lead assembly. The small holes (a to i) indicate the places where activation samples are inserted. The capitals A stands for lead assembly, B the beam entrance hole, C the lead target which can be replaced to diffrent one.

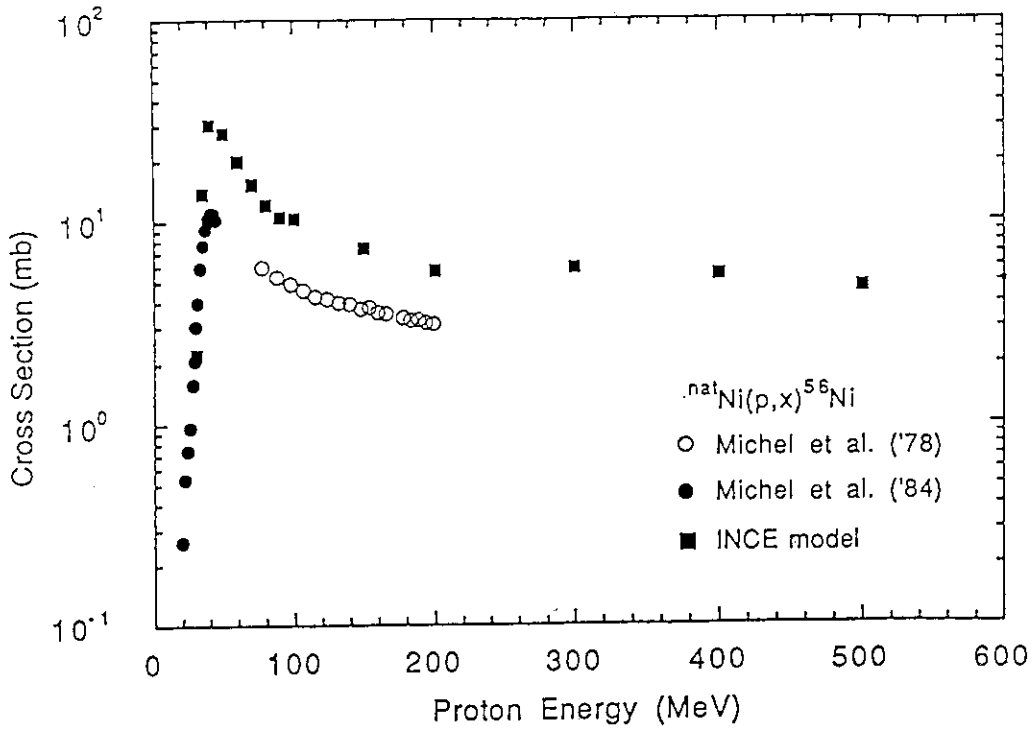

Figure 2 Excitation function for ^{nat}Ni(p,x)^{56}Ni reaction. Experimental data are shown by open and solid circles. Calculated results by intranuclear cascade evaporation (INCE) model are plotted by solid squres.

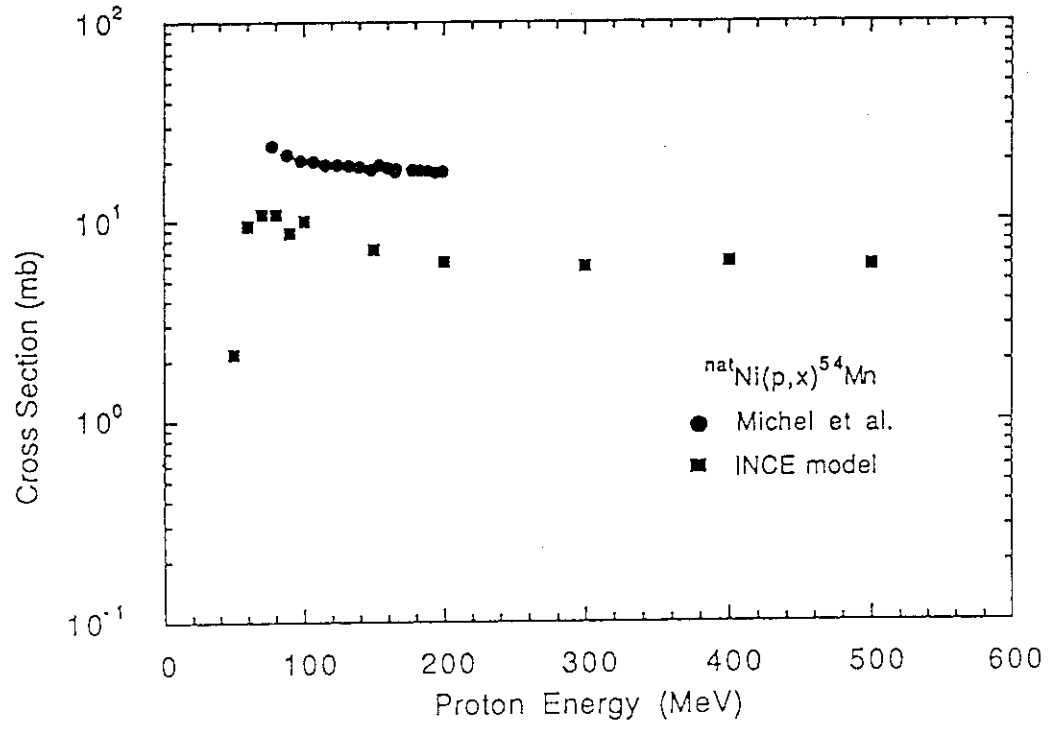

Figure 3. Excitation function for ^{nat}Ni(p,x)^{54}Mn reaction. Experimental data are shown by solid circles. Calculated results by intranuclear cascade evaporation (INCE) model are plotted by solid squres.

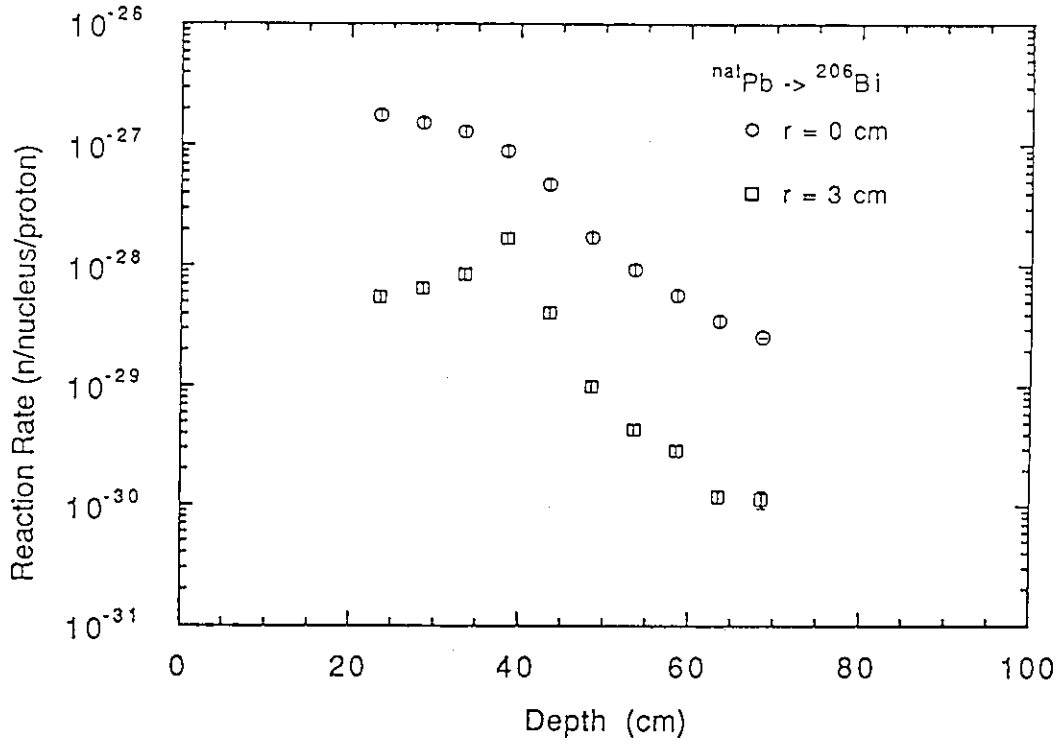

Figure 4. Spatial distribution of the reaction rate for ^{206}Bi produced in in the lead samples for 500 MeV protons injected in the lead assembly.

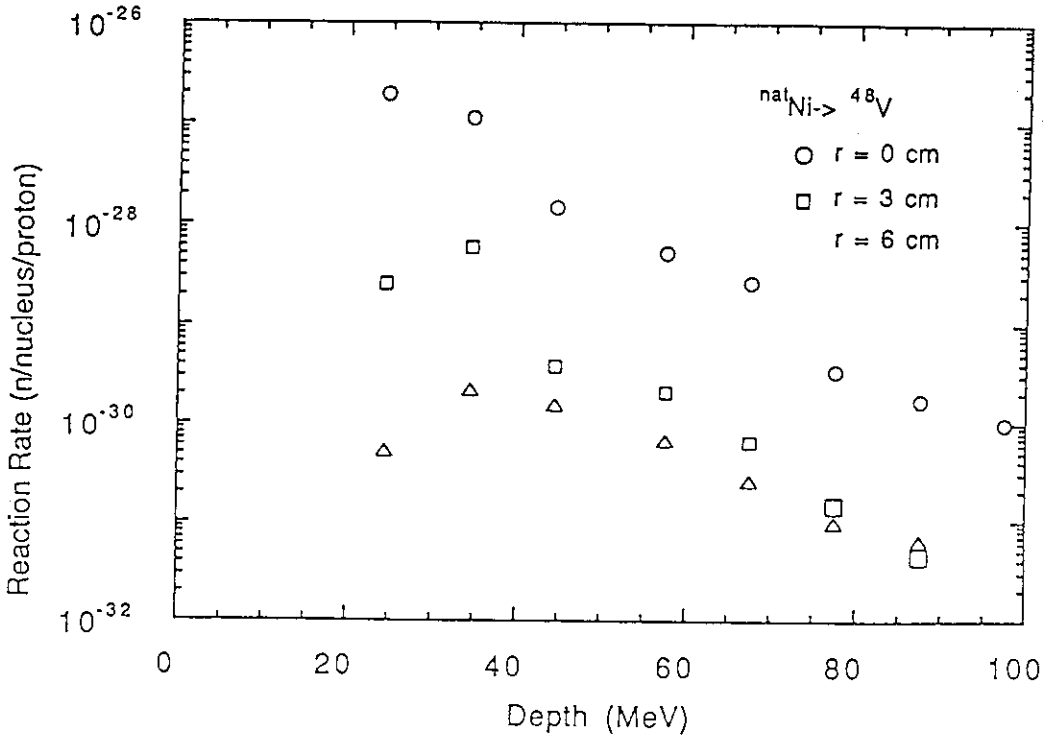

Figure 5. Spatial distribution of the reaction rate for ^{48}V produced in in the nickel samples for 500 MeV protons injected in the lead assembly.

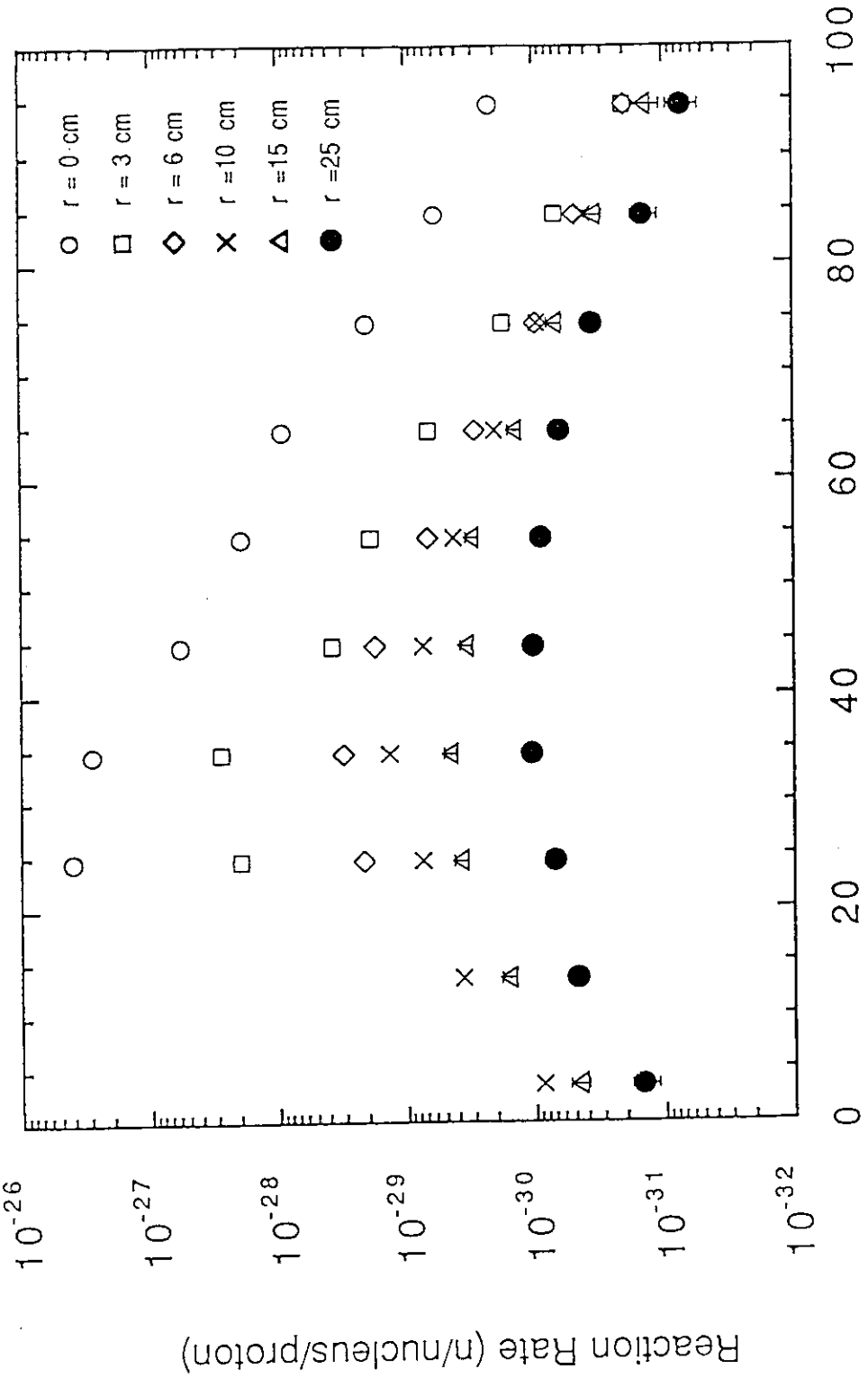

Figure 6. Spatial distribution of the reaction rate for ^{57}Ni produced in in the nickel samples for 500 MeV protons injected in the lead assembly.

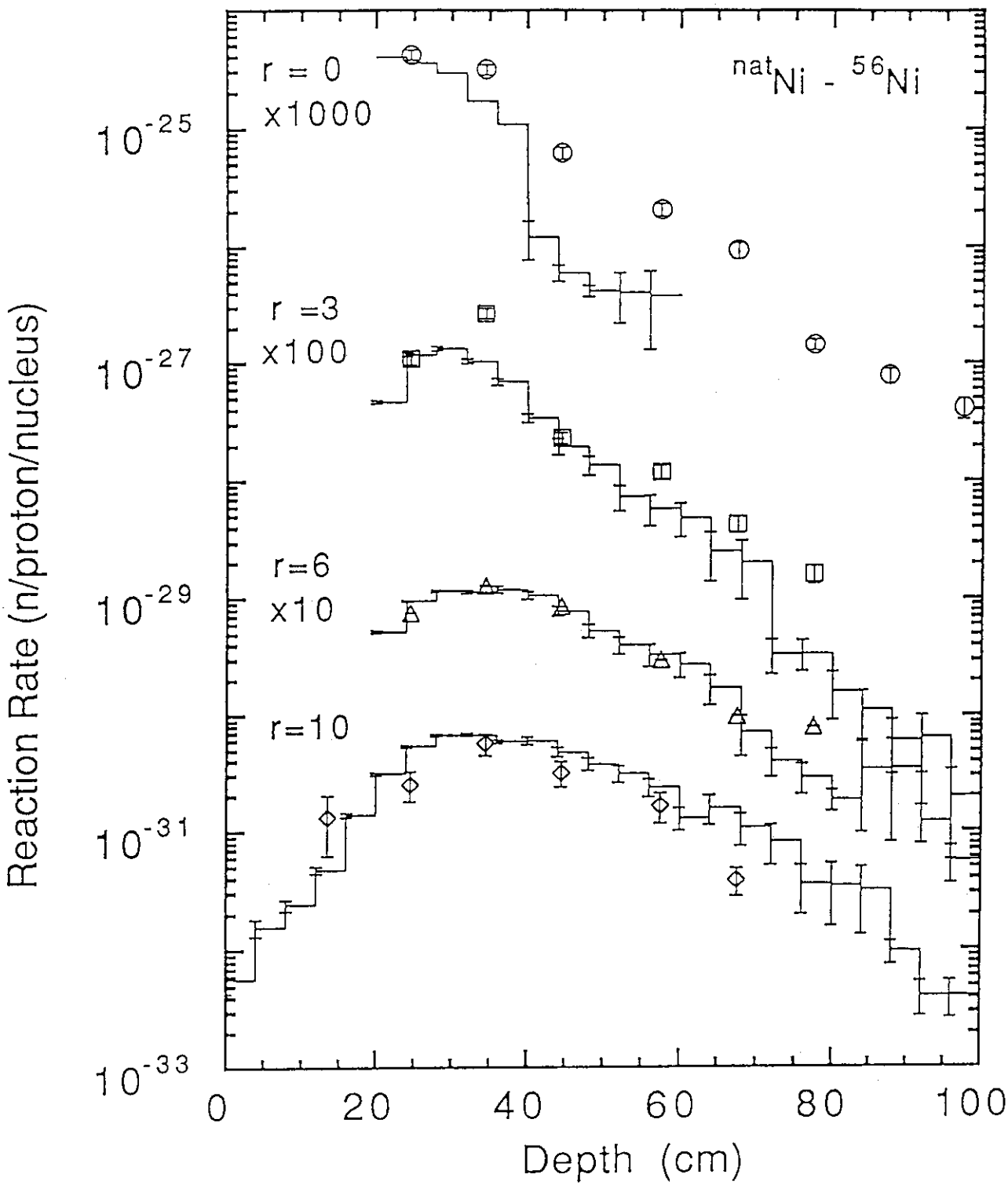

Figure 7 Spatial distribution of the reaction rate for ^{56}Ni produced in the nickel samples for 500 MeV protons injected in the lead assembly. Open marks stands for the experimental results. Lines represents the calculated ones.

1.2 Thick Target Neutron Yield for Charged Particles

Kazuo Shin and Kagetomo Miyahara
Department of Nuclear Engineering, Kyoto University
Yoshida, Sakyo-ku, Kyoto 606, Japan

Yoshitomo Uwamino
Institute for Nuclear Study, University of Tokyo
Midori-cho 3-2-1, Tanashi, Tokyo 188, Japan

ABSTRACT

The systematics of the inclusive neutron yield by light and heavy ions was studied. Measurements of neutron yield data were made for combinations of thick targets (C, Al, Cu, Pb) and projectiles (40-MeV α , 120-MeV ^{12}C, 153-MeV ^{16}O). Obtained neutron angular spectra together with those in previous works (30- and 52-MeV p, 65-MeV α) were analyzed by the moving source model. Using obtained data, a simple expression for the systematics of equilibrium neutron yield was derived. For the nonequilibrium component, the neutron yield was proportional to the geometrical cross section. The threshold for the nonequilibrium neutron production affected the yield for low energy projectiles. The obtained expressions from measured data were extended with some modifications to describe higher energy data, which were generated at 337 MeV/u by a intranuclear cascade-evaporation code HIC.

I. INTRODUCTION

Inclusive neutron production data from charged particles are fundamental for the shielding study of ion accelerators, since they are source data for shielding calculations. However, the number of inclusive neutron production data existing is not enough,[1] especially for heavy ions the data are very rare. Therefore, it is important to study the systematics of the neutron yield to assess unknown data.

We measured the neutron production data from C, Fe, Cu and Pb thick targets bombarded by 30- and 52-MeV p 33-MeV d, 65-MeV ^3He and 65-MeV α .[2-4] In this work the measurement was extended to heavy ions and the systematics of the inclusive neutron yield covering both light and heavy ions is studied. The objective of the study is to derive approximate expressions for the neutron yield from general combinations of projectiles and targets.

The intranuclear cascade evaporation(INCE) model was showed to give a good prediction to secondary proton-like spectra at higher energies of 400 MeV/u and 800 MeV/u.[5] The method was applied in this work to systematically generate inclusive neutron production data at 337 MeV/u.

The expressions which were obtained from the studies on the measured neutron yield data are applied to the calculated higher energy data with some modifications.

II. EXPERIMENTAL PROCEDURES

The measurement of secondary neutron-energy and angular distributions was made at the SF-cyclotron facility at the Institute for Nuclear Study, University of Tokyo. The experimental arrangement is shown in Fig. 1. The ion beams used in this work were 40-MeV α , 120-MeV ^{12}C and 153-MeV ^{16}O. Targets of C, Al, Cu and Pb which were thicker than the ion stopping range were bombarded by the ions and neutron spectra were detected by an 3 in. dia. by 3 in. length NE-213 scintillator at angles 0°, 30°, 75°, 120° and 150°. The detector was located 2 m down stream from the target. The obtained pulse height spectra were analyzed by the unfolding method by FERDO-U code[6] with a

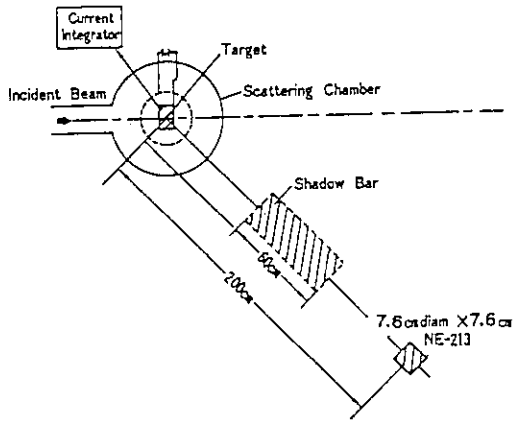

Fig.1 Experimental arrangement.

response matrix which was constructed from measured and calculated response functions.[7] The background was estimated by similar measurements with an iron and polyethylene shadow shield inserted between the target and the detector.

III. EXPERIMENTAL RESULTS AND DISCUSSIONS

A. Moving Source Analysis

Measured neutron angular spectra of this work and the previous works (data of 30- and 52-MeV p, and 65-MeV α) were fitted by the two-component moving source model of Eqs. (1) and (2):

$$\phi(E_n, \theta) = \sum_{i=1}^{2} M_i \frac{E_n}{2(\pi \tau_i)^{3/2}} \exp(-\frac{E_s}{\tau_i}), \quad (1)$$

$$E_s = E_n - 2\varepsilon_i E_n \cos\theta + \varepsilon_i, \quad (2)$$

where M_i is the source intensity, τ_i the nuclear temperature, ε_i the source moving energy in terms of the kinetic energy of a nuclon, E_n the neutron energy and θ the neutron emission angle in the laboratory frame.

As is illustrated by Fig. 2, which is for the case of the ^{12}C ion on the Pb target, the neutron angular spectra are very well reproduced by two sources components, one with smaller ε (equilibrium neutron: EN) and the other with higher source speed (nonequilibrium neutron: NEN). The total neutron yield is dominated by the EN component. The contribution by the NEN component is about one-tenth.

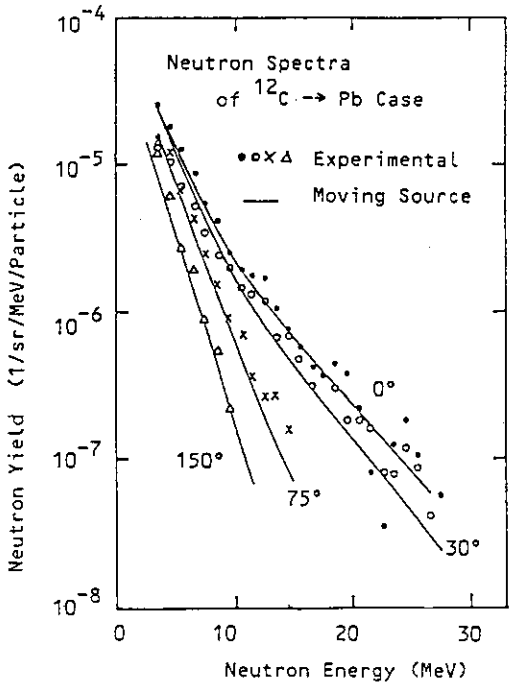

Fig.2 Fitting by the moving source model.

The systematics of the neutron yield was studied separetely for the EN and NEN components using M_i values obtained by the data fitting.

B. Equilibrium Neutron Component

Fig. 3 summarizes the nuclear temperature of the EN component, where the temperature τ is plotted vs the excitation energy that projectile-like or target-like fragment shared and is calculated by Eq. (3);

$$E = \{ E_P \frac{A_T}{A_P+A_T} - (V-Q) \} \frac{A}{A_P+A_T}, \quad (3)$$

where E_P is the projectile energy, A_P and A_T the mass of the projectile and the target, A the mass of the fragment, V the Coulomb barrier, Q the effective Q value for the (n,p) reaction. The value Q is set zero for other projectiles. Data of the 40-MeV α are not included in Fig. 3. The reason will be described later. The figure shows that the nuclear temperature data for each target are closely on a unique curve and the shape of the curves for different targets resembles one another.

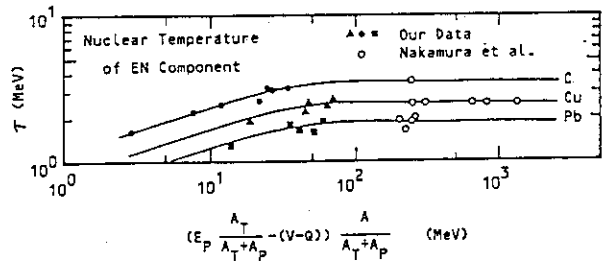

Fig.3 Nuclear temperature of EN component.

The temperature τ is proportional to $A_T^{-1/5}$. Then, we use the relation $E = a\tau^2$ between the excitation energy E and τ with the level density parameter a, and assume the proportionality of a to A_T, i.e. $a = A_T/8$, to obtain E is proportional to $A_T^{3/5}$.

For this excitation energy, the neutron multiplicity from excited nuclei was estimated using calculated data of Dostrovsky et al.[8] by the evaporation model, with the assumption that the multiplicity was proportional to the excitation energy. The result was that the neutron multiplicity was approximately proportional to the target mass number A_T.

The neutron production cross section for the EN component from the target in the central collision would be expressed by the target

geometrical cross section times the nucleon number in the projectile times the neutron multiplicity. The exchange of A_T with A_P would give the cross section for the projectile evaporation. So the total EN cross section would be,

$$\sigma_n = g(A_P, E_P)\ (A_P A_T^{5/3} + A_T A_P^{5/3})\ f\ , \qquad (4)$$

where g is a function of A_P and E_P. The factor f is the correction for the Coulomb barrier,

$$f = 1 - \frac{A_T + A_P}{A_T}\ \frac{V-Q}{E_P}\ . \qquad (5)$$

In Fig. 4, the result of the equations (4) and (5) with assuming a constant g is compared with measured data of the total neutron production cross section by heavy ions of 10-MeV/u energy given by Hubbard et al.[9] The dependence of the neutron cross section on the target and projectile mass numbers is very well reproduced. Note that at the 10-MeV/u energy the neutron yield is dominated by the EN component as was already pointed out for Fig. 2.

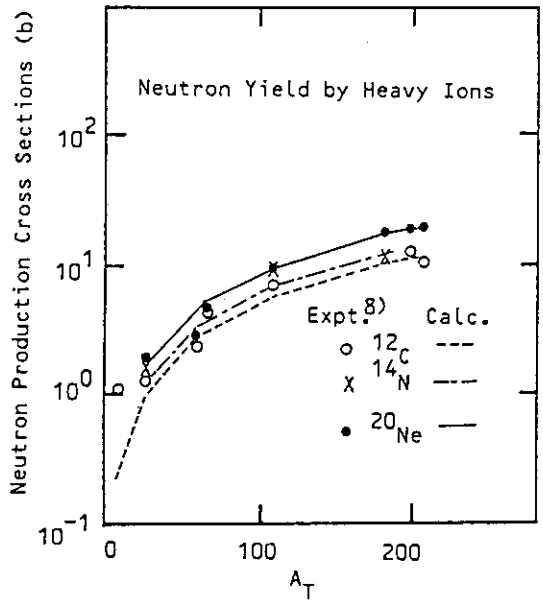

Fig.4 Neutron production cross sections by 10 MeV/u heavy ions.[9]

In thick target, the projectile ion slows down by the ionization energy loss. When the energy of the projecttile is low, the dominant nuclear reaction is the complete fusion. The neutron production cross section by this reaction was derived as

$$\sigma_n = g'(A_P, E_P)\ \pi R_B^2\ (A_P + A_T + 15) f, \qquad (6)$$

where $R_B = \sigma_0 (A_P^{1/3} + A_T^{1/3})$.

The neutron multiplicity was assumed to be proportional to $A_T + A_P + 15$ from the consideration on nuclear temperature of the 40-MeV α case, where the fusion reaction seemed to be the dominant process. The value σ_0 was assumed as $\sigma_0 = 1.0$ for $2.04(V-Q) < E_C$, and $\sigma_0 = 1.4$ for $E_C \leqq 2.04(V-Q)$, where E_C is the center of mass energy of the system.

Above E_C=6.0 MeV, it was considered that the neutron production was dominated by the fusion-like central collision, and hence the neutron production cross section was giveb by Eq. (4). For heavier targets, the upper limit energy of the complete fusion reactions decreases. Corresponding to this, E_C=2.6 MeV was used for the Pb target.

In the calculated data by the evaporation model of Dostrovsky et al.,[3] the neutron multiplicity seemed to increase in proportion to the square root of the excitation energy. Using these data, the function g or g' in Eq. (4) or (6) was assumed as,

$$g(A_P, E_P) = \frac{E_C - V}{A_P}\ g_0, \qquad (7)$$

where g_0 is a constant. For the function g', g_0 is replaced by another constant g_0'.

The level density parameter a exhibits oscillation with A_T at low excitation energies due to the shell effect.[11] This effect should be incorporated in Eqs. (4) and (6) when E_P is small. So far we simply assumed that the neutron multiplicity was proportional to the nucleus excitation energy which in turn was proportional to a, where we assumed the relation $a = A_T/8$. Hence, for the correction for the above effect, σ_n of Eqs. (4) and (6) should be multiplied by the ratio of the level density parameter to A_T. In this work, we took theoretically calculated level density parameter data[11] which depended on both the nucleus and its excitation energy.

The thick target neutron yield is given by the following, neglecting the neutron production by secondary ions,

$$Y_n = \int_{E_m}^{E_P} N \sigma_n(E) \left(\frac{dE}{dx}\right)^{-1} dE \qquad (8)$$

where N is the target atomic density, E_m the minimum energy for $f \geqq 0$.

Figure 5 summarizes the comparison of the results of Eq. (8) with our measured data and other ones[9, 12] for 100-MeV p and ~10-MeV/u N and Ne. The ratio $g_0'/g_0 = 1.8$ was assumed so that the

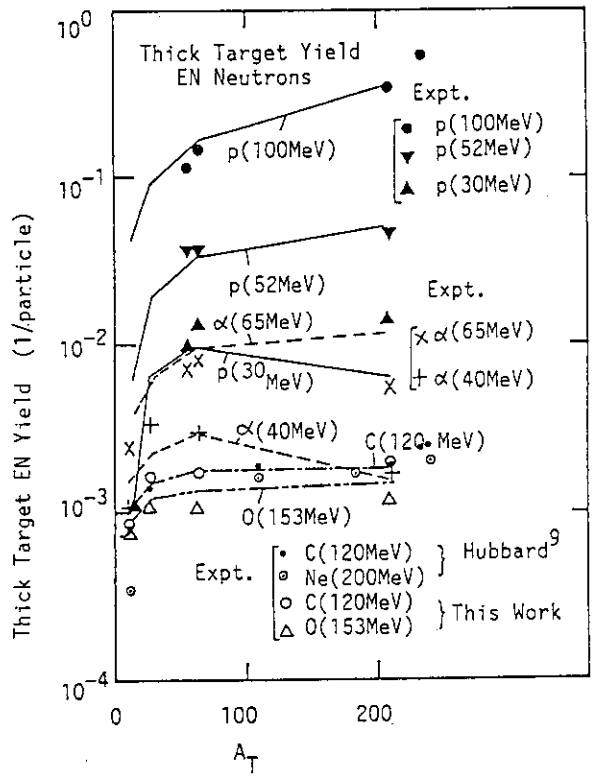

Fig.5 EN neutron yield by ligh and heavy ions.

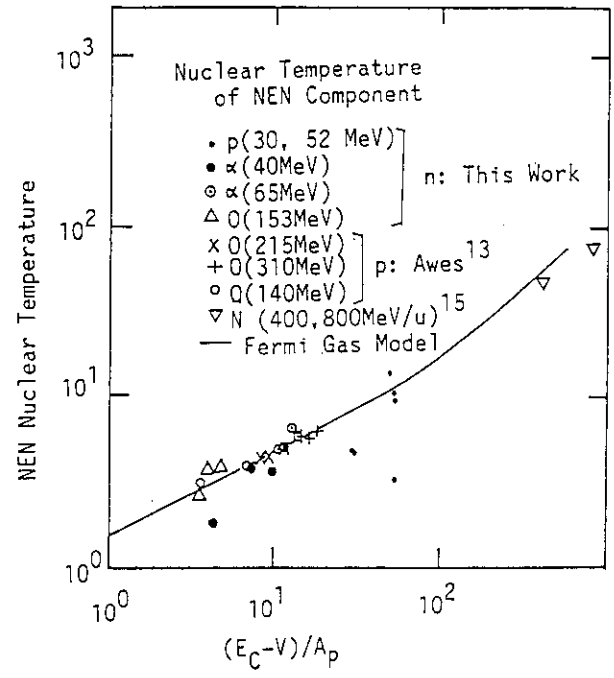

Fig.6 Nuclear temperature of NEN component.

best fit to the measured data might be obtained. Then the dependence of the neutron yield on the target, projectile and the ion energy is reproduced well by the present model.

C. Nonequilibrium Neutron Component

The temperature τ of nonequilibrium protons emitted from heavy ion reactions was reproduced well by the local hot spot(LHS) model.[13] In the model, the nonequilibrium protons were emitted from a thin layer where the target and the projectile nuclei were contacting. The same model was assumed in this work for the NEN production.

Measured nuclear temperature of the NEN component is summarized in Fig. 6, where the temperature of nonequilibrium protons is cited from Ref. 13. The solid curve in the figure was calculated by the Fermi gas model assuming the LHS region was composed of nucleons from the projectile and the target at the ratio of 1:2.5. The experimental data are fitted well by the LHS model except for the cases of the proton incidence. For protons, the hot zone would be formed by the preequilibrium process strongly depending on the target mass.

The neutron production rate from the LHS should be proportional to the probability of contact (geometrical cross sections) times the probability of neutron existing in the region,

$$\sigma_n = s(A_P, E_P)\, f\, \frac{A_T - Z_T}{A_T}\, \frac{A_P - Z_P}{A_P}\, A_P^{2/3} A_T^{2/3}\, \Delta, \quad (9)$$

where s is a function of A_P and E_P, and Z_T and Z_P the Z number of the target and the projectile. The factor Δ depends on the thickness of the hot spot. We assumed the same correction f for the Coulomb barrier as for the EN component.

The thick target neutron yield of the NEN component was given by inserting Eq. (9) into Eq. (8), where we assumed constant values for the function s and the thickness Δ. At this moment, the energy dependence of the yield is not described by Eq. (9), since the energy dependence of s and Δ is not taken into consideration. This very simple description well reproduced the target dependence of our data for 30- and 52-MeV p and 65-MeV α but failed in the cases of 40-MeV α and heavy ions. The projectile energy in the latter cases are ~10 MeV/u, while the former are 30, 52 and 16.3 MeV/u, respectively.

We considered that there was a threshold in the velocity of contacting nuclei to produce nonequilibrium neutrons. Unless the velocity is larger tha E_0 in terms of nucleon kinetic energy, the NEN is not produced. Then the lower boundary E_m of the integration of Eq. (8) was given for the NEN component by,

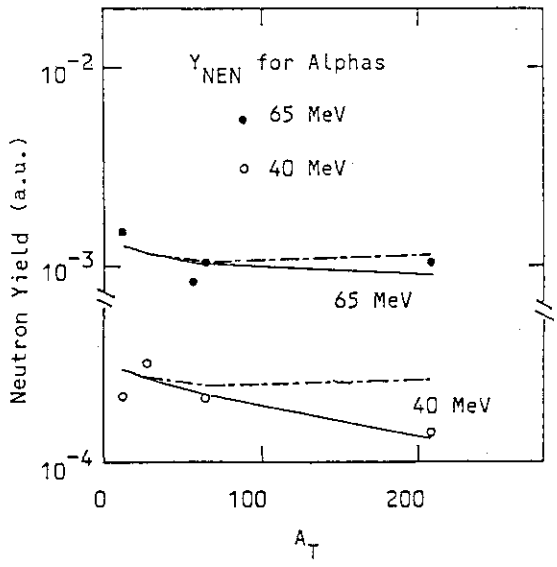

Fig.7 NEN yield by α particles.

$$E_m = A_P E_\Omega + (A_T + A_P)(V-Q)/A_T \ . \qquad (10)$$

The target dependence of all our data for the NEN yield were fitted well by the above model with E_Ω = 2 MeV. This is demonstrated by the solid line in Fig. 7 for the cases of the α particle incidence. The dashed lines are the results for E_Ω = 0 MeV.

IV. CALCULATION BY INCE MODEL

The INCE model code HIC[14] was used to generate the inclusive neutron yield data for higher energy projectiles. Before carring out the systematic calculations, the accuracy of the code was tested by comparing calculated results with experimental data of proton-like spectra by Nagamiya et al.[15] made by 400- and 800-MeV/u ^{20}Ne and ^{40}Ar for the targets of KCl, NaF and Pb, and data of neutron spectra produced by 337-MeV/u ^{20}Ne incidence on C, Al, Cu and ^{238}U targets by Cecil et al.[16]

Figure 8 demonstrates the comparisopn of the HIC calculation with Cecil experiment for the case of the Cu target. The absolute value of the data may be overestimated by about 40 %, and also in the calculated spectrum at the forward angle the edge due to the knockout of the target nucleons seems to be too large. Except these points, the overall spectral shape and angular distribution of the experimental data was well reproduced by the HIC calculation.

The proton-like spectra of Nagamiya's data were reproduced well by the HIC calculation.

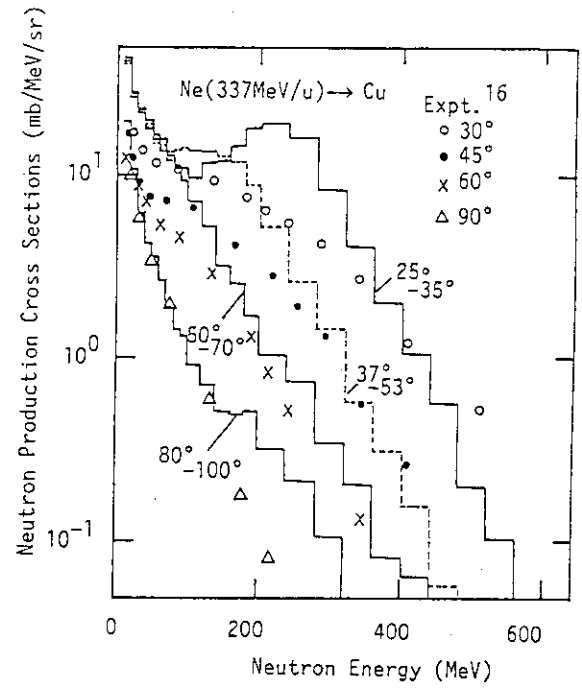

Fig.8 Neutron angular spectra produced by 337 MeV/u Ne on Cu.

The systematic calculations of neutron production cross sections were made by the code for projectiles of α, C, Ne, Ar of 337-MeV/u energy injected on C, Fe, Pb or ^{238}U target. Numbers of neutrons due to the target evaporation and the projectile evaporation were summed to yield the EN component. The angular distribution of the cascade component from the both nuclei at angles larger than 30° was smoothly extrapolted to 0° to yield the NEN component. The knockout component, which appeared only at the very forward angles, was removed by the process.

The neutron yield data from reactions of Pb projectiles with α, C, Ne and Ar targets, which were reversed reactions of α, C, Ne, Ar projectiles on the Pb target, should be the same as those of the reversed reactions, if the knockout component was the same. This was assumed in the following analysis.

V. RESULTS OF CALCULATION AND DISCUSSIONS

A. Nonequilibrium Neutron Component

It is needed to decide the projectile and the target dependence of the LHS thickness Δ to apply Eq. (9) to the HIC caluclated results. As NEN neutrons were produced from the hot thermal spot where nucleons made multiscattering with each other and followed a diuffusion-like

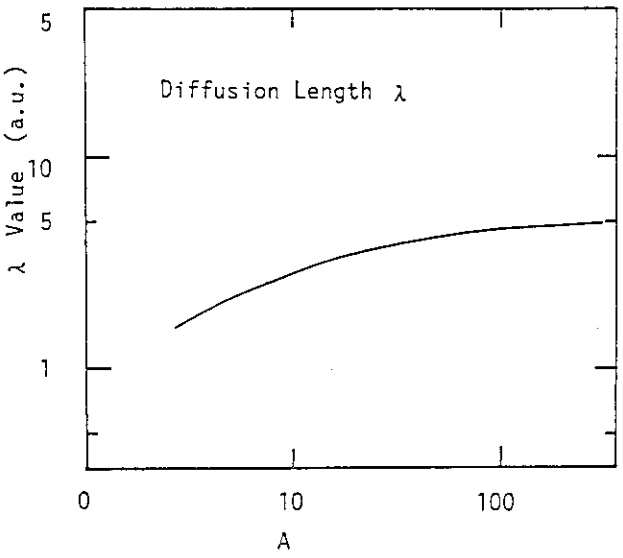

Fig.9 λ values as a function of nucleus mass.

process. Hence, we utilized the following expression for Δ,

$$\Delta = \int_0^{A_P^{1/3}} p(x, \lambda_T)dx \int_0^{A_T^{1/3}} p(x, \lambda_P)dx \quad , \qquad (11)$$

where $p(x, \lambda)=\exp\{-(x/\lambda)^2\}$,

and λ is diffusion length.

Figure 9 shows λ as a function of the mass of nucleus, which was decided so that Eq. (9) with Δ of Eq. (11) best fit the calculated NEN yield. The results of the comparison of the NEN yield are shown in Fig. 10, where

$$\sigma = \sigma_n / \{A_T/(A_T-Z_T)\} / \{A_P/(A_P-Z_P)\} \quad , \qquad (13)$$

is plotted vs the mass of the target for each projectile. The function s was assumed to be constant. The overall behavior of the NEN yield on the target and the projectile is very well reproduced by the above simple model.

B. Equilibrium Neutron Component

For the EN component, Eq. (4) is applied and the dependence of the function g on A_P is tested at the high energy.

The reproducibility of the target dependence of the EN yield by Eq. (4) with a constant g is demonstrated in Fig. 11 for the incidence of Ne on C, Al, Cu and U targets. For the other projectiles, Eq. (4) also reproduced the target dependence of the En yield if the g value was reduced for heavier projectile.

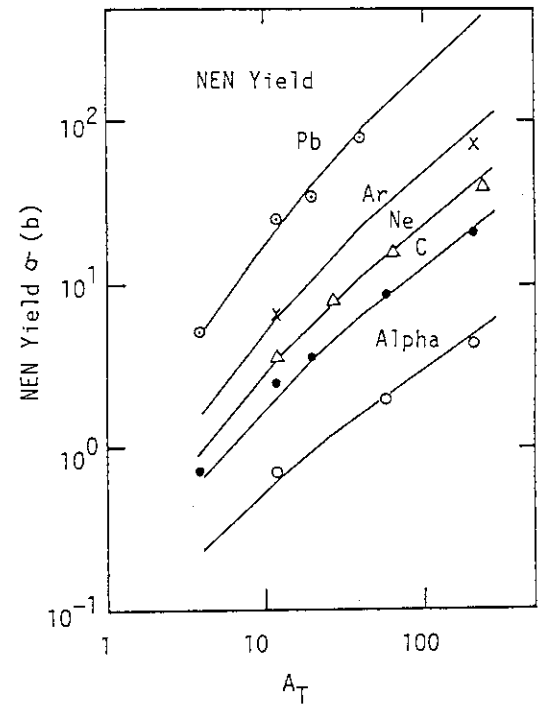

Fig.10 NEN yield at 337 MeV/u energy.

The heavier projectile produced more number of NEN in each reaction. This means more energy was taken out before reaching the nulear equilibrium. This situation was simply express by the following equation;

$$g \sim g_0 \{1-\beta(A_T, A_P)\Delta\} \quad , \qquad (14)$$

where Δ is given by Eq. (11), β the reduction rate of the remaining excitation energy per NEN. Here we assumed β to be constant, then Eq. (14) is rewritten to Eq. (15),

$$g \sim g_0(1-\beta)^{\Delta} \quad . \qquad (15)$$

The value of g was calculated by comparing the remaining part of Eq. (4) with the HIC calculated EN yield. The results are showed in Fig. 12. The best fit to these results was obtained by Eq. (15) with β =0.132, g_0=9.1x10^{-4}.This is illustrated in the figure by solid lines.

Another interpretation is possible for the reduction in the g value. Lately it was showed that the thermal energy of hot nuclei had an upper limit of ~ 800 MeV for the $^{40}Ar+^{232}Th$ system[17] because of the reaction dynamics. If this upper limit is also used in our systems, the reduction rate in the excitation energy by

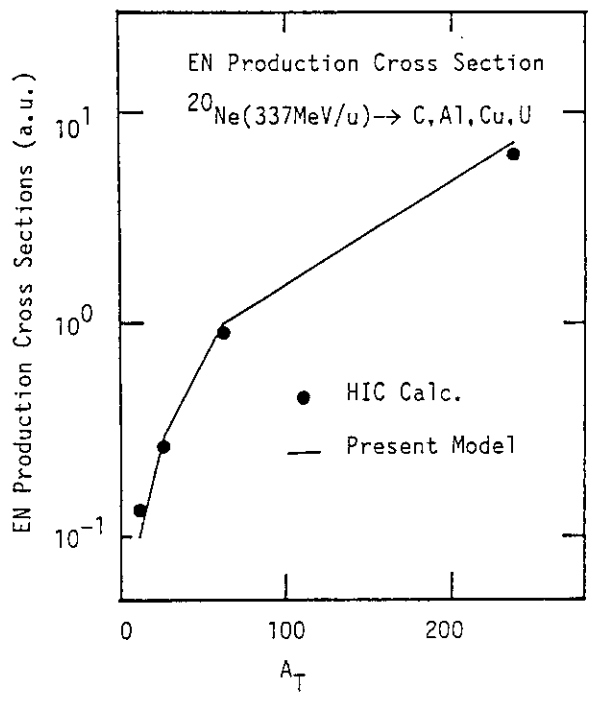

Fig.11 EN yield for 337 MeV/u Ne on C, Al, Cu and ^{238}U.

nonequilibrium particle emission should be ~ 800/(337A_P). As was alread discussed, the EN neutron multiplicity was closely proportional to the square root of the excitation energy. Hence, the reduction rate in the EN yield caused by the reduction in the excitation energy should be,

$$g \sim k\sqrt{\frac{800}{337A_P}} \quad , \qquad (16)$$

where k is a constant. Results by Eq. (16) are showed in Fig. 12 by dotted lines. It is seen in the figure that Eq. (16) approximately describes the projectile dependence of the g value.

As a conclusion, an approximate form of the function g at the higher energy is ,

$$g = g_0 \frac{1}{A_P}, \qquad (17)$$

where g_0 is a constant. Due to the saturation of the excitation energy at high energies, the energy dependence of the function g is switched from Eq. (7) to Eq. (17)

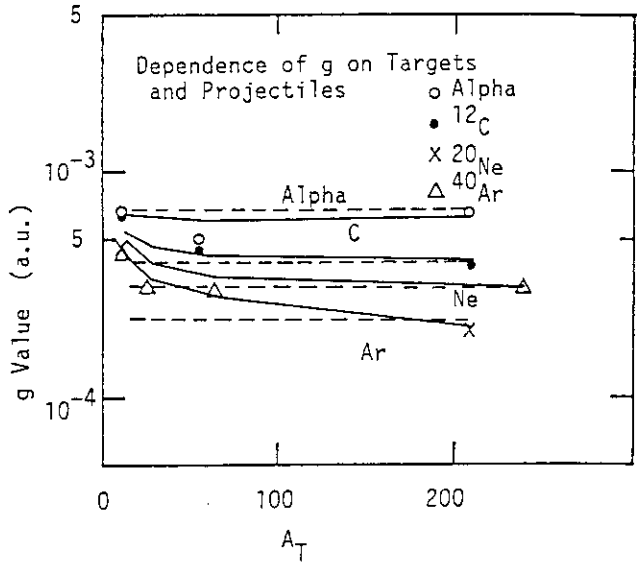

Fig.12 Dependence of the function g on projectiles and targets.

References

1. T. Nakamura et al.,"Annotated References on Neutron and Photon Production from Thick Targets Bombarded by Charged Particles" INS-TS-20, Institute for Nuclear Study, Univ. Tokyo (1981)
2. T. Nakamura, M. Yoshida and K. Shin, Nucl. Instr. Methods 151, 493 (1978)
3. T. Nakamura, M. Fujii and K. Shin, Nucl. Sci. Eng. 83, 444 (1983)
4. K. Shin, K. Hibi, M. Fujii, Y. Uwamino and T. Nakamura, Phys. Rev. C29, 1317 (1984)
5.Y. Yariv and Z. Fraenkel, Phys. Rev. C 20, 2227 (1979).
6. K. Shin, Y. Uwamino and T. Hyodo, Nucl. Technol. 53, 78 . (1981)
7. K. Shin et al., Nucl. Instr. Methods in Phys. Res., A308, 609 (1991).
8. I. Dostrovsky, P. Rabinowitz and R. Bivins, Phys. Rev. 111, 1659 (1958)
9. E. L. Hubbard, R. Main and R. Pyle, Phys. Rev. 118, 507 (1960)
10.H. Gutbrod et al., Nucl. Phys., A213, 267 (1973).
11.T. Matsuse and S. Lee, "Recent Topics on Nuclear Fission Accompanied with High Spin", in Proc. Specialists' Meeting on Physics and Engineering of Fission and Spallation, Ed. Y. Nakagome, Res. React. Inst., Kyoto Univ. (1988).
12 R. Lambert et al., Nucl. Instr. and Methods, 214, 349 (1983).
13. T. Awes et al., Phys. Lett. 103B, 417 (1981)
14. H. Bertini et al., "HIC1: A First Approach to the Calculation of Heavy-Ion Reactions at Energies ≧ 50 MeV/Nucleon" ORNL-TM-4134 (1974).
15. S. Nagamiya et al., Phys. Lett., 81B, 147 (1979).
16. R. Cecil et al., Phys. Rev. C24, 2013 (1981).
17. D. Jiang et al, Nucl. Phys. A503, 560 (1989).

1.3 Measurement of Neutron Activation and Photoneutron Cross Sections

Takashi Nakamura

Cyclotron and Radioisotope Center, Tohoku University
Aoba, Aramaki, Sendai 980, Japan

Abstract

Using a semi-monoenergetic neutron field which was produced from a Be target bombarded by protons of 9 different energies between 20 and 40 MeV, we measured the neutron activation cross sections of natural samples of Na, Mg, Al, Si, Ca, V, Cr, Mn, Cu, Zn and Au in the energy range of 10 to 40 MeV.

We also measured the average photoneutron cross sections of ^{137}Cs, ^{84}Sr, ^{86}Sr, ^{88}Sr, ^{85}Rb, ^{87}Rb, ^{98}Ru and ^{104}Ru isotopes in giant dipole resonance region from 9 to 25 MeV, using bremsstrahlung radiation of 60 MeV maximum energy. For the measurement of ^{137}Cs(γ,n) cross section, we used the nuclear recoil separation method coupled with the internal standard (natural ^{133}Cs) technique. We investigated the isotopic dependence of the average photoneutron cross sections in giant resonance region from our experimental data and other experimental data for Ge, Se, Zr, Mo, Sn, Te, Ce, Nd and Sm isotopes.

1. Measurement of Neutron Activation Cross Sections

Neutron activation cross sections above 20 MeV are very scarce due to the poor availability of monoenergetic neutron source and no evaluated data files exist, despite of the increasing request as basic data for neutron dosimetry, radiation safety and material damage study.

Using a proton beam and a target system consisting of Be disk and water coolant, an intense semi-monoenergetic neutron field for activation experiment of energy up to 40 MeV was developed[1] at the SF cyclotron of the Institute for Nuclear Study, University of Tokyo. Proton beams of energies

of 20, 22.5, 25, 27.5, 30, 32.5, 35, 37.5 and 40 MeV were impinged to 1-mm-thick (E_p= 20 to 37.5 MeV) and 2-mm-thick (E_p= 40 MeV) Be targets backed by water coolant which also was used as proton beam stopper. The neutron energy spectra measured with a NE-213 scintillator are shown in Fig. 1. Since the Be target is not thin, a high energy peak due to the ^{9}Be(p,n) reaction in the neutron spectrum is rather broad and a low energy tail coming from the Be target and the water beam stopper is present. The vertical bars are the unfolding errors estimated by the FERDO code.

Activation experiment in this neutron field has been performed with natural samples of Na, Mg, Al, Si, Ca, V, Cr, Mn, Cu, Zn and Au. This work has already been published in journals[2,3] and is to be published soon[4]. The reaction rates of the irradiated samples were obtained from the gamma-ray spectrometry using a Ge detector. For long-lived isotopes of ^{26}Al (7.2×10^{5} y) produced by the ^{27}Al(n,2n) reaction, the reaction rates were measured by using accelerator mass spectrometry system at the tandem Van de Graaf accelerator of University of Tokyo which has been equipped for this method.

Since the neutron fields used in this activation experiment are not purely monoenergetic, excitation functions cannot directly be obtained, but can be obtained by using the unfolding method, SAND-II[5] and NEUPAC[6] codes, and the least square fitting from the reaction rates at 9 different semi-monoenergetic neutron fields. An initial guess of excitation function is necessary for these techniques, and was mostly calculated by the ALICE/LIVERMORE82 code[7] when no published data are available. In the least square fitting (LSF), an initial value calculated by the ALICE code was adjusted to the 9 measured reaction rates. The NEUPAC code evaluates the propagation of errors of initial guess values, neutron spectra and reaction rates to the resultant excitation function. Errors of the neutron spectra are about 10% in the peak region and about 30 to 50% in the low energy tail as shown in Fig. 1, and errors of reaction rates are about 10%. Errors of initial guess values are unknown. If experimental data are available, these errors were estimated by comparing the initial guess value with experimental data, otherwise, they were assumed to be 100%.

Among of many cross section data obtained, several experimental results are exemplified in Figs. 2a through 2g, where the results obtained by the SAND-II and NEUPAC unfolding codes are shown in a thick zigzag solid line

and a histogram, respectively. The vertical bars attached on the histogram show errors estimated by the NEUPAC code. The LSF results are shown in a thick dotted line. If some reference data are available, they are also shown in a thin solid line for ENDF-B/V[8], in a thin dotted line for ENDF-B/IV[9], in a thin dashed line for IAEA report[10], in a thin dash and dot line for the Greenwood's data[11], and in circles for BNL-325[12]. The results and discussions are described for each reactions in the following.

1) $^{23}Na(n,2n)^{22}Na$

The two unfolded results of SAND-II and NEUPAC agree well each other as shown in Fig. 2a, and they are close to the curve of IAEA. The initial guess was calcurated by ALICE and the error was set to be 70%. The LSF result is lower than the others in the energy region below 25 MeV reflecting that the ALICE result has a gentler rising slope. The experimental data collected in the BNL-325 can be classified into 3 groups, and our results of SAND-II and NEUPAC are close to the middle data of Menlove et al.[13] below 20 MeV. The ENDF-B/IV evaluation seems to give underestimation between 15 MeV and 20 MeV, and the ENDF-B/V evaluation fitted to the upper data of Liskien et al.[14] might be overestimated.

2) $^{27}Al(n,\alpha)^{24}Na$

The initial guess was derived from the data of Greenwood and the error was set to be 15%. Our two unfolded results in Fig. 2b agree almost completely with the BNL-325 data and also the evaluation of Greenwood and ENDF-B/V within the error. A small bump at 25 MeV seen in the SAND-II result might be caused by the $^{27}Al(n,n^{3}He)^{24}Na$ reaction of which the threshold energy is 24.6 MeV.

3) $^{63}Cu(n,3n)^{61}Cu$

The ALICE result was used as an initial guess of the unfolding process and the initial guess error was set to be 100%. The LSF result shows higher value than the two unfolded results as shown in Fig. 2c. No reference data are avilable for this reaction.

4) $^{63}Cu(n,2n)^{62}Cu$

The ALICE result was used as an initial guess with the assumed error of 80%. Our three results are shown in Fig. 2d, together with the reference data and are all in good agreement below 30 MeV. A small bank at 32 MeV in the SAND-II result might come from the $^{65}Cu(n,4n)^{62}Cu$ reaction of which the

threshold energy is 28.7 MeV. Our results have lower values than the BNL-325 data in the energy region above 15 MeV.

5) $^{197}Au(n,4n)^{194}Au$

The ALICE result was used as an initial guess with the assumed error of 40%. Our three results shown in Fig. 2e resemble each other. The estimation by Greenwood shows a factor of 2 higher value in the whole energy region. Our results show good agreement with the data by Bayhurst et al.[15] at 26 MeV.

6) $^{197}Au(n,2n)^{196}Au$

The initial guess for unfolding was derived from the Greenwood's data and the error was set to be 15%. As shown in Fig. 2f, the two unfolded results and the LSF result show good agreement each other except for the SAND-II result at high energy. Our results are about 15% lower than the Greenwood's estimation in the whole energy region and agree well with the lower BNL-325 data by Paulsen[16] in the peak energy region.

7) $^{27}Al(n,2n)^{26}Al$

The ALICE result was used as an initial guess with the assumed error of 30%. Our two unfolded results shown in Fig. 2g show good agreement each other. For near-threshold neutron energies, our results are compared with other experimental data[17-19], and our data are lower than those other three results but closer to Sasao's data[18]. Our results are the first experimental data that have been obtained above 15 MeV.

2. Measurement of Photoneutron Cross Sections

The photoneutron cross sections in the giant dipole resonance region obtained with monoenergetic photons have been compiled, but no experimental data presently exist for $^{90}Sr(\gamma,n)$ and $^{137}Cs(\gamma,n)$ reactions, which are of basic importance for the transmutation study of long-lived fission products in high level radioactive wastes.

It is quite difficult to measure the very weak ^{89}Sr and ^{136}Cs activities produced from $^{90}Sr(\gamma,n)$ and $^{137}Cs(\gamma,n)$ in ^{90}Sr and ^{137}Cs targets under the very strong ^{90}Sr and ^{137}Cs target activities, respectively, and also impossible to use the chemical separation technique between ^{89}Sr and ^{90}Sr, ^{136}Cs and ^{137}Cs. For the cross section measurement of $^{137}Cs(\gamma,n)$ reaction, we used the recoil separation method of ^{136}Cs atoms from the ^{137}Cs

target accompanying with neutron recoil. In order to get the absolute value of the cross section, it is necessary to get the recoil fraction of ^{136}Cs atom from the ^{137}Cs target in good accuracy, but it is quite difficult to get it because of its very low recoil energy. We therefore measured the cross section ratio of ^{137}Cs(γ,n) and ^{133}Cs(γ,n), $\sigma_{137}/\sigma_{133}$, by using the internal standard method which used natural ^{133}Cs atom as an internal standard.

We made 1 to 10 μm/cm^2 thick targets by evaporating CsCl in a small vacuum chamber onto an aluminum foil. The two kinds of CsCl solution were prepared; undiluted ^{137}CsCl solution, and mixture of undiluted ^{137}CsCl solution and ^{133}CsCl solution. The targets were assembled as a stack consisting of each target backed by an aluminum catcherfoil to collect recoil ^{136}Cs and ^{132}Cs atoms from the target. The target assembly also contained a gold foil to monitor the incident bremsstrahlung fluence by using the ^{197}Au(γ,n)^{196}Au reaction.

The target irradiation was carried out by using the electron linear accelerator of Laboratory of Nuclear Science, Tohoku University. The 60 MeV and 45 MeV electrons extracted from the Linac were injected on an 1-mm thick platinum plate to produce bremsstrahlung radiation. The electrons passed through the platinum converter were bended downward with a clearing magnet and only the bremsstrahlung beam hit the target 60 cm downstream from the converter.

After the chemical separation of Cs atoms recoiled into the aluminum catcherfoil, the gamma-ray activities of Cs atoms were measured with a Ge detector. Figure 3 shows an example of the measured gamma-ray spectrum, which indicates the photopeaks of 341, 819 and 1048 keV from the ^{136}Cs nuclei produced by ^{137}Cs(γ,n) and 668 keV from ^{132}Cs by ^{133}Cs(γ,n), together with the 662 keV photopeak from the ^{137}Cs target nuclei escaped from the target foil.

The ratios of ^{137}Cs(γ,n) and ^{133}Cs(γ,n) reaction cross sections are 1.10 ± 0.05 and 1.22 ± 0.11 for 45 MeV and 60 MeV bremsstrahlung, respectively. Both results agree well within their statistical errors, since the giant dipole resonance region is between 10 and 25 MeV photon energies. The ratios larger than 1 indicate that the average cross section of ^{137}Cs(γ,n) is higher than that of ^{133}Cs(γ,n). This work is now submitted for publication.[20]

We further investigated the isotopic dependence of the average (γ,n) cross section for each nuclide around Sr (Z=38) and Cs (Z=55) from our experimental data and the data given in Ref. (21). In Ref. (21), the excitation functions of the (γ,Xn) reactions in giant dipole resonance region are given for stable isotopes of Ge, Se, Zr, Mo near Sr, and Sn, Te, Ce, Nd, Sm near Cs. We also measured the average (γ,n) cross sections for enriched stable isotopes of ^{84}Sr, ^{86}Sr, ^{88}Sr, ^{85}Rb, ^{87}Rb, ^{98}Ru and ^{104}Ru which are lacking in Ref. (21). The sample irradiation was done by using the 60 MeV bremsstrahlung radiation under the same experimental setup as in the ^{137}Cs(γ,n) cross section measurement.

The cross sections in the giant resonance region from 9 MeV to 25 MeV were averaged by weighting with the bremsstrahlung energy spectrum calculated by the EGS-4 code.[22] Figure 4 shows the isotopic dependence of average (γ,n) cross sections thus obtained. The figure reveals the following systematics.

1) The average cross sections increase as the neutron number approaches the magic numbers of N=50 and 82, and have highest values for those magic number nuclei of Rb, Sr, Zr, Cs, Ce, Nd and Sm, except for only Mo.

2) For Se and Ru which have no neutron magic number nuclei, the average cross section values also increase with approaching the neutron magic number of N=50.

3) For Ge, Te and Sn which are separated from the neutron magic number of N=50, the isotopic dependence of the average cross section is rather flat with mass number.

These interesting systematics indicate that once the (γ,n) reaction occurs above its threhold energy which is higher for neutron magic number nuclei than for other nuclei , the neutron emission becomes easier and then the (γ,n) reaction cross section larger for neutron magic number nuclei than for other nuclei, excluding Mo nucleus. There hitherto exist no theoretical and experimental considerations on this systematics. This work is also to be submitted for publication.[23]

References

1) Y. Uwamino, T. Ohkubo, A. Torii and T. Nakamura, Nucl. Instr. and Meth., A271, 546 (1988).
2) M. Imamura, H. Nagai, M. Takabatake, S. Shibata, K. Kobayashi, K. Yoshida, H. Ohashi, Y. Uwamino and T. Nakamura, Nucl. Instr. and Meth. B52, 595 (1990).
3) T. Nakamura, H. Sugita, M. Imamura, Y. Uwamino, H. Nagai and K. Kobayashi, Phys. Rev. C43, 1831 (1991).
4) Y. Uwamino, H. Sugita, Y. Kondo and T. Nakamura, to be published in Nucl. Sci. Eng.
5) W. N. McElroy, S. Berg, T. Crockett and R. G. Hawkins, AFWL-TR-67-41, Air Force Weapons Laboratory (1967).
6) T. Taniguchi, N. Ueda, M. Nakazawa and A. Sekiguchi, NEUT Research Report 83-10, Department of Nuclear Engineering, University of Tokyo (1984).
7) M. Blann and J. Bisplingshoff, Lawrence Livermore National Laboratory Report No. UCID 19614 (1983).
8) ENDF/B Summary Documentation, BNL-NCS-17541 (ENDF-201), 3rd Edition (ENDF/B-V), Brookhaven National Laboratory (1979).
9) ENDF/B Summary Documentation, BNL-NCS-17541 (ENDF-201), 2nd Edition (ENDF/B-IV), Brookhaven National Laboratory (1975).
10) V. N. Manokhin, A. B. Pashchenko, V. I. Plyaskin, V. M. Bychkov and V. G. Pronyaev, "Activation Cross-Sections Induced by Fast Neutrons" in "Handbook on Nuclear Activation Data", Technical Reports Series No. 273, International Atomic Energy Agency (1987).
11) L. R. Greenwood, ANL/FPP/TM-115, Argonne National Laboratory (1978).
12) V. McLane, C. L. Dunford and P. F. Rose, "Neutron Cross Sections", Vol. 2, "Neutron Cross Section Curves", Academic Press Inc. (1988).
13) H. O. Menlove, K. L. Coop, H. A. Grench and R. Sher, Phys. Rev., 163, 1299 (1967).
14) H. Liskien and A. Paulsen, Nucl. Phys., 63, 393 (1965).
15) B. P. Bayhurst, J. S. Gilmore, R. J. Prestwood, J. B. Wilhelmy, N. Jarmie, B. H. Erkkila and R. A. Hardekopf, Phys. Rev. C12, 451 (1975).
16) A. Paulsen, H. Liskien and R. Widera, Atomkernenergie, 26, 34 (1975).
17) R. K. Smither and L. R. Greenwood, J. Nucl. Mater. 122&123, 1071 (1984).
18) M. Sasao, T. Hayashi, K. Taniguchi, A. Takahashi and T. Iida, Phys. Rev. C35, 2327 (1987).

19) S. Iwasaki, J. R. Dumais and K. Sugiyama, Proc. Intern. Conf. on Nuclear Data for Science and Technology, Mito, 1988, p. 295.

20) A. Yamadera, Y. Uno, T. Nakamura, I. Fujiwara, S. Shibata and T. Kase, to be submitted in Phys. Rev.

21) S. S. Dietrich and B. L. Berman, "Atlas of Photoneutron Cross Sections Obtained with Monoenergetic Photons", UCRL-94820 (1986).

22) W. R. Nelson, H. Hirayama and D. W. O. Rogers, SLAC-Report-265, Stanford Linear Accelerator Center (1985).

23) T. Nakamura, Y. Uno, A. Yamadera and T. Kase, to be submitted in Phys. Rev.

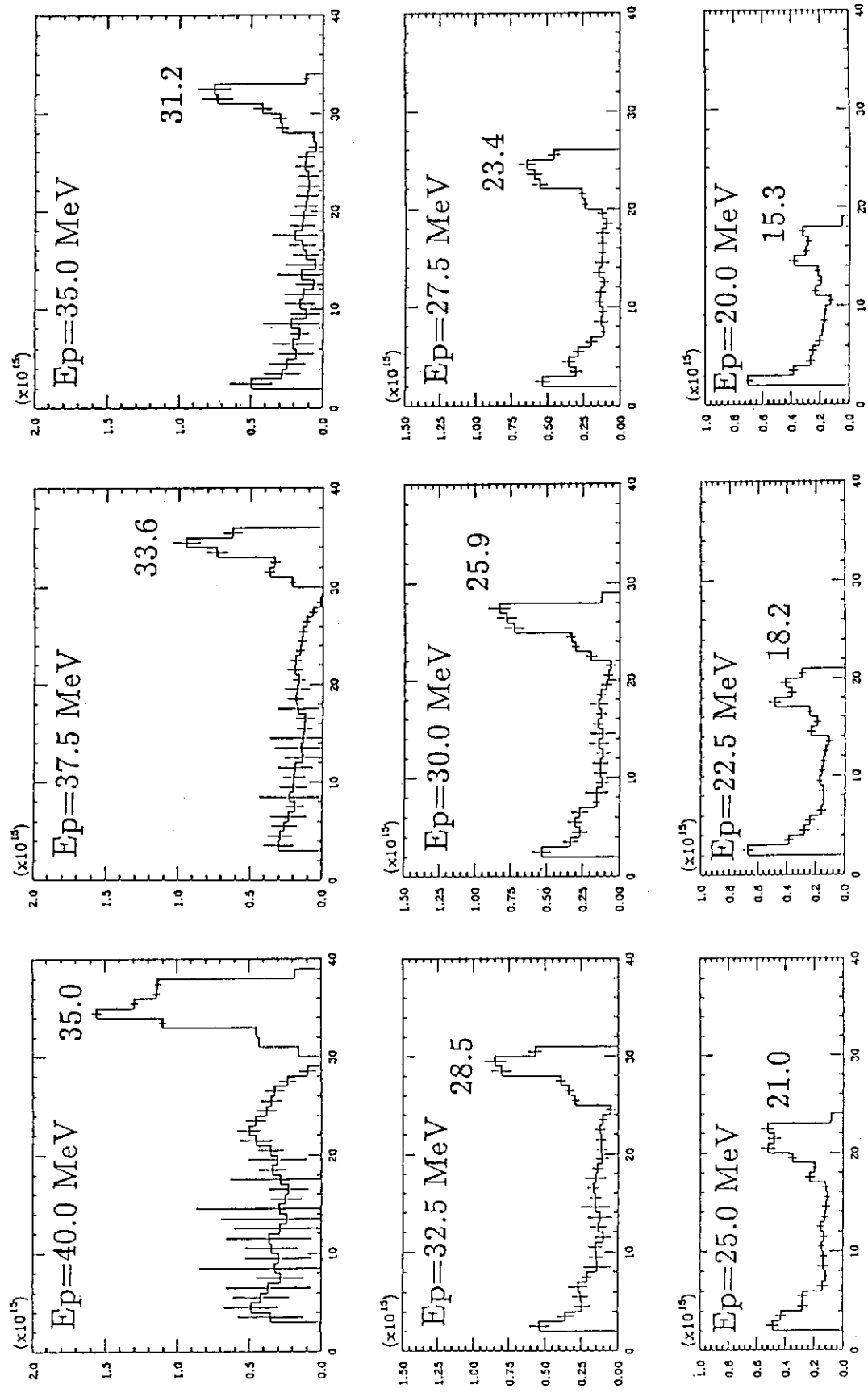

Fig. 1 Measured energy spectra of the semi-monoenergetic $^{9}Be(p,n)$ neutron field for irradiation. The digits in the figure show the incident proton energies (E_p) and average peak neutron energies.

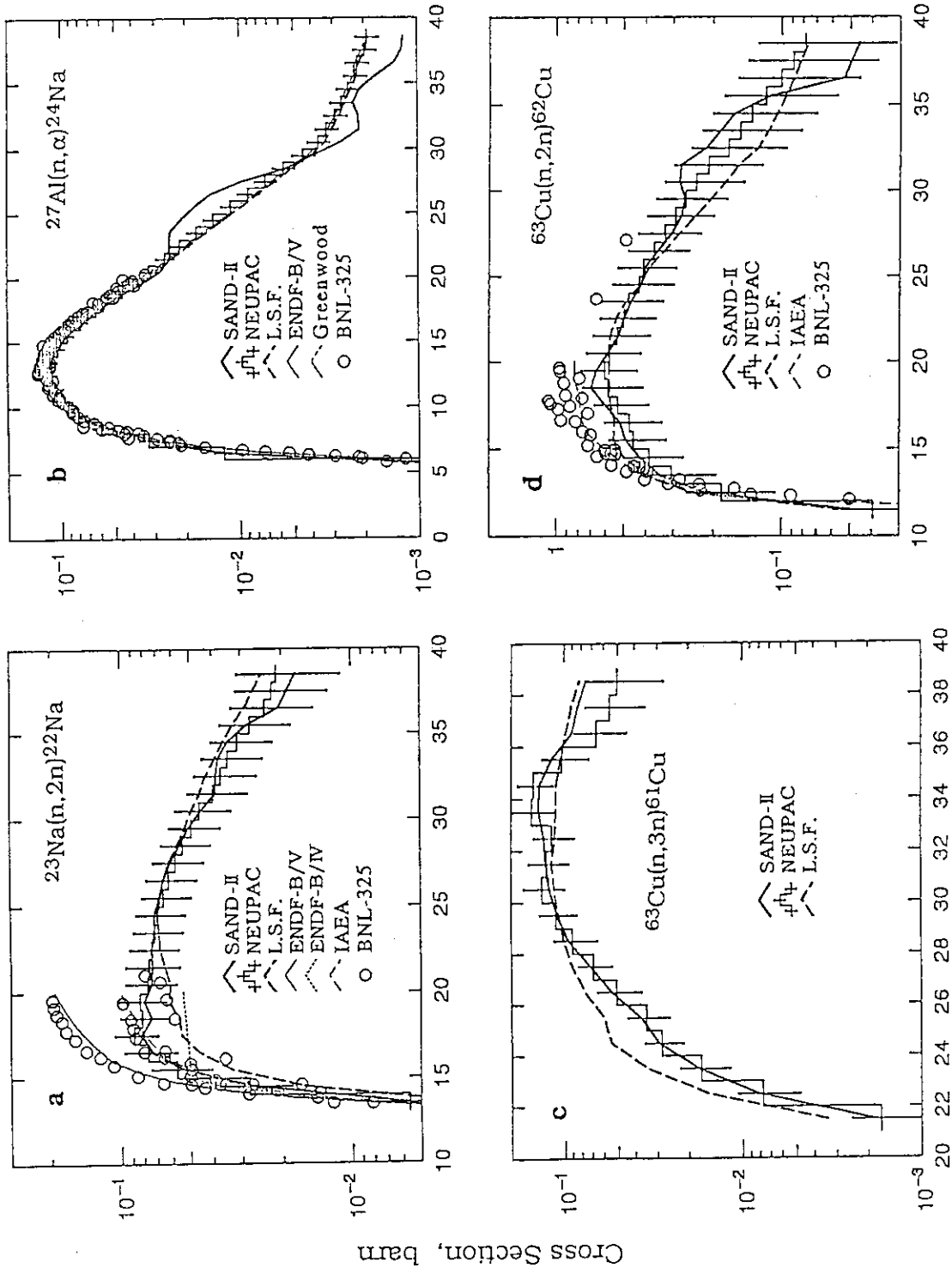

Fig. 2 Measured excitation function curves for (a) ^{23}Na(n,2n), (b) ^{27}Al(n,α), (c) ^{63}Cu(n,3n), (d) ^{63}Cu(n,2n), (e) ^{197}Au(n,4n), (f) ^{197}Au(n,2n), and (g) ^{27}Al(n,2n) reactions.

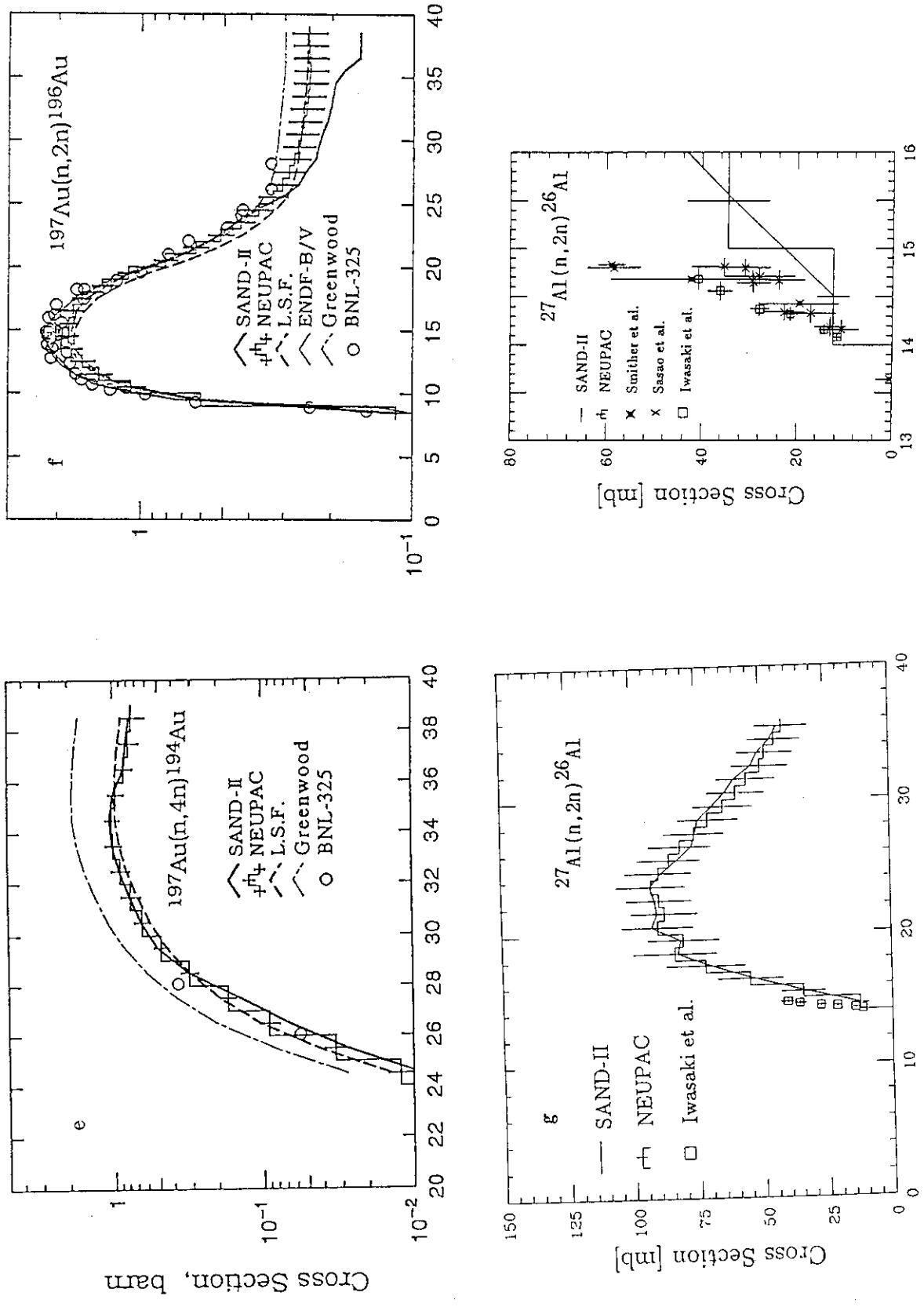

Fig. 2 Continued

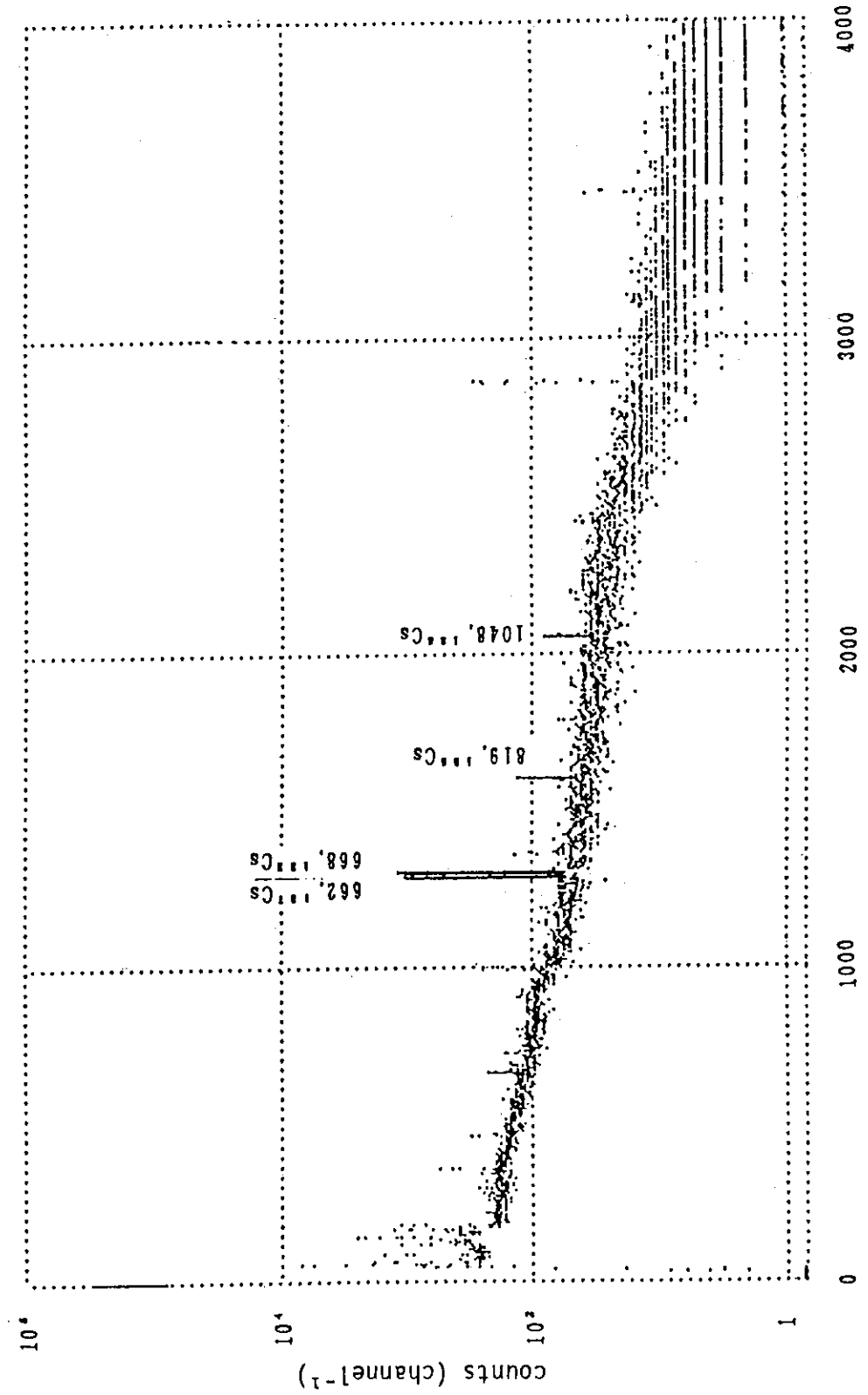

Fig. 3 Gamma-ray spectrum of Cs atoms collected onto a catcherfoil measured with a Ge detector. Several peaks from natural activity can be seen other than ^{137}Cs, ^{136}Cs and ^{132}Cs gamma rays.

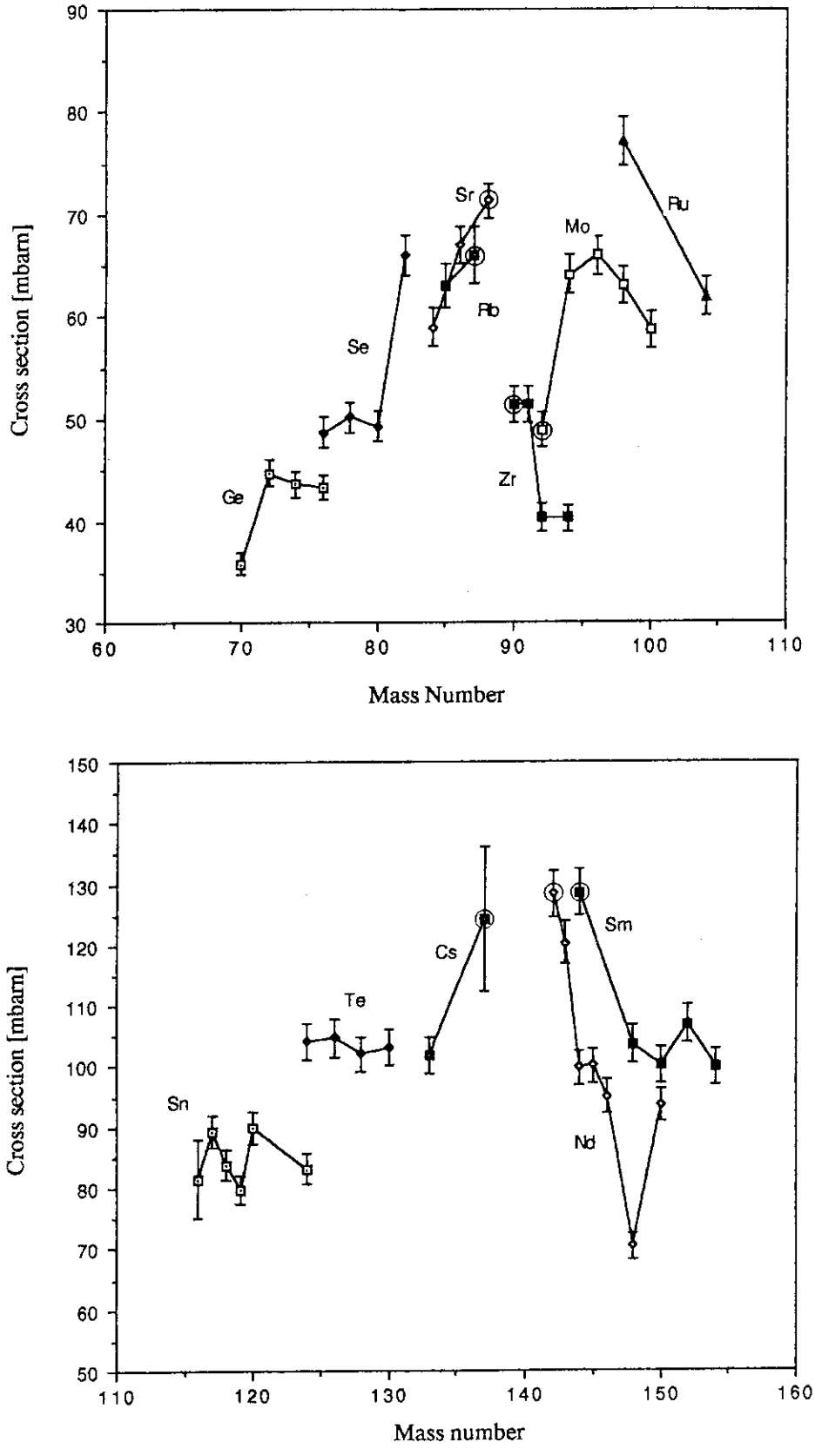

Fig. 4 Isotopic dependence of average photoneutron cross sections in giant dipole resonance region, (a) around Sr, and (b) around Cs. The data surrounded with a circle are those for neutron magic number nuclei, N = 50 and 82.

2.1 Japanese Hadron Project and Shielding Calculation

Yoshitomo Uwamino
Institute for Nuclear Study, the University of Tokyo
3-2-1, Midori-cho, Tanashi, Tokyo 188 Japan

abstract

In the Japanese Hadron Project(JHP), a 1 GeV 200 μA proton beam will be handled, and the radiation shield of the facility will be very massive concrete and iron lump. Since the constructing cost is strongly affected by the shielding design, the design must be severely performed.

Neutron yields in thin targets and a beam dump were calculated by the HETC-KFA-2 Monte Carlo code. Comparing the calculational results with experimental data, the calculated angular distribution of high energy neutrons was found to have stronger forwardness than the measurement.

High energy neutron transport in thick iron and ordinary concrete slabs was calculated with the HETC code and also with the ANISN code. The difference of the shielding lengths calculated by these two codes was smaller than 6% for both cases.

Induced radioactivity produced in cooling water was simply estimated, and it was found that the amount of ^{3}H prevent from draining of the primary circuit water.

The duct streaming of high energy neutrons was estimated for the case of a thermal neutron beam course shield at SINQ spallation neutron source facility of PSI, Switzerland. The intensity of streaming neutrons is strongly affected by the design of beam duct.

1. Introduction

The institute for Nuclear Study has a future plan named Japanese Hadron Project (JHP) which cultivate undeveloped interdisciplinary research field. In the safety design of this high-intensity medium-energy accelerator complex, we must grope our way with limited knowledge and techniques.

Here the outline of JHP is briefly described and estimations of the secondary neutron production, their penetration through thick shields, induced radioactivity produced in the cooling water system, and duct streaming of high energy neutrons are discussed.

2. Outline of JHP

The accelerator system of the Japanese Hadron Project(JHP) consists of a 1 GeV high intensity linac, a compressor/stretcher ring, and a heavy ion linac. Average beam current is 200 μA. Three major experimental facilities of Meson Arena, Neutron Arena, and Exotic Nuclei Arena are to be constructed.

The Meson Arena provides short pulsed μ and ν beams and continuous π and μ beams. The Neutron Arena supplies high intensity pulsed thermal neutrons. The Exotic Nuclei Arena will have an on line mass separator and a heavy ion linac to select out desired radioisotopes from the target bombarded by 1 GeV protons and to accelerate them up to 6 MeV/nucleon. The layout of the JHP is shown in Fig. 1.

Serious activation will occur at injection and extraction points of the compressor/stretcher ring, target stations for meson, neutron and exotic nuclei production, and beam dumps. Beam losses of these points produces tremendous secondary particles which penetrate the shielding and make serious contribution to the radiation level at the site boundary. Therefore the main facilities are constructed deep underground. The beam line are presently planed to be placed at 14 meters below the ground level.

3. Neutron Yield at Targets

The intra-nuclear-cascade-evaporation Monte Carlo code, HETC-KFA-2, in the HERMES code system,[1] is a very powerful tool for the evaluation of secondary neutron production by light ions and also of penetration of high energy neutrons through shield. Cierjacks et al.[2] measured double differential neutron production cross sections of C, Al, Fe, Nb, In, Ta, Pb, and U elements using 585 MeV protons from SIN cyclotron. Their data are very good for a benchmark calculation of the HETC code. Neutron production at these targets was calculated by the HETC code. The non-isotropic evaporation option was selected for the calculation of C and Al, and the high energy fission option was selected for the other elements. Neutron yield analysis was performed with an angular bin structure of 20 deg intervals between 0 and 180 deg.

Calculational result of the Fe double differential cross section is shown in Fig. 2 in small marks connected by straight lines, and the experimental data of Cierjacks are shown in big marks. The Cierjacks' 90 deg data, for example, are shown in big open triangles, and the corresponding calculational results of neutron emission between 80 and 100 deg are also shown in solid triangles of which size is small. A low energy neutron yield for heavier element, E_n<10 MeV, showed good agreement between calculation and measurement. Since the sum of calculated neutron yield below 1 MeV is marked at 1 MeV, the calculational results are larger than the experiment at 1 MeV.

The experimental data have larger values at a high energy region, E_n>100 MeV, than the calculation in general, and the experimental spectrum is similar to the calculational one of more forward direction, that is, the experimental spectrum of high energy region at 90 deg is similar to the calculational one of between 60 deg and 80 deg.

Angular distributions of neutron yield are shown in Fig. 3 for C, Al, Fe, In and Pb elements. A high energy neutron emission distribution, E_n>100 MeV, is presented with small solid triangles connected with straight lines for the calculation, and with big open triangles for the measurements. In the same manner, squares are for the neutrons of medium energy between 100 MeV and 10 MeV, and circles are for low energy neutrons below 10 MeV. The distribution of low energy neutrons is very flat for all elements. The agreement between calculation and experiment is good for low and medium energies. The calculation gave an under estimation at 90 deg and 150 deg for high energy neutrons. The measured neutron yields at 90 deg and 150 deg are similar to the calculations at about 70 deg and 100 deg, respectively. The high energy neutron yield at 90 deg is the most important data for the lateral shielding calculation. From the above consideration, the calculational neutron yield at 60 deg can be conservatively used as the source data of a shielding calculation at lateral direction.

Raupp et al[3], measured neutrons produced by bombardment of 590 MeV protons on a thick (full stop) uranium target. Their double differential neutron yields were also used for a benchmark calculation of the HETC-KFA-2 code. At a low energy region, the experiment and the calculation show good agreement for emission angles of 90 deg and 150 deg. The calculation also reproduces high energy neutron spectra which agree well with the experimental data of 90 and 150 deg when the previously mentioned angular biasing is introduced.

4. Deep Penetration of High Energy Neutrons

1) HETC Calculation

Neutron deep penetration was estimated by the HETC-KFA-2 code for an 8 m thick ordinary concrete slab and for a 5 m thick iron slab. The neutron sources of these calculation were derived from a HETC-KFA-2 calculation performed with a 10 cm diam by 60 cm long copper beam dump bombarded by 1 GeV protons. The neutron yields between 0 deg and 10 deg and between 50 deg and 70 deg were selected for the source. The latter angular interval is selected as the source for a lateral shield.

Since the neutrons attenuate by several decades with these thick shields, a Monte Carlo calculation in a whole slab is unrealistic. The calculation was divided into 1 m slabs, that is, a 1-m-thick slab calculation was performed with the source neutrons which normally hit the center of the slab, and the secondary calculation in the next 1-m-thick slab was performed with the neutron, proton and negative pion source which escaped from

the back surface of the previous slab. A slab was divided into 4 regions of 25 cm thicknesses, and the neutron flux was evaluated by the track length estimator at each region. Since the lower cutoff energy of neutrons was set at 14.9 MeV, neutron spectra were obtained above 14.9 MeV. The calculation was performed with 100 000 histories for each slab, and the cpu time was about 30 minutes on a FACOM-M780 computer.

2) ANISN Calculation

A deterministic radiation transport code, ANISN[4], based on a one dimensional discrete ordinates methods can perform a deep penetration calculation in much shorter time than a Monte Carlo code.

Using the same neutron source, high energy neutron penetration through an 8 m thick ordinary concrete slab and a 5 m thick iron slab was calculated by the ANISN code with the DLC-87/HILO[5] group cross sections. This neutron and gamma coupled group cross sections has neutron energy structures of from thermal to 400 MeV.

The ANISN shell source was placed at the left surface of the slab geometry to incorporate a normal incidence source. Calculations were performed with sources of all the 8 directions. The source spreads up to 1 GeV, and the neutrons with energies above 400 MeV were treated as neutrons of 400 MeV. For the conservation of the total energy, weights of the neutrons were increased by the ratio of the original energy and 400 MeV. The cpu time was only several minutes for each calculation, which is less than 1/60 of the HETC calculation.

3) Results and Discussion

The calculated neutron spectra at 9 depths in the 8 m thick concrete slab are shown in Fig. 4. The source neutrons used are the yield in the copper beam dump at the angle between 50 and 70 deg. The calculated results of the HETC code are shown in small marks and the histograms represent the results of the ANISN code. The spectral shapes of these calculations are in good agreement. The jump at the top energy group in the ANISN spectra at shallow depths came from the energy truncation of the source spectrum mentioned in the previous section. The absolute value of the ANISN calculation, however, decreases faster than that of the HETC calculation.

Attenuation curves of the dose equivalent rate (H_{1cm}) in the concrete slab are shown in Fig. 5. The open and solid circles are of the HETC calculation, and the lines are of the ANISN calculation. The dose rates directly calculated by the HETC code are just the contribution of high energy (>15 MeV) neutrons. The HETC results shown here are the value corrected by using the ANISN spectrum to represent the contribution of neutrons of whole energy region and also the secondary gamma rays.

With the increase of the emission angle of the source neutrons, the absolute value of the dose rate becomes small and the slant becomes steep. At the entrance of the slab, the ANISN results are larger than that of HETC because of the weight increase in the energy

truncation of the source spectrum. The difference between the HETC and the ANISN calculations is only a factor of 4 at 8 m depth, and it can be concluded that the ANISN calculation with the DLC-87/HILO group cross sections gives good results compared with the HETC code.

High energy accelerator shielding experiments were performed by Gilbert[6] and Ban[7], and their data were abstracted into the parameters of the Moyer model. The results of these experiment are also shown in Fig. 5, where the data of Gilbert is noted as CERN-LBL-Rutherford and that of Ban as KEK. These lines have smaller values and gentler slants.

5. Radioactive Water[8]

Cooling water in the high radiation field produces radioactive nuclides in it. Therefore the cooling water system has to incorporate a water purification system such as ion exchange column. Using the purification system the most radioactive nuclides will be removed except tritium. The cooling water system consists of threefold circuit. The primary cooling circuit is used to cool devices which produce high induced radioactivity such as beam dumps and secondary particle production targets. The heat of the primary cooling circuit is removed by the secondary cooling water through heat exchangers. The secondary cooling water also cools components in the beam lines and the accelerator. The raw water cools the secondary cooling circuit through heat exchangers. The threefold cooling circuit system will prevent the hazard of the raw water system being contaminated by the primary cooling water which is highly activated.

The concentration of radioisotopes produced in the primary cooling water for the beam dump which stops 1 GeV 100 μA protons is calculated. Secondary particles produced in the beam dump is calculated by using the Monte Carlo code. The spallation cross sections for various nuclides produced from oxygen nucleus bombarded by nucleons with energies above 20 MeV are assumed to be 30 mb except ^{7}Be for which the spallation cross section is assumed to be 10 mb.

The other source of the radioisotopes contained in the cooling water is due to dissolving of the radioactive cooling pipe. The amount of these nuclides dissolved into the cooling water was estimated based on the measured values at LAMPF. The measured ratio of the amount of tritium and these nuclides were used for calculations. The calculated results are shown in table 1.

The total tritium produced in the primary cooling system for a beam dump after 5000 hours operation is about 6 TBq. It is difficult to drain this amount of tritium by dilution of the cooling water in compliance with regulations. Therefore these cooling water is kept until the radioisotopes decay to the level at which it can safely be drained.

The tritium produced in the secondary cooling water for the accelerator is orders of magnitude less than the primary cooling system. Therefore the secondary cooling water will be exchanged at a certain period and drained after dilution.

6. Duct Streaming

High intensity thermal neutron beam from moderators placed around a spallation target are utilized at the Neutron Arena. High energy neutron duct streaming from thermal neutron beam ducts penetrating through very massive bulk shield is a severe problem. These streaming neutrons disturb measurements and necessitate massive shield around a experimental equipment.

Duct streaming was estimated for a similar neutron facility named SINQ which is under construction at Paul Scherrer Institute in Switzerland. Spallation neutrons are produced by 1-mA 590-MeV protons at a Pb-Bi target which is placed at the center of a 2-m-diam D_2O tank. Thermal neutron beam ducts penetrate through 5-m-thick iron bulk shield. A duct is aligned to see the moderator placed near the spallation target but not to see the target itself.

The streaming neutrons consist of two components; one is the neutrons coming from the moderator surface and the other is the neutrons coming from the duct wall. The former was estimated by Pepin[9] using the HETC code. The latter was estimated by using the angular neutron flux distribution calculated by the ANISN code.

Each component is shown in Fig. 6. The neutron lethargy flux at the outlet of the beam duct coming from the moderator surface is shown in a thick dash-dot line. Flux coming from a part of the duct wall between 0 and 100 cm from the moderator is shown in a thin dotted line, that between 100 and 150 cm in a thin broken line, that between 150 and 200 cm in a thin dash-dot line, and that between 200 cm and the outlet in a thick solid line, respectively. The total flux is drawn at the top in a solid line.

The intensity of high energy (>100 MeV) neutrons dominates the shielding thickness, and must be lowered as low as possible. It can be concluded that the beam duct of 100-cm length from the moderator surface must not be seen from the outlet. Using the source flux density obtained on this condition, two dimensional dose equivalent distribution in a iron shield placed just outside of the duct outlet was calculated with the DOT4.2 code.[10] The result is shown in Fig. 7. To reduce the dose rate at the surface lower than 10μSv/h, a 210 cm thick and 300 cm wide iron shield will be necessary. About 10 cm thick boron containing polyethylene will also be required to shield the piled-up low energy (<1MeV) neutrons in iron.

References

1) P.Cloth, D.Filges, R.D.Neef, G.Sterzenbach, Ch.Reul, T.W.Armstrong, B.L.Colborn, B.Anders, H.Brueckmann, Jül-2203, Kernforschungsanlage, Jülich (1988).

2) S.Cierjacks, Y.Hino, F.Raupp, L.Buth, D.Filges, P.Cloth and T.W.Armstrong, Phys. Rev. C 36, 1976 (1987).

3) F.Raupp, S.Cierjacks, Y.Hino, S.D.Howe, M.T.Rainbow, M.T.Swinhoe, and L.Buth, ICANS-V, Jül-Conf-45, Jülich p333 (1981)

4) W. W. Engle, Jr., "A User's Manual for ANISN, A One Dimensional Discrete Ordinates Transport Code with Anisotropic Scattering", K-1693, Oak Ridge Gaseous Diffusion Plant (1967).

5) R. G. Alsmiller, Jr. and J. Barish, Nucl. Sci. Eng., 80 (1982) 448.

6) W. A. Gilbert et al., "1966 CERN-LBL-RHEL Shielding Experiment at the CERN Proton Synchrotron", Lawrence Berkeley Laboratory, University of California, Report UCRL-17941 (1968).

7) S. Ban, "Shielding Study on High Energy Proton Synchrotron", Kyoto University Doctor Thesis (1982). (in Japanese)

8) T. Shibata, "Radiation Safety System of Japanese Hadron Project", Proc. The 2nd International Symp. on Advanced Nuclear Energy Research -Evolution by Accelerators-, p194, Japan Atomic Energy Research Institute, Mito (1990).

9) M. Pepin, "The High-Energy Neutron Background at SINQ", Proc. ICANS-IX, p649, Swiss Institute for Nuclear Research, Villigen (1986).

10) W. A. Rhoades et al., "The DOT-IV Two-Dimensional Discrete Ordinates Transport Code with Space-Dependent Mesh and Quadrature", ORNL/TM-6529, Oak Ridge National Laboratory (1978).

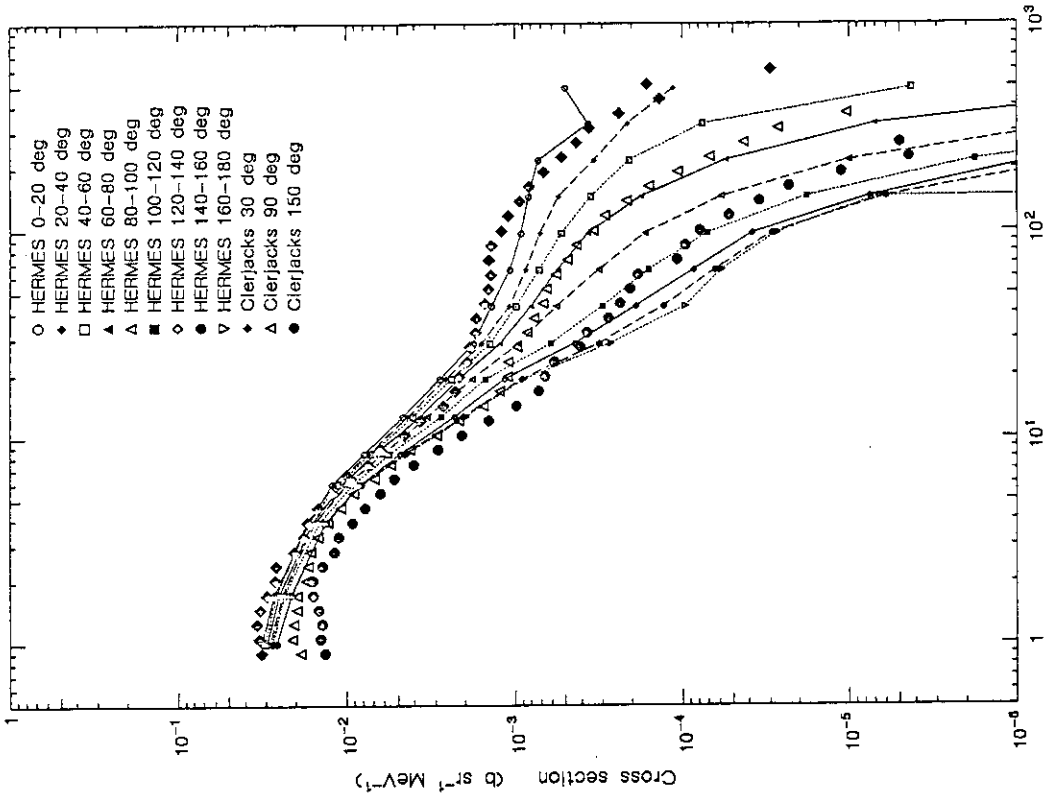

Fig. 2 Calculated and measured double differential neutron production cross sections of iron bombarded by 585 MeV protons.

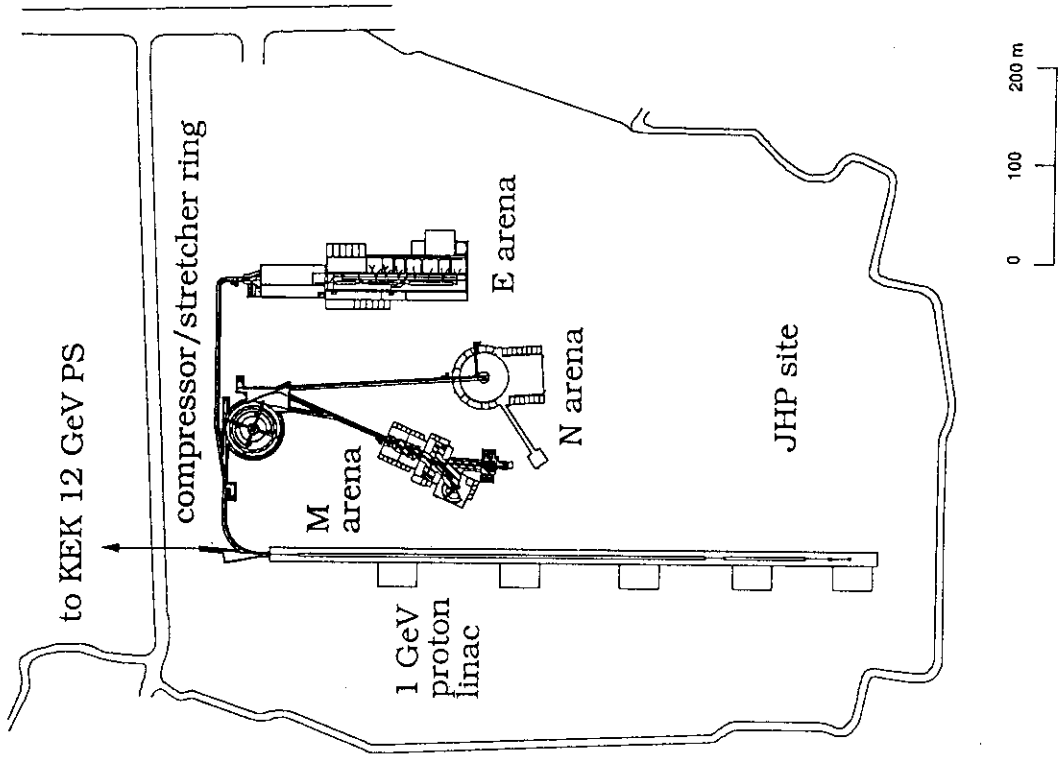

Fig.1 Layout of the Japanese Hadron Project.

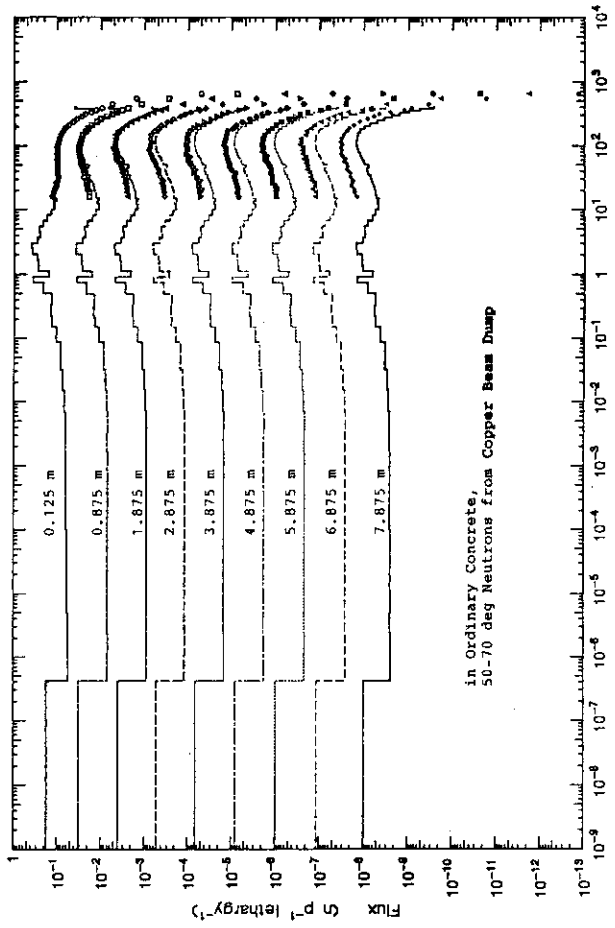

Fig. 4 Calculated neutron lethargy spectra in a 8 m thick ordinary concrete slab. The source was the neutrons produced between 50 deg and 70 deg in a copper beam dump bombarded by 1 GeV protons.

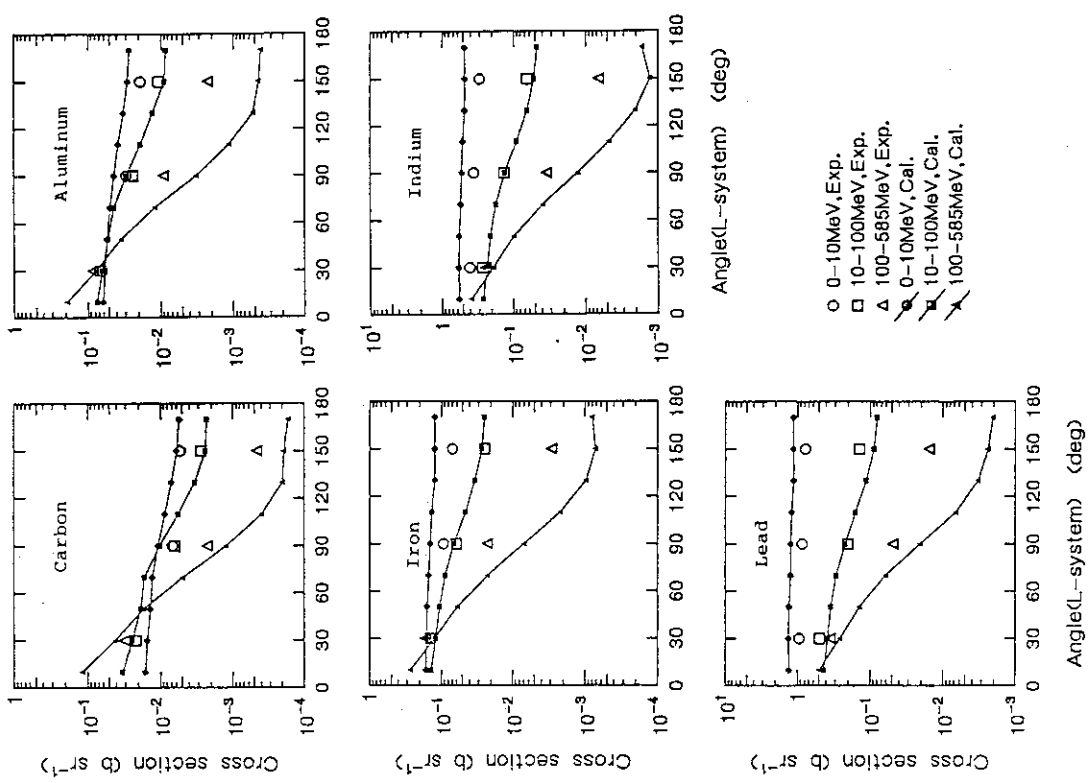

Fig. 3 Calculated and measured angular distribution of neutron yield from C, Al, Fe, In, and Pb elements bombarded by 585 MeV protons.

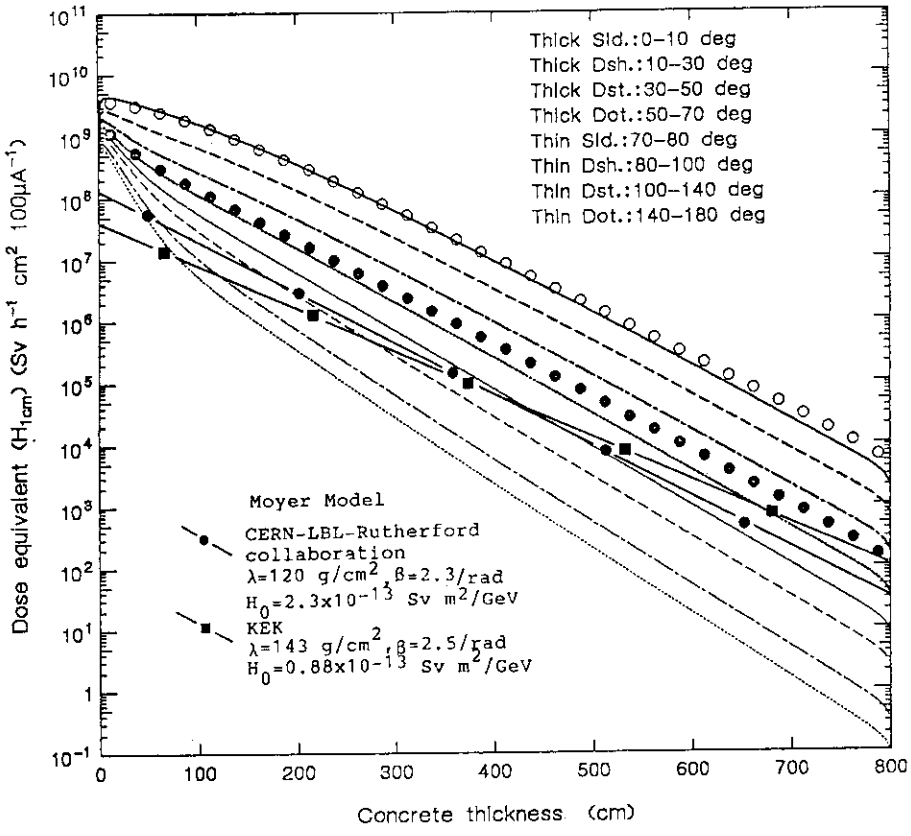

Fig. 5 Dose equivalent attenuation through concrete shielding calculated by HETC and ANISN.

Table 1 Amount of radioisotopes in cooling water after 5000-hour operation and 1-day cooling.

Nuclide	$T_{1/2}$	Activity (Bq)
^{3}H	12.3y	5.7×10^{11}
^{7}Be	53.5d	5.5×10^{12}
^{14}C	5730y	1.2×10^{9}
^{24}Na	15.0h	1.7×10^{10}
^{46}Sc	83.8d	4.2×10^{10}
^{52}Mn	5.59d	4.5×10^{10}
^{54}Mn	312d	1.9×10^{10}
^{56}Co	78.8d	4.3×10^{10}
^{57}Co	271d	2.1×10^{10}
^{58}Co	70.8d	4.4×10^{10}

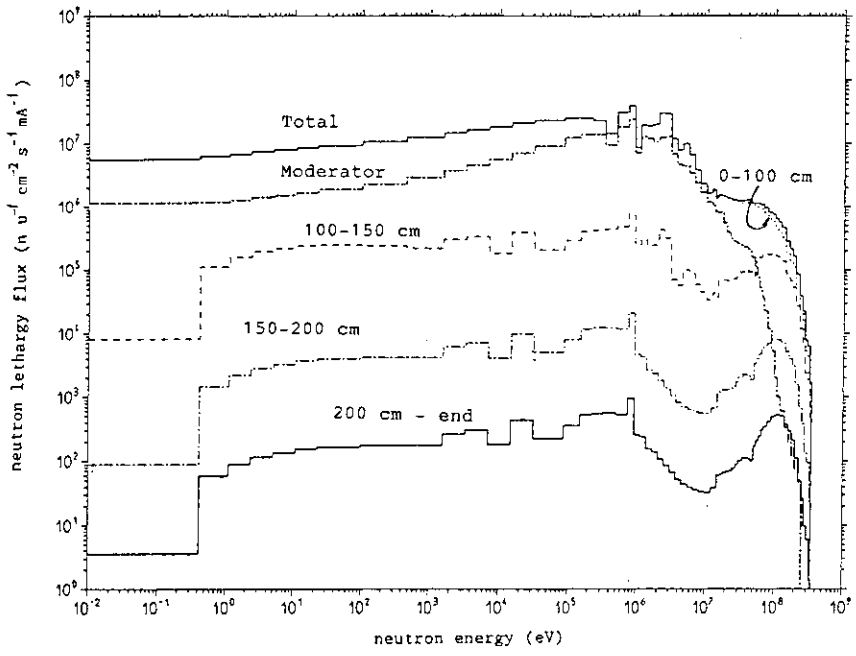

Fig. 6 Neutron lethargy flux at the outlet of a thermal neutron beam duct of SINQ facility.

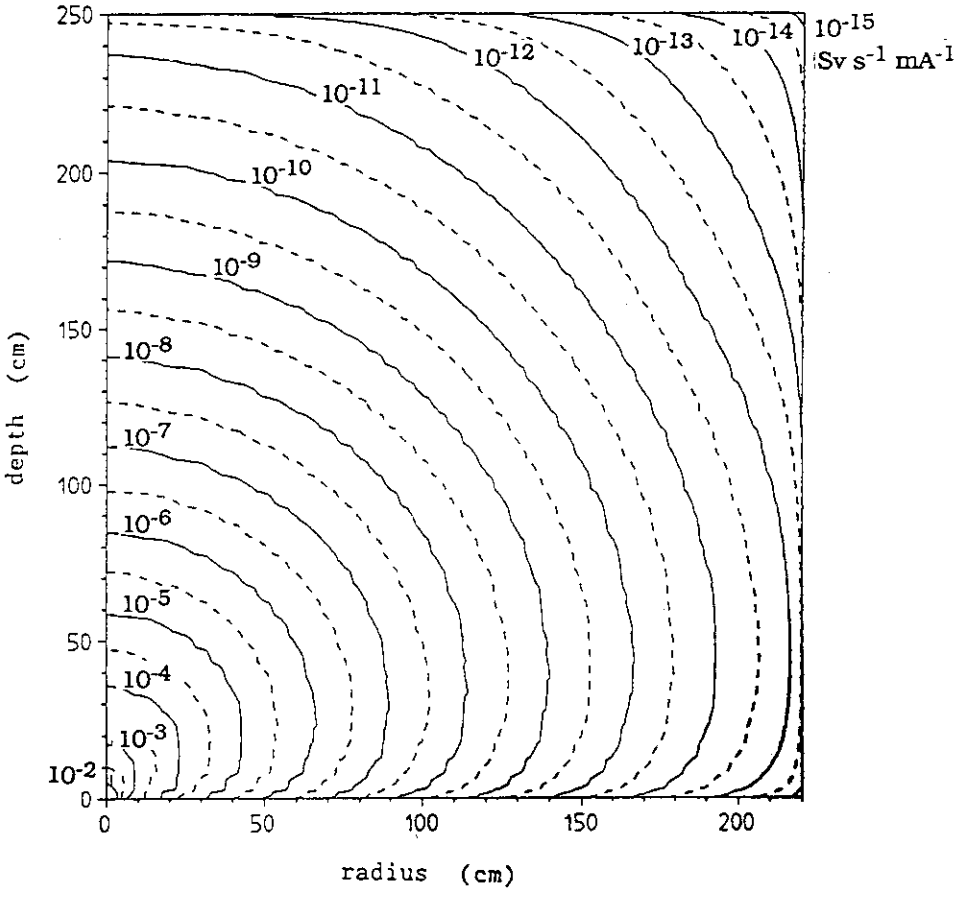

Fig. 7 Neutron dose equivalent contour map in a iron shield placed outside of the duct outlet.

2.2 High Intensity Proton Linear Accelerator Development Plan and Acclerator-based Nuclear Waste Transmutation

Motoharu Mizumoto

Accelerator Engineering Laboratory
Department of Reactor Engineering
Japan Atomic Energy Research Institute
Tokai-mura, Naka-gun, Ibaraki-ken 319-11

A conceptual design study has been carried out for an accelerator-driven actinide transmutation system with sodium-cooled subcritical target using spallation reactions. The high intensity proton linear accelerator (ETA: Engineering Test Accelerator) with an energy of 1.5 GeV and a current of 10 mA has been proposed by Japan Atomic Energy Research Institute, JAERI. Various engineering tests will be performed using this accelerator for the accelerator-driven transmutation system. In a course of the development, the R&D works for the low energy portion of the linear accelerator (BTA: Basic Technology Accelerator) with an energy of 10 MeV and a current of 10 mA are being currently made, since the beam current and quality are mainly determined by this low energy portion. In this report, brief descriptions of the transmutation system and accelerator development plan will be given together with the high energy nuclear data requirements.

1. Introduction

Studies of basic technologies for the transmutation of nuclear wastes and nuclide partitioning have continued for the last several years. The Japanese Atomic Energy Commission has concluded that R&D efforts for these technologies should be strengthened as a national research project, where the possible use of valuable resources in the waste and improvements of safety assurance in management processes have

to be evaluated. This national program called OMEGA (Options Making Extra Gains of Actinides and Fission Products) has started by aiming at promoting the research and development of the new technologies on nuclear waste partitioning and transmutation. As a part of this program, JAERI has laid out the R&D plans for accelerator-based actinide (transuranium: TRU) transmutation system.

High energy proton beams will also produce intense neutron, muon and pion fluxes, that can be utilized for the other nuclear energy related applications such as nuclear fuel production, nuclear data measurements, material sciences, radio isotope productions and muon catalyzed fusion[1].

2. A study of the transmutation system

The basic concept of the transmutation system with proton spallation reactions has been studied at JAERI[2]. The main goal of this program is to process the TRU of which the yearly production rate is typically 30 kg for a 1000 MWe LWR. The detailed description of a transmutation target, neutronics calculation and power dissipation calculation is given in the previous paper[3]. Only the essential part of the scheme is described in this paper. Figure 1 shows a schematic flow diagram for an accelerator driven target system in combination with a subcritical reactor. Table 1 shows the operating condition of the system.

The target and fuel assembly in the reactor proposed here are similar to that used for the common fast breeder reactor with the Na coolant. A harder neutron spectrum is preferable in order to make the transmutation more effective, because the fission reaction rate exceeds the capture rate for increasing the neutron energy. Primary nuclear spallation reactions and the subsequent particle transport processes were simulated using the NMTC/JAERI code[4] for the neutron energy range above the cutoff energy of 15 MeV. Below this energy, a three dimensional Monte Carlo transport code was used. The k_{eff} value was taken to be 0.89 for the calculation. The maximum achievable thermal power was limited by maximum allowable temperature that was set at 900 C in fuel and cladding. The calculated maximum thermal output powers were 820 MW.

Accordingly, the averaged power densities were 400 W/cc using the incident proton beam current of 39 mA for these target powers.

From these calculations, the spallation neutrons and the subsequent induced fission neutrons can transmute the TRU produced by nearly ten LWR in a Na cooled subcritical assembly. As a by-product, this system can be used to produce excess electric power of about 246 MW, a part of which can be used to operate the proton accelerator.

3. Framework of the accelerator development.

The conceptual design of the engineering test accelerator, ETA, proposed by JAERI with a beam energy of 1.5 GeV and a current of 10 mA is shown in Fig. 2. The engineering test accelerator represents a large scale system when compared to the contemporary proton accelerators that are used mainly for basic nuclear physics experiments. In particular, an average proton beam current of 10 mA is nearly 10 - 50 times larger than that for existing accelerators. Beam spill should be minimized not to cause serious problems due to the high level activities induced in the accelerator structures. The major technical issues for the accelerator development are listed in Table 2.

As the first step in the development, the low energy portion of the accelerator (BTA : Basic Technology Accelerator) as shown in Fig. 3 is being studied, since the beam quality is determined mainly by this low energy portion. This section consists of the following components; ion source, radio frequency quadruple (RFQ) and drift tube linac (DTL). The high energy portion of the accelerator (high β structure) will be studied in advance of the 2nd stage development. The basic specification of BTA is given in Table 3. Various tests of the operational characteristics of the accelerator structures will be conducted to accumulate the design and operational experiences.

4. Nuclear Data Requirement

Various nuclear data are required for the development of the accelerator-based transmutation system including the spallation target and subcritical reactor core, and high energy accelerator structure. The

cross section data for the transuraniums are not well evaluated except the nucleus of ^{237}Np. The data requirements are given in Table 4 - 6. From the major evaluated data files such as JENDL-3, JEF and ENDF-6, the examples for the ^{234}Am fission cross section and ^{234}Am capture cross section are shown in Fig. 4 and Fig. 5, respectively. In general, capture cross section data for many actinides seem not well established.

The data for several proton induced cross sections and subsequent neutron emissions are also important for the development of the target system and accelerator. The integral type experiments are being performed by JAERI in cooperation with High Energy Physics Laboratory, KEK, using 500 MeV proton beams[5]. The thick target neutron yields and angular distributions from (p,n) reactions have been also measured in the JAERI Tandem Accelerator Neutron Facility for the accelerator structural materials such as C, Al, Ti, Fe, Ni, Cu, Pb and SUS304 at 10 MeV[6]. These data are useful for the shielding calculations for the BTA developments. The typical examples for these data are shown for Al and Cu in Figs. 6 and 7, respectively.

Acknowledgement

The author wish to thank all the collaborators of Nuclear Spallation Study Groups (Accelerator and Target).

References

(1) Y. Kaneko et al., "High Intensity Proton Accelerator Programs", JAERI-M 91-095 (1991)
(2) T. Nishida et al., "Research of TRU Transmutation System with Proton Accelerator" NEA/CRP 32 Meeting, Argonne, 1989.
(3) T. Takizuka et al., "A Conceptual Design of Transmutation Plant", Specialist Meeting on Accelerator-Driven Transmutation Technology for Radwaste and other Applications, 1991, Stockholm, Sweden
(4) Y. Nakahara et al., "NMTC/JAERI A Simulation Code System for High Energy Nuclear Reactions and Nucleon -Meson Transport Processes", JAERI-M 82-198 (1982)
(5) H. Takada et al.,"Integral Experiment on Lead Bulk System Bombarded with High Energy Protons", Specialist Meeting on Accelerator-Driven Transmutation Technology for Radwaste and other Applications, 1991, Stockholm, Sweden.
(6) S. Chiba et al., Private communication (1991)

Table 1. Operating condition of the accelerator-based transmutation system.

Proton Beam Energy		1.5 GeV
Proton Beam Current		39 mA
Actinide Inventory		3160 kg
K_{eff}		0.89
No. of Neutrons		40 n/p
No. of Fissions	(>15MeV)	0.45 f/p
	(<15MeV)	100 f/p
Neutron Flux		$4x10^{15}$ n/cm^2s
Mean Neutron Energy		690 keV
Burnup		250 kg/y
Thermal Output		820 MW
Power Density	(max)	930 MW/m^3
	(ave)	400 MW/m^3
Maximum Temperature		
Outlet Coolant		473 C
Fuel		890 C
Clad		528 C
Electric Output		246 MW

Table 2. Major accelerator technical issues

Large Average Beam Current	Several tens of mA
Low Beam Loss	< 1 nA/m(10^{-5} - 10^{-4})
High Beam Quality	
Large Bore to Beam Ratio	> 10
Good Power Conversion Efficiency	> 50 %
RF Source Development	
High Accelerator Availability	> 70 %
High Reliability Requirement	

Table 3. Basic Specification of BTA

Accelerator Particle	Proton
Operation Mode	Pulse
Duty Factor	10 %
Output Energy	10 MeV
Average Beam Current	10 mA
Peak Beam Current	100 mA
Target Specification	
Normalized Transverse Emittance	0.5 πcm.mrad
Energy Resolution	1 %

Table 4. Nuclear data required for the spallation target

Target	Quality	Energy Range	Accuracy	Comment
Na	$\sigma_{p,xpyn}(E,\theta)$			Spallation Reaction
Fe		100 MeV	30 %	
Zr	$\sigma_{n,xpyn}(E,\theta)$	- 1.5 GeV		If possible
Y				(π,Nucleus)
W				(Nucleus,π)
Pb	$\sigma_{p,xdytz\alpha\gamma}(E)$			
Bi				
^{238}U	$\sigma_{p,xnf}(E)$			Particle Evaporation
^{237}Np		10 MeV	30 %	High Energy Fission
^{238}Pu	$\sigma_{n,xdytz\alpha\gamma}(E)$	- 500 MeV		
^{239}Pu				If possible
^{241}Am	$\sigma_{n,xnf}(E)$			(π, xdytz$\alpha\gamma$)
^{243}Am				(π,xnf)

These nuclides are candidate materials for target, fuel, coolant and clad.

Table 5. Data required for the 1.5 GeV accelerator (ETA: Engineering Test Accelerator)

Target	Quality	Energy Range	Accuracy	Comment
	$\sigma_{p,xpyn}(E,\theta)$	- 1.5 GeV	30 %	Neutron Emission
	$\sigma_{p,xpyn}(E,\theta)$	- 1.5 GeV	30 %	γ ray emission
	$\sigma_{p,xpyn}(E)$	- 1.5 GeV	30 %	Activation
	Spallation Product Yields	- 1.5 GeV	30 %	Activation
	High Energy Fission Product Yields	- 1.5 GeV	30 %	Activation
(1) Air, Water	N, O, Ar			
(2) Concrete	O, Na, Mg, Al, Si, Ca, Mn, Fe			
(3) Aluminum Beam Pipe	Mg, Al, Zn, Cu			
(4) Stainless Steel	Cr, Mn, Fe, Co, Ni			
(5) Accelerating Structure	Al, Cu, Fe			

Table 6. Data required for the BTA Development (10 - 15 MeV)

Target	Quality	Energy Range (MeV)	Accuracy	Comment
	(MeV)			
(1) Air, Water				
^{14}N	$\sigma_{p,n}(E)$	6.35 - 15	20 %	Neutron Emission
^{16}N	$\sigma_{p,n}(E)$	3.77 - 15	20 %	Neutron Emission Subsequent Capture
(2) Concrete				
^{16}O	$\sigma_{p,n}(E)$	3.77 - 15	20 %	Neutron Emission
^{27}Al	$\sigma_{p,n}(E)$	5.80 - 15	20 %	Neutron Emission
^{nat}Fe	$\sigma_{p,n}(E)$	Eth - 15	20 %	Neutron Emission Subsequent Capture
(3) Aluminum Beam Pipe				
^{27}Al	$\sigma_{p,n}(E)$	5.8 - 15	15 %	Neutron Emission Subsequent Capture
(4) Stainless Steel				
^{nat}Cr	$\sigma_{p,n}(E), \sigma_{p,n}(E,\theta)$	Eth - 15	15 %	Neutron Emission
^{nat}Fe	$\sigma_{p,n}(E), \sigma_{p,n}(E,\theta)$	Eth - 15	15 %	Neutron Emission
^{nat}Ni	$\sigma_{p,n}(E), \sigma_{p,n}(E,\theta)$	Eth - 15	15 %	Neutron Emission Subsequent Capture
^{53}Cr	$\sigma_{p,\gamma}(E)$	- 15	15 %	Activation of ^{54}Mn
^{54}Cr	$\sigma_{p,n}(E)$	2.19 - 15	15 %	Activation of ^{54}Mn
^{56}Fe	$\sigma_{p,\gamma}(E)$	- 15	15 %	Activation of ^{57}Co
^{56}Fe	$\sigma_{p,n}(E)$	5.43 - 15	15 %	Activation of ^{56}Co
(5) Accelerating Structure				
^{nat}Cu	$\sigma_{p,n}(E), \sigma_{p,n}(E,\theta)$	Eth - 15	15 %	Neutron Emission Subsequent Capture
^{63}Cu	$\sigma_{p,n}(E)$	4.21 - 15	15 %	Activation of ^{63}Zn
^{65}Cu	$\sigma_{p,n}(E)$	2.15 - 15	15 %	Activation of ^{65}Zn

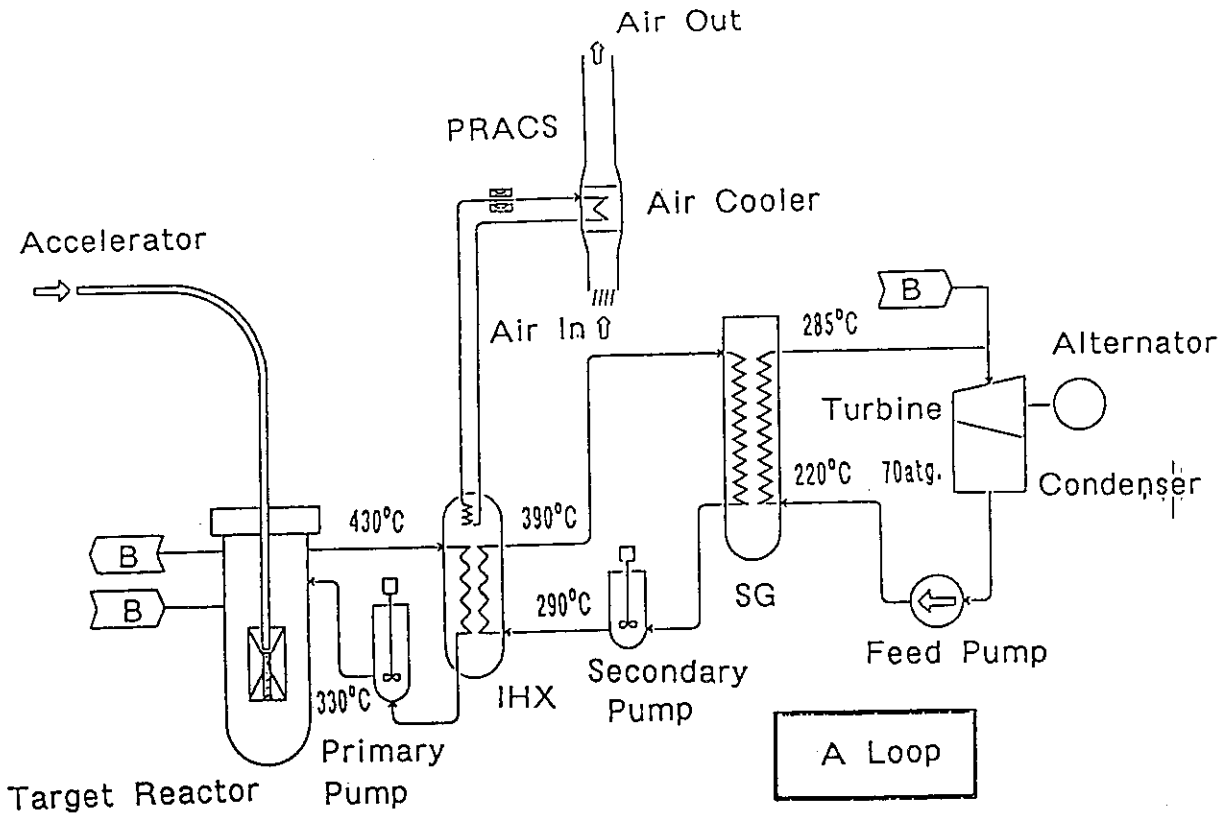

Fig. 1. A conceptual flow diagram of actinide transmutation system

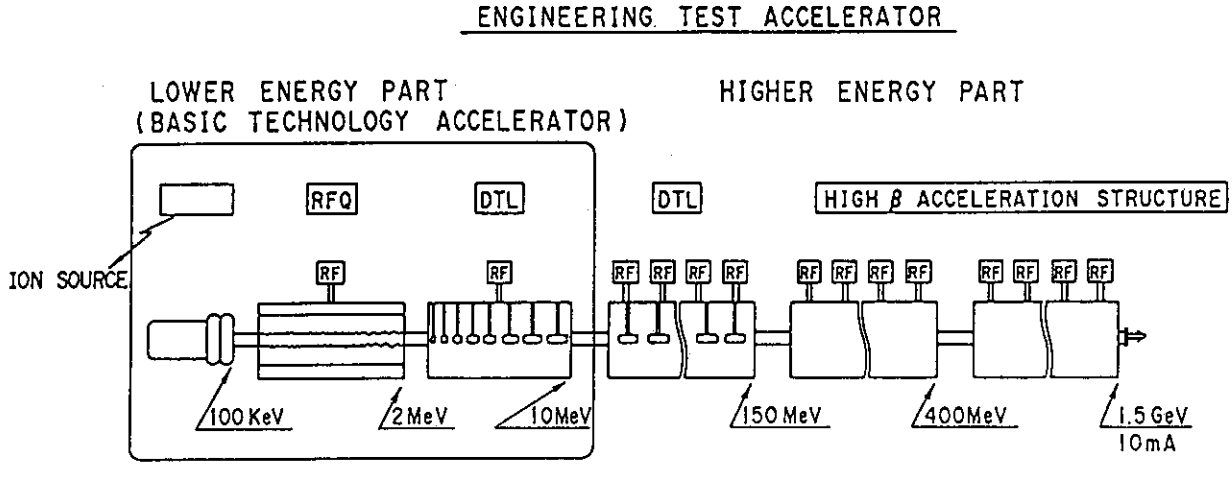

Fig. 2. A Conceptual layout of the Engineering Test Accelerator (ETA)

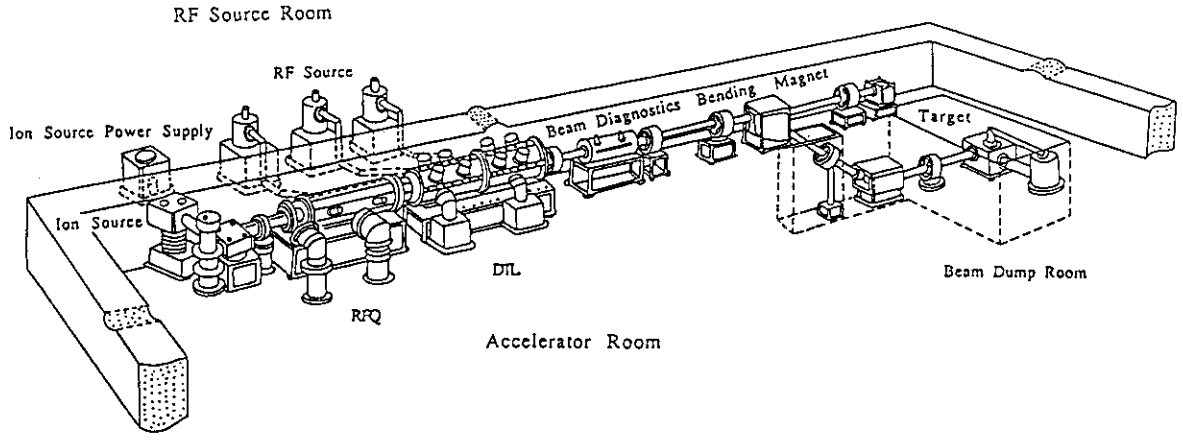

Fig. 3. Schematic layout of the Basic Technology Accelerator (BTA)

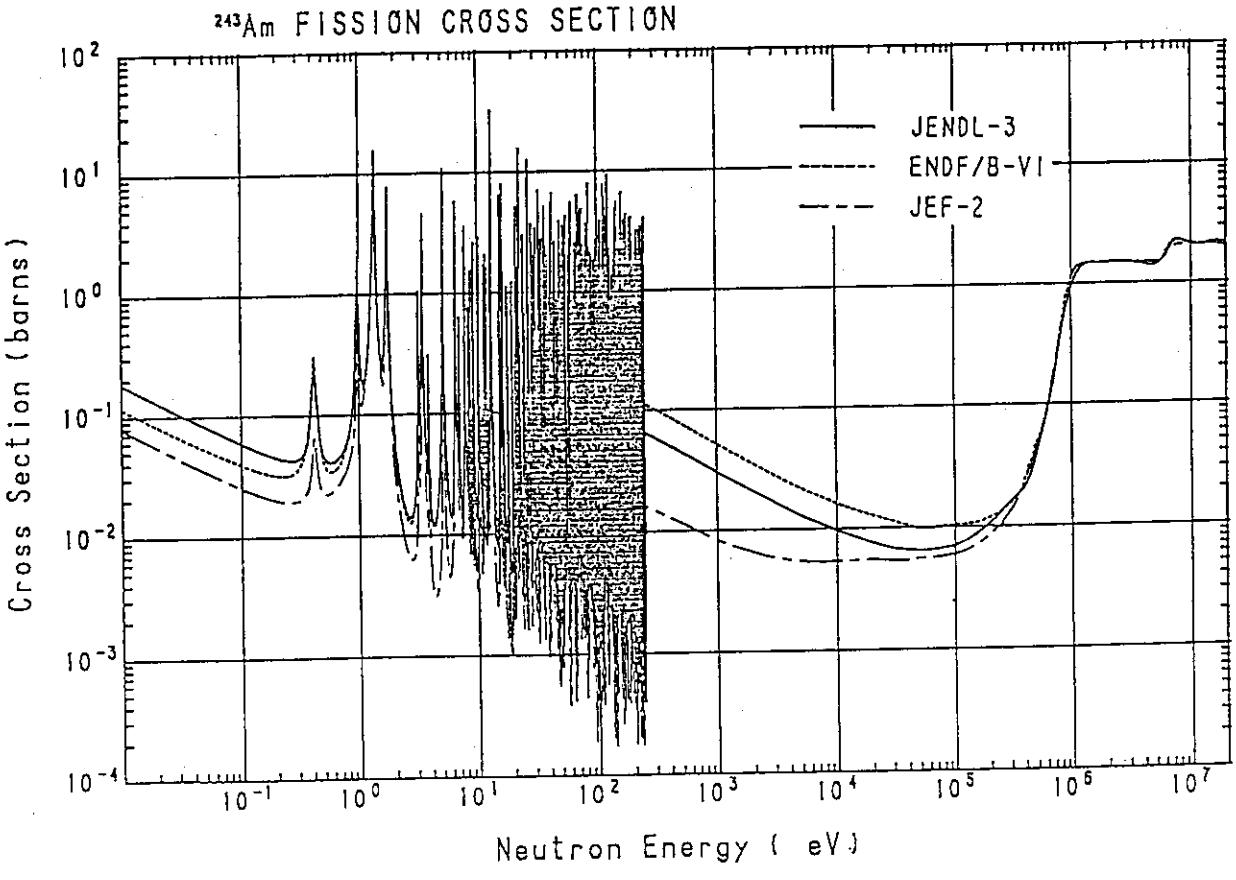

Fig. 4. A comparison of the fission Cross Section of ^{243}Am

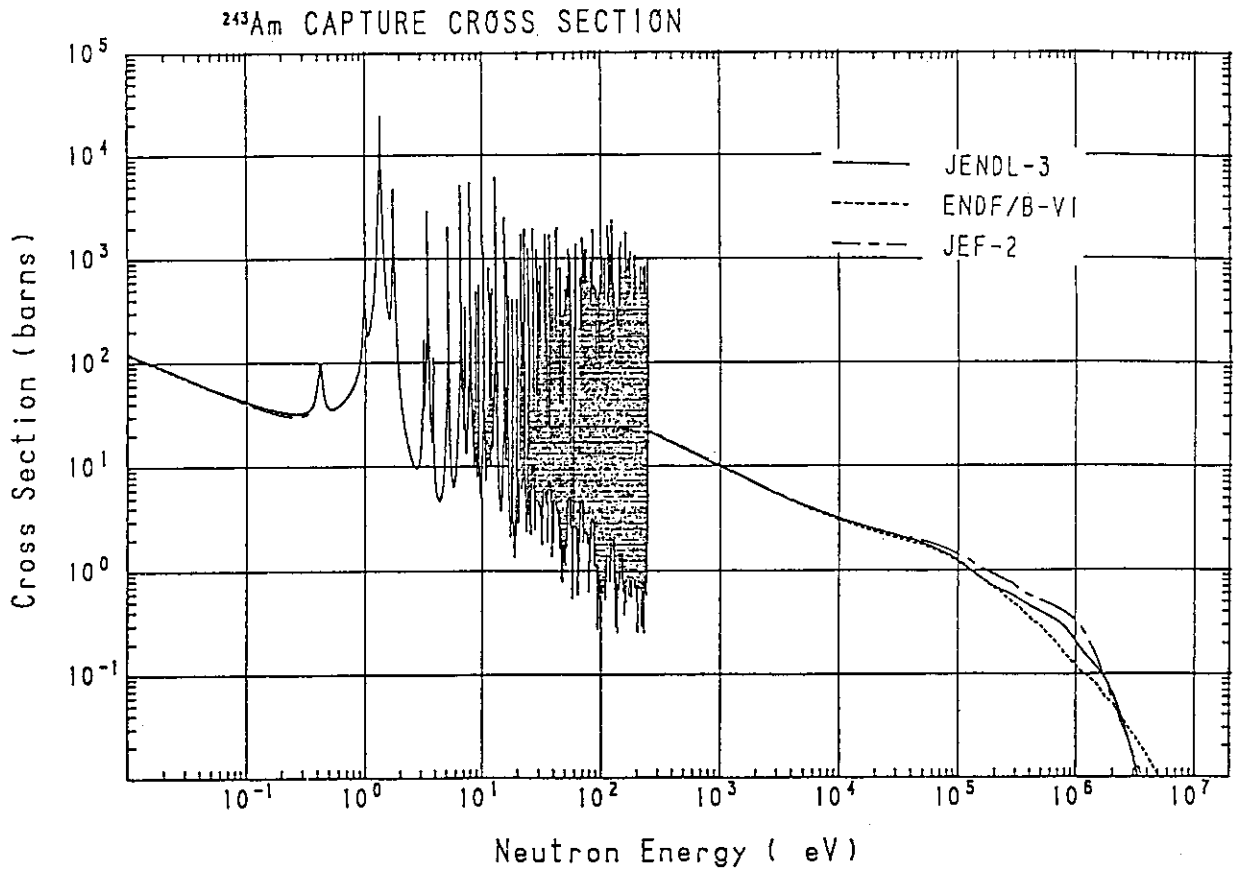

Fig. 5. A comparison of the capture cross section of ^{243}Am

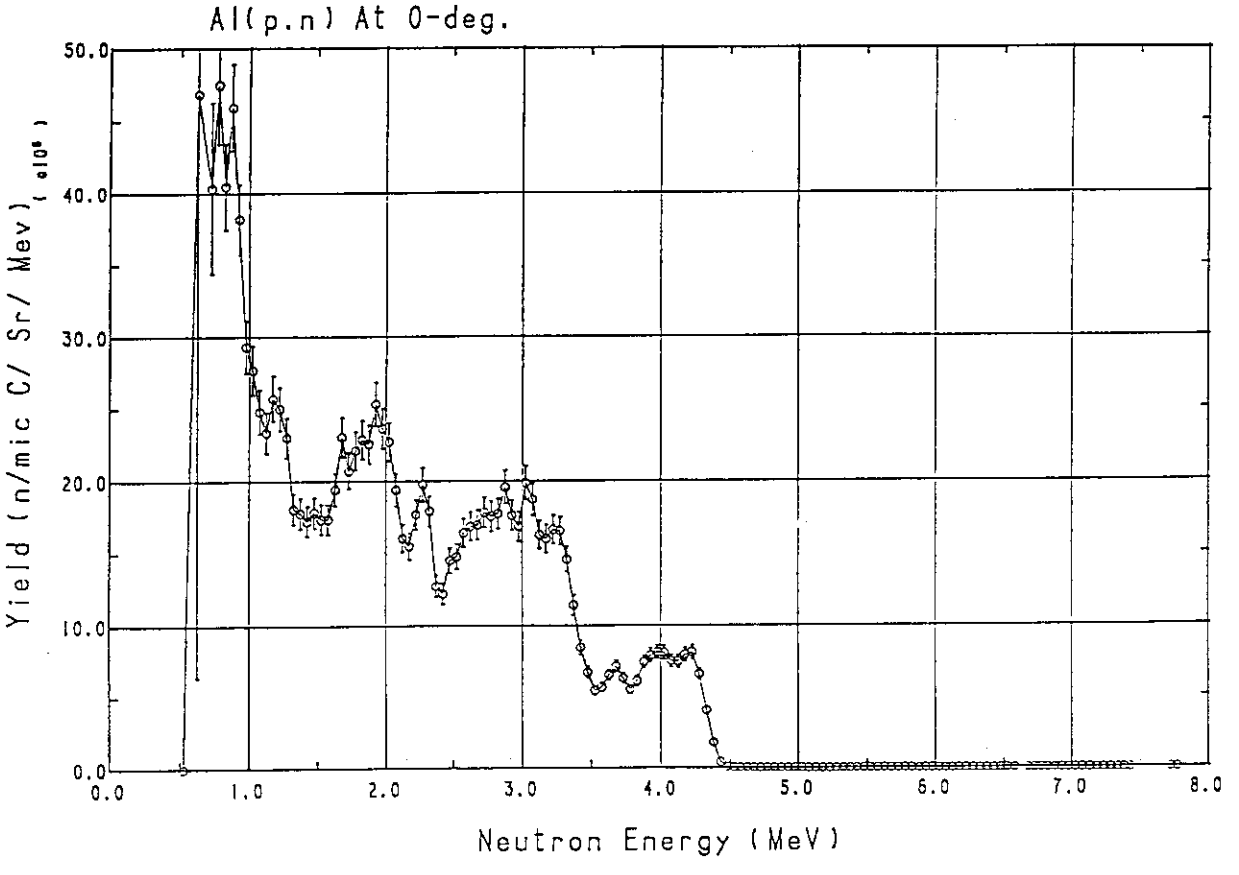

Fig. 6. Thick target yields for the (p,n) reaction of Al at 10 MeV

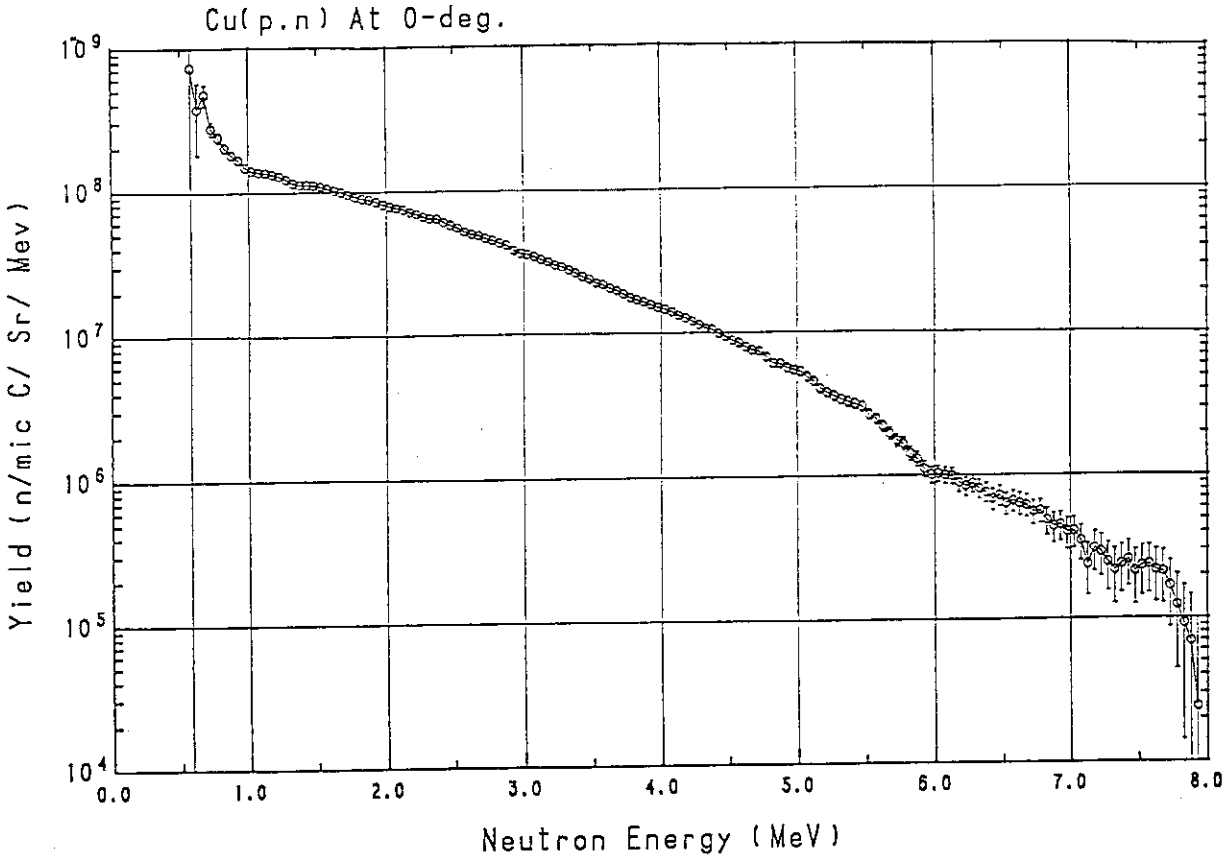

Fig. 7. Thick target yields for the (p,n) reaction of Cu at 10 MeV

2.3 Acceleration of Proton Beams with RIKEN Ring Cyclotron

Akira Goto
RIKEN (The Institute of Physical and Chemical Research)

Abstract: Proton beams of 70, 135 and 210 MeV were accelerated with RIKEN Ring Cyclotron, and delivered for two experiments: an experiment of single event upset rates of a memory chip for use in space and a test of time-of-flight (TOF) measurement system. Performance and current status of the proton acceleration using the Ring Cyclotron are presented together with a brief description of the RIKEN Accelerator Research Facility.

1. Brief Description of RIKEN Accelerator Research Facility

Figure 1 shows a general layout of the RIKEN Accelerator Research Facility (RARF). RARF has an accelerator complex consisting of a K540 ring cyclotron (RIKEN Ring Cyclotron, RRC) and its two injectors of a heavy-ion linac (RIKEN Heavy-Ion Linac, RILAC) and a K70 AVF cyclotron. The accelerator complex can accelerate a variety of ions from proton to very heavy ions such as lead and uranium in a wide range of energies. These ions are used by various users in the fields of nuclear physics, atomic physics, nuclear chemistry, condensed matter physics, applications to biology and medicine, and so on.

The ion beams accelerated with the accelerator complex so far are listed in Table 1, and are shown in Fig.2 together with the designed region of acceleration energies. The designed maximum energies are 210 MeV for proton, 135 MeV/nucleon for deuteron, 185 MeV/nucleon for helium-3, 135 MeV/nucleon for light heavy ions and about 20 MeV/nucleon for very heavy ions. The minimum energies can go down to 7 MeV/nucleon.

The details of RARF were reported elsewhere.[1,2)]

2. Acceleration of Proton Beams and their Use

We successfully accelerated proton beams at 70, 135 and 210 MeV with a combination of the AVF cyclotron and RRC. For 70 and 135 MeV proton beams, we used the H_2^+ acceleration technique. The injection energies of RRC were 10 MeV for 210 MeV proton beam, and 4 and 7 MeV/nucleon (of H_2^+ ions) for 70 and 135 MeV proton beams,

respectively. The output beam currents were about 100, 30 and 30 nA for 70, 135 and 210 MeV proton beams, respectively.

The designed energy of proton beam ranges from 3.8 MeV to 14.5 MeV with the AVF cyclotron only, and from 67 MeV to 210 MeV with a combination of the AVF cyclotron and RRC. The value of 14.5 MeV is restricted from the geometry of the center region of the RF dee of the AVF cyclotron that is designed only for use in an injector of RRC (harmonics of the AVF cyclotron equal to be 2) for the time being, though it has a potentiality to accelerate a proton beam up to 60 MeV. A dangerous resonance of vertical betatron frequency ($\nu_z = 0.5$) in RRC determines the nominal maximum energy of 210 MeV. The trim coil power supplies, however, has a potentiality to produce an isochronous field for a proton beam of higher energy. We tried an acceleration at 270 MeV where vertical betatron frequency reaches an actually allowable limit ($\nu_z \approx 0.2$). We found that we could clear the dangerous resonance and successfully accelerate up to 270 MeV proton beam, although we failed to extract it and part of the beam was lost near the resonance.

Using the proton beams, two experiments were made: an experiment of single event upset rates of a memory chip and a test of time-of-flight (TOF) measurement system. The former experiment was made at these three energies to evaluate tolerance to proton upset for a memory chip (32-bit microprocessor V70, NEC) that will be used in space. The E5 room in Fig. 1 was used for this experiment. The analysis of the experimental data is in progress. The latter experiment of the TOF measurement system was made at 210 MeV by use of part of a high-resolution spectrometer SMART (Swinger and Magnetic Analyzer with a Rotator and a Twister) that is located in the E4 room of Fig. 1. The experimental setup is shown in Fig. 3. A 20 cm$^{\phi}$ x 5 cm^{t} liquid scintillator NE213 (see Fig. 4) was set 14 m downstream from the target position. By setting a Li foil 150 mg/cm2 thick at the target position, we obtained a mono-energetic spectrum of neutrons from ^{7}Li (p,n)^{7}Be (g.s. + 1st.) reaction. Figure 5 shows the obtained spectrum. Continuous energy spectrum of neutrons was also obtained by placing a carbon target 10 cm thick, in place of the Li foil, at the position 12.5 m upstream from the neutron counter. The thickness of 10 cm is the range of 210 MeV protons in carbon. The result is shown in Fig. 6.

We measured leakage radiation of neutrons and gamma rays at various places by taking a chance when the experiment of single event upset for 210 MeV protons was made. One measurement was made when a proton beam was stopped with a Faraday cup just after RRC. The beam intensity was 25 nA. We detected no leakage at measured places in the controlled area, except for the place just in front of an entrance/exit door of the RRC vault which door is located at the basement of RRC. The radiation level at this place was 60 and 13 μSv/h for neutrons and gamma rays, respectively. We, however, judge that this leakage causes no problem because this place is a very restricted area where nobody enters and stays for a long time during operation. A permanent gamma-ray monitor inside the RRC vault (3 m

downstream from the Faradaycup and 4.5 m higher than the beam line) indicated a radiation level of 8600 μSv/h. The other measurement was made when a proton beam was stopped with a Faradaycup in the E5 room. The beam intensity was 20 - 40 pA. We detected no leakage at measured places in the controlled area and ouside the building. Permanent neutron and gamma-ray monitors inside the E5 room (4 m downstream from the Faradaycup and 0.6 m higher than the beam line) indicated a radiation level of 400 and 40 μSv/h, respectively.

3. Summary

We obtained proton beams at 70, 135 and 210 MeV with an accelerator complex of the ECR ion source, the K70 AVF injector cyclotron and the K540 Ring Cyclotron. The intensities of the 70, 135 and 210 MeV proton beams were about 100, 30 and 30 nA, respectively. We made two experiments using the proton beams: an experiment of single event upset rates of a memory chip for use in space and a test of TOF measurement system. We obtained mono-energetic neutrons as well as continuous neutrons with the TOF system. We also measured leakage radiation of neutrons and gamma-rays from the cyclotron vault and the experimental room, and found that there was no problem.

We are constructing a polarized proton/deuteron ion source. It will be completed in the spring of next year.

Acknowlegements

The measurement of neutrons in the TOF system was made by SMART group. The author is very grateful to Dr. T. Niizeki for offering us the results of neutron spectra.

References

1. Y. Yano "Status Report on RIKEN Accelerator Research Facility", Proc. 8th Symp. on Accel. Sci. Tech., RIKEN, Saitama, 25 - 26 November 1991, pp 10 -12.
2. A. Goto "Status of Injector AVF Cyclotron at RIKEN", Proc. 7th Symp. on Accel. Sci. Tech., RCNP, Osaka, 12 -14 December 1989, pp 51 - 53.

Table 1 RRC beams during April 1987 - December 1991.

Particle	Charge	RF F (MHz)	h	Energy (MeV/nucleon)	Intensity (pnA)
p	1	24.6	5	70	100
	1	32.6	5	135	30
	1	38.7	5	210	30
	1	42.2	5	270	-
d	1	24.6	5	70	50
	1	32.0	5	130	10
	1	32.6	5	135	30
^{12}C	5	35	9	42	40
	6	32.6	5	135	60
^{13}C	6	35	9	42	10
^{14}N	6	28	9	26	30
	6	35	10	34	30
	6	32	9	35	50
	6	35	9	42	30
	7	26	5	80	100
	7	32.6	5	135	230
^{15}N	5	20.187	10	10.65	20
	6	35	10	34	8
	6	35	9	42	8
	7	24.6	5	70	160
	7	30.5	5	115	30
^{16}O	8	32.6	5	135	60
^{18}O	7	35	9	42	3
	8	24.6	5	70	100
	8	29	5	100	180
^{20}Ne	9	33	9	37	17
^{22}Ne	8	28	10	21	5
^{24}Mg	11	29	5	100	3
	12	29	5	100	12
^{27}Al	13	29	5	100	5
^{40}Ar	11	20	10	10.3	140
	12	28	10	21	17
	13	28	9	26	46
	14	33	9	37	10
	16	26	5	80	2.5
	17	28.1	5	95	20
^{40}Ca	14	28	9	26	0.7
^{58}Ni	13	18	11	7	2
	8	18	11	7	18
^{64}Zn	20	25	9	20.6	0.5
^{65}Cu	8	18	11	7	3
	18	25	10	17	0.5
^{84}Kr	18	20	10	10.3	4
^{132}Xe	21	18	11	7	2.4
^{136}Xe	23	18	10	8.5	4
	33	28	9	26	1.8
^{166}Er	32	22.3	9	16	2

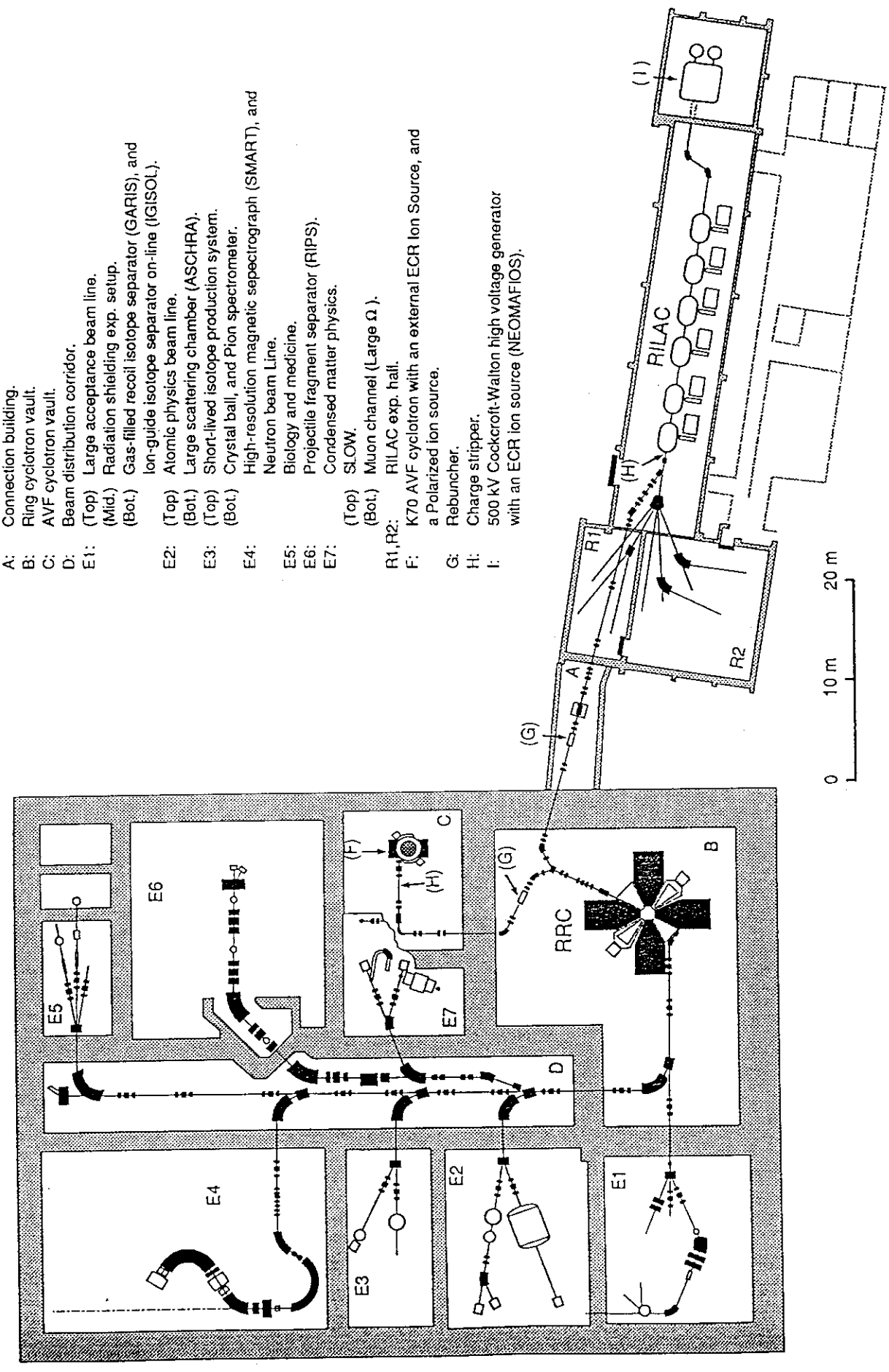

Fig. 1. Layout of the RIKEN Accelerator Research Facility (RARF).

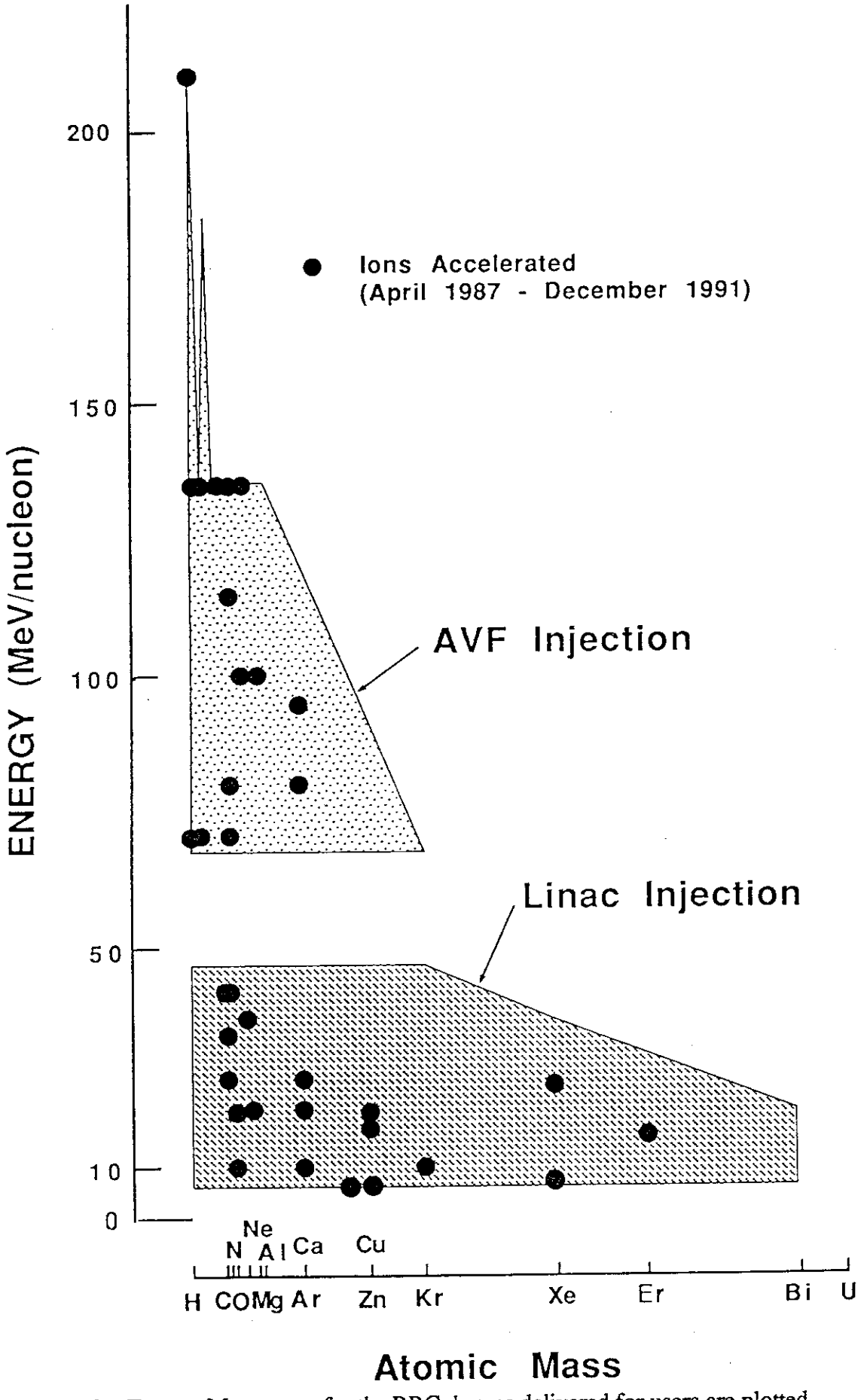

Fig. 2. Energy-Mass curve for the RRC; beams delivered for users are plotted.

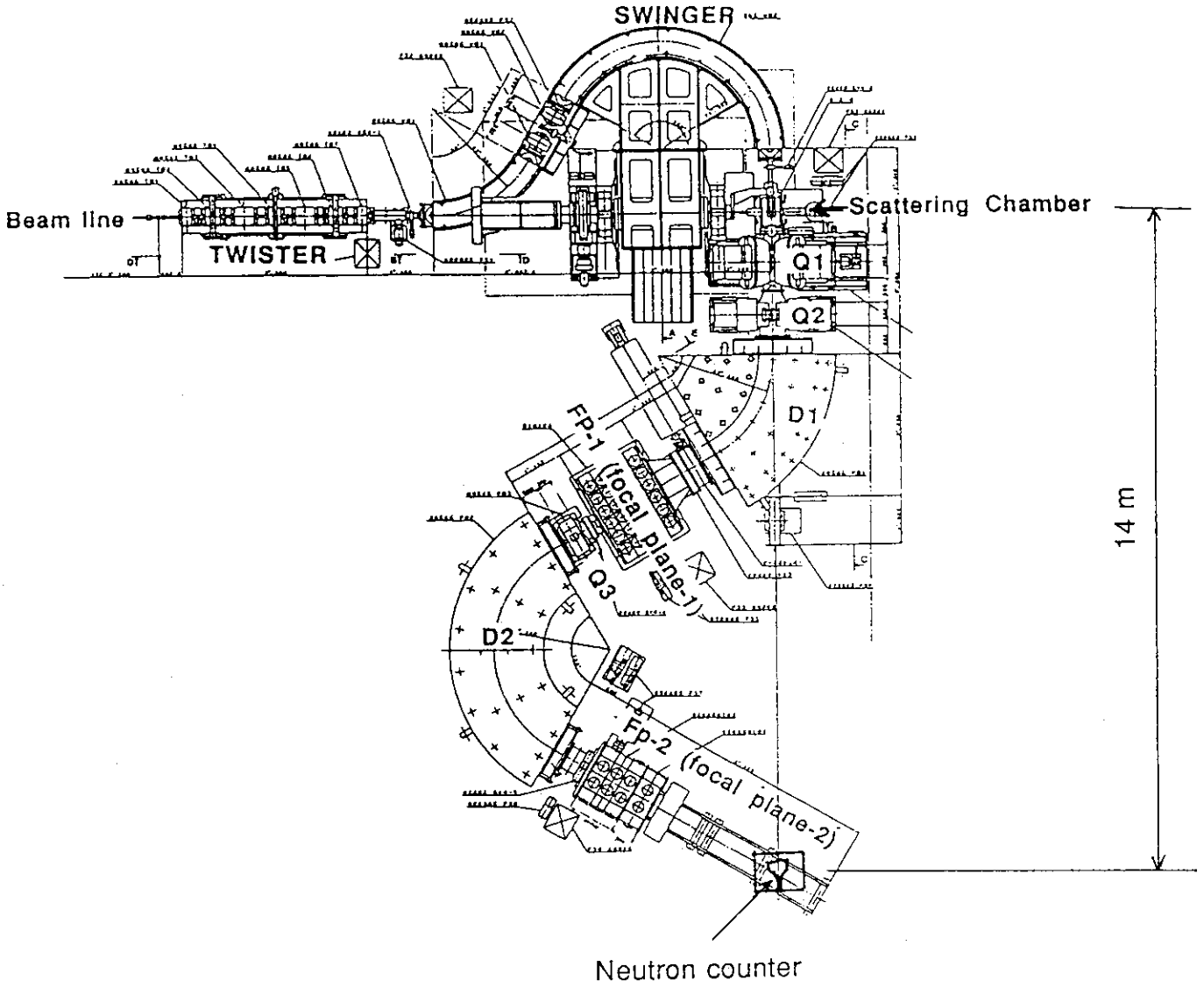

Fig. 3. Experimental setup of SMART and a neutron TOF measurement system.

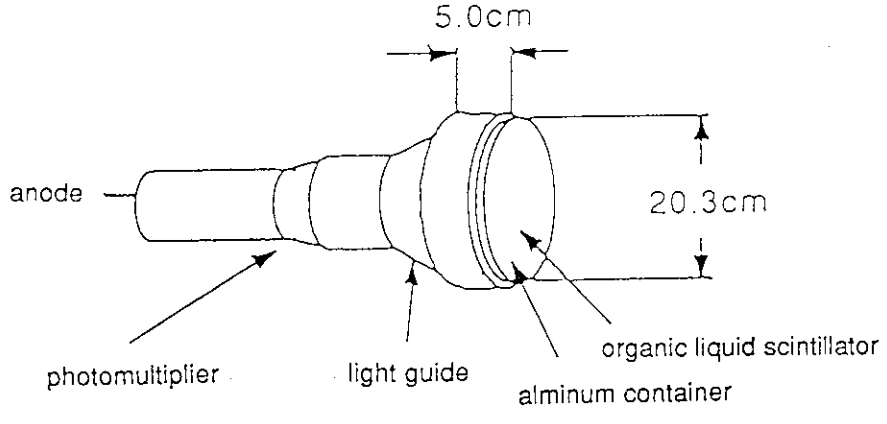

Fig. 4. Liquid scintillator NE213 used in the neutron TOF measurement system.

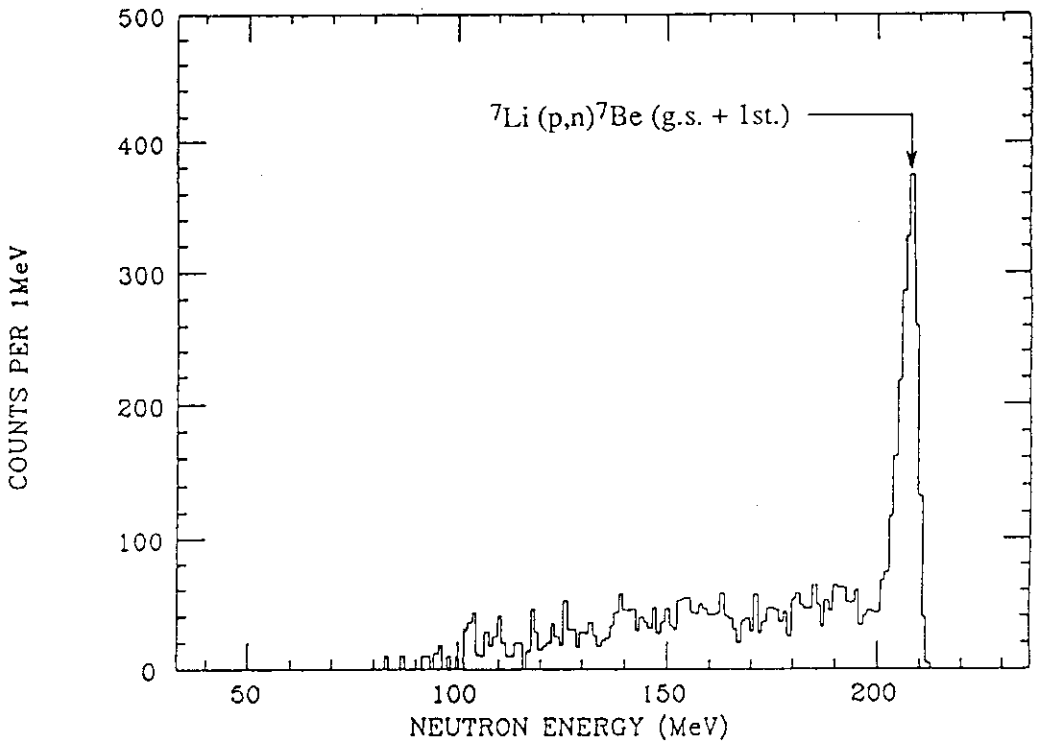

Fig. 5. Mono-energetic spectrum of neutrons from ^{7}Li (p,n)^{7}Be (g.s. + 1st.) reaction at E_p = 210 MeV.

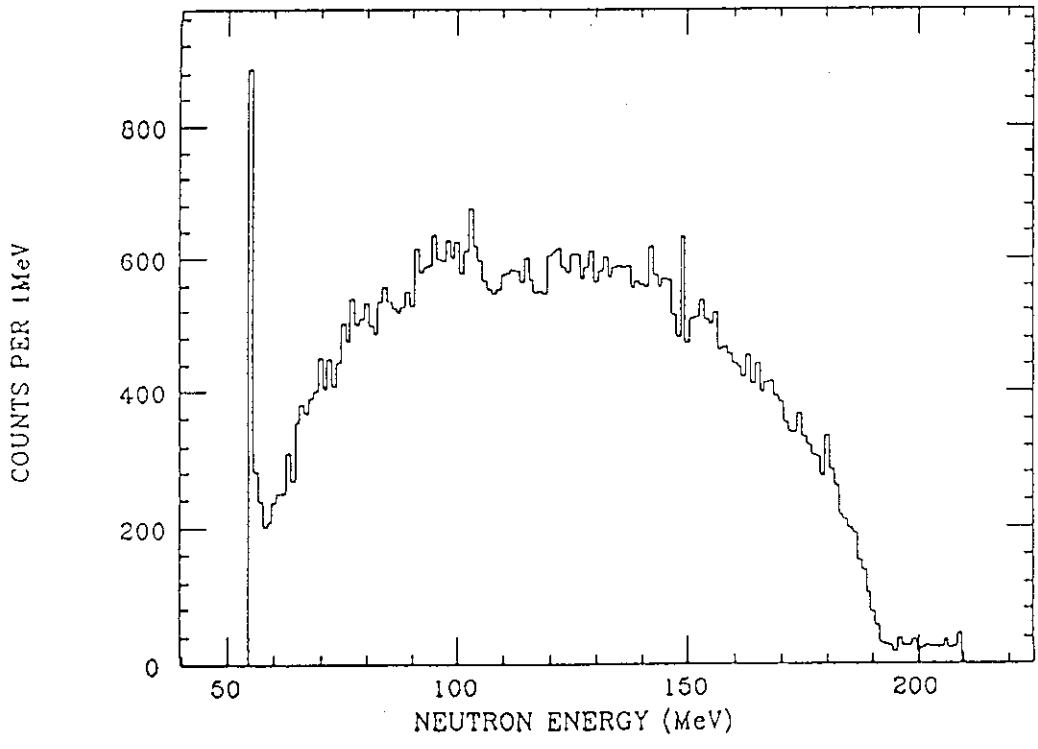

Fig. 6. Continuous spectrum of neutrons obtained by hitting a thick carbon target with 210 MeV protons. The thickness of the carbon target is 10 cm.

3.1 High Energy Electron-Photon Transport Calculation by Monte Carlo Method

HIDEO HIRAYAMA

KEK, National Laboratory for High Energy Physics
1-1 Oho, Tsukuba-shi, Ibaraki, 305 Japan

ABSTRACT

Treatments of high energy electron-photon cascade calculation in Monte Calro method were presented. Sampling methods, reactions treated in electron-photon cascade, reaction cross sections and their sampling, treatments of continuous energy loss and multiple scattering are explained mainly based on the manual of EGS4 code (SLAC-265).

1. Introduction

Electro-magnetic cascade must be treated in the calculation of high energy electron-photon transport calculation. For this purpose, Monte Calro method is used most commonly. To understand the methods used in Monte Calro method for electro-magnetic cascade, EGS4[1] was selected as the typical one. Sampling methods, reactions to be treated in electro-magnetic cascade, reaction cross sections and their sampling methods and treatments of continuous energy loss and multiple scattering of charged particles were presented based on mainly SLAC-265.

2. Sampling Method

2.1. Direct Method

If E is a logical expression involving some random variables, then we shall write $Pr\{E\}$ for the probability that E is true. We call F the cumulative distribution function of $\hat{x}$ if

$$F(x) = Pr\{\hat{x}\},$$

where $\hat{x}$ is a random variable. When $F(x)$ is differentiable, then

$$f(x) = F'(x)$$

is the probability density function of $\hat{x}$ and

$$Pr\{a < \hat{x} < b\} = \int_a^b f(x)dx.$$

In the other case that is commonly of interest, $\hat{x}$ takes values x_i with probabilities p_i and

$$F(x) = \sum_{x_i \leq x} p_i.$$

We call P the probability function of $\hat{x}$ if

$$P(x) = p_i \quad \text{if } x = x_i$$

$$= 0 \quad \text{if } x \text{ equal none of the } x_i.$$

Such a random variable is called a discrete random variable.

In the direct method for continuous random variable, we set

$$F(x) = \zeta$$

and solve for x. Where ζ is a random number between 0 to 1.

In the case of a discrete random variable, x is set to x_i, when

$$\sum_{j=1}^{i} p_j \leq \delta < \sum_{j=1}^{i+1}.$$

2.2. Combination of the "composition" and "rejection" techniques

Suppose f and f_i are density functions, α_i are positive real numbers, and $g_i(x) \in [0, 1]$. When the density function f given by

$$f(x) = \sum_{i=1}^{n} \alpha_i f_i(x) g_i(x),$$

$\hat{x}$ can be sampled as follows:

1. Pick ζ_1 and let i be such that

$$\sum_{j=1}^{i-1} \alpha_j < \zeta_1 \sum_{j=1}^{n} \alpha_j \leq \sum_{j=1}^{i} \alpha_j.$$

2. Pick x from $f_i(x)$, possibly by solving

$$\int_{-\infty}^{x} f_i(x)dx = \zeta_2.$$

3. Pick ζ_3. Terminate the algorithm and accept value of x if

$$\zeta_3 < g_i(x).$$

4. Otherwise, go back to step 1.

This sampling method is the one so called "composition" and "rejection" techniques. If all the $g_i = 1$, we have the pure "composition" method; and if $n = 1$, we have the pure "rejection" method.

3. Reactions Treated in Elecron-Photon Cascade

3.1. Photon Interactions

Elementary photon interactions summarized by Hubbell[2] are shown in Table 1. Within these interactions, photoelectric effect, pair production in field of nucleus and electron, and Compton scattering are taken into account by the EGS4 Code system. Inelastic scattering can be treated as a scattering photon with a free electron (Compton scattering) except low-energy photon. For low-energy photons, a binding effect affects both to the cross- section and angular distribution. Incoherent scattering including this effect was introduced in EGS4 by several authors.

3.2. Electron and Positron Interactions

In principle, the direct simulation of all the physical interactions (sometimes referred to as 'microscopic' simulation) could be used for electrons. The only difficulty in doing so is to keep track of all generations of electrons and photons produced during successive interactions. However, the very large number of interactions that take place during electron slowing down (of the order of 10^4 collisions in aluminum, from 0.5 MeV to 1 keV[3]), makes it unrealistic to simulate all the physical interactions in the majority of applications. This aspect has motivated the development of the so called 'condensed history' or 'macroscopic' techniques, where interactions are grouped indifferent ways. Physical interactions of electrons are classified into groups which provide a detailed 'macroscopic picture' of the physical process. The transition from a step to next step accounts for many interactions where multiple collision models, like multiple scattering or stopping-power theory, are considered. According to Berger[4] the 'condensed history' technique can be classified in two procedures:

(1) Class I, which groups all the interactions and uses a predetermined set of pathlength, the random sampling of interactions being performed at the end of the step.

(2) Class II, which groups only *minor* collisions where energy loss or deflection are small, but considers the individual sampling of *major* events, where a large energy loss or deviation occurs (Figure 1)[5]. EGS4 is a Class II code where the production of knock-on electrons (Møller scattering [e^-e^- scattering] and Bhabha scattering [e^+e^- scattering] and bremsstrahlung above each cut-off energy are treated individually.

4. Simulating the Physical Processes

4.1. Particle Transport

The mean free path, λ, of a particle is given in terms of its total cross section, σ_t — or alternatively, in terms of its macroscopic cross section, Σ_t — according to the expression

$$\lambda = \frac{1}{\Sigma_t} = \frac{M}{N_a \rho \sigma_t},$$

where

N_a = Avogadro's number,

ρ = density,

M = molecular weight,

σ_t = total cross section per molecule.

The number of mean free paths traversed will be

$$N_\lambda = \int_{x_0}^{x} \frac{dx}{\lambda(x)}.$$

If $\hat{N}_\lambda$ is a random variable denoting the number of mean free paths from given

point until the next interaction, then it can be shown that $\hat{N}_\lambda$ has the distribution function

$$Pr\{\hat{N}_\lambda < N_\lambda\} = 1 - \exp(-N_\lambda) \quad for\ N_\lambda > 0.$$

Using the direct sampling method and the fact that 1- ζ ia also uniform on (0,1) if ζ is, we can sample N_λ using

$$N_\lambda = -\exp\zeta.$$

The photon transport procedure is as follows. First, pick the number of mean free paths to the next interaction. Then perform the following steps:

1. Compute λ at the current location.
2. Let $t_1 = \lambda N_\lambda$.
3. Compute d, the distance to the nearest boundary along the photon's direction.
4. Lets t_2 equal the smaller of t_1 and d. Transport by distance t_2.
5. Deduce t_2/λ from N_λ. If the result is zero (this happen when $t_2 = t_1$), then it is time to interact - jump out of the loop.
6. This step is reached if $t_2 = d$. Thus, a boundary was reached. Do the necessary bookkeeping. If the new region is a different material, go to Step 1. Otherwise, go to step 2.

This procedure is shown in Figure 2

Charged particle (electron or positron) transport is complicated in several way. First of all, due to continuous energy loss the cross section varies along the path of the electron; in addition, the electron path is no longer straight. The fact that the electron total cross section for discrete interactions decreases with decreasing energy — and hence, decreases along the path of the electron — makes possible the following trick, which is used to account for the change in λ along the path, in EGS4. An additional fictious interaction is introduced

which, if it occurs, results in straight-ahead scattering (*i.e.*, no interaction at all). The magnitude of this cross section is assumed to be such that the total cross section along the path. That is,

$$\sigma_{t,fict}(x) = \sigma_{t,real} + \sigma_{fict}(x) = \text{ constant} = \sigma_{t,real}(x_0).$$

The location of the next "interaction" is then sampled with the total fictious cross section, $\sigma_{t,fict}$. When the point of interaction is reached, a random number is chosen. If it is larger than $\sigma_{t,real}(x)/\sigma_{t,real}(x_0)$, then the interaction is fictious and the transport is continued from that point without interaction. Otherwise, the interaction is real and the type of the interaction is determined. This scheme samples the distance between interactions correctly provided that the total cross section decreases with decreasing energy. Unfortunately, this is not the case for very low values of cut-off energy, AE (*e.g.*, for AE $\leq$ 580 keV [total energy] for low Z materials.). This introduces a small systematic error in low energy problems as discussed by Rogers[6]

4.2. Particle Interaction

When a point of interaction has been reached it must be decided which of the competing processes has occurred. The probability that a given type of interaction occurred is proportional to its cross section. Suppose the type of interactions possible are numbered 1 to n. Then $\hat{i}$, the number of the interaction to occur, is a random variable with cumulative distribution function

$$F(i) = \frac{\sum_{j=1}^{i} \sigma_j}{\sigma_t},$$

when σ_j is the cross section for jth type of interaction and σ_t is the total cross section ($=\sum_{j=1}^{n} \sigma_j$). The $F(i)$ are the *branching ratios*. The number of the interaction to occur, i, is selected by picking a random number and finding i which satisfies

$$F(i-1) < \zeta < F(i).$$

Once the type of interaction has been selected, the next step is to determine the parameters for the product particles.

4.3. Example of Parameter Determination — Pair Production

As the example of parameter determination used in EGS4, procedures of the pair production are shown.

We start with the following formula for the pair production differential cross sections:

$$\frac{d\sigma_{Pair}(Z,\check{k},\check{E}_+)}{d\check{E}+} = \frac{A'_p(Z,\check{k})r_0^2\alpha Z(Z+\xi(Z))}{\check{k}^3} \times \left\{ (\check{E}_+^2+\check{E}_-^2)\left[\phi_1(\delta)-\frac{4}{3}\ln Z-(4f_c(Z) \text{ if } \hat{k}>50,\ 0)\right] + \frac{2}{3}\check{E}_+\check{E}_-\left[\phi_2(\delta)\frac{4}{3}\ln Z-(4f_c(Z) \text{ if } \check{k}>50,\ 0)\right]\right\}$$

where

$$\delta = 136Z^{-1/3}2\Delta,$$

$$\Delta = \frac{\check{k}m}{2\check{E}_+\check{E}_-},$$

A'_p : empirical correction factor,

$$f_c(Z) = a^2\sum_{\nu=1}^{\infty}\frac{1}{\nu(\nu^2+a^2)},$$

$$a = \alpha Z,$$

α : fine structure constant,

$\xi(Z)$: constant for bremsstrahlung and pair production of atomic electrons.

$(4f_c(Z)$ if $\check{k} > 50,\ 0)$ means that $4f_c(Z)$ if $\check{k} > 50$ and 0 otherwise. For arbitrary screening, ϕ_1 and ϕ_2 are given by

$$\phi_1(\delta) = 4\int_{\Delta}^{1}(q-\Delta)^2[1-f(q,Z)]^2\frac{dq}{q^3}+4+\frac{4}{3}\ln Z,$$

$$\phi_2(\delta) = 4\int_{\Delta}^{1}\left[q^3-6\Delta^2 q\ln\left(\frac{q}{\Delta}\right)+3\Delta^2 q-4\Delta^3\right]\times[1-F(q,Z)]^2\frac{dq}{q^4}$$

$$+\frac{10}{3}+\frac{4}{3}\ln Z,$$

where $F(q,Z)$ is the atomic form factor for an atom with atomic number Z. Butcher and Messel[7] have approximated the screening functions to within 1-2% by the formulas

$$\phi_1(\delta) = (20.867 - 2.242\delta + 0.625\delta^2 \text{ if } \delta \leq 1,\ 21.12 - 4.184\ln(\delta + 0.952))$$

and

$$\phi_2(\delta) = (20.029 - 1.930\delta - 0.086\delta^2 \text{ if } \delta \leq 1,\ 21.12 - 4.184\ln(\delta + 0.952)).$$

By using several new variables, we obtain the following formula.

$$\begin{aligned}\frac{d\check{\Sigma}\_Pair}{d\epsilon} = &\left(\frac{Z_A + Z_B - (Z_F \text{ if } \check{k} > 50,\ 0)}{Z_{AB} - Z_F}\right) \\ &\times \left\{\left[\frac{2}{3} - \frac{1}{36\ln 183[1 + (Z_U \text{ if } \check{k} > 50,\ Z_P)]}\right][1]C(\delta') \right. \\ &+ \left[\frac{1}{12}\left(\frac{4}{3} + \frac{1}{9\ln 183[1 + (Z_U \text{ if } \check{k} > 50,\ Z_P)]}\right)\right] \\ &\left.\times \left[12\left(\epsilon - \frac{1}{2}\right)^2\right] A(\delta')\right\},\end{aligned}$$

where

$$\epsilon = \frac{\check{E}}{\check{k}},$$

$\check{E}$: the energy of on of the secondary electrons,

$\check{k}$: the incident photon energy,

$$Z_T = Z + \xi(Z),\ Z_A = Z_T \ln 183,\ Z_B = Z(Z + \xi(Z))\ln Z^{-1/3},$$

$$Z_F = Z(Z + \xi(Z))\dot{f}_C(Z),\ Z_{AB} = Z(Z + \xi(Z))L_{rad}(Z),$$

$$Z_U = (Z_B - Z_F)/Z_A, Z_P = Z_B/Z_A$$

$$\delta' = \Delta_C \Delta_E,$$

$$\Delta_C = 136 m e Z_G,$$

$$\Delta_E = \frac{1}{\check{k}\epsilon(1-\epsilon)},$$

$$A(\delta') = \frac{3\phi(\delta') - \phi_2(\delta') + (Z_V \text{ if } \check{k}_0 > 50, Z_G)}{\frac{2}{3} + 8\left[\in 183 + (Z_V \text{ if } \check{k} > 50,\ Z_G)\right]},$$

$$C(\delta') = \frac{3\phi_1(\delta') + \phi_2(\delta') + 16(Z_V \text{ if } \check{k}_0 > 50, Z_G)}{-\frac{2}{3} + (16 \ln(183 + (Z_V \text{ if } \check{k} > 50,\ Z_G))}.$$

We sample this equation with a combination of the "composition" and "rejection" techniques by the following decompositions:

$$\alpha_1 = \left[\frac{2}{3} - \frac{1}{36 \ln 183[1 + (Z_U \text{ if } \check{k} > 50,\ Z_P)]}\right],$$

$$f_1(\epsilon) = 1,\ \epsilon \in (0,1),$$

$$g_1(\epsilon) = \left(C(\delta'(\epsilon)) \text{ if } \check{k}\epsilon \in (m, \check{k} - m), 0\right),$$

$$\alpha_2 = \frac{1}{12}\left(\frac{4}{3} + \frac{1}{9 \ln 183[1 + (Z_U \text{ if } \check{k} > 50,\ Z_P)]}\right)$$

$$f_2(\epsilon) = 12\left(\epsilon - \frac{1}{2}\right)^2, \quad \epsilon \in (0,1),$$

$$g_2(\epsilon) = \left(A(\delta'(\epsilon)) \text{ if } \check{k}\epsilon \in (m, \check{k} - m), 0\right).$$

The sampling procedure is as follows:

1. Sample ϵ in the following way: If $\alpha_1 \geq (\alpha_1 + \alpha_2)\zeta_1$ use $\epsilon = \zeta_2$. Else, use $\epsilon = \frac{1}{2} + \left[\frac{1}{4}(\zeta_2 - \frac{1}{2})\right]^{1/3}$.
2. Calculate rejection function $g_1(\epsilon)$ or $g_2(\epsilon)$. If $\zeta_3 < g_1(\epsilon)$ or $g_2(\epsilon)$, reject and return to Step 1.

4.4. Continuous Electron Energy Loss

Continuous loss is the result of interactions in which the energy transfer to the secondary particles is not sufficient to put them above the discrete transport energy thresholds. The secondary particles are either soft bremsstrahlung photons, or atomic electrons which absorb some energy. The mean total continuous energy loss per unit length is thus given by

$$-\left(\frac{dE_\pm}{dx}\right)_{\substack{Total\\Continuous}} = -\left(\frac{dE_\pm}{dx}\right)_{\substack{Soft\\Bremsstrahlung}} - \left(\frac{dE_\pm}{dx}\right)_{\substack{Sub-Cutoff\\Atomic\ Electrons}}$$

where $\pm$ denotes positive or negative electrons. The first term on the right-hand side is the same for electrons and positrons in EGS4 system.

The second term may be expressed as the integral of the differential cross section for transferring a specified amount of energy, T, to an atomic electron, times the amount of the energy transfer over the range of energy transfers which still give rise to soft final state secondary electrons. The formulas recommended by Berger and Seltzer[8] for restricted stopping power are used in EGS4 as the approximation of the second term.

The formula that we use for the restricted stopping power (*i.e.*, due to sub-cutoff electrons) is

$$\left(-X_0\frac{d\check{E}_\pm}{dx}\right)_{\substack{Sub-Cutoff\\Atomic\ Electrons}} = \frac{X_0 n 2\pi r_0^2 m}{\beta^2}\left[\ln\frac{2(\tau+2)}{(\bar{I}_{adj}/m)} + F^\pm(\tau,\Delta) - \delta\right]$$

where X_0 = radiation length,

$\gamma = \check{E}_0/m$ = usual relativistic factor,

$\eta = \sqrt{\gamma^2-1} = \beta\gamma = \check{p}_0 c/m$,

$\beta = \sqrt{1-\gamma^{-2}} = v/c$ for incident particle,

$T'_E = T_E/m$ = K.E. cutoff in electron mass units,

$$\tau = \gamma - 1,$$

T'_{max} = maximum energy transfer = (τ if positron, $\tau/2$ if electron),

Δ = restricted maximum energy transfer = $min(T'_E, T'_{max})$,

$\bar{I}\_adj$ = average adjusted mean ionization energy,

δ = density effect correction

$$F^-(\tau,\Delta) = -1 - \beta^2 + \ln[(\tau-\Delta)\Delta] + \tau/(\tau-\Delta) + \left[\frac{\Delta^2}{2} + (2\tau+1)\ln\left(1-\frac{\Delta}{\tau}\right)\right]/\gamma^2,$$

$$F^+(\tau,\Delta) = \ln(\tau\Delta) - \frac{\beta}{\tau}\left\{\tau + 2\Delta - \frac{3\Delta^2 y}{2} - (\Delta - \Delta^3/3)y^2 - (\Delta^2/2 - \tau\Delta^3/3 + \Delta^4/4)y^3\right\},$$

$$y = (\gamma+1)^{-1}.$$

Collision stopping power of lead for different AE in shown Table 2 together with unrestricted stopping power.

4.5. Miltiple Scattering

When an electron passes through matter, it undergoes a large number of elastic collisions with the atomic nuclei. These have the effect of changing the electrons' direction, but do not significantly change its energy. To take into account these scatterings, Molière's theory[9] of multiple scattering as formulated by Bethe[10] is used in EGS4. Suppose an electron in normally incident on a slab of thickness $s(cm)$, as shown in Figure 3. Whenthe electron reaches the other side of the slab, it will have traveled a total distance of $t(cm)$, will achieved lateral displacements from its initial direction of Δx and Δy, and will be headed

in a direction specified by Θ and ϕ. That is, the final position is $(\Delta x, \Delta y, s)$, and the final direction is $(\sin\Theta\cos\phi, \sin\Theta\sin\phi, \cos\Theta)$. s is called as the straight line distance and t the total distance traveled. In EGS4 simulation we neglect the lateral deflections Δx and Δy, but correct for the difference between s and t. In order to be able to do this without introducing significant errors the size of the electron transport steps must be restricted to be less than certain limits. Our procedure then is to transport the electron in a straight line a distance (step size) s along its initial direction. The scattering angle Θ is sampled from a probability distribution function which depends on the material, the total distance traveled, t, and on the particle energy. The azimuthal angle ϕ is then chosen randomly.

4.6. How to Follow Cascade

In electron-photon cascade, the number of particle increases at each reaction. To simulate this, stack number, NP, is used in EGS4 as follows.

1. Set $NP = 1$ to the incident particle.
2. At each reaction, $NP = NP + 1$ is applied to the particle having smaller total energy and NP to the other one.
3. Follow the particle having the most large NP.
4. If the particle is discarded, the particle having $NP = NP - 1$ is followed next.
5. Discard of the $NP = 1$ particle means the end of history.

This procedure schematically is shown in Figure 4.

REFERENCES

1. Nelson, W. R, Hirayama, H, and Rogers, D. W. O.:EGS4 Code System, *SLAC-265*,(1985).
2. Hubbell, J. H.:Photon Cross Sections, Attenuation Coefficients, and Energy Absorption Coefficients from 10 keV to 100 GeV, *NSRDS-NBS 29.*
3. Berger, M. J., and Wang, R.:Multiple-scattering angular deflections and energy-loss straggling, pp 21-56, Monte Carlo Transport of electrons and Photons , ed Jenkins, T. M., Nelson, W. R., and Rindi, A. (New York:Plenum)
4. Berger, M. J.:Monte Calro calculation of the penetration and diffusion of fast charged particles, pp135- 215, Method in Computational Physics Vol. 1 ed Alder, B., Fernbach, S., and Rotenberg, M. (New York: Academic)
5. Andreo, P.:Monte Carlo techniques in medical radiation physics, *Phys. Med. Biol.* **Vol.36,** 861-920 (1991).
6. Rogers, D. W. O. :Low Energy Electron Transport With EGS,*Nucl. Instr. Meth.* **A227,** 535(1984).
7. Butcher, J. C., and Messel, H.:Electron Number Distribution in Electron Photon Showers in Air and Aluminum Absorbers,*Nucl. Phys.* **20,** 15(1960).
8. Berger, M. J., and Seltzer, S. M.:Table of Energy Losses and Ranges of Electrons and Positrons, National Aeronautics and Space Administration Report Number *NASA-SP-3012* (1964).
9. Molière, G. Z.: Theorie der Streuung scneller geladener Teilchen II. Mehrfach- und Vielfachstreuung,*Z. Naturforsch* **3a** ,231(1963).
10. Bethe, H. A.: Molière's Theory of Multiple Scattering,*Phys. Rev.* **89,** 1256(1953).

Table 1 Classification of elementary photon interaction[2]

Type of interaction / Interaction with:	Absorption (a)	Scattering: Elastic (coherent) (b)	Scattering: Inelastic (incoherent) (c)	Multi-photon effects (d)
(1) Atomic electrons	Photoelectric effect τ_{pe} { $\sim Z^4$ (low energy); $\sim Z^5$ (high energy) }	Rayleigh scattering, $\sigma_R \sim Z^2$ (low energy limit	Compton scattering, $\sigma_C \sim Z$	Two-photon Compton scattering, $\sim Z$
(2) Nucleons	Photonuclear reactions (γ, n), (γ, p), photo-fission, etc. $\sigma_{n.} \sim Z$ ($E \gtrsim 10$ MeV)	Elastic nuclear scattering, $(\gamma, \gamma) \sim Z^2$	Inelastic nuclear scattering, (γ, γ')	
(3) Electric field surrounding charged particles	(1) Electron-positron pair production in field of nucleus, $\varkappa_n \sim Z^2$ ($E \geqq 1.02$ MeV)	Delbrück scattering, $\sim Z^4$		
	(2) Electron-positron pair production in electron field, $\varkappa_e \sim Z$ ($E \geqq 2.04$ MeV)			
	(3) Nucleon-antinucleon pair production ($E \gtrsim 3$ GeV)			
(4) Mesons	Photomeson production, ($E \gtrsim 150$ MeV)	Modified (γ, γ)		

Table 2 Collision stopping power of lead for different AE together with unrestricted stopping power, cm^2/g. (Fitted results by PEGS4)

Energy	Unrestricted		AE=1.5 MeV		AE=0.521 MeV	
	e^+	e^-	e^+	e^-	e^+	e^-
1.0 MeV	0.968	0.996	0.997	1.03	0.731	0.732
10.0	1.16	1.20	1.09	1.10	0.803	0.803
100.0	1.385	1.43	1.18	1.18	0.884	0.884
1000.0	1.54	1.58	1.20	1.20	0.903	0.903

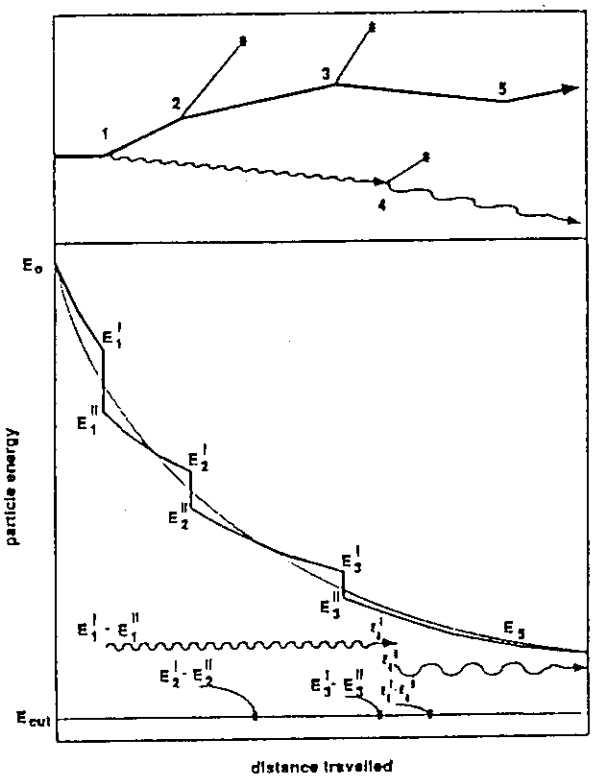

Fig. 1
Energy-distance diagram of the Class II procedure used to describe the electron (and photon) tracks shown in the upper part of the figure. Electron 'catastrophic' collisions occur at position 1 (bremsstrahlung interaction), 2 and 3 (knock-on inelastic collisions), and 5 (elastic collision, no energy loss). The photon is scattered by a Compton interaction at position 4. All secondary electrons (bottom of lower figure) are followed down to the transport cut-off of the simulation, E_{cut}, where they are absorbed (stars). The broken descendent line from E_0 corresponds to a calculation of the electron energy loss based on the continuous-slowing-down approximation (CSDA)[5].

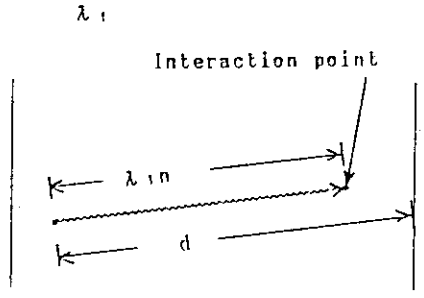

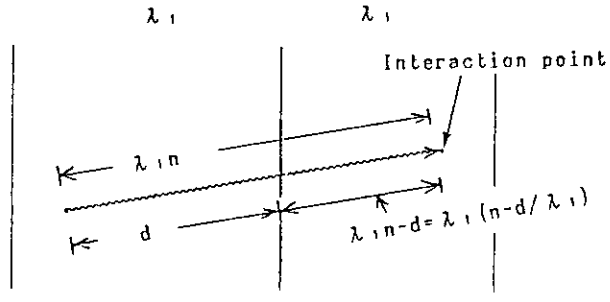

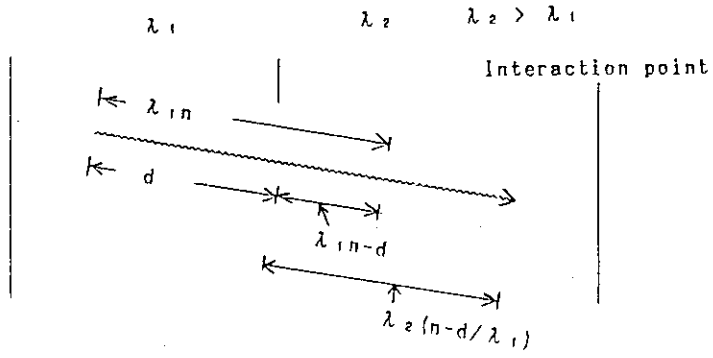

Fig. 2 Schematic diagram of photon transport.

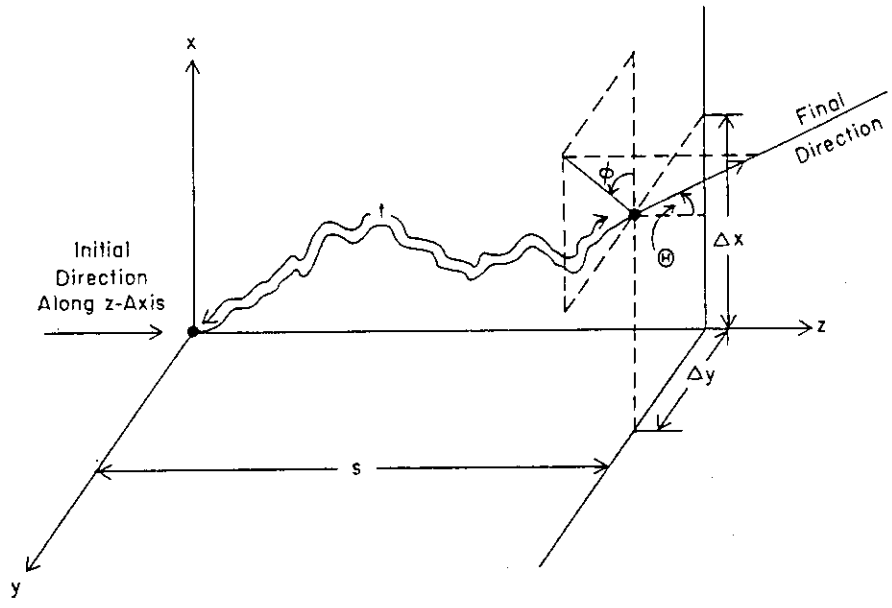

Fig. 3 Multiple scattering diagram[1].

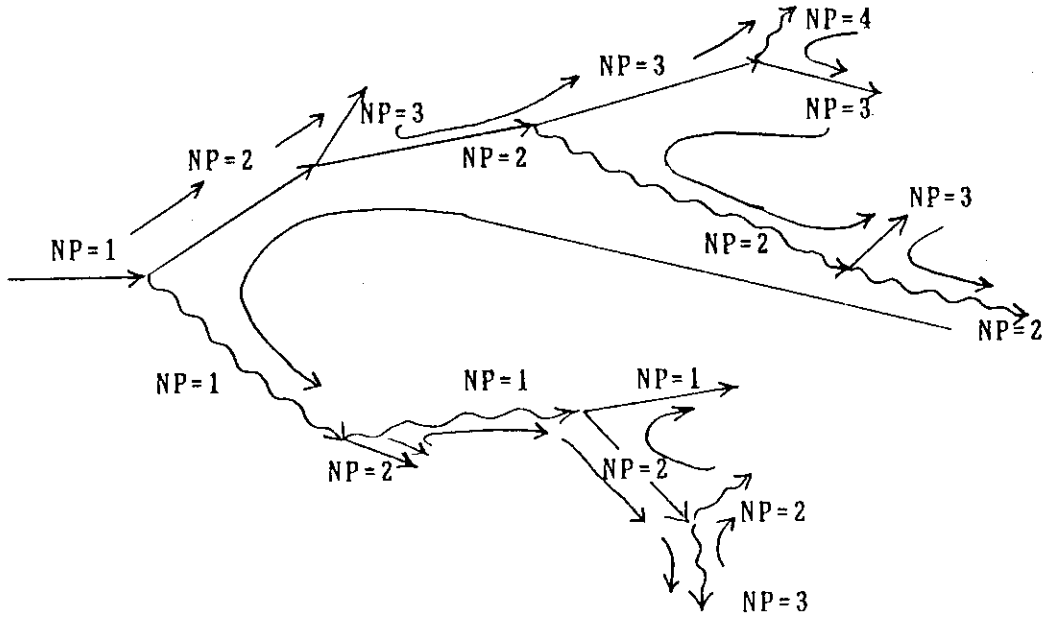

Fig. 4 Flow control of cascade in EGS4.

3.2 Recent Topics on Heavy-Ion Nuclear Reactions in Tandem Energy Region

Y. Sugiyama
Department of physics, JAERI, Tokai−mura, Ibaraki−ken

Abstruct

A simple overview of the heavy−ion nuclear reactions at energies close to the Coulomb barrier is presented. The effect of channel coupling on elastic scattering and fusion reactions is discussed.

1. Introduction

There is great interest in the study of the heavy−ion nuclear reactions at energies close to and below the Coulomb barrier. The initial motivation for this interest came from the observation of the anomalous behavior of cross sections for complete fusion in this energy region. The observed magnitude of this quantity frequently were orders of magnitude larger than predictions based on simple tunneling through a one−dimensional potential barrier. A second kind anomaly was observed in the elastic scattering of heavy ions at energies close to the Coulomb barrier. The real part of the optical potential was observed to increase sharply as the bombarding was decreased toward the barrier. At the same time , the imaginary potential at the strong absorption radius was observed to decrease rapidly. This phenomenon is termed the "threshold anomaly".

It has been suggested that the enhancement of sub−barrier fusion cross sections and the threshold anomaly are manifestations of the same phenomenon. I will present an overview of the phenomena observed in heavy−ion collisions at energies close to the Coulomb barrier.

2. Elastic Scattering

In Fig.1 we show the variation of the normalization of real double−folded potential and the imaginary potential at the strong absorption radius (12.4 fm) in the analyses of the elastic scattering of $^{16}O+^{208}Pb$.[1] The decrease of the imaginary potential as one approaches the Coulomb barrier is due to the closing of the effective

open channels which can lead to absorption of flux from the elastic channel. However the striking increase of the strength of the real potential is completely unexpected. This rapid, localized energy variation in the potential is known as the threshold anomaly. Nagarajian et al. were able to understand this energy variation as a consequence of a dispersion relation in the nuclear potential.[2] A dispersion relation describes the relationship between the real and imaginary parts of any physical quantity, in this case the real (V) and imaginary (W) parts of the nuclear optical potential. The dispersion relation implies that any localized energy variation in the imaginary part of the potential must reflect in a similarly localized energy variation in the real part (and vice versa).

As formulated by Nagarajan et al. the dispersion relation for the nuclear optical model potential is

$$U(E,r)=V(E,r)+iW(E,r)$$

$$V(E,r)=V_o(r)+\frac{P}{\pi}\int_{-\infty}^{+\infty}\frac{W(E',r)}{(E'-E)}\,dE'$$

where P denotes the principle part of the integral. V_o is the energy independent real potential which is modified by an energy dependent contribution arising from the energy dependence in the imaginary potential. The solid lines in Fig.1 show the application of the dispersion relation to the $^{16}O+^{208}Pb$ data. Assuming a simple description of the energy variation in W (a linear increase across the barrier region as more reaction channels open followed by a saturation at higher energies) gives the energy variation for V shown in the upper part of the figure. This gives a very good description of the energy variation down to the lowest energies. Interestingly , the dispersion relation predicts that at even lower energies the real potential should again decrease to the energy independent value.

The dispersion relation implies a direct connection between the elastic channel and the non−elastic channels. The energy dependent term in the real potential represents the effect on the elastic scattering of the coupling between the elastic and all other channels. In the optical model this complex process is reduced to a one channel description by the use of an imaginary potential to describe the loss of flux out of the elastic to the other channels. A more rigorous description would include these channels explicitly by evaluating the full coupled reactions channel (CRC) problem. If a complete CRC calculation were possible there would be no need for an imaginary potential , as all of the flux loss processes would be treated exactly. Such a

calculation is beyond present capabilities and the best which can be done is to include the most important channels.

We have performed such a detailed calculation for the ^{28}Si+^{58,64}Ni system.[3] Quasielastic–scattering cross sections have been measured at various energies around the Coulomb barrier. Elastic scattering angular distributions of ^{28}Si+^{58}Ni and ^{28}Si+^{64}Ni are shown in Fig. 2 . The dashed lines are CRC calculations including inelastic excitation only. The solid lines are CRC calculations including the one–neutron transfer channels also. A single energy– and isotope–independent optical potential is used in these calculations. The CRC calculations including the inelastic and transfer channels reproduce the data very well. The calculation also reproduces the measured cross sections in the inelastic, transfer and fusion channels at energies around the Coulomb barrier. In the present CRC calculation the threshold anomaly does not appear and a single energy– and isotope–independent bare potential is successful for explaining the data. The threshold anomaly is therefore seen to be a consequence of attempting to apply a simple one channel description to a complex multi–channel process.

3. Heavy–Ion Fusion

Another area which has generated a lot of interest in recent years has been the investigation of fusion cross sections at energies well below the Coulomb barrier. The striking feature of these studies has been the large enhancement of the measured yield over that expected from simple one dimensional barrier penetration calculations. The usual framework for these calculations is Barrier Penetration Model (BPM) in which the penetration through the elastic channel potential barrier is evaluated and the assumption made that all flux penetrating the barrier leads to fusion. The potential barrier aries from the combined Coulomb, nuclear and centrifugal potentials with the nuclear part usually described by an optical potential which fits elastic scattering data at energies above the barrier. It should be noted that this simple BPM does not take account of dumping due to the imaginary potential in the barrier region but the effect of this is relatively small.

The accepted consensus is that the failure of the BPM arises from the coupling to non–elastic channels, some of which allow for a lowering of the effective barrier leading to enhanced fusion. It is now becoming clear that transfer channels are an important coupling as well as inelastic channels. The extent of the increase in fusion cross section which occurs as a result of channel couplings[4] can be seen in Fig.3. where the measured fusion cross sections for the ^{28}Si+^{58,64}Ni systems are shown.

The dashed curves show the results when the couplings are switched off. The dotted curves include the inelastic excitation couplings while the solid curves include one and two nucleon transfer couplings in addition. The inelastic couplings produce a significant enhancement in the low–energy fusion cross sections which is essentially sufficient to account for the ^{28}Si+^{58}Ni data but is clearly insufficient for the ^{28}Si+^{64}Ni case. Adding the transfer couplings improves the agreement in this case while only a minor effect for ^{28}Si+^{58}Ni which has a relatively small transfer cross sections.

The present results , together with the one for the elastic scattering , indicates that the CRC method is a unified approach for describing the elastic, quasielastic and fusion cross sections at energies around the Coulomb barrier.

References

1) J.S.Lilley et at.,Phys. Lett. 151B (1985) 181.
2) M.A.Nagarajan et al., Phys. Rev. Lett. 54 (1985) 1136.
3) Y.Sugiyama et al., Phys. Rev. Lett. 62 (1989) 1727.
4) S.Landowne et al., Phys. Rev. C35 (1987) 597.

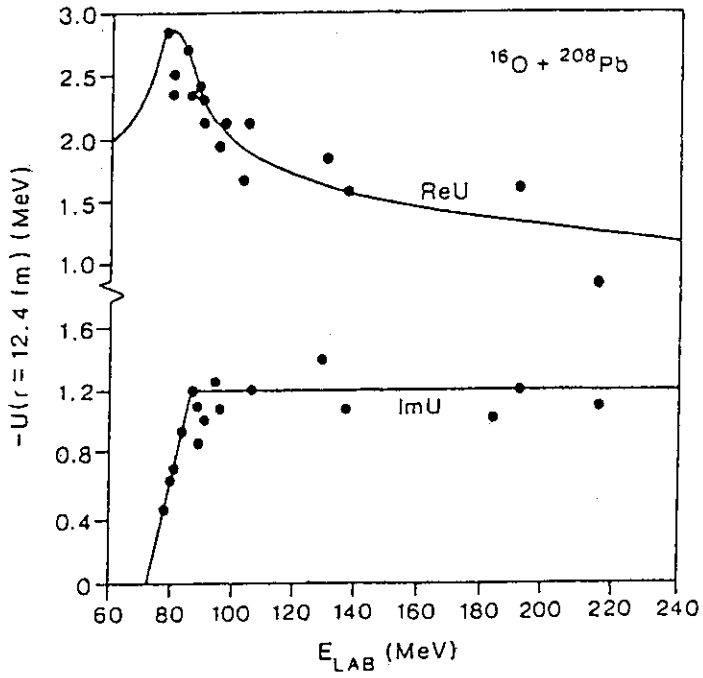

Fig.1 The strength of the optical potential , evaluated in the surface region, as extracted from fits to $^{16}O+^{208}Pb$ elastic scattering data. The solid lines indicate the results of a dispersion relation fit.

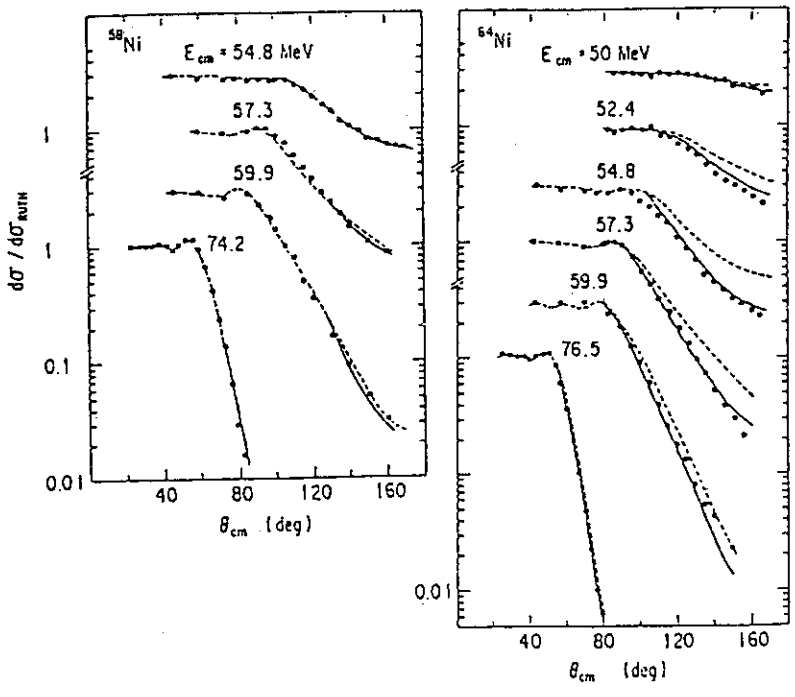

Fig.2 Elastic scattering angular distributions for $^{28}Si+^{58,64}Ni$ at different center−of−mass energies. The dashed lines are coupled−channels calculations including inelastic excitation. Solid lines are calculations including the one−neutron−transfer channel also.

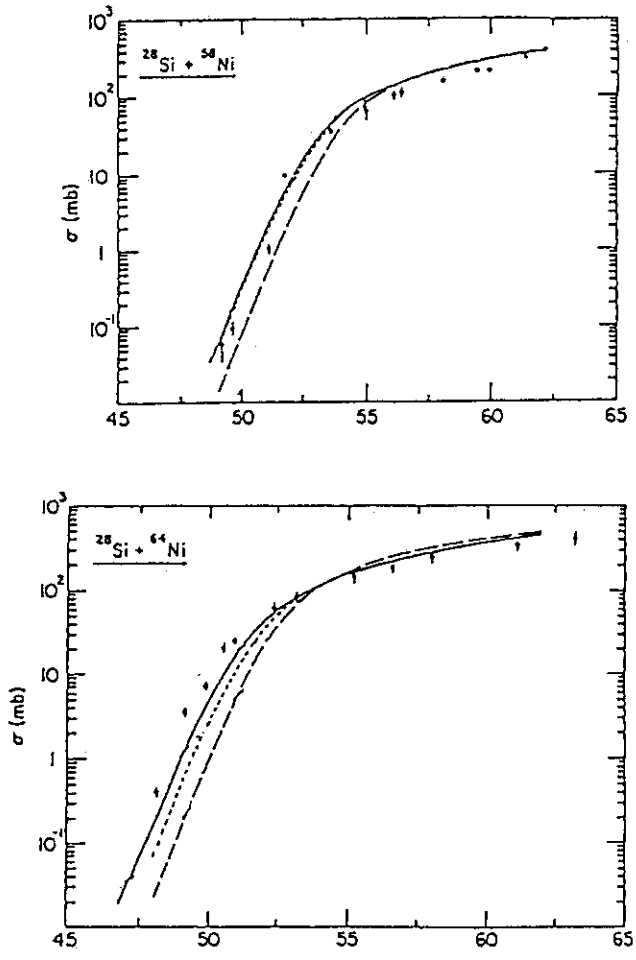

Fig.3 Calculated fusion cross sections for ^{28}Si+^{58,64}Ni. The dashed curves show the no−coupling limit. Including inelastic excitation channels gives the dotted curves and further adding the transfer channels gives the solid curves.

3.3 The Database Activity of Charged-Particle Nuclear Reaction Data Group

Masaki CHIBA
Faculty of Social Information
Sapporo Gakuin University
Bunkyodai-11, Ebetsu 069, JAPAN

Abstract:

Recent activities of the Japan Charged-Particle Nuclear Reaction Data Group are reported. The activities include data compilation of CPND produced in Japan with NRDF format, and its data conversion into EXFOR for international cooperation and coordination in the field of nuclear reaction database. As an achievement of the past 16 years of the effort of compiling CPND, some figures of the CPND compiled with NRDF and the data obtained with EXFOR are presented.

1. Introduction

Nowadays CPND produced in Japan are being compiled with a format named NRDF by the Japan Charged-Particle Nuclear Data Group. There is also another activity in compiling CPND in RIKEN. The RIKEN group compiles CPND with EXFOR for medical applications.

The NRDF format was devised as the result of a research project beginning in 1973[1], which was conducted by Professor H. Tanaka of Hokkaido University. The NRDF format has several distinctive features. It has a data language for data compiling. This language allows free format data description, set-structure of information blocks and so on [1,2]. This data compiling scheme makes the introduction of newly comming data types easy and sufficient information is included for understanding the data compiled.

The data compiling activity has been continued since 1979[3]. There was a turning point in the activity in 1987[4]; The status of the activity was changed into standing work from a research project. With this as a turning point, the Japan Charged-Particle Nuclear Data Group has been reorganized.

This group is composed of two committees and working staff[5]. The Advisory Committee consists of 11 members all over the nuclear research fields in Japan. The Executive Committee consists of 9 members near or in Sapporo. They are responsible for the activity of the group. Four members of the working staff are for data selection from journals, data coding, key-input or clerical work.

2. Data compiling with NRDF format

2.1 Amount of data compiled

Total data amount compiled with the NRDF is 1,146 entries, 62 MB by 1991. Table 1 shows the progress of the data compiling for the past years from 1980 to 1990.

Table 1. Amount of data compiled with NRDF format

year	data compiled in a year		accumulated data	
	number of record	amount	number of record	amount
1980	2,144	5.96 (MB)	2,144	5.96(MB)
1981	1,824	6.81	3,968	12.78
1982	1,801	6.52	5,769	19.30
1983	2,252	6.53	8,021	25.83
1984	1,703	5.03	9,724	30.86
1985	2,170	5.50	11,894	36.36
1986	962	3.14	12,856	39.50
1987	1,364	3.16	14,220	42.66
1988	1,384	3.30	15,604	45.96
1989	1,224	3.20	16,828	49.16
1990	1,282	2.90	18,100	52.06

2.2 Contents of NRDF data

Here we will introduce the content of NRDF data by showing several aspects. The 723 entries (where about 9,600 data tables are contained) out of total data compiled are loaded on a data storage and retrieval system of the NRDF data. This system is specific for the NRDF data only[2]. The system has a special list command "LISTX3". This command displays aggregated information about inverted index for each data item. The features of NRDF data given hereafter are reduced from the data obtained by using this "LISTX3" command.

2.2.1 Published year and data tables for the year

Table 2 shows years and the number of data tables which were published in each year.

2.2.2 Data source

The NRDF compiles CPND from articles published in journals. Table 3 shows major journals from which data is taken, and ratios of the data.

Table 2. Number of data tables for the year

year	number of data tables
1969	3
1973	51
1974	109
1975	6
1976	108
1977	154
1978	803
1979	1443
1980	712
1981	312
1982	902
1983	1293
1984	1495
1985	1328
1986	557
1987	185
1988	117
1989	10

Table 3. Data source

journal	ratio
NP/A	35.1 %
PR/C	34.2
PL/B	7.5
JPJ	6.3
PRL	4.5
77TOKYO	3.4
SNP	1.5
CJP	1.1
NIM	0.8
JP/G	0.8
AUJ	0.6

2.2.3 Physical quantities

The NRDF contains about 150 kinds of physical quantities for CPND. Each entry of the NRDF usually contains several kinds of physical quantities. Table 4 shows some ratios of physical quantities contained in the entries in high ranking.

2.2.4 Institute

The NRDF contains the data produced in Japan in the rate of 48.3 percent. The NRDF is now primarily compiling CPND produced in Japan. However in the early stage of the data compiling activity, proton-induced data not limited in Japan were also compiled.

Table 5 shows the institutes in Japan at which experiments were performed, and the rate of data for each institute.

Table 4. Physical quantities

physical quantity	ratio
ANGL-DSTRN	66.9 %
DSIGMA/DOMEGA	60.5
ANALPW	27.5
ENGY-SPEC	24.0
XSECTN	22.3
OPT-POL-PARA	18.0
EXC-FUNCT	17.6
SPIN	17.1
PTY	16.5
EXC-ENGY	16.4

Table 5. Institute and its data rate

institute	rate of data
INS	20.2 %
IPC	4.7
JAE	2.3
JCL	1.2
KEK	0.3
KTO	2.4
KYU	6.1
OSA	2.3
RCN	47.8
TIT	2.3
TOH	2.1
TSU	8.1

3. International data exchange

In the worldwide view point, nuclear reaction data is exchanged in a format named EXFOR. This format was originally developed in 1969 for neutron data exchange. In 1976, it was extended for the exchange of all nuclear reaction data[6].

In order to participate in the international nuclear data community, the data in NRDF should be transformed into EXFOR. Therefore we developed a database translator named NTX in 1982[7], which was revised later. Using the NTX, we have been transforming the CPND of NRDF produced in Japan into EXFOR, and sent them to NDS of IAEA since 1982.

3.1 Data transmission

When we send some nuclear reaction data entries to other centers, the data entries are merged in a magnetic tape which is called TRANS tape. Each TRANS tape has its original center identification and sequential number such as E001, E002, and so on[8]. Original center identification 'E' is assigned to the Japan Charged-Particle Nuclear Reaction Data Group.

We submitted TRANS E001 to NDS in 1982 as a trial of NTX translation, which contained only one entry. Then in 1983 TRANS E002 was sent to NDS in order to check the achievement of the translation. This TRANS contained several tens entries. The result of the conversion was discussed with NDS staff in Vienna. There were several defects found in conversion principles and in the NTX program itself. The principal defect to cause difficulty in translation was that this version of NTX tried to convert all quantities to EXFOR.

The conversion principle was altered to a new one. That was: to select quantities which correspond to the quantities defined in the EXFOR system from a NRDF entry, and to convert only these selected quantities to EXFOR entries. The second version of NTX was revised with this principle in 1984.

In 1988, TRANS E003 and E004 was submitted. The TRANS E004 was a first TRANS that was registered in the EXFOR E series library in NDS. In 1989 TRANS E005 and E006, in 1990 TRANS E007 and E008, and in 1991 E009 were submitted

The TRANS E009 contains 19 entries. These 19 entries were selected from the NRDF data which were compiled in 1990. In 1990 we compiled 59 entries as a whole with NRDF. So thirty percent of the NRDF data were transformed into EXFOR.

At the same time, we sent a representative of the Japan Charged Particle Nuclear Data Groupe to "IAEA Consultants' Meeting of the Nuclear Reaction Data Centers" and "IAEA Specialists Meeting on Technical Aspect of Nuclear Data Processing and Exchange" from 1989 every year.

3.2 Received data in EXFOR

We have received several TRANS tapes from NDS. These TRANS contained CPND and photo-nuclear data in EXFOR. The data received are accumulated in a disc file of the computer system of Hokkaido University Computing Center.

A index database of the received data is also prepared. The EXFOR accumulated file and the index database can be accessed through the computer system of Hokkaido University Computing Center. A index listing can be produced from the index database by using the index listing program prepared. The programs for the index database and for the index listing were installed with the NDS Data Index System[9] and the NDS Data Dictionary System[10].

The total amount of the data recieved is 27 MB, 991 entries and 14,780 subentries by 1991. There are 11 original files identified. The number of entries of each file is listed in Table 6.

Fig. 1 shows the contribution of the NRDF to the international activity of CPND compiling by drawing the data on table 6.

Table 6. EXFOR data received

originating center	file id.	number of entries	content
NRDF	E	33	CPND
NDS	3	15	NND
CAJAD	A	267	CPND
KACHAPAG	B	180	CPND
NNDC	C	280	CPND
NDS	D	27	CPND
NDS	G	1	Photo
CDFE	M	25	Photo
NDS	P	144	MacGowen file
RIKEN	R	10	CPND
CNDC	S	9	CPND

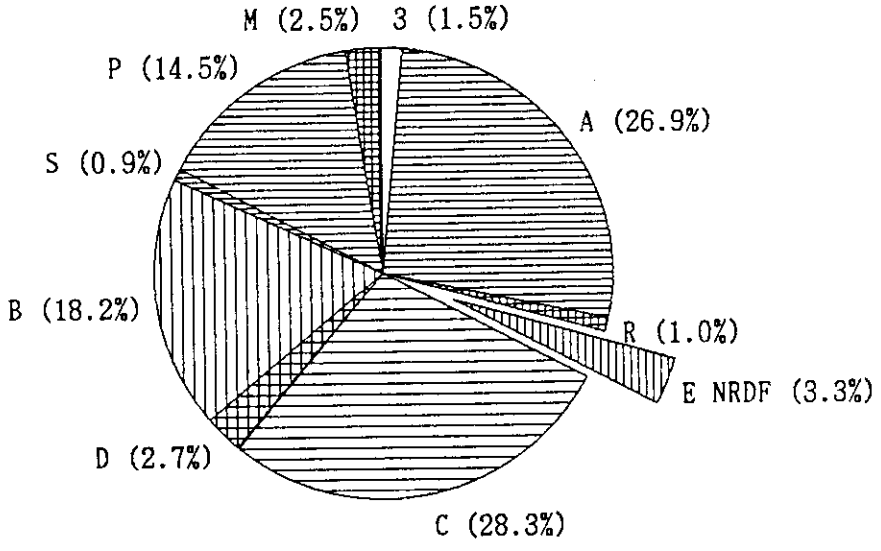

Fig. 1. Contribution of NRDF
Data received from NDS by 1991/10

4. Concluding remarks

Practical experience of the Japan Charged-Particle Nuclear Reaction Data Group was depicted by showing some figures of the CPND compiled with NRDF and the received data with EXFOR. We showed that this is one of the successful ways for constructing a database covering a certain field of science by cooperating and coordinating internationally. As fig.1 shows, the contribution of the NRDF is not so high at the present. We are supposed to increase the ratio of the contribution.

There are also some problems which remain for the data compiling with NRDF. One of them is to establish a way of the direct data acquisition from authors. Another one is to find a covienient way to get author's proof.

As the amount of stored data grows, new data needs arises. In order to meet this new needs, the data storage and retrieval system of NRDF is to be revised by using some database management system on the market.

Acknowledgement

Author would like to thank Dr. Y. Akaishi and Dr. K. Kato of Hokkaido University for valuable discussions.

References

[1] M. Togashi and H. Tanaka, Scientific information system for nuclear physics research, in Scientific Information in Japan, H. Inose(ed.), North-Holland Publishing Company 1981.

[2] M. Togashi and H. Tanaka, An information management system for charged particle nuclear reaction data, Journal of Information Science, Vol. 4, No. 5, 1982, pp. 213-224.

[3] H. Tanaka(ed.), Research and Development Report of Charged-Particle Nuclear Reaction Database(in Japanese), Japan Charged Particle Nuclear Reaction Data Group, 1981.

[4] NRDF Annual Report 87, Japan Charged-Particle Nuclear Reaction Data Group, 1988.

[5] NRDF Annual Report 90, Japan Charged-Particle Nuclear Reaction Data Group, 1991.

[6] A. Calamand and H. D. Lemmel, Short Guide to EXFOR, IAEA-NDS-1, 1981.

[7] M. Chiba, T. Katayama and H. Tanaka, A database translator of nuclear reaction data for international data exchange, Journal of Information Science, Vol. 12, No. 4, 1986, pp153-165.

[8] V. McLane(ed.), EXFOR Manual, 1989.

[9] P. M. Attree and P. M. Smith, System Specification for the NDS Data Index System, IAEA-NDS 6, 1979.

[10] P. M. Attree and P. M. Smith, System Specification for the NDS Dictionary System, IAEA-NDS 6, 1979.

4.1 Systematics of Neutron-Production Cross Section for Proton-Induced Spallation Reactions

Kenji ISHIBASHI, Kazuhiko HIGO, Shouitirou SAKAGUCHI,
Yuzuru MATSUMOTO*, Yoshihisa WAKUTA
Department of Nuclear Engineering, Kyushu University
Hakozaki, Fukuoka 812, Japan
and
Hiroshi TAKADA, Takahiko NISHIDA, Yasuaki NAKAHARA
Japan Atomic Energy Research Institute
Tokai-mura, Naka-gun 319-11, Japan

The parameterization of the double differential cross section is made for the neutron emission from proton-induced spallation reaction. The neutron data for incident proton energy of 600 to 800 MeV are well analyzed by the moving source model on the basis of the Maxwell-like energy distribution. In the incident energy region below about 400 MeV, however, the use of this method leads to an unsuccessful parameterization result. Then, the Watt distribution is introduced into the moving source model in this energy region. The combination of the two distributions enables us to parameterize the double differential cross section of neutron emission for the incident protons of 25 to 800 MeV and to find the systematics of moving source model parameters for a wide variety of target nuclei.

1. INTRODUCTION

The spallation reaction is caused by bombarding target nuclei with particles such as nucleons having an energy above a few hundred MeV. The reaction produces a number of neutrons. This reaction then is usable for providing an intense spallation neutron source or transmuting long-lived radioactive nuclides. In spite of the usefulness for engineering purposes, the accumulation of the measured neutron data[1]-[6] is poor for the proton induced spallation reaction. Therefore, it is important to find the systematic behaviors in the neutron data, and to parameterize them to extend to different incident energies and target nuclei.

Pearlstein[7] has parameterized the double differential cross section on the neutron emission from the proton induced reaction. He employed the four-component evaporation model, and made the parameter fitting to the experimental neutron spectra. An evaporation component requires two parameters for specifying its nuclear temperature and intensity. The feature of this method is the use of angle-dependent values of the nuclear temperature and the intensity. For describing the spectra at whole angles, the author found the relationship among parameters of different directions. The relationship was expressed by

---

* Present address: Kyushu Teikyo Junior College, Shinkattachi-machi, Omuta 836, Japan.

Legendre polynomials up to the second order. The number of parameters which needed to be finally determined was six multiplied by the number of evaporation components. Because of the large number of parameters, this method may be inconvenient for studying the systematics of the spallation reaction.

On the other hand, a moving source model[8] (MS model) has been utilized by Shibata et al.[9] for describing the protons emitted by several-GeV proton induced spallation reactions. This method made use of angle-independent values such as the nuclear temperature and the intensity. Three parameters were required in the model for specifying each evaporation component of experimental spectra, and were determined with simultaneous consideration of whole-direction data. This model successfully reproduced the angular distribution for each evaporation component of the proton spectra. The total number of parameters to be determined is less than in the angle-dependent fitting method mentioned above. At present, the experimental neutron spectra in the spallation reaction are available at only a few incident energies and emission angles. In addition, the quality of neutron emission data is not excellent in comparison to that of proton ones. For these reasons, the MS model may be better suited for reproducing the angular characteristics of neutron data for the spallation reaction. We will apply this model to study the systematic structure of the neutron data for the incident proton energy region of 600 to 800 MeV. In the incident-energy region below the pion emission threshold of about 400 MeV, the primary cascade develops quasi-elastically in a nucleus. In this energy region, we will introduce the moving source model based on the Watt distribution (Watt MS model) in accordance with the change of the collision mechanism.

2. EVALUATION MODELS

2.1 Experimental data

For the proton induced spallation reaction, the data of the double differential cross section on neutron emission are available at the incident energies of 800[1,2], 585[3], 318[1,2,7], 256[4], 113[5], 80.5 MeV[6]. While the data at 585, 256 and 113 MeV cover many targets and a wide range of emission angles, those at 800 and 80.5 MeV were taken less numerously. For the incident energy of 800 MeV, the data at 7.5 and 30 deg were published[1], while those in other directions were unpublished and described in an internal report[2]. We combine these 800 MeV data in the present study. The data at 318 MeV were measured at emission angles of only 7.5 and 30 deg.

2.2 Moving source model based on a Maxwell-like distribution (Maxwell MS model)

The MS model[8] had originally been proposed to represent the high-energy collision phenomena where a locally heated spot is moving with evaporating particles in a nucleus. The authors attempt to apply the model to evaluation of the double differential cross section on neutron emission for the intermediate-energy proton induced reaction. Since the particle emission behavior in this reaction is also explained to a considerable extent by

such models as the intranuclear-cascade model[10], the reaction may not always produce the physical moving source. The authors think that the MS model is applicable[9] to various reactions including the intranuclear-cascade process. The situation of the reaction is illustrated in Fig. 1, where a projectile particle interacts with the nucleus that is indicated by a large circle. The illustration on the left shows the collision phenomena in the laboratory frame, whereas that on the right indicates the same phenomena which is seen from an observation point moving with an appropriate velocity β (moving frame). Neutrons are assumed to be emitted isotropically with an exponential-type energy distribution[8],[9] of a temperature T(MeV) when the moving frame is chosen.

For describing phenomena in the relativistic region, introduction of the invariant cross section $E_{tot}(d^3\sigma/dp^3)$ is useful, where total energy E_{tot} is the sum of rest mass m and kinetic energy E_{kin}. For convenience, momentum p is expressed by a unit MeV/c, where c is the light velocity. Since $d^3p = p^2dpd\Omega$ is written as $pE_{tot}dE_{kin}d\Omega$, the invariant cross section is related to the double differential cross section as

$$E_{tot}(d^3\sigma/dp^3) = p^{-1}(d^2\sigma/dE_{kin}\, d\Omega) \quad . \tag{1}$$

This equation holds good regardless of the frames chosen.

By the use of the exponential function, the invariant cross section is expressed[8],[9] by

$$E_{tot}(d^3\sigma/dp^3) = A\ \exp(-E_{kin}^*/T) \ , \tag{2}$$

where A(mb/sr(MeV/c)^{2}c) is the constant, E_{kin} the kinetic energy (MeV) of the neutrons, and an asterisk indicates the value in the moving frame. If E_{kin}^* is small and in the region below 100 MeV, for example, the corresponding momentum p^* is well approximated by $(2ME_{kin}^*)^{1/2}$ as a nonrelativistic case, so that the double differential cross section is described in the moving frame as

$$d^2\sigma/dE_{kin}^*d\Omega^* \propto (E_{kin}^*)^{1/2}\exp(-E_{kin}^*/T) \quad . \tag{3}$$

This form coincides with the usual Maxwell distribution. Equation (2) is taken as the extension of the Maxwell distribution to the relativistic case and is regarded as a Maxwell-like kinetic energy distribution. Thereafter in this study, we designate the model of Eq. (2) a Maxwell-like moving source (Maxwell MS) model, in order to distinguish it from the model described in the next section.

The Lorentz transformation into the laboratory frame is written with the unit system of c=1 by

$$E_{kin}^* + m = (E_{kin} + m - p\beta\ \cos\theta)(1-\beta^2)^{-1/2} \ , \tag{4}$$

where m is the neutron mass(MeV), β the velocity, θ the emission angle, and E_{kin} the neutron kinetic energy (MeV) in the laboratory frame. Equation (2) is converted into the equation in the laboratory frame as

$$E_{tot}\left(\frac{d^3\sigma}{dp^3}\right) = \frac{1}{p}\ \frac{d^2\sigma}{d\Omega dE_{kin}} = A\ \exp\left\{-\left(\frac{E_{kin}+m-p\beta\cos\theta}{(1-\beta^2)^{1/2}} - m\right)/T\right\} \ . \tag{5}$$

The parameters A, T, and β are adjustable in fitting the equation with the experimental differential cross section data. We call A amplitude parameter, T temperature parameter,

and β velocity parameter. For the spallation reaction, the Maxwell MS model is applied in a form of summation of three components as

$$E_{tot}\left(\frac{d^3\sigma}{dp^3}\right) = \frac{1}{p}\frac{d^2\sigma}{d\Omega dE_{kin}} = \sum_{i=1}^{3} A_i \exp\{-(\frac{E_{kin}+m-p\beta_i\cos\theta}{(1-\beta_i^2)^{1/2}} - m)/T_i\} . \quad (6)$$

The three components correspond to the intranuclear-cascade, the preequilibrium and nuclear-evaporation (equilibrium) processes, respectively.

Figure 2 shows both the experimental neutron spectra and the results of fitting for the 585 MeV proton incidence on the lead target. The solid curves are in a good agreement with the measured data. The three components of cascade, preequilibrium and evaporation processes are plotted by dashed curves for the spectrum of 150 deg. Results obtained for 585 MeV protons on iron and 800 MeV on lead are plotted in Figs. 3 and 4, respectively. In Fig.3, the solid curve at 30 deg. slightly deviates from the experimental data in the region below 3 MeV. The slight deviation also appeared for target nuclei lighter than iron. While the agreement between the fitting and experiment was good for the 585 MeV data for the two targets, it was worse for the 800 MeV data particularly below 5 MeV. This may be because the 800 MeV data were compiled from different studies[1),2)], and may include some experimental inconsistency in the data at 45 and 112 deg.

The mass number dependence of parameters was obtained from the fitting results for the 585 MeV data. The results on the parameters A, T and β are shown in Figs. 5, 6 and 7, respectively. The values of T_{1-3} and β_{1-2} are nearly constant for all targets, while A_{1-3} depend on mass number strongly. It can be seen that A_1 has a tendency to be proportional to the nuclear radius rather than the cross-sectional area; A_2 and A_3 own the dependence on the nuclear volume and its square value, respectively. The dependence of β_3 on the target mass is considered to reflect the recoil momentum of the struck nuclei bacause the compound nuclei themselves are regarded as a moving source. Since the development of the cascading is almost determined by the incident energy and the properties of the nuclear matter, the constant behavior of T_1 and β_1 is understandable from the viewpoint of the cascade model.

2.3 Moving source model based on the Watt distribution (Watt MS model)

In the incident proton energy region below a few hundred MeV, the above Maxwell MS model reproduced the experimental data unsuccessfully. The results of fitting by the MS model are shown by the dashed curves in Fig. 8 for the 113 MeV proton incidence on iron. In the forward direction of 7.5 and 30 deg., the dashed curves are in poor agreement with the data of the neutron energy above several ten MeV. The neutrons in this energy range are emitted from the intranuclear-cascade process. The dashed curves in Fig. 9 indicate the results of fitting by the Maxwell MS model for the 256 MeV proton incidence on iron target. As in the 113 MeV case, one can see the disagreement of the dashed curves with the spectrum of neutrons emitted from the intranuclear-cascade process.

As described in the preceding section, the particles emitted by the evaporation were assumed to have Maxwell-like kinetic energy distribution in the moving frame. However, the

disagreement in Fig. 8 suggests that the measured energy spectra are not originated from the simple exponential function, and another distribution is preferred which produces a shoulder in the spectra. As is well known in the research of fission neutron spectra, the Watt distribution[11] reproduces higher-energy neutrons in spectra in comparison with the Maxwell one. The Watt distribution includes the effect of the isotropic motion of the fission fragments[11] that emit neutrons of the Maxwell. The Watt distribution includes the effect of the fragment motion in an analytical form. This distribution is introduced into the MS model in the present study, and is written as

$$\exp(-E_{kin}^{*}/T_w)\sinh(2(E_{kin}^{*}E_w)^{1/2}/T_w) \tag{7}$$

in the same moving frame as in the Maxwell MS model. The parameter E_{kin}^{*} is again the kinetic energy of neutrons, and E_w the characteristic energy in the Watt distribution. For the spallation reaction, E_w is regarded as a measure of the motion of the neutron-emitting sources, as discussed in Section 3.1. The cross section in the laboratory frame is written as

$$E_{tot}\left(\frac{d^3\sigma}{dp^3}\right) = \frac{1}{p}\frac{d^2\sigma}{d\Omega dE_{kin}} = \frac{A_w}{p^{*}}\exp(-E_{kin}^{*}/T_w)\sinh(2(E_{kin}^{*}E_w)^{1/2}/T_w)\ . \tag{8}$$

By the use of values in the laboratory frame, E_{kin}^{*} is given by Eq. (4) and p^{*} is written by $p^{*}=(E_{kin}^{*2}+2mE_{kin}^{*})^{1/2}$. We call this model a Watt moving source (Watt MS) model. The parameter A_w is the amplitude in the Watt MS model. The parameters T_w and E_w are designated Watt-moving-source temperature and energy, respectively. Since the Watt MS model applies to the case of relatively low incident energy, the kinetic energy of emitted neutrons mostly falls into the region that can be treated nonrelativistically. The Watt distribution approximately produces an average kinetic energy $E_{av}=3/2T_w+E_w$, while the Maxwell distribution gives $E_{av}=3/2T$ in the nonrelativistic case. Hence, it may be meaningful that T_w and E_w in the Watt MS model are converted into the equivalent temperature T_1' of the Maxwell distribution as

$$T_1'=T_w+2/3\ E_w\ . \tag{9}$$

The Watt MS model is considered to be applicable only to the initial process, i.e. the intranuclear-cascade process, that is directly induced by the incident protons as explained in Section 3.1. The solid curves in Fig. 8 show the results of fitting by the combination of Watt and Maxwell MS models. The Maxwell MS model was used for both the preequilibrium and the evaporation processes for the figure. The experimental data are expressed better by the solid than the dashed curves.

The mass number dependence of parameters is shown in Figs. 10, 11 and 12. The tendency of the dependence is similar to that in Figs. 5, 6 and 7. The value of A_w increases linearly with mass number M in Fig. 10, i.e. proportional to the nuclear volume, while A_1 changes more slowly with a dependence of $M^{0.406}$ in Fig. 5. The reason for the disagreeing behavior between A_1 and A_w is not clearly understood, but it may be ascribed either to the different treatments of the MS model or to some change of a physical phenomenon. In the latter case, it is supposed from the steeper dependence of A_w in Fig. 10

that the cascading phenomenon extends into a deeper location of nuclei than in the case of the higher-incident energy in Fig. 5. The occurrence of the cascade collision into the deeper location may be produced by a longer mean free path due to some nuclear effects including the Pauli principle[12]. The behavior of T_w and E_w is shown in Fig. 11. While T_w is a monotonously increasing function of mass number, E_w is that of decreasing mass number. These parameters are converted into the equivalent temperature T_1' by Eq. (9), as shown by the chain line in Fig. 11. The values of T_1' exhibit almost no dependence on the target mass, in the same way as T_1 in Fig. 6. The values of β_3 in Fig. 12 are interpolated with the function which is different from that in Fig. 7. When the same function as in Fig. 7 is used, a poorer reproduction is obtained in Fig. 12. The change of the function form is not easily explained, but may be ascribed to the difference in the reaction mechanism appearing in the two experiments.

The results of fitting by the combination of the Watt and Maxwell MS models are shown by the solid curves in Fig. 9 for 256 MeV proton incidence. The experimental spectrum at 7.5 deg. at energies above 100 MeV is reproduced by the solid curve in an averaged manner. The fitting by the solid curves is more successful than that of the dashed ones. The results for the 80.5 MeV data are shown in Fig. 13. It can be seen that the method is applicable to the 80.5 MeV data.

The three-component fitting by the combination of the Watt and the Maxwell MS models was carried out for the data[13] of the 25 MeV proton incidence on zirconium and lead. The parameters, however, did not converge. Instead, the two-component fitting easily lead to a convergence. Emitted neutron spectra for the 25 MeV proton incidence on zirconium are shown in Fig. 14, where the fitting was made by the Watt MS model for the higher-energy component and by the Maxwell MS model for the lower. The calculational results shown by solid curves are in good agreement with the experimental data at energies below 15 MeV. In the region around 17 MeV, the experimental spectra have broad lumps which originate from the reaction reflecting the nuclear shell structure. The solid curves do not reproduce these lumps at all, but represent the data on an average at energies above 15 MeV. The overall agreement in the entire energy range seems to be acceptable. A result similar to that in Fig. 14 was obtained in the fitting to the data for lead. As is well known in this incident-energy region, the calculational higher-energy component corresponds to the preequilibrium process. Although the Watt MS model was developed for the intranuclear-cascade process, it also applies to the preequilibrium process when the incident particle induces this process directly. For the 25 MeV case, the Maxwell MS model indicates the nuclear-evaporation process (the equilibrium process).

For the 318 MeV proton incidence, experimental data are available only in the direction of 30 deg. It is recalled that the velocity parameter β is determined mainly by the angular distribution, whereas the temperature parameter T (T_w or E_w) is influenced predominantly by the energy distribution. Because of the lack of angular distribution in the other direction, the complete fitting could not be performed with the present models.

Then, the values for T_{2-3} and β_{1-3} were obtained by assuming their linear dependence on the incident energies of 80.5, 113, 256, 585 and 800 MeV, and were fixed through determination of the other parameters. The emitted neutron spectra and the fitting results for lead are shown in Fig. 15. The experimental data are well reproduced as a whole, but some deviation appears in the region around 200 MeV.

Parameter sets were obtained for the incident energy of 80.5 to 800 MeV. Results are shown for lead by open marks in Figs. 16, 17 and 18, where the subscripts 1, 2 and 3 indicate the intranuclear-cascade, preequilibrium, and nuclear-evaporation processes, respectively. Black-painted marks in these figures indicate that the parameters at the incident energy of 318 MeV were evaluated by the incomplete parameter fitting mentioned above. In Fig. 16, the values of A_2 and A_3 are almost constant in the wide range of the incident proton energy. The parameter A_w for 80.5 to 318 MeV data was scaled by the use of

$$A_1' = A_w (3/2T_w + E_w + m)^{-1/2} \tag{10}$$

for an easy display, and is plotted together with A_1 at the other energies. For A_1 (or A_1'), the values are scattered with a weak dependence on the incident proton energy. The solid curves on A_1 (or A_1') show the interpolation results on all incident energies. In contrast, the dashed curve is drawn neglecting A_1' at 80.5 and 318 MeV, because the value at 80.5 MeV is exceptionally low and the parameter fitting was incompletely made at 318 MeV. The dashed curve in this figure has a tendency to increase with decreasing incident energy down to 100 MeV.

The values of T_w for 80.5 to 318 MeV data were converted by Eq. (9) into T_1' of the Maxwell MS model, and are plotted in Fig. 17 together with T_1 at the other energies. The values of T_1 to T_3 are raised smoothly with the incident proton energy. The neutron yield is proportional to the product of A and T in the Maxwell MS model. Since A_1 to A_3 are almost constant, the neutron yields for the preequilibrium and the evaporation processes increase with the incident energy. For the cascade process, the product of A given by the dashed curve in Fig. 16 and T_1 (or T_1') slightly decreases with increasing incident energy. However, the decrease in the neutron yield is not plausible in a physical sense. The reason for this inconsistency is uncertain, and it is desirable to accumulate further experimental data including elements besides lead. In Fig. 18, the values of β_1 to β_3 show a smooth dependence on the incident proton energy.

3. DISCUSSION

3.1 Physical interpretation of the Watt MS model

The Watt distribution was successfully incorporated into the moving source model. This suggests that a qualitative explanation may be made as follows. For incident energies above several hundred MeV, the typical collision phenomena was illustrated on the left of Fig. 1. Since the incident energy is sufficiently high, the cascading may be developed further after the first collision in the nucleus. In addition, pions can be generated by the quasi-inelastic collision at this energy, and they have a much shorter mean free path than

nucleons. When the incident energy is above the threshold of the inelastic collision, the intranuclear cascade may produce some branches, as shown in Fig. 1.

At energies below several hundred MeV, the situation may differ from the above: The cascading develops less extensively than in the case of the higher energy incidence. Simple illustrations are shown in Fig. 19. When the moving frame is close to the center of mass (cm) frame with respect to the first collision, striking nucleons go away with almost the same kinetic energy, as shown in the right illustration in this figure. The striking nucleons may make further collisions to a smaller extent than in the case of Fig. 1. Since no quasi-inelastic scattering is allowed at the incident energy less than 400 MeV, and the quasi-elastic collision produces only two branches at each scattering.

The original paper[11] for the Watt distribution has assumed that fission fragments themselves isotropically move with a given kinetic energy and they isotropically evaporate neutrons with the Maxwell spectrum of temperature T_w, while moving. The value of E_w stands for the kinetic energy of fragment divided by its mass number, i.e. kinetic energy per nucleon. When the original assumption made for the Watt distribution is taken into account in the present moving frame, one can see that the initial branching on the right-hand side in Fig. 19 is approximated to isotropically take place. In addition, the parameter E_w in Eq. (7) is considered as a measure of the kinetic energy of the initial branching nucleons. Since the Watt distribution itself is based on the particle emission from the isotropically-moving evaporation-source, the Watt MS model results in having two kinds of moving sources: one is the usual moving source in the direction of the incident particles, and the other that corresponding to the isotropic motion of the initial branching nucleons. Hence, the Watt MS model may be regarded as a double moving source model from this point of view.

In the case of 25 MeV proton incidence, the Watt MS model was acceptably applied to the preequilibrium reaction of the first process. This enables us to consider that the double branching takes place in an approximate manner when a proton of the low energy enters a nucleus.

3.2 Values of the parameters β and T

For the intranuclear-cascade process, the discussion on the parameters β and T is made by the following simple method. The velocity of the center of mass β_{cm} is easily obtained in the ultimate case, where the two-body collision takes place between the incident proton and nucleon at rest. The velocity is written as

$$\beta_{cm} = \frac{p}{m_p + m_n + E_p} \quad , \tag{11}$$

where m_p is the proton mass, m_n the nucleon mass, p the proton momentum, and E_p the proton energy. The kinetic energy of nucleon E_{cm} corresponding to β_{cm} is expressed by

$$E_{cm} = m_p\{(1-\beta_{cm}^2)^{-1/2}-1\} \ . \tag{12}$$

The values of β_{cm} and E_{cm} were calculated for incident energies up to 800 MeV. They are

listed in Table 1 together with the velocity and temperature parameters obtained by the fitting for the data for lead. The dashed curve given in Fig. 18 indicates the values of β_{cm}. As shown in the figure, β_{cm} is larger than the results of β_1 specially in the case of the higher incident energy. The reason is considered as follows: The intranuclear-cascade process is made of a series of collisions, producing the collision branches. The velocity parameter β_1 expresses the velocity of the moving point where the neutron emission looks isotropic. Thus, β_1 is the velocity value averaged over the entire cascading, so that it is smaller than β_{cm}. As indicated in Table 1, the value of E_{cm} is 70 to 80 % of 3/2T or E_w+3/2T_w in the region of 113 to 800 MeV. The understanding of the Watt MS model in the case of Fig. 19 may be plausible as well as the conversion in Eq. (9). The values of E_{cm} coincide with 3/2T_w+E_w at 80.5 MeV. This is because the cascade development is negligible at this incident energy.

4. CONCLUSION

The use of the moving source model based on the Maxwell-like distribution (Maxwell MS model) reproduced the experimental neutron spectra in the incident proton energy region of 600 to 800 MeV. At the energies of 80 to 300 MeV, the introduction of the Watt distribution into the moving source model (Watt MS model) were found to lead to good agreement with the experimental spectra of the cascade process. For the incident energy of 25 MeV, the use of two components of the Maxwell and Watt MS models gave acceptable results. The dependence of fitting parameters on the target mass number was obtained for the incident proton energies of 585 and 113 MeV. The incident energy dependence of the parameters was obtained for lead in the proton energy range of 80 to 800 MeV, and the tendency was considered to be understandable. The Maxwell and Watt MS models were found to be applicable to the nuclear data evaluation for a wide range of target masses and incident energies.

The authors gratefully acknowledge Prof. A. Katase of Tohwa University and Dr. T. Sakae of Kyushu University for their useful discussions about this work.

REFERENCES

(1) MEIER, M.M. et al.: Rad. Effects, 96, 73 (1986)
(2) HOWE, S.D. et al.: Los Alamos National Laboratory Report LANL-85-3360 (1985)
(3) CIERJACKS, S. et al.: Phys. Rev. C, 36, 1976 (1987)
(4) MEIER, M.M. et al.: Los Alamos National Laboratory Report LA-11656-MS (1989)
(5) MEIER, M.M. et al.: Nucl. Sci. and Eng., 102, 310 (1989)
(6) TRABANDT, M. et al.: Phys. Rev. C, 39, 452 (1989)
(7) PEARLSTEIN, S.: Nucl. Sci. and Eng., 95, 116 (1987)
(8) BOGATSKAYA, I.G. et al.: Phys. Rev. C, 22, 209 (1980)
(9) SHIBATA, T.-A. et al.: Nucl. Phys., A408, 525 (1983)
(10) BERTINI, H.W.: Phys. Rev., 188, 1711 (1969)

(11) TERRELL, J.: Phys. Rev., 113, 527 (1957)

(12) KIKUCHI, K., KAWAI, M.: Nuclear Matter and Nuclear Reactions, North Holland (1968)

(13) SCOBEL, W. et al.: Lawrence Livermore National Laboratory Report UCID-20101 (1984)

Table 1 Values of β_{cm} and E_{cm} estimated by simple equations, and those of β_1, 3/2T and $3/2T_w+E_w$ obtained by the parameter fitting for lead

E_p (MeV)	β_{cm}	β_1	E_{cm} (MeV)	3/2T (MeV)	$3/2T_w+E_w$ (MeV)
800	0.547	0.237	182	124	—
585	0.478	0.226	136	114	—
318	0.380	0.198	76.3	—	56.8
256	0.346	0.292	62.0	—	44.8
113	0.238	0.185	27.8	—	22.5
80.5	0.203	0.128	19.9	—	19.9

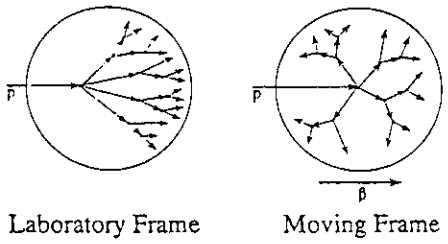

Fig. 1 Illustration of the Maxwell-like moving source model (Maxwell MS model).

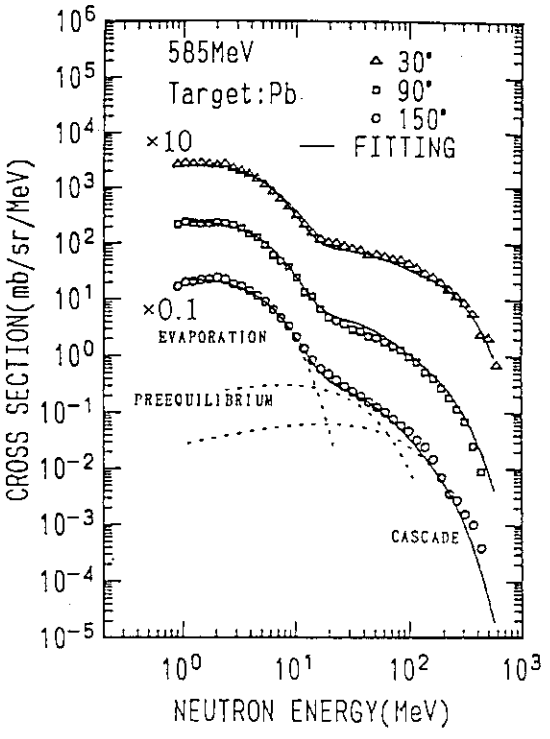

Fig. 2 Experimental neutron spectra and the results of fitting by the Maxwell MS model for the 585 MeV proton incidence on lead.

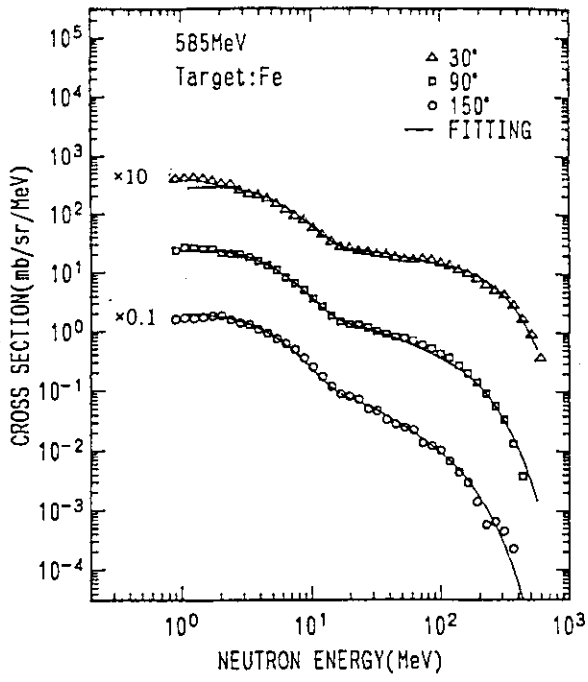

Fig. 3 Experimental neutron spectra and the results of fitting by the Maxwell MS model for the 585 MeV proton incidence on iron.

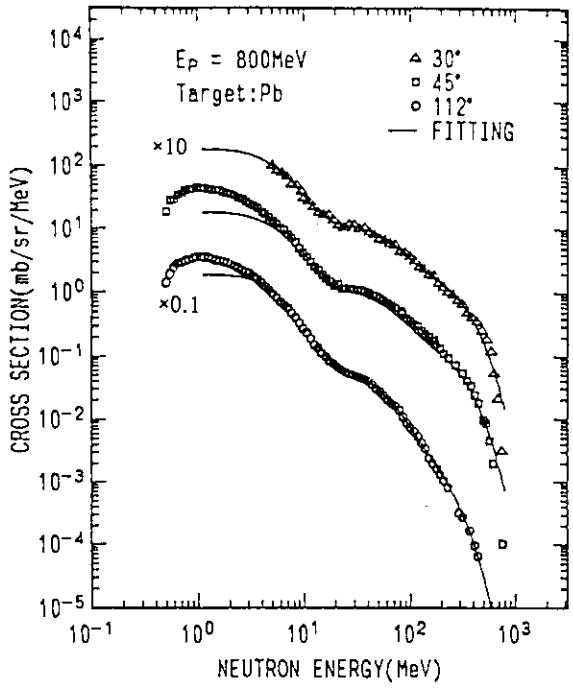

Fig. 4 Experimental neutron spectra and the results of fitting by the Maxwell MS model for the 800 MeV proton incidence on lead.

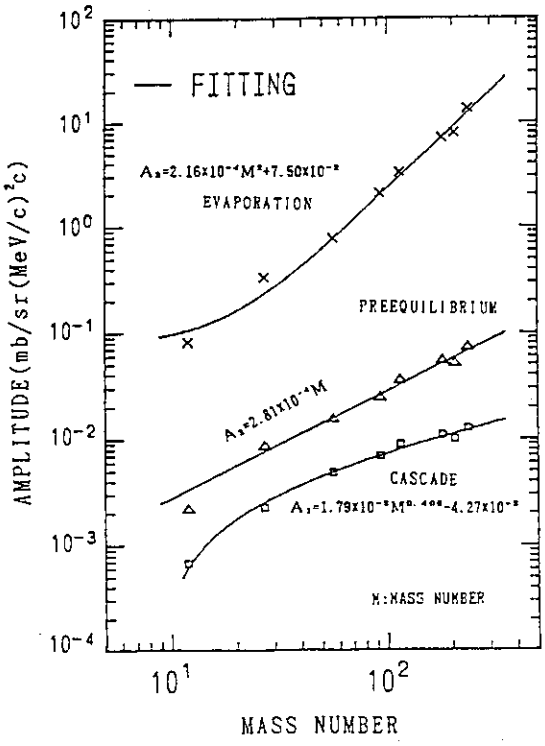

Fig. 5 Mass number dependence of the amplitude parameter A for the incident protons of 585 MeV.

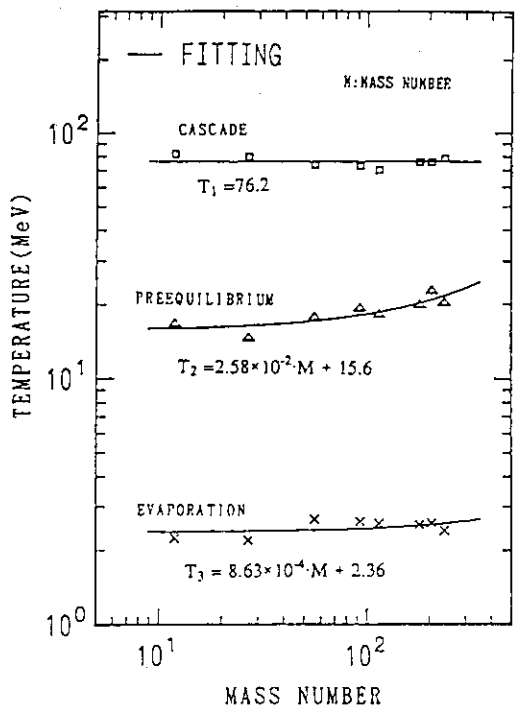

Fig. 6 Mass number dependence of the temperature parameter T for the incident protons of 585 MeV.

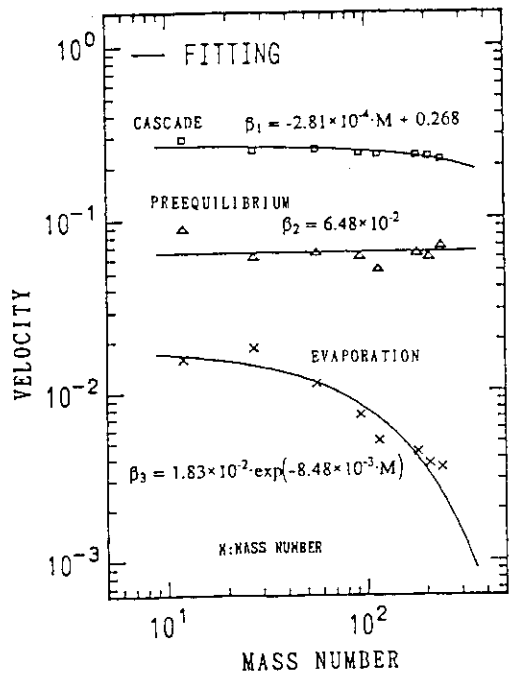

Fig. 7 Mass number dependence of the velocity parameter β for the incident protons of 585 MeV.

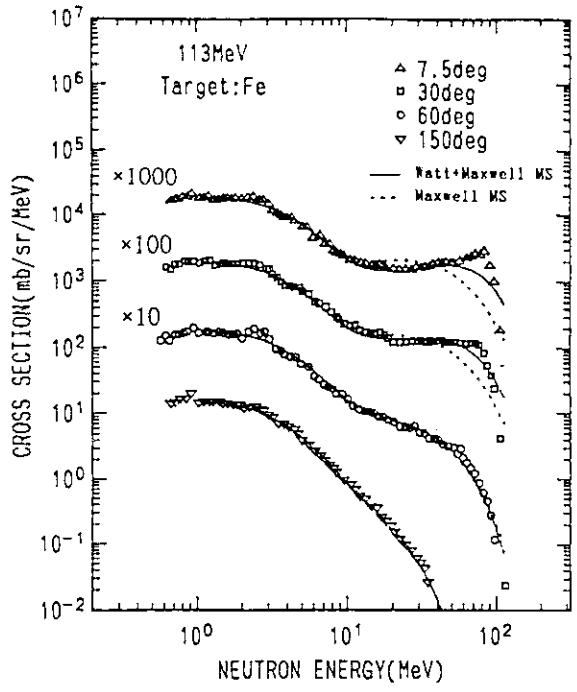

Fig. 8 Experimental spectra and fitting results. Dashed curves show the Maxwell MS model, and solid ones indicate the combination of the Watt and Maxwell MS models.

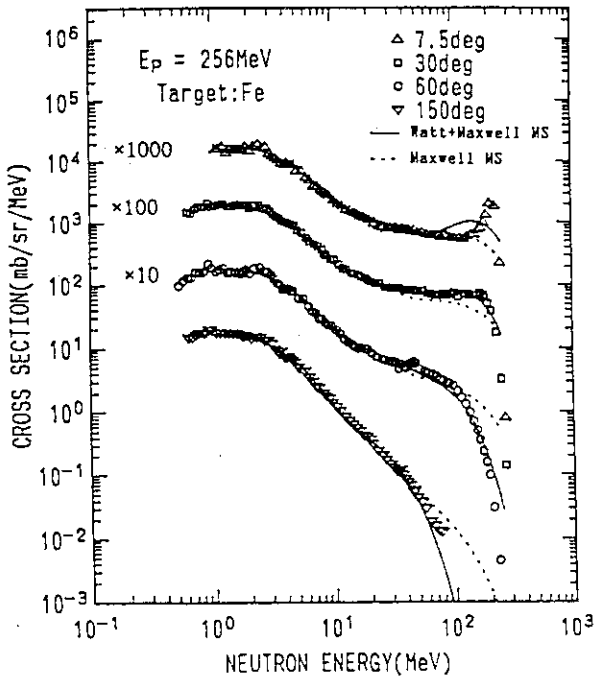

Fig. 9 Experimental spectra and fitting results. Dashed and solid curves indicate the same models as in Fig. 8.

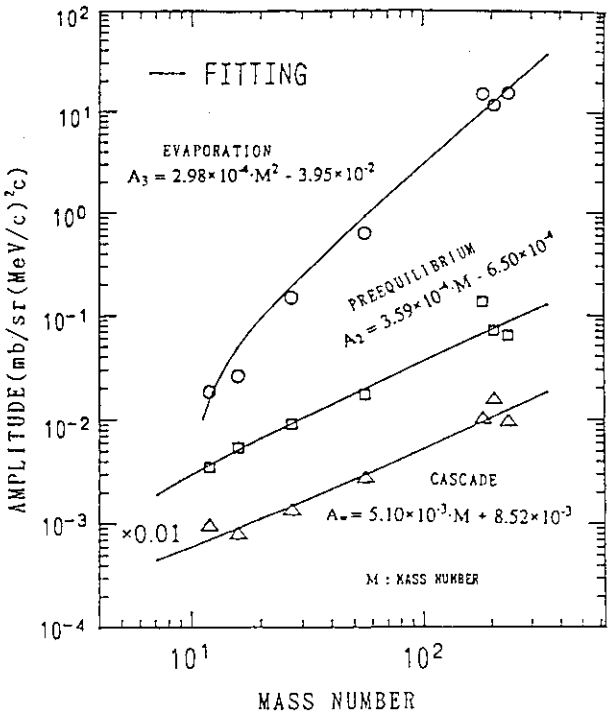

Fig. 10 Mass number dependence of the amplitude parameter A for incident protons of 113 MeV.

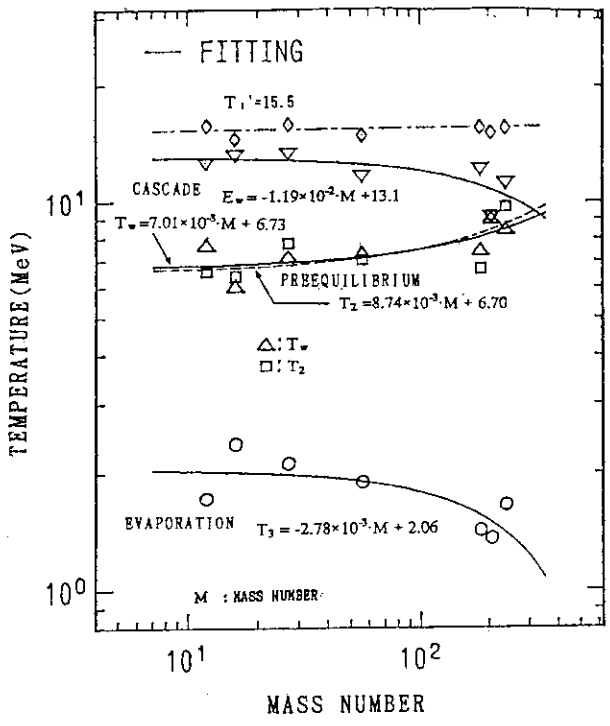

Fig. 11 Mass number dependence of the temperature T for incident protons of 113 MeV. Values of T_1' from Eq. (9) are presented.

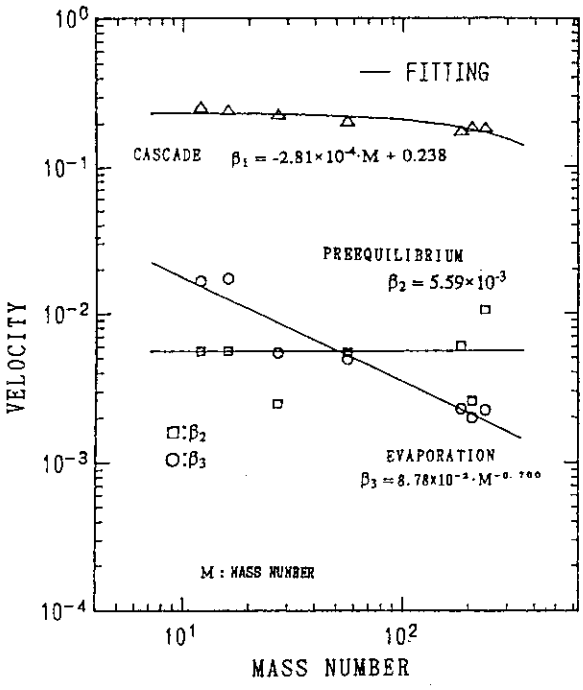

Fig. 12 Mass number dependence of the velocity β for incident protons of 113 MeV.

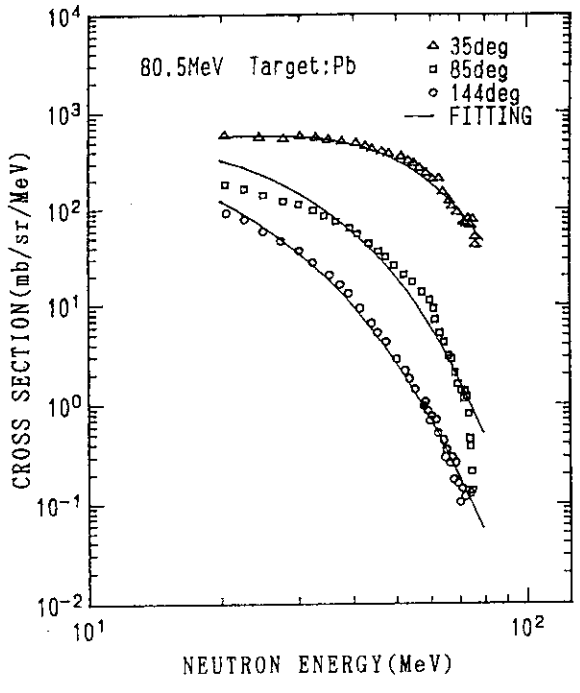

Fig. 13 Experimental spectra and the results of fitting by combination of the Watt and Maxwell MS models for 80.5 MeV proton incidence on lead.

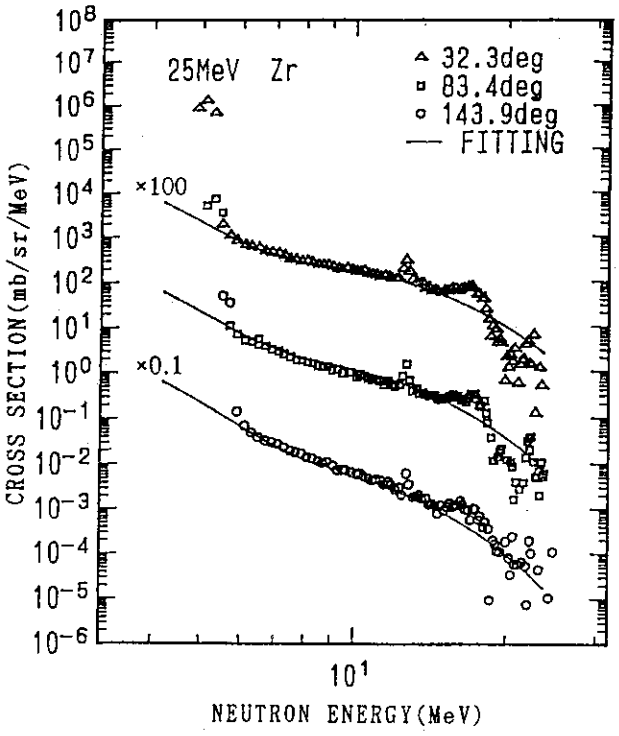

Fig. 14 Experimental spectra and the results of fitting. Two-component fitting was made by combination of the Watt and Maxwell MS models.

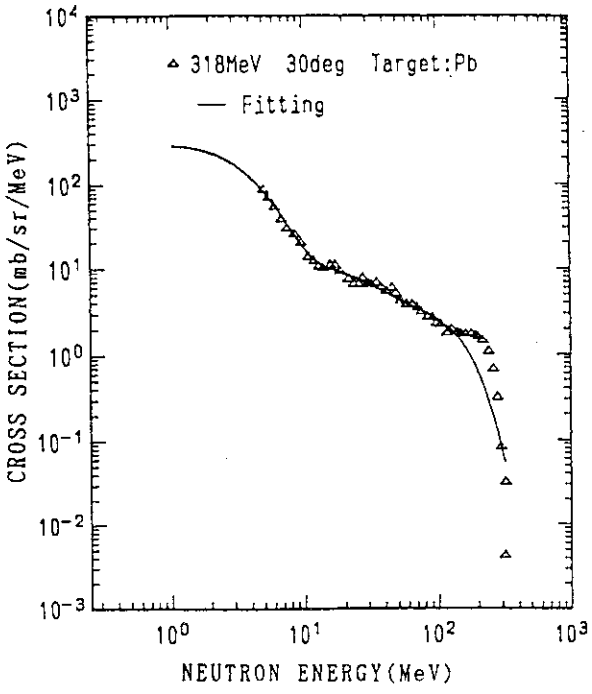

Fig. 15 Experimental spectra and the results of fitting by combination of the Watt and Maxwell MS models for 318 MeV proton incidence on lead.

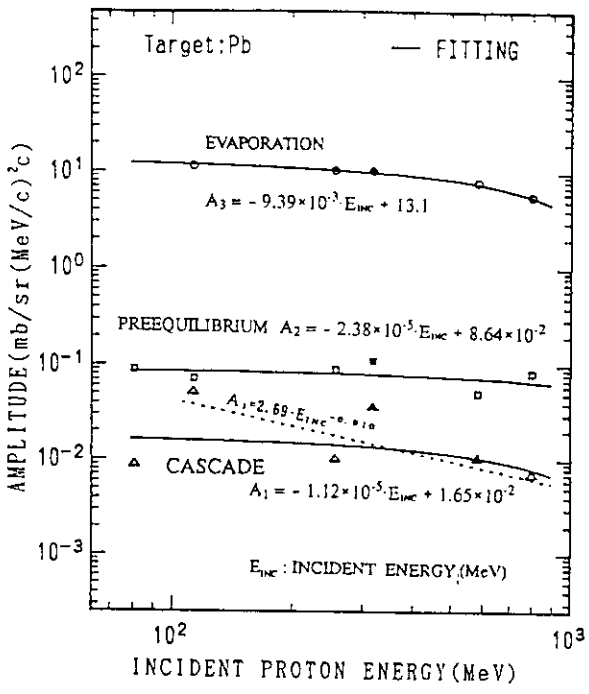

Fig. 16 Amplitude parameter A for lead. Black marks indicate incomplete fitting. The dashed curve neglects the 80.5 and 318 MeV data.

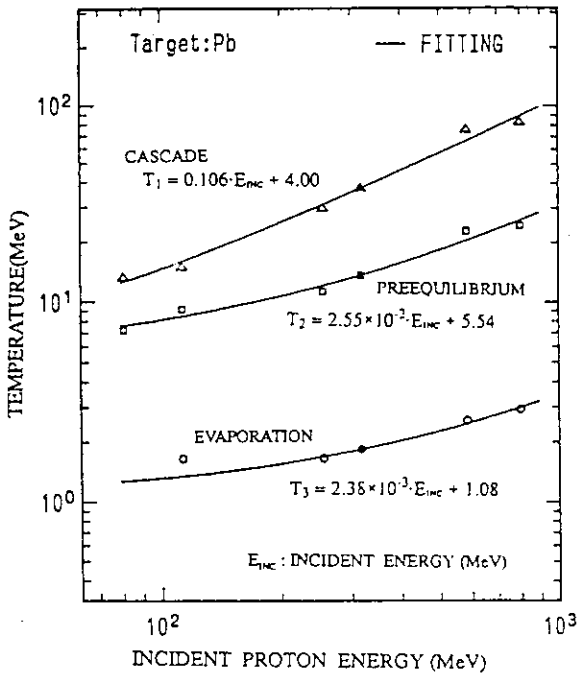

Fig. 17 Temperature parameter T for lead. Marks are the same as in Fig. 16.

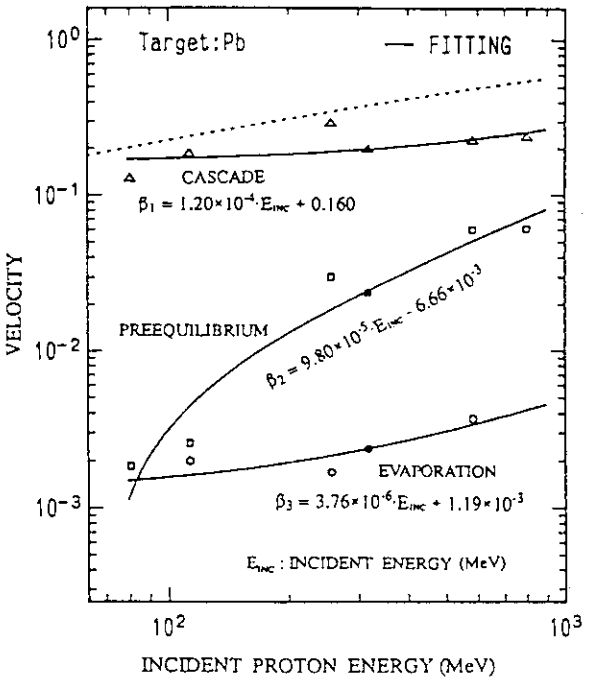

Fig. 18 Velocity parameter β for lead. Marks are the same as in Fig. 16. Dashed curve shows β_{cm} that is described in Section 3.2.

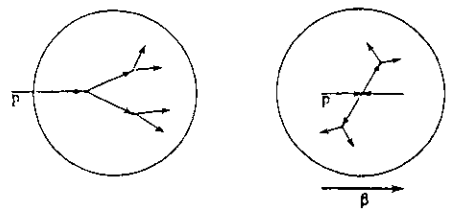

Laboratory Frame　　Moving Frame

Fig. 19 Explanation of the Watt MS model.

4.2 ALICE-F Calculation of Nuclear Data up to 1 GeV

Tokio FUKAHORI
Nuclear Data Center, Japan Atomic Energy Research Institute,
Tokai-mura, Naka-gun, Ibaraki, 319-11 Japan

In design of a spallation neutron source and accelerator shielding, medical and space applications etc., medium energy nuclear data are required in the 1-1000 MeV range. Evaluated nuclear data for proton induced reactions in this energy region, however, have not been prepared enough. In this paper, calculations of neutron and proton induced nuclear data for ^{208}Pb and ^{209}Bi have been performed in the energy range from 20 MeV to 1 GeV by using ALICE-F code. A search of the best ALICE-F parameters and options has been carried out. The Pearlstein's systematics for the energy-angular distributions of emitted neutrons was employed. The calculated results are in good agreement with the experimental data.

1. Introduction

Many applications, such as spallation neutron sources for radioactive waste treatment, accelerator shielding design, medical isotope production, radiation therapy, the effects of space radiation on astronauts and their equipments, and the cosmic history of meteorites and other galactic substances, need medium energy nuclear data. For example, natural lead is used in the design of spallation neutron source. For fission and fusion applications, the neutron nuclear data below 20 MeV is well evaluated; e.g. JENDL-3[1], ENDF/B-VI[2]. Nuclear data in the medium energy region, however, have never been prepared, except those of iron[3].

Evaluation in the medium energy region might be performed by either using theoretical codes or based on experimental data. Several available codes were compared by Pearlstein[4]. The theoretical code, ALICE[5], using evaporation and preequilibrium theories, has been modified to ALICE-P by Pearlstein[3], and in the present study the 1989 version of ALICE[6] was modified to ALICE-F. The modifications consist mainly of changes in optical model parameters and the calculation of inverse cross sections. The ALICE-F

variables referred to in this paper are the same as those of 1989 version of ALICE.

In this paper, calculations of neutron and proton induced nuclear data for ^{208}Pb and ^{209}Bi have been performed in the energy range from 20 MeV to 1 GeV by using ALICE-F and nuclear systematics[7] used in PEND6F which is a compilation code to the ENDF-6 format. The best ALICE-F parameters were searched and the calculated results are compared with experimental data and discussed.

2. Mass Calculations

The ALICE-F code has several options for mass calculation. However, the calculated results for isotope production cross sections using these options did not reproduce most of the experimental data. This discrepancy should be resolved in the evaluation. On the other hand, ten latest mass formulas and a mass table have been introduced in ref. 8. They are given by Pape and Antony, Dussel et al., Moeller and Nix, Moeller et al., Comay et al., Stapathy and Nayak, Tachibana et al., Spanier and Johannson, Janecke and Masson, and Masson and Janecke with the experimental data compiled by Wapstra et al.

The number of available nuclear masses given by Pape and Antony, and Spanier and Johannson, would be insufficient to calculate all the binding energies needed for the ALICE-F calculations. The calculated masses of Moeller and Nix, and Moeller et al. have larger chi-square values than the others. The distributions of calculated binding energies compared with those by the Wapstra's masses show the values of Pape and Antony, and Satpathy and Nayak are not acceptable. The mass formulas of Pape and Antony, Dussel et al., Moeller and Nix, Spanier and Johannson, and Masson and Janecke, are not acceptable since they cannot predict all the binding energies. From the above discussion and the comparison of chi-square values, the masses predicted by Tachibana et al. were judged to be the best. The installed mass table and formula in ALICE-F have been replaced by the latest Wapstra's table and Tachibana's formula.

3. The Parameter Determination

ALICE-F has a lot of options to be selected by the user; the level density formulas (LDOPT) and parameter (a=A/PLD), mean free path multiplier (1.0+COST), exciton starting points (TD, EX1, EX2), and systematics for emitted particles (IADST or ESYS in PEND6F). The level density formulas

can be selected from Fermi Gas Model, the method of Ramamurthy[9] and Liquid Drop Model, and the systematics from Kalbach-Mann[10,11] and Pearlstein[7]. The summary of the parameter comparison is given in Table 1. The determination of the above options and parameters was made by using the experimental data of neutron double differential cross section (DDX), angular integrated neutron emission spectra (EDX), and isotope production cross sections.

The three level density formulas gave similar results, except for the low energy region of the (p,n) reaction. The results of comparison among three values of level density parameter for three methods were similar to each other. Although the calculated DDX and EDX have similar shapes and the difference was only a few percents, in the case of isotope production cross sections for more particle emission, rather big differences, about 10%, were shown. The result calculated by Ramamurthy's formula had the most agreement with experimental data systematically.

The effect of different initial exciton number (TD) was examined. The shape of DDX and EDX depends on the TD value and the gradient of curve was small when the TD value was small. In the case of (p,xn) reaction cross section, large TD value gave sharp peak and cross section decreased rapidly when the energy increased. The shape with TD=3.0 was the most suitable to reproduce experimental data. The examination of the dependence on neutron fraction to initial exciton number (EX1), while TD was equal to 3.0, was carried out. It was reasonable that the large value of EX1 gave large neutron emission and (p,xn) cross sections and small (p,pxn) cross sections.

The mean free path multiplier, the correction factor of the mean free path to incorporate with the diffuse edge of nucleus, was also examined. The shape of DDX and EDX for COST=0.0 seemed to be the best fit to experimental data. In general, for isotope production cross sections, a large COST value gave large cross sections in the case of a few particle emission and small in that of many particle emission. In the case of the (p,pxn) reactions, the peak energy shifted with increasing COST value, especially for high x values.

The angular distributions based on the systematics of Kalbach-Mann and Pearlstein were compared with the ALICE-F calculation and experimental data. The results showed that the Pearlstein's systematics could almost reproduce DDX and EDX while the other two calculations did not agree with the experimental data.

4. Calculated Results and Discussions

In the present work, the best parameters or option sets were obtained. In this chapter, the some calculated results with them are compared with experimental data and discussed.

The total, elastic scattering and reaction cross sections were calculated by the ALICE-F optical model[3]. The elastic scattering angular distributions were based on a diffraction model[12] amended for relativistic effects and empirical fits to high energy data. The results for ^{208}Pb (n,tot) and (n,non) cross sections are compared with the ^{nat}Pb experiments in Figs.1 and 2. They are in good agreement with each other.

Figures 3 shows the calculated results of the ^{208}Pb DDX of emitted neutrons with the experimental data at 30°, 90° and 150° by 590 MeV proton. The calculation of neutron emission cross section with Pearlstein's systematics reproduces the experimental data. On the other hand, charged particle emission cross section has no experimental data. The comparison with other calculation illustrates that the production cross section of composite particle such as alpha-particle is not reproduces by the ALICE-F calculation, since the ALICE-F code cannot calculate the composite particle emission in the preequiliblium process.

In the case of isotope production cross section, the ALICE-F code can mostly reproduce the experimental data. The calculated results of ^{209}Bi (p,4n) and (p,4np) reaction cross sections are shown in Figs.4 and 5 with experimental data. However, few experimental data exists for the isotope production cross section of more than two proton emission. These experiments are required not only to solve the problem of composite particle emission described above but also to verify the results of calculations.

5. Conclusion

The nuclear data for ^{208}Pb and ^{209}Bi for proton and neutron incident reactions in the energy region 20 MeV to 1 GeV were calculated by using ALICE-F including Tachibana's mass formula and the latest Wapstra's mass, and systematics of secondary neutron emission spectra. The results are in good agreement with experimental data. However, improvements is necessary to calculate the composite particle emission in the preequiliblium process and to get more accuracy.

Acknowledgements

The author is grateful to Dr. M. Blann for valuable discussions about the physical modelling used in the ALICE code. The author also wishes to thank Dr. S. Pearlstein for advising for the evaluation method in the medium energy nuclear data.

References

1) Shibata K., Nakagawa T., Asami T., Fukahori T., Narita T., Chiba S., Mizumoto M., Hasegawa A., Kikuchi Y., Nakajima Y. and Igarasi S., JAERI-1319, (1990).
2) Rose P.F. and Dunford C.L. (Ed.), BNL-NCS-44945 (1990).
3) Pearlstein S., J. Astrophys., 346, 1049 (1989).
4) Pearlstein S., BNL-NCS-52155, (1988).
5) Blann M., CODE ALICE/85/300, UCID-20169, (1985).
6) Blann M., CODE ALICE/89, private communication. (1989)
7) Pearlstein S., Nucl. Sci. Eng., 95, 116 (1987).
8) mass formulas and experimental mass table; Atomic Data and Nuclear Data Tables, 39 (1988).
9) Ramamurthy V.S., Asghar M. and Kataria S.K., Nucl. Phys., A398, 544 (1983).
10) Kalbach C., Phys. Rev., C37, 2350 (1988).
11) Kalbach C. and Mann F.M., Phys. Rev., C23, 112 (1981).
12) Pearlstein S., Nucl. Sci. Eng., 49, 162 (1972).

Table 1 The Summary of Examined Parameters

LDOPT	PLD	TD	EX1	EX2	COST	IADST	ESYS
0*[a]	8.0	3.0*	0.82*	1.18*	0.0*	1*	250*
0*[a]	9.0*	3.0*	0.82*	1.18*	0.0*	1*	250*
0*[a]	10.0	3.0*	0.82*	1.18*	0.0*	1*	250*
1[b]	8.0	3.0*	0.82*	1.18*	0.0*	1*	250*
1[b]	9.0*	3.0*	0.82*	1.18*	0.0*	1*	250*
1[b]	10.0	3.0*	0.82*	1.18*	0.0*	1*	250*
2[c]	8.0	3.0*	0.82*	1.18*	0.0*	1*	250*
2[c]	9.0*	3.0*	0.82*	1.18*	0.0*	1*	250*
2[c]	10.0	3.0*	0.82*	1.18*	0.0*	1*	250*
0*[a]	9.0*	3.0*	0.90	1.10	0.0*	1*	250*
0*[a]	9.0*	3.0*	0.70	1.30	0.0*	1*	250*
0*[a]	9.0*	5.0	1.20	1.80	0.0*	1*	250*
0*[a]	9.0*	7.0	1.60	2.40	0.0*	1*	250*
0*[a]	9.0*	3.0*	0.82*	1.18*	0.5	1*	250*
0*[a]	9.0*	3.0*	0.82*	1.18*	1.0	1*	250*
ALICE-F[d]						1*	900
Kalbach-Mann[d]						3	900
Pearlstein[d]						1*	50

* ALICE-F and PEND6 default values.

[a] Fermi Gas Model.

[b] Ramamurthy.

[c] Liquid Drop Model.

[d] Other parameters than IADST and ESYS are default values.

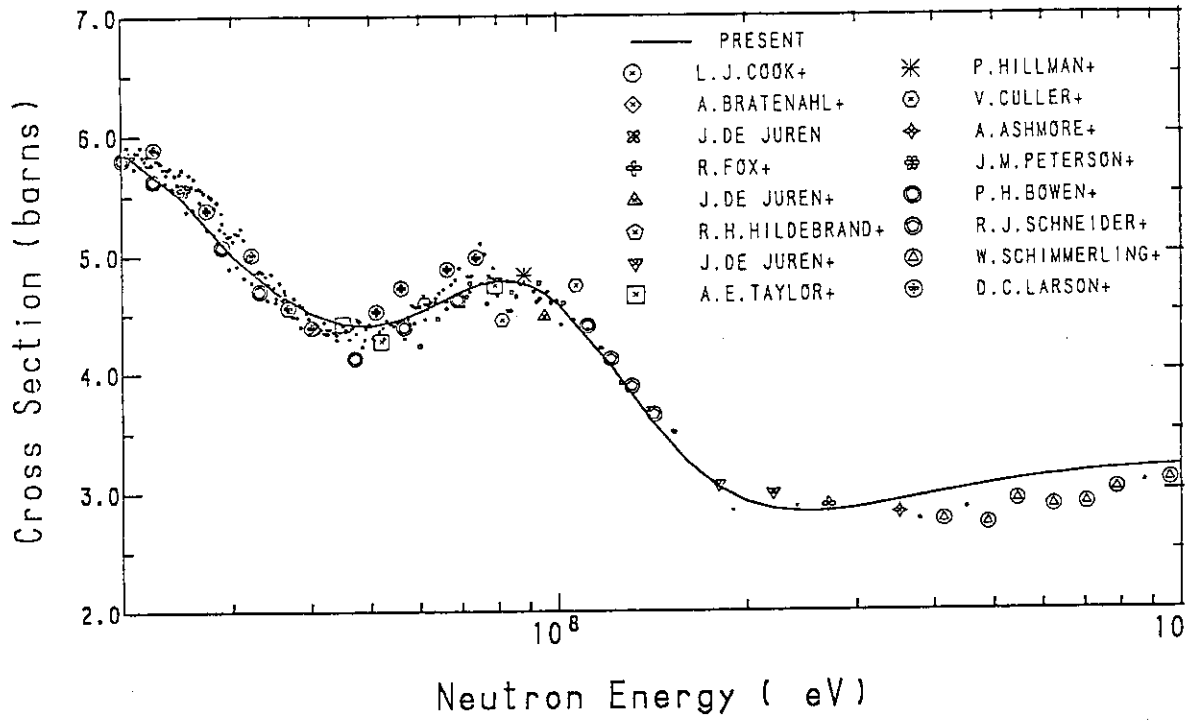

Fig. 1 The calculated result for ^{208}Pb (n,tot) cross section compared with ^{nat}Pb experimental data.

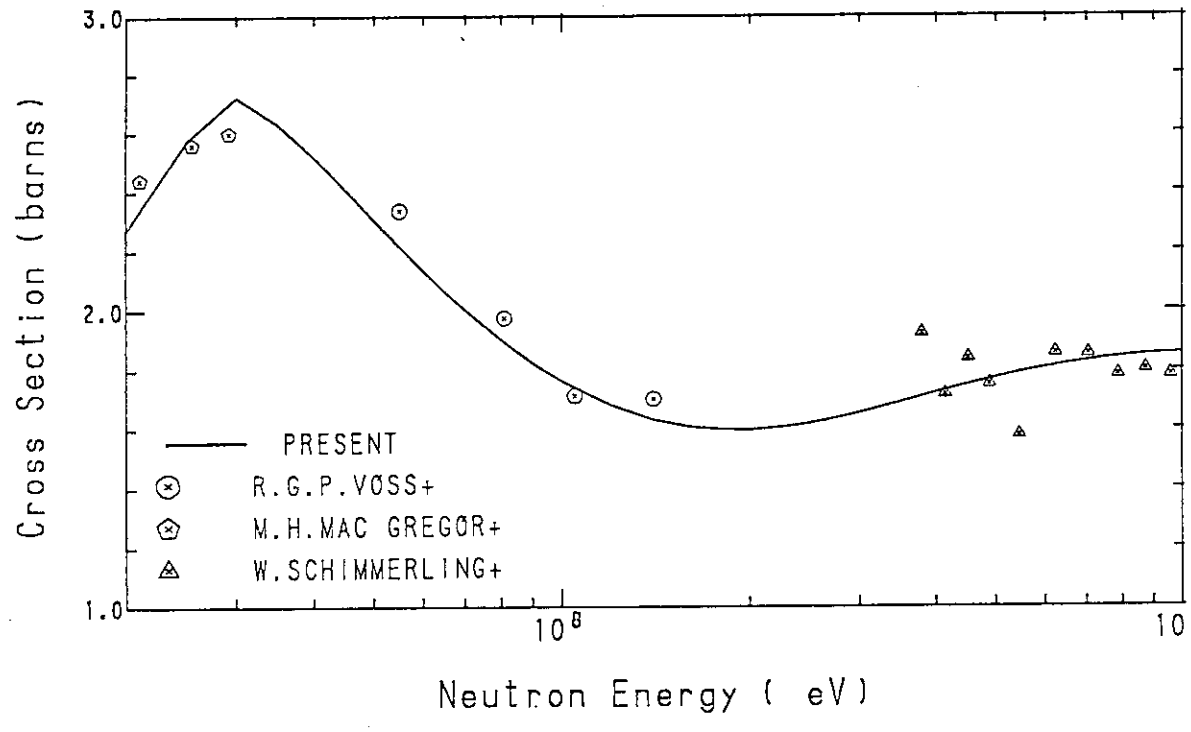

Fig. 2 The calculated result for ^{208}Pb (n,non) cross section compared with ^{nat}Pb experimental data.

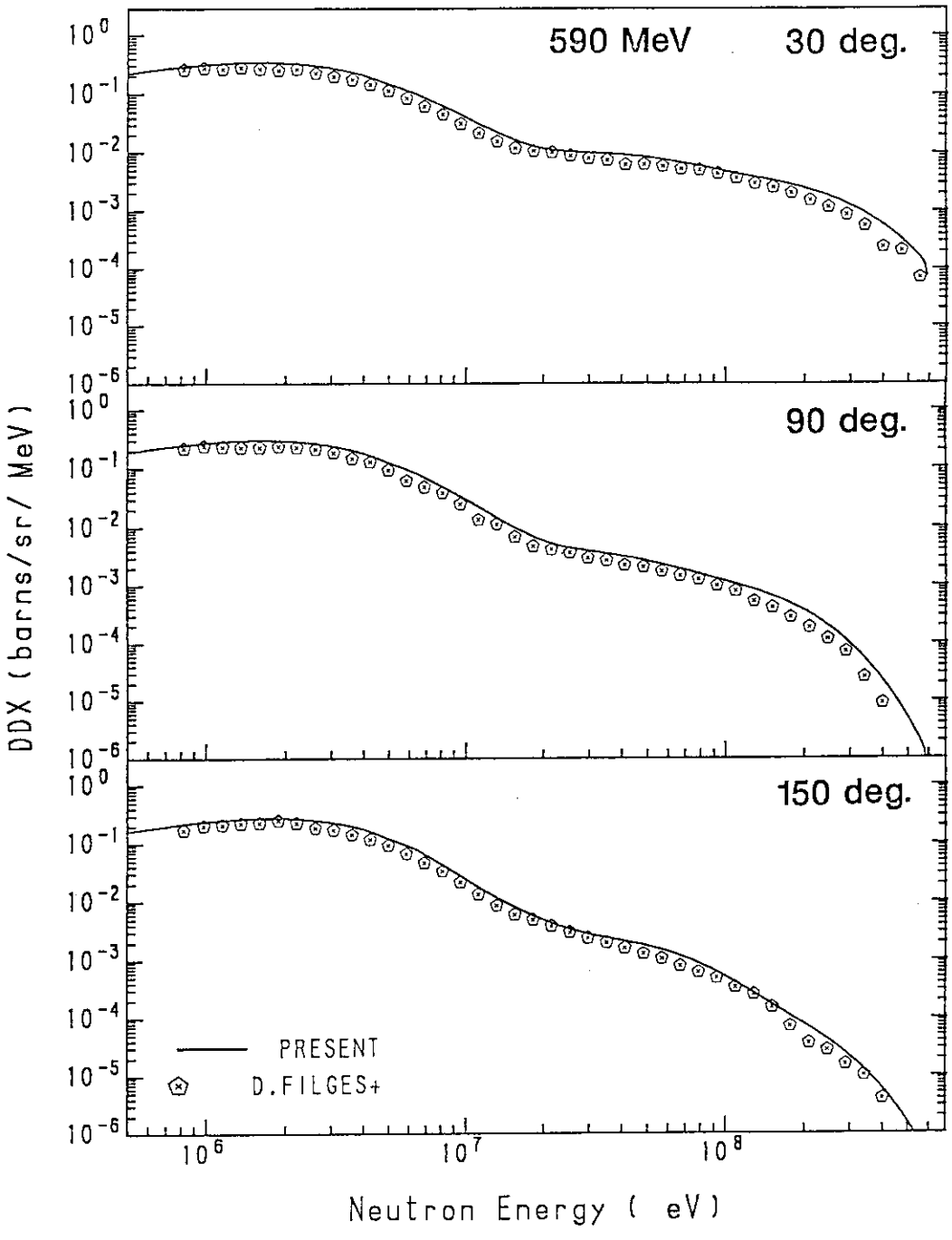

Fig. 3 The calculated result for ^{208}Pb DDX of emitted neutrons at 30°, 90° and 150° by 590 MeV proton.

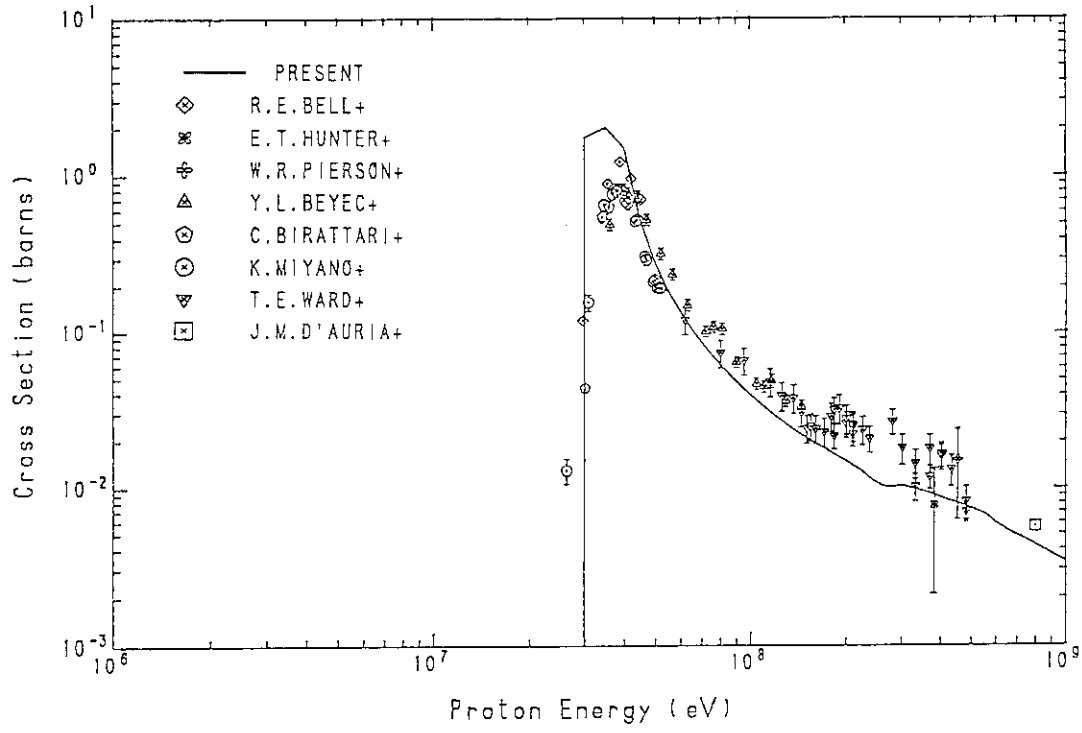

Fig. 4 The calculated result for ^{209}Bi (p,4n) cross section.

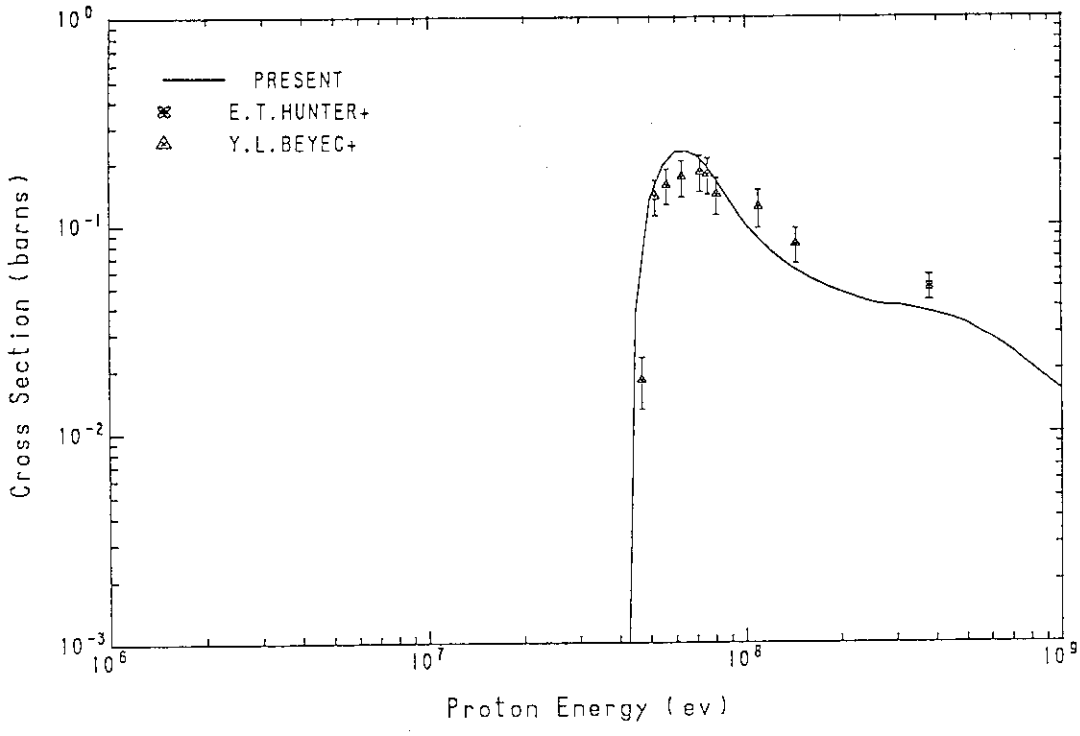

Fig. 5 The calculated result for ^{209}Bi (p,4np) cross section.

4.3 Comparison between Calculated Cross Sections by MCEXCITON and ALICE-P for Medium-Energy Nucleon Induced Reactions on ^{208}Pb and ^{209}Bi

Norio Kishida
CRC Research Institute Inc.
1-3-D17, Nakase, Chiba-shi, Chiba-ken, JAPAN

Medium-energy particle-production and nucleus-formation cross sections in the incident nucleon energy range 20–1000 MeV were calculated for ^{208}Pb and ^{209}Bi targets using MCEXCITON code. The cross sections were compared with not only experimental cross sections but also calculated ones by ALICE–P. As concerns nucleus-formation cross sections, overall agreement between experimental and two kinds of the calculated cross sections are fairly well. But as for particle-production cross sections for d, t, ^{3}He and α, the two codes produce remarkably different results. The difference stems from difference in nuclear reaction models incorporated into the two codes. In this medium-energy range, it was made clear that there still exsists large uncertainty between evaluated cross sections which are calculated using some theoretical nuclear reaction models.

1 Introduction

Evaluation for medium-energy nuclear data has been started by some authors[1,2] for many applications. They evaluated many kinds of cross sections of nucleon induced reactions for ^{56}Fe, ^{208}Pb and ^{209}Bi in the energy range up to 1000 MeV. They theoretically evaluated particle-production and nucleus-formation cross sections using a modified version of the nuclear model code ALICE[3], *i.e.* ALICE–P.[1] As concerns nucleus-formation cross sections, they compared the theoretical values with experimental ones in the incident energy to ~100 MeV. On the other hand, as for particle-production cross sectios, they, however, did not carried out such comparison. Hence, the author felt that in the energy range above 100 MeV it is still unclear what degree of reliability exists in those evaluated cross sections. For this reason, the author tried to compare model cross sections by ALICE–P with those by another nuclear model code MCEXCITON[4], and made clear reliability of the theoretically evaluated nuclear data. In this report, particle-production and nucleus-formation cross sections of nucleon induced reactions for ^{208}Pb and ^{209}Bi are to be exhibited in the incident energy range 20–1000 MeV.

2 Calculation

2.1 MCEXCITON Code

The MCEXCITON code[4] is a nuclear model code in which pre-equilibrium and equilibrium particle-emission processes are embedded and it can calculate various kinds of cross sections. Since detailed calculational models of the code has been described in Ref. 4, in this report the author intends to explain only reaction process newly added to the code: pre-equilibrium emission process for cluster particles, *i.e.* d, t, ^{3}He and α-particles. This process becomes very important in proportion with nucleon incident energy. Iwamoto and Harada model[5,6] for its process is adopted in the MCEXCITON code. A reason why their model is adopted is as follows: it is thought that the model is the strictest model for the cluster-particle emission process from theoretical nuclear reaction model point of view. The model takes into account the possibility that some of the particles which form the cluster particle may come from levels below the Fermi level. This is the special feature of cluster-particle emission where the center of mass energy of the particle is positive but the constituent nucleons could have negative energy on account of the binding energy. This emission component looks like the pick-up process in direct reaction theory and is completely neglected in the ALICE−P code.

2.2 Calculated Cross Sections

2.2.1 Absorption Cross Sections

Since this report aims to estimate uncertainty of calculated cross sections which originate from difference of nuclear reaction models adopted in the two codes, in the present calculation the author employes the same nucleon-absorption cross sections which were evaluated by Fukahori and Pearlstein in Ref. 2.

2.2.2 Model Parameters

The MCEXCITON code has two variable parameters: level-density parameters for pre-equilibrium and equilibrium process. In the pre-equilibrium process, the value A/13 MeV^{-1}, where A is the mass number, was used as the equi-distant single-particle level density by Ericson.[7] On the other hand, in the equilibrium process the statistical evaporation model by Weisskopf and Ewing[8] was employed. The value of level-density parameter were adjusted in such a way that various excitation functions of calculated nucleus-formation cross sections overall reproduced those of experimental ones fairly well.

2.2.3 Calculated Results

A number of calculated excitation functions of nucleus-formation and particle-production cross sections for ^{208}Pb+n, ^{208}Pb+p, ^{209}Bi+n and ^{209}Bi+p reactions are shown in Fig. 1–39 together with the experimental cross sections and those by ALICE–P.[2)] The solid circles show the calculated values by the MCEXCITON code and the dashed lines are the curves which are drawn by eye guide. The solid lines represent the cross sections which Fukahori and Pearlstein[2,9)] evaluated using the ALICE–P code. From Fig. 1–3, Fig. 10–13, Fig. 20–21 and Fig. 28–33, it is found that MCEXCITON and ALICE–P have the same ability to reproduce the measured excitation functions. However, all the neutron-production cross sections calculated by MCEXCITON is fairly less than those by ALICE–P in the energy region above 100 MeV (cf. Figs. 4, 14, 22 and 34). This fact implies that MCEXCITON produces harder neutron energy spectra to ALICE–P. For the proton-production cross sections, both the codes give the almost same results(cf. Figs. 5, 15, 23 and 35). For the d-, t-, ^{3}He- and α-production cross sectons, MCEXCITON produces much larger cross sections than ALICE–P in the energy region below 200 MeV(cf. Fig. 6–9, Fig. 16–19, Fig. 24–27 and Fig. 36–39). These large differences between the two codes originate from the difference between the pre-equilibrium models for cluster-particle emission. Since measured excitation functions for these cluster particles scarcely exist, the author cannot conclude which codes give the values closer to the true cross sections. Judging from evaluated (n,α) cross sections at 14 MeV,[10)] the author feels that ALICE–P produces too small cross sections in this energy region.

3 Summary

Medium-energy particle-production and nucleus-formation cross sections in the incident nucleon energy range 20–1000 MeV were calculated for ^{208}Pb and ^{209}Bi targets using the MCEXCITON code. The cross sections were compared with not only experimental cross sections but also calculated cross sections by ALICE–P. The two codes reproduced the measured excitation functions for nucleus-formation cross sections fairly well. But as for particle-production cross sections, especially for d, t, ^{3}He and α ones, the two codes produced remarkably different results. The difference results from difference in the nuclear reaction models incorporated into the two codes. The author believes that the theoretical evaluated cross sections in this medium-energy region still have large uncertainty.

References

1) Pearlstein, S. : *Astrophys J.*, **346**, 1049(1989).

2) Fukahori, T. and Pearlstein, S. : *BNL-45200*, (1990).

3) Blann, M. : *CODE ALICE/85/300*, LLNL, UCID 20169, (1984).

4) Kishida, N. and Kadotani, H. : *in Proc. Int. Conf. on Nuclear Data for Science and Technology*, May/June 1988, Mito, Japan(Edited by S. Igarasi), p. 1209, Saikon, Tokyo (1988).

5) Iwamoto, A. and Harada, K. : *Phys. Rev. C*, **26**, 1821(1982).

6) Sato, K., Iwamoto, A. and Harada, K. : *Phys. Rev. C*, **28**, 1527(1983).

7) Ericson, T. : *Adv. in Phys.*, **9**, 425(1960).

8) Weisskopf, V. F. and Ewing, D. H. : *Phys. Rev.*, **57**, 472(1940).

9) Fukahori, T. and Pearlstein, S. : Private Communication.

10) McLane, V., Dunford, C. L. and Rose, P. F. : *Neutron Cross Sections Volume 2, " Neutron Cross Section Curves"*, p. 672 and p. 675, Academic Press, Inc., San Diego(1988)

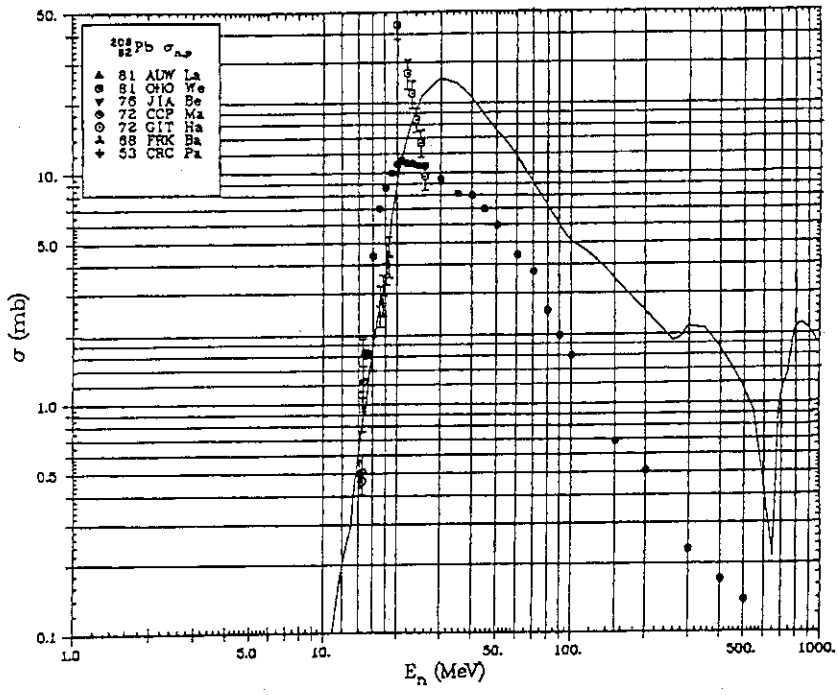

Fig. 1 Calculated and experimental excitation functions for the ^{208}Pb(n,p)^{208}Tl reaction. The solid circles represent calculated cross sections by the MCEXCITON code. The solid line represents those by the ALICE–P code.

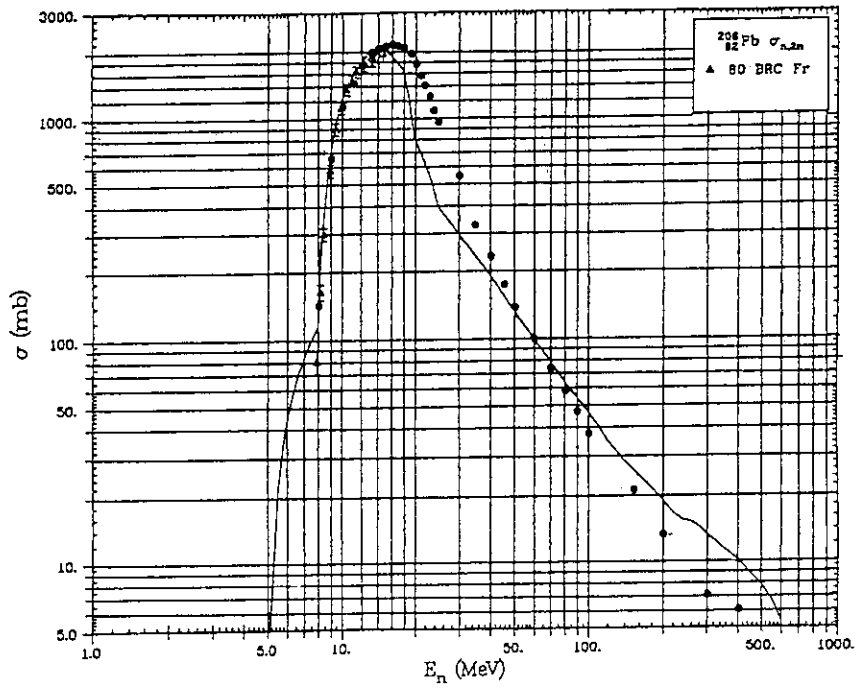

Fig. 2 Calculated and experimental excitation functions for the ^{208}Pb(n,2n)^{207}Pb reaction. Remainder of caption as in Fig. 1.

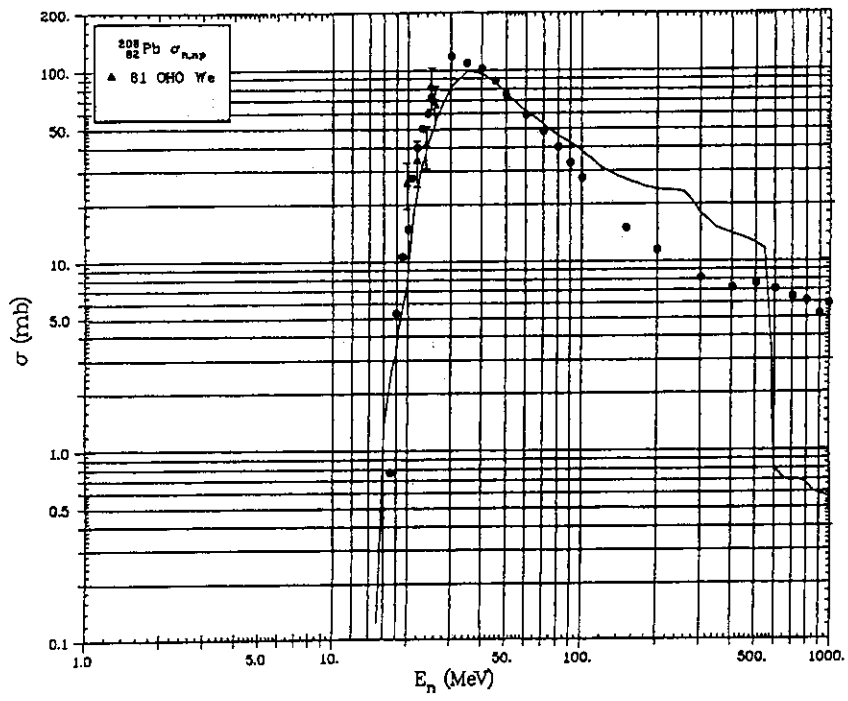

Fig. 3 Calculated and experimental excitation functions for ^{207}Tl-formation cross sections in the ^{208}Pb+n reaction. Remainder of caption as in Fig. 1.

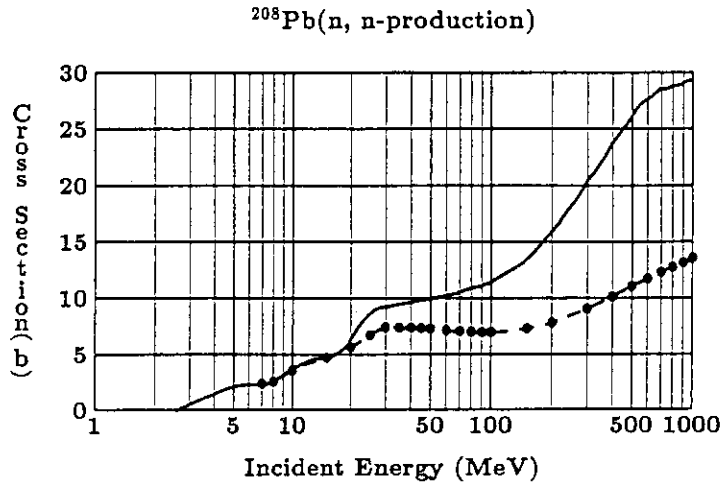

Fig. 4 Calculated excitation functions for neutron-production cross sections in the ^{208}Pb+n reaction. Remainder of caption as in Fig. 1.

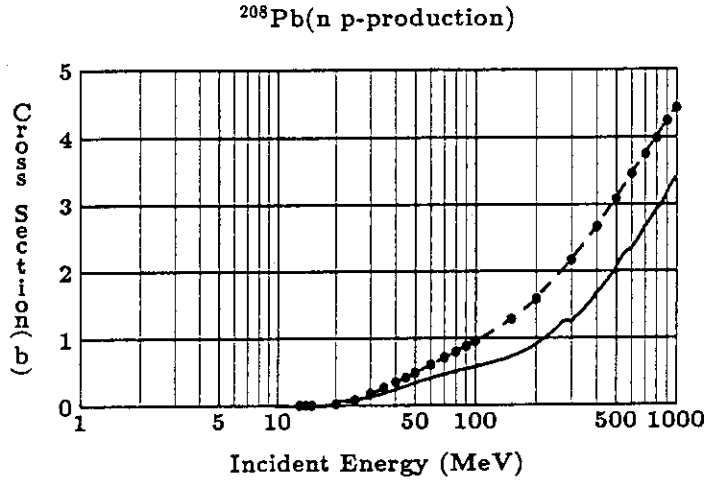

Fig. 5 Calculated excitation functions for proton-production cross sections in the ^{208}Pb+n reaction. Remainder of caption as in Fig. 1.

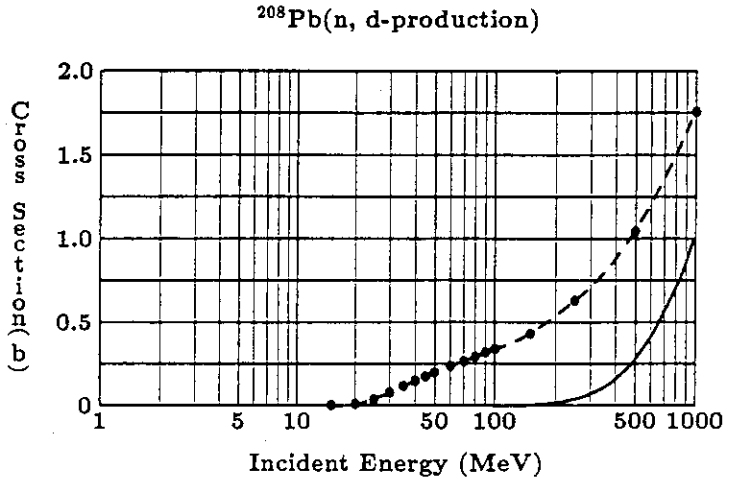

Fig. 6 Calculated excitation functions for deuteron-production cross sections in the ^{208}Pb+n reaction. Remainder of caption as in Fig. 1.

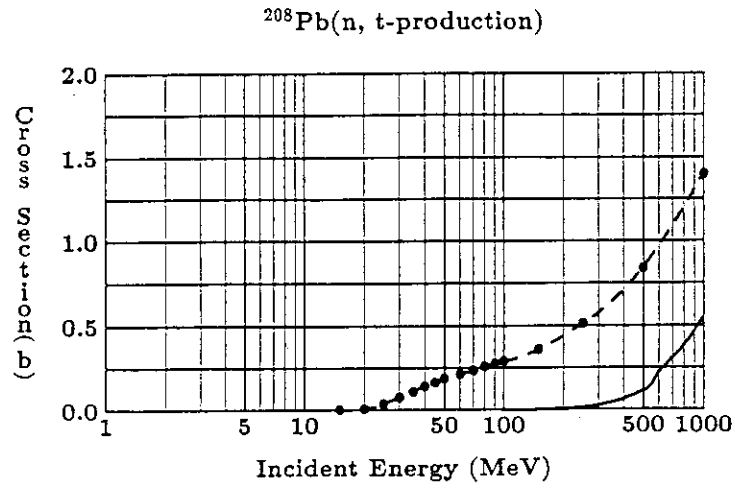

Fig. 7 Calculated excitation functions for triton-production cross sections in the ^{208}Pb+n reaction. Remainder of caption as in Fig. 1.

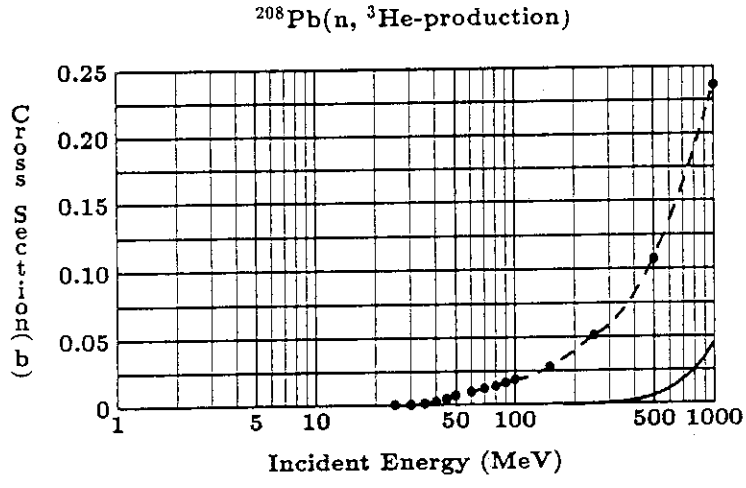

Fig. 8 Calculated excitation functions for ^{3}He-production cross sections in the ^{208}Pb+n reaction. Remainder of caption as in Fig. 1.

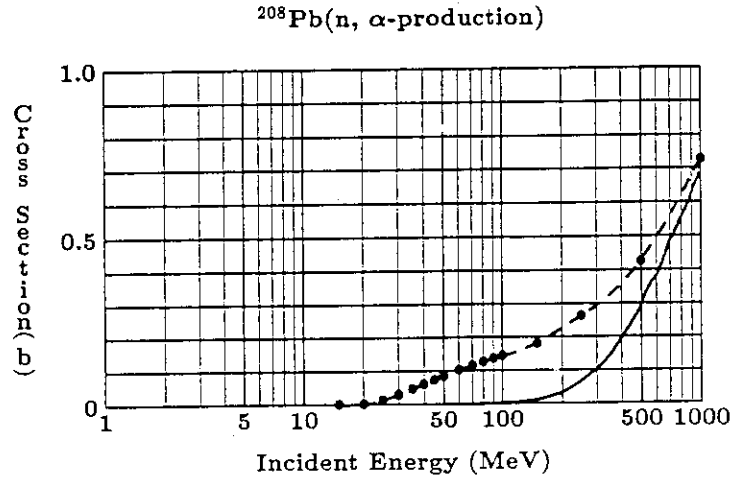

Fig. 9 Calculated excitation functions for α-production cross sections in the ^{208}Pb+n reaction. Remainder of caption as in Fig. 1.

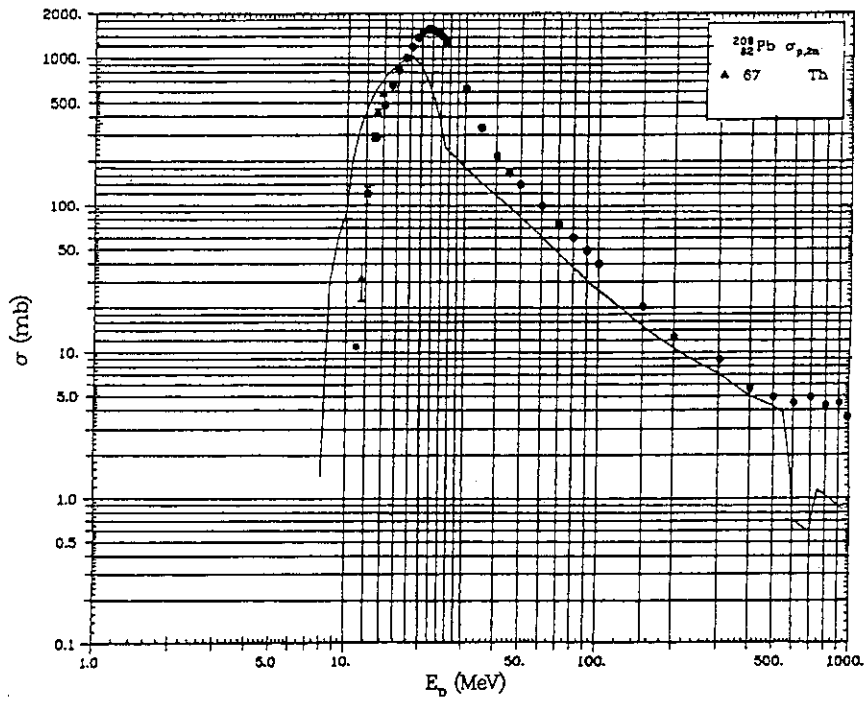

Fig. 10 Calculated and experimental excitation functions for the ^{208}Pb(p,2n)^{207}Bi reaction. Remainder of caption as in Fig. 1.

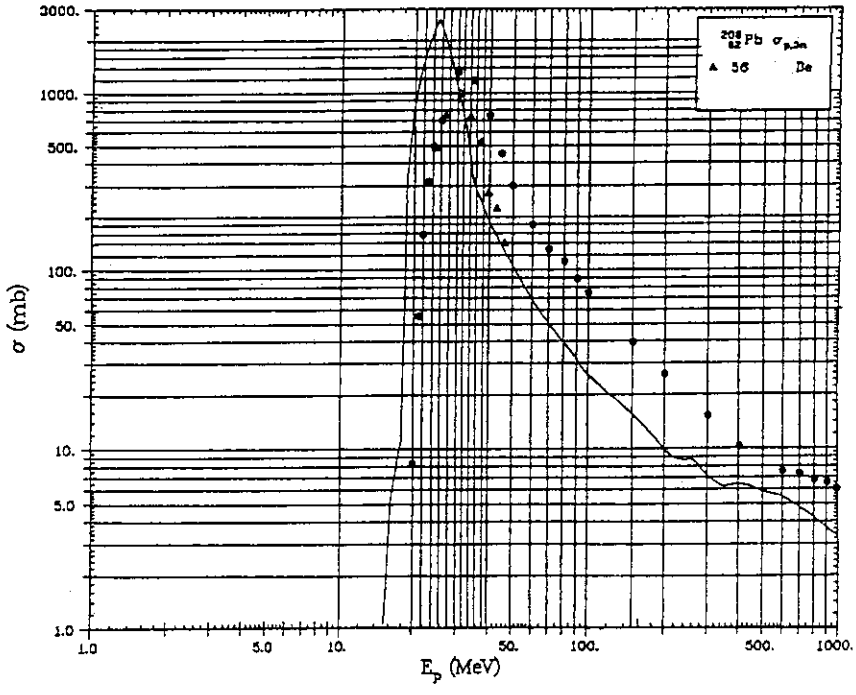

Fig. 11 Calculated and experimental excitation functions for the ^{208}Pb(p,3n)^{206}Bi reaction. Remainder of caption as in Fig. 1.

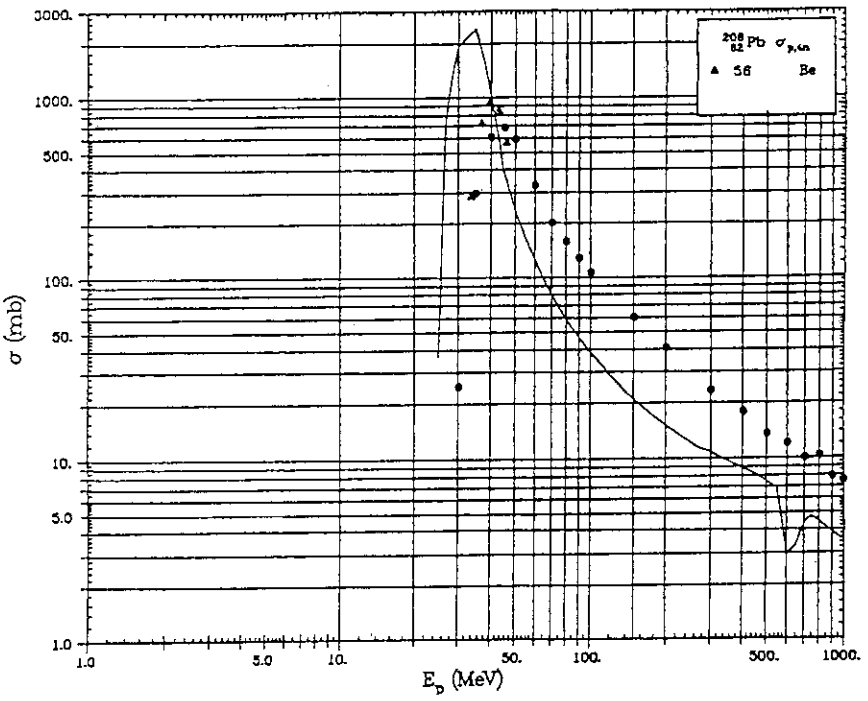

Fig. 12 Calculated and experimental excitation functions for the ^{208}Pb(p,4n)^{205}Bi reaction. Remainder of caption as in Fig. 1.

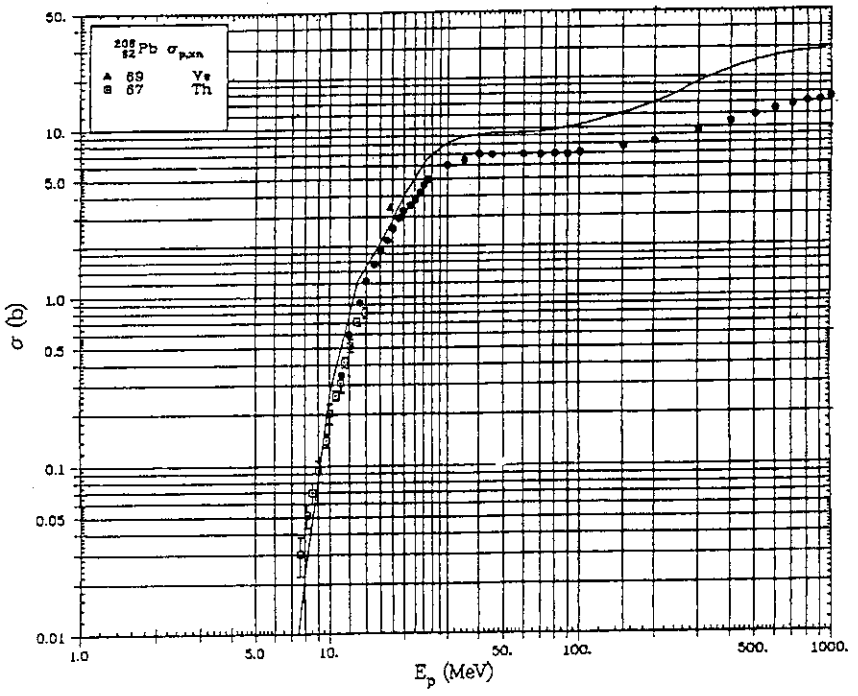

Fig. 13 Calculated and experimental excitation functions for neutron-production cross sections in the ^{208}Pb+p reaction. Remainder of caption as in Fig. 1.

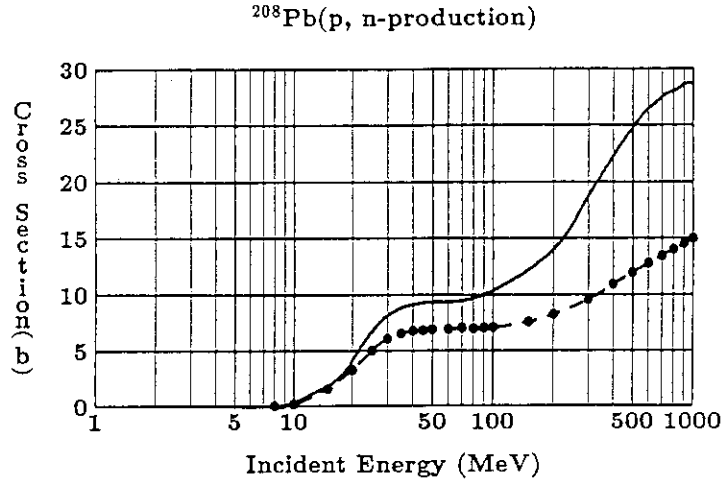

Fig. 14 Calculated excitation functions for neutron-production cross sections in the ^{208}Pb+p reaction. Remainder of caption as in Fig. 1.

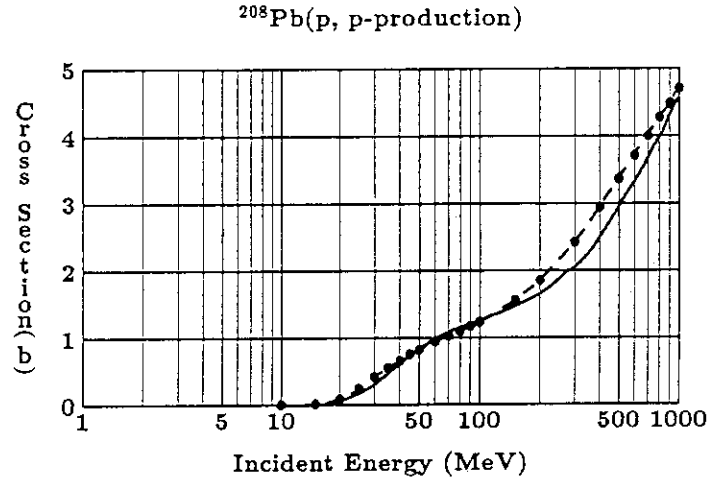

Fig. 15 Calculated excitation functions for proton-production cross sections in the ^{208}Pb+p reaction. Remainder of caption as in Fig. 1.

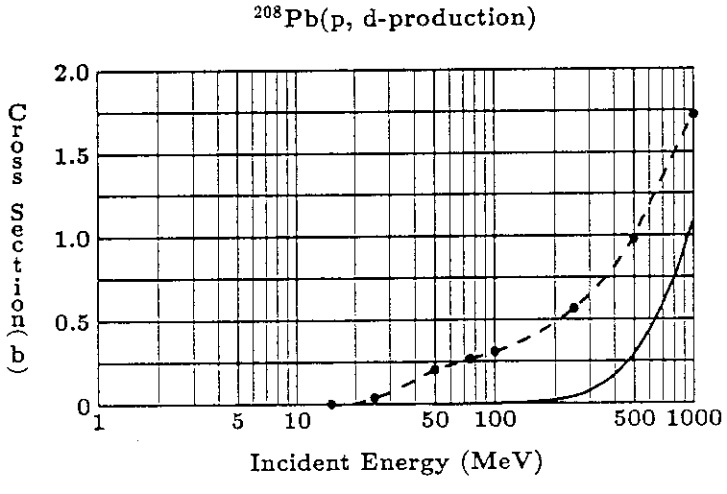

Fig. 16 Calculated excitation functions for deuteron-production cross sections in the ^{208}Pb+p reaction. Remainder of caption as in Fig. 1.

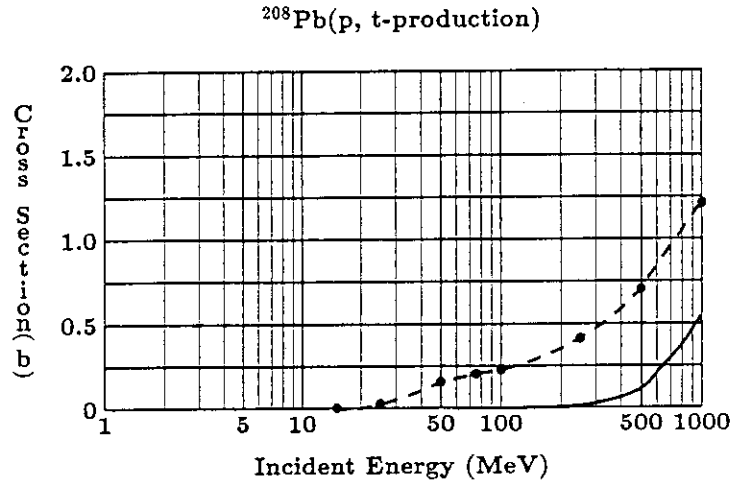

Fig. 17 Calculated excitation functions for triton-production cross sections in the ^{208}Pb+p reaction. Remainder of caption as in Fig. 1.

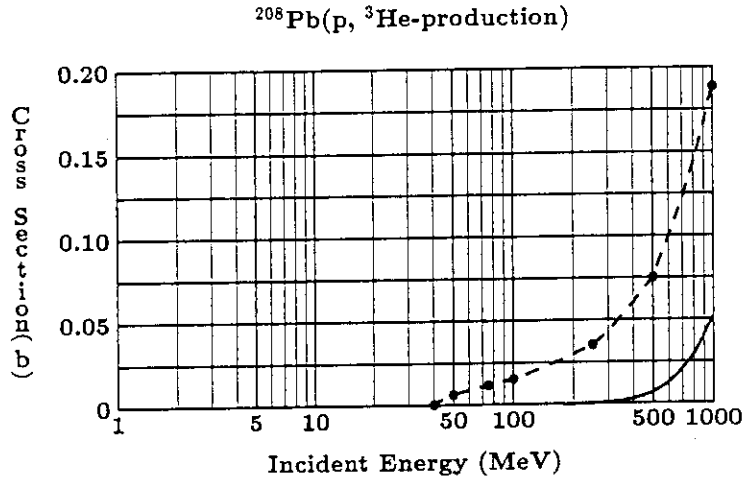

Fig. 18 Calculated excitation functions for ^{3}He-production cross sections in the ^{208}Pb+p reaction. Remainder of caption as in Fig. 1.

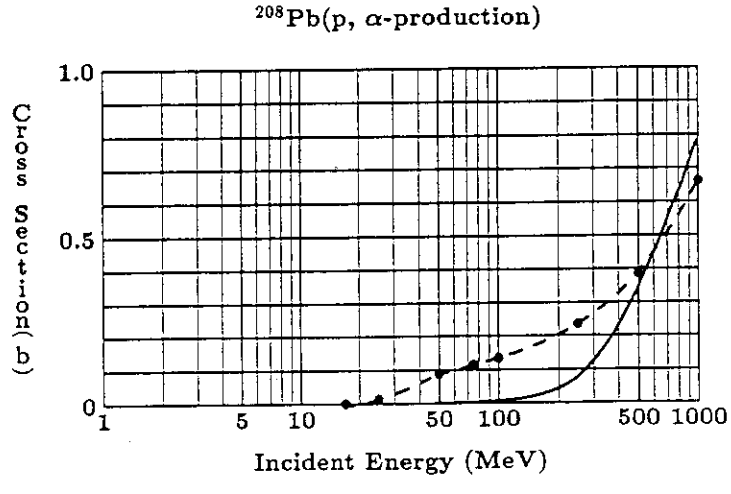

Fig. 19 Calculated excitation functions for α-production cross sections in the ^{208}Pb+p reaction. Remainder of caption as in Fig. 1.

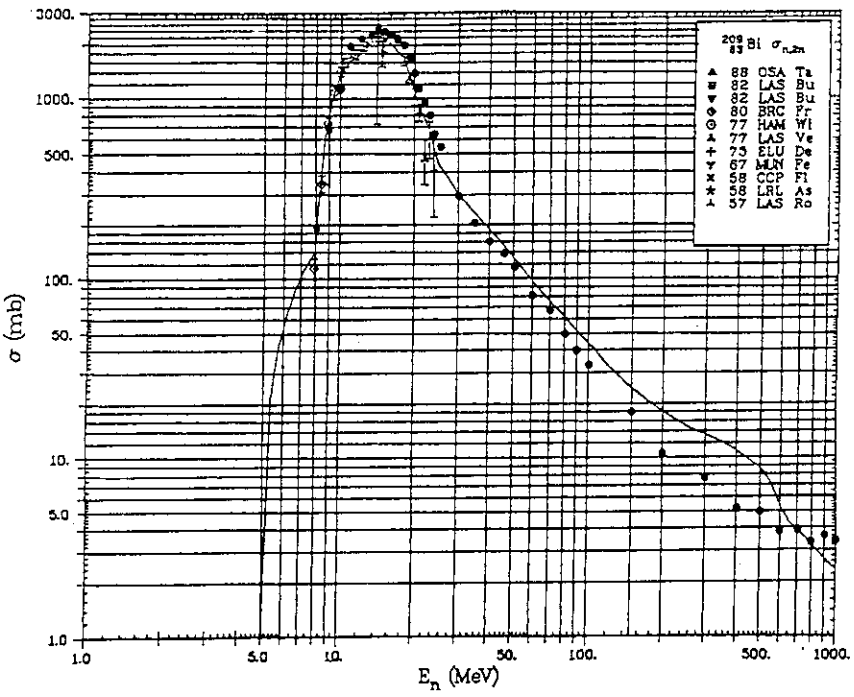

Fig. 20 Calculated and experimental excitation functions for the ^{209}Bi(n,2n)^{208}Bi reaction. Remainder of caption as in Fig. 1.

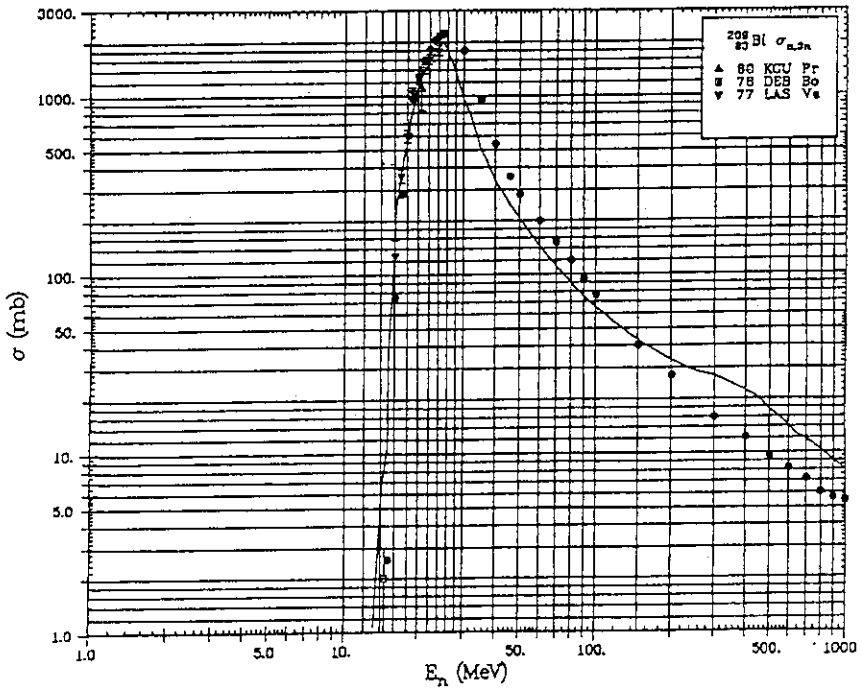

Fig. 21 Calculated and experimental excitation functions for the ^{209}Bi(n,3n)^{207}Bi reaction. Remainder of caption as in Fig. 1.

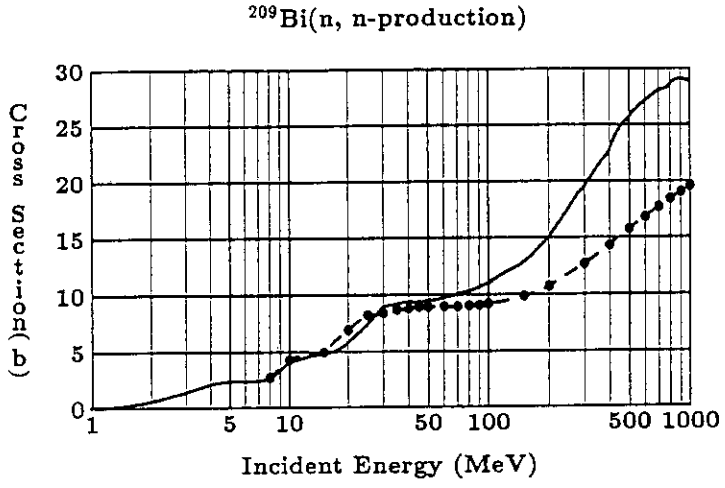

Fig. 22 Calculated excitation functions for neutron-production cross sections in the ^{209}Bi+n reaction. Remainder of caption as in Fig. 1.

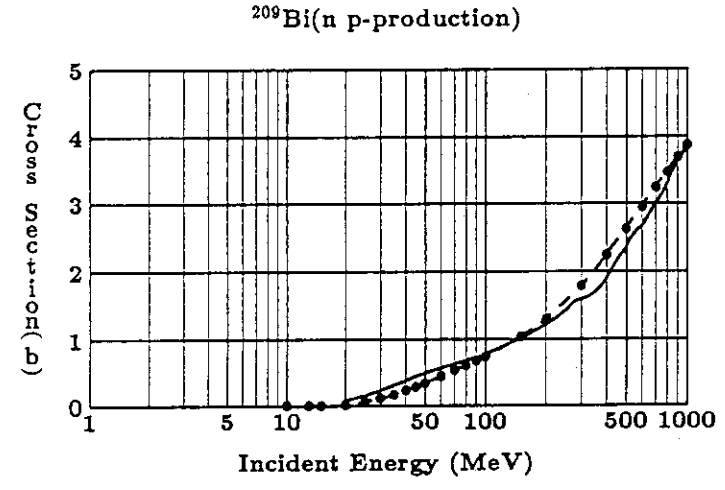

Fig. 23 Calculated excitation functions for proton-production cross sections in the ^{209}Bi+n reaction. Remainder of caption as in Fig. 1.

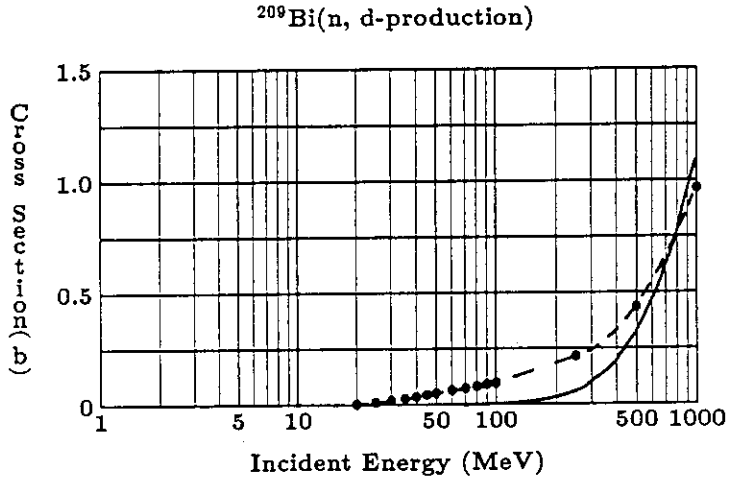

Fig. 24 Calculated excitation functions for deuteron-production cross sections in the ^{209}Bi+n reaction. Remainder of caption as in Fig. 1.

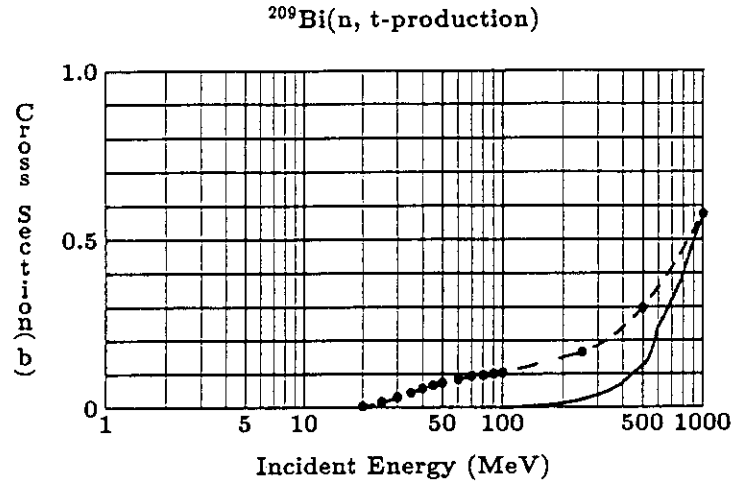

Fig. 25 Calculated excitation functions for triton-production cross sections in the ^{209}Bi+n reaction. Remainder of caption as in Fig. 1.

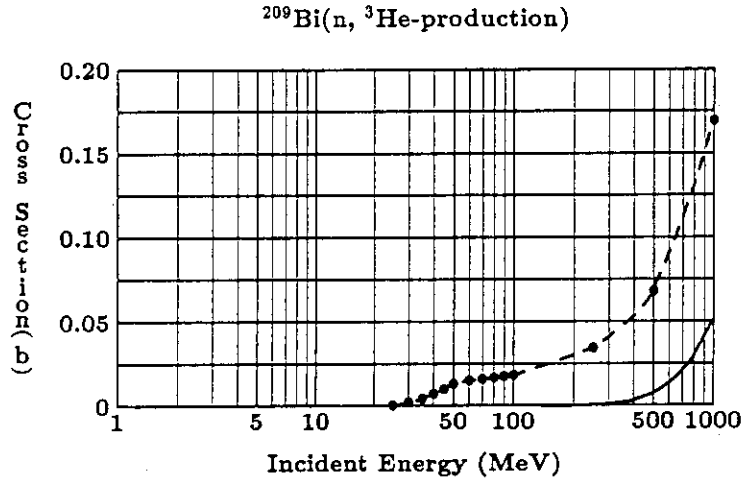

Fig. 26 Calculated excitation functions for ^{3}He-production cross sections in the ^{209}Bi+n reaction. Remainder of caption as in Fig. 1.

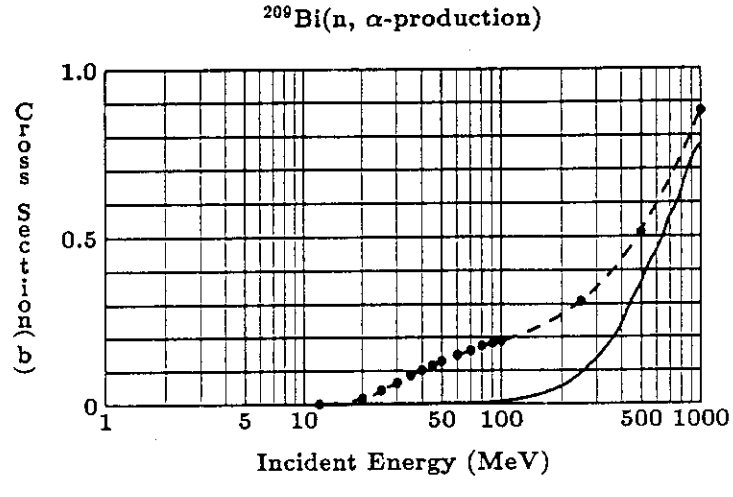

Fig. 27 Calculated excitation functions for α-production cross sections in the ^{209}Bi+n reaction. Remainder of caption as in Fig. 1.

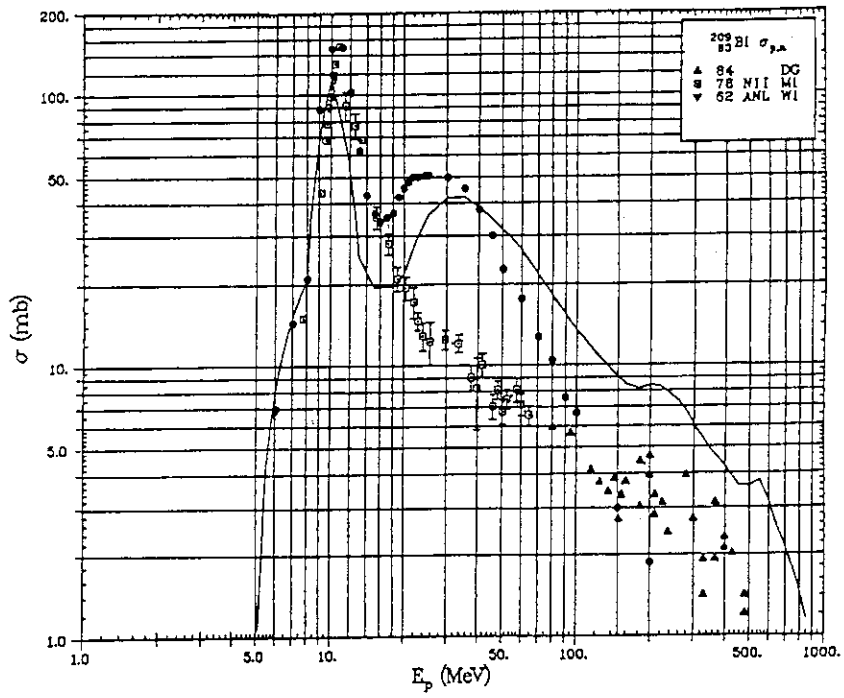

Fig. 28 Calculated and experimental excitation functions for the ^{209}Bi(p,n)^{209}Po reaction. Remainder of caption as in Fig. 1.

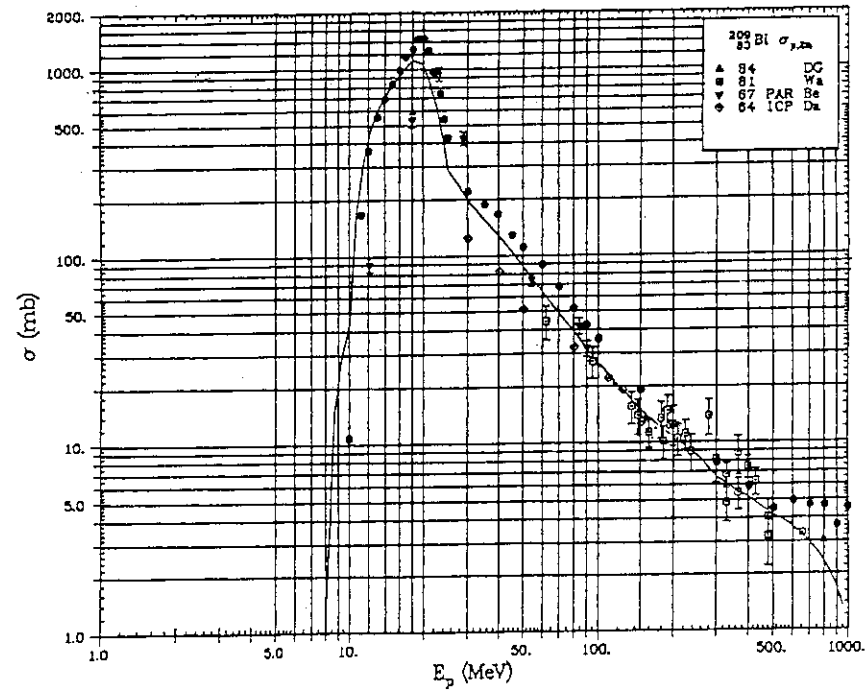

Fig. 29 Calculated and experimental excitation functions for the ^{209}Bi(p,2n)^{208}Po reaction. Remainder of caption as in Fig. 1.

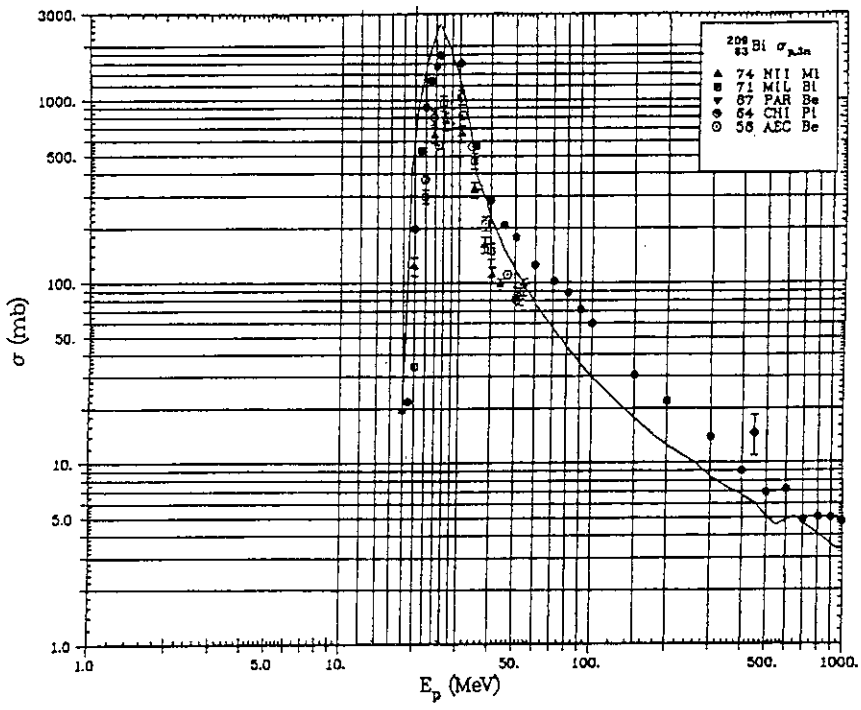

Fig. 30 Calculated and experimental excitation functions for the ^{209}Bi(p,3n)^{207}Po reaction. Remainder of caption as in Fig. 1.

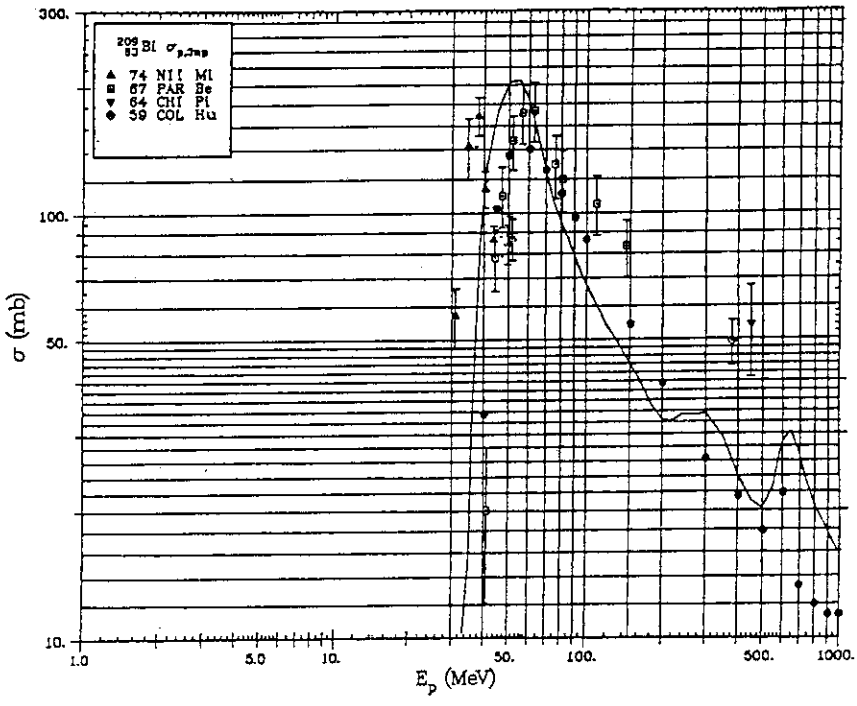

Fig. 31 Calculated and experimental excitation functions for ^{206}Bi-formation cross sections in the ^{209}Bi+p reaction. Remainder of caption as in Fig. 1.

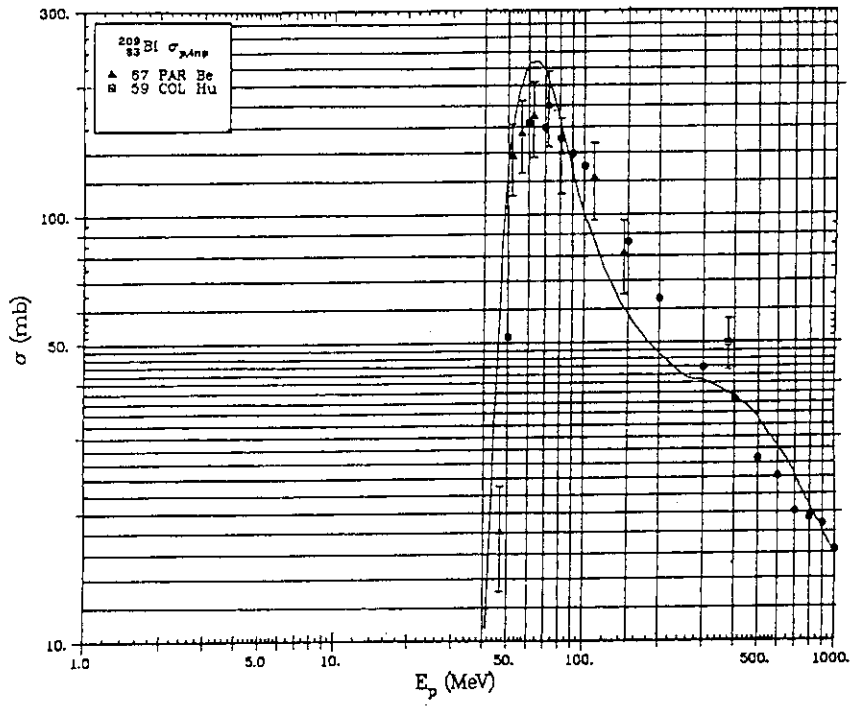

Fig. 32 Calculated and experimental excitation functions for ^{205}Bi-formation cross sections in the ^{209}Bi+p reaction. Remainder of caption as in Fig. 1.

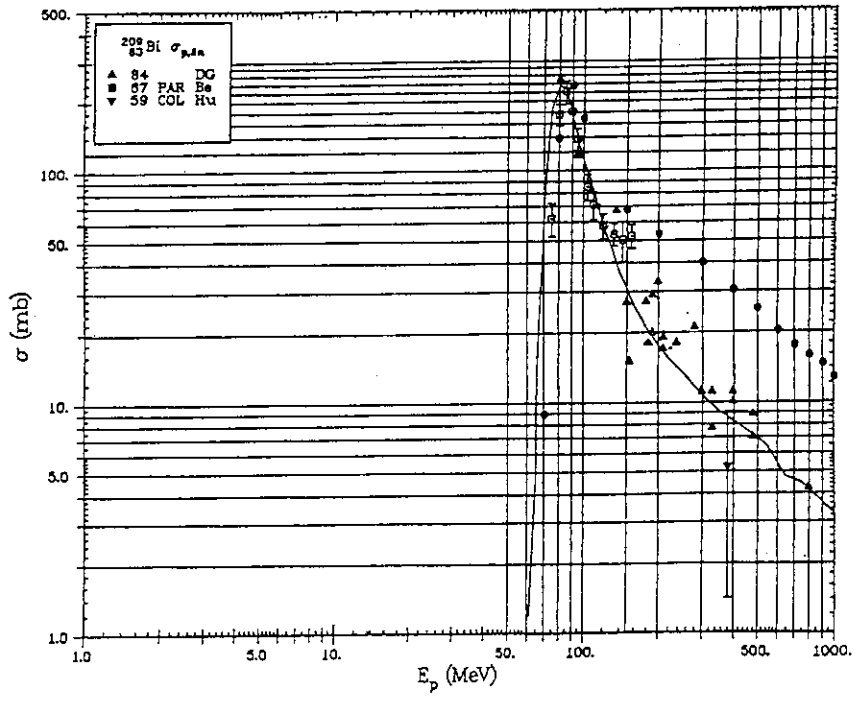

Fig. 33 Calculated and experimental excitation functions for the ^{209}Bi(p,8n)^{202}Po reaction. Remainder of caption as in Fig. 1.

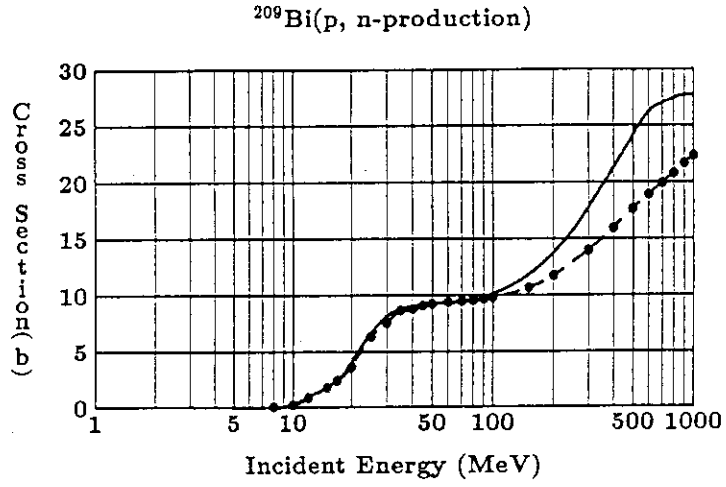

Fig. 34 Calculated excitation functions for neutron-production cross sections in the ^{209}Bi+p reaction. Remainder of caption as in Fig. 1.

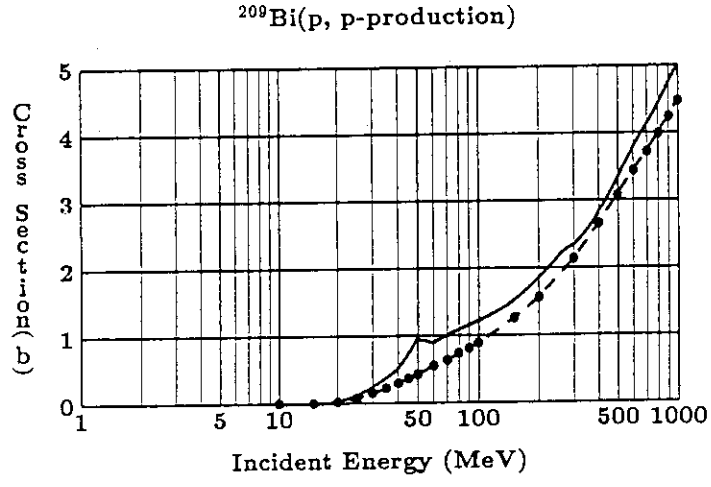

Fig. 35 Calculated excitation functions for proton-production cross sections in the ^{209}Bi+p reaction. Remainder of caption as in Fig. 1.

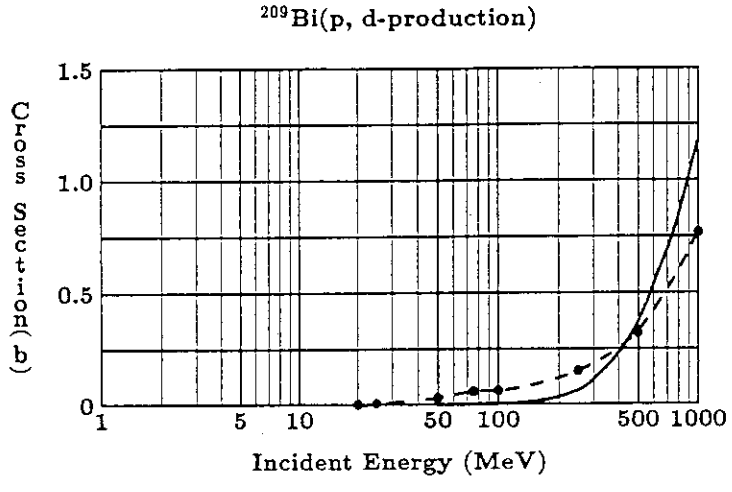

Fig. 36 Calculated excitation functions for deuteron-production cross sections in the ^{209}Bi+p reaction. Remainder of caption as in Fig. 1.

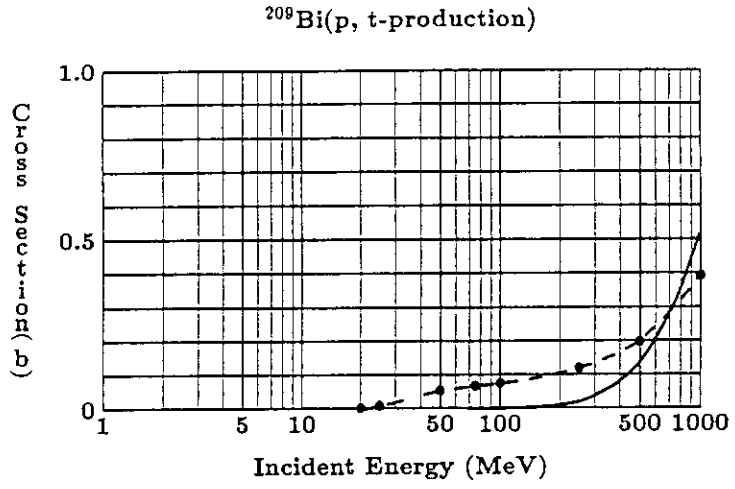

Fig. 37 Calculated excitation functions for triton-production cross sections in the ^{209}Bi+p reaction. Remainder of caption as in Fig. 1.

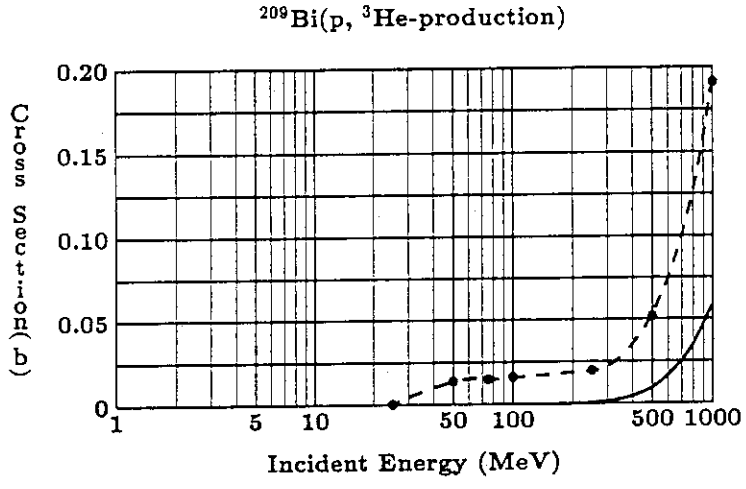

Fig. 38 Calculated excitation functions for ^{3}He-production cross sections in the ^{209}Bi+p reaction. Remainder of caption as in Fig. 1.

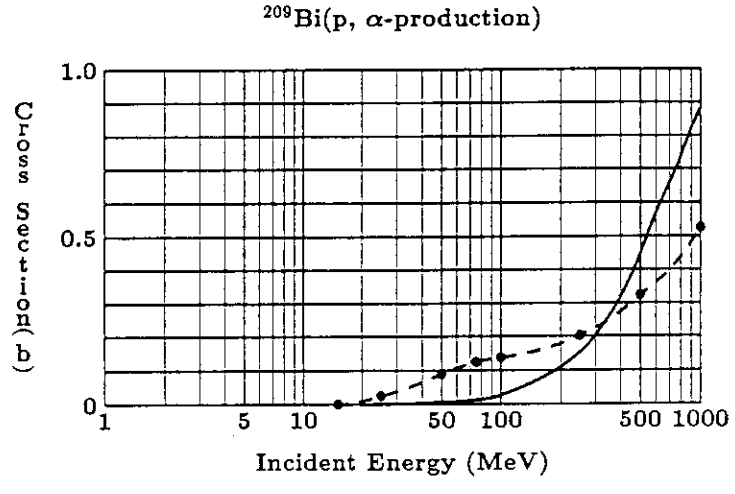

Fig. 39 Calculated excitation functions for α-production cross sections in the ^{209}Bi+p reaction. Remainder of caption as in Fig. 1.

5.1 Luo-Kawai Model and its Application to Nuclear Data Evaluation

Yukinobu Watanabe

Department of Energy Conversion Engineering,
Kyushu University, Kasuga, Fukuoka 816, Japan

A semiclassical distorted wave model proposed by Luo and Kawai is briefly reviewed. The model calculations are compared with several experimental angular distributions and proton energy spectra of (p,p') scattering at 20 - 200 MeV. Some problems relating to the application to high energy nuclear data evaluation are discussed.

1. INTRODUCTION

A feature of nuclear reactions at intermediate energies (20MeV - 1 GeV) is that the energy spectrum of emitted particle has continuous portion between the regions dominated by direct and evaporation processes. Such particle emissions to the continuum arise from so-called preequilibrium reaction process.

Various theoretical models for the preequilibrium process have been proposed[1]. They are generally classified into two categories: semiclassical models and fully quantum-mechanical (QM) models. The formers include the exciton model[2], the geometry-dependent hybrid (GDH) model[3], and their modified versions[1]. These models have been applied to neutron nuclear data evaluation and found to be successful[1].

On the other hand, the QM models have been developed recently. There are the MSDR (TUL) theory[4], the FKK theory[5], the NWY theory[6], and the SMD-SMC model[7] and so on. In the QM theories, one can regard the preequilibrium process as the statistical multistep process, which is distinguished into multistep direct (MSD) and multistep compound (MSC) processes. Previous analyses have indicated that the MSD predominates in the high energy portion of the energy spectrum, and one- and two-step processes are the most important reaction mechanism.

More recently, a semiclassical distorted wave model has been proposed for one-step nucleon inelastic scattering process leading to continuum by Luo and Kawai[8,9]; hereafter the model is referred to as the LK model. The LK model gives a simple closed-form formula for the double differential cross sections, and has no adjustable parameter if one uses a free nucleon-nucleon scattering cross sections and nuclear optical potentials as the distorting potentials. Moreover, the LK model has proved that a basic assumption of the cascade model[10] that the collision at different points of the nucleus do not interfere

with each other can be verified within the framework of the DWBA. In contrast to the cascade model, however, this model can incorporate the effect of distorting potentials, reflection and refraction, and absorption of incident and outgoing fluxes.

In the present paper, the formulation of the LK model is briefly described along Refs. 8 and 9. Some results of the calculations and comparisons with recent experimental (p,p') data on several nuclei at energies of 20-200 MeV are presented. Comparisons with the generalized exciton model and the MSD models are also made. Finally, a possibility of the application to high energy nuclear data evaluation and the related problems are considered.

2. LUO-KAWAI MODEL

The Luo-Kawai (LK) model[8,9] is a semiclassical distorted wave model for one step process of the inclusive nucleon inelastic scattering to continuum. The detail has been described in Ref. 9. The essential formula is summarized here.

The double differential inclusive cross section of nucleon inelastic scattering to continuum is defined in terms of the DWBA expression:

$$\frac{\partial^2\sigma}{\partial\varepsilon_f\,\partial\Omega_f}=\frac{1}{2}\sum_{s_i}\sum_{s_f}\frac{\mu^2}{(2\pi\hbar^2)^2}\frac{k_f}{k_i}\sum_f\left|\langle\hat{\chi}_f^{(-)}\psi_f|V|\psi_i\hat{\chi}_i^{(+)}\rangle\right|^2\delta(E_f-E_i)\,, \tag{2.1}$$

where μ is the reduced mass, k are the wave numbers, E are the total energies, ψ are the nuclear wave functions, and χ are the distorted waves of the nucleon. The subscripts i and f stand for the initial and final states, respectively. We denote the energy and direction of emission by ε_f and Ω_f respectively, and the incident energy by ε_i. The cross section is an average over the projectile spin directions s_f and a sum over the ejectile spin directions s_f and all the final nuclear states f. The potential V is a sum of two-body interaction potentials.

By introduction of a semiclassical approximation for the distorted waves and the Thomas-Fermi model of the nuclear states, Eq. (2.1) is reduced to the following closed-form expression:

$$\frac{\partial^2\sigma}{\partial\varepsilon_f\,\partial\Omega_f}=\left[\frac{A}{A+1}\right]^2\int d\mathbf{r}\,|\chi_i(\mathbf{r})|^2|\chi_f(\mathbf{r})|^2\frac{k_f/k_f(\mathbf{r})}{k_i/k_i(\mathbf{r})}\left[\frac{\partial^2\sigma}{\partial\varepsilon_f(\mathbf{r})\partial\Omega_f(\mathbf{r})}\right]_{\mathbf{r}}\rho(\mathbf{r})\,, \tag{2.2}$$

where $\left[\partial^2\sigma/\partial\varepsilon_f(\mathbf{r})\partial\Omega_f(\mathbf{r})\right]_{\mathbf{r}}$ is the local average cross section of two-nucleon scattering defined in Ref. 11. The quantity A is the mass number of the target nucleus. The local momentum $k_c(\mathbf{r})$ ($c=i$ or f)is given by

$$k_c(\mathbf{r}) = \sqrt{k_c^2 - 2\mu/\hbar^2 V_{c,eff}(r,k_c)}\ , \tag{2.3}$$

$$V_{c,eff}(r,k_c) = \frac{1}{2}\left[\frac{\hbar^2 k_c^2}{2\mu} + V_c(\mathbf{r}) - \sqrt{\left(\frac{\hbar^2 k_c^2}{2\mu} - V_c(r)\right)^2 + W_c^2(r)}\ \right], \tag{2.4}$$

under a semiclassical approximation. The nucleon density of the target nucleus $\rho(\mathbf{r})$ is derived from the local Fermi momentum $k_F(\mathbf{r})$.

The local scattering angle $\theta = \angle\,(k_f(\mathbf{r}), k_i(\mathbf{r}))$ at $\mathbf{r}$ point inside the nucleus is calculated by a quantum mechanical method. The flux of the particle at $\mathbf{r}$ is given by

$$\begin{aligned}\mathbf{J}_c(\mathbf{r}) &= -i\hbar\left[\chi_c^*(\mathbf{r})\nabla\chi_c(\mathbf{r}) - \chi_c(\mathbf{r})\nabla\chi_c^*(\mathbf{r})\right] \\ &\approx \frac{\hbar}{m}|\chi_c(\mathbf{r})|^2 k_c(\mathbf{r})\ .\end{aligned} \tag{2.5}$$

Thus

$$\cos\theta = \frac{\mathbf{k}_i(\mathbf{r})\cdot\mathbf{k}_f(\mathbf{r})}{k_i(\mathbf{r})\cdot k_f(\mathbf{r})} \approx \frac{\mathbf{J}_i(\mathbf{r})\cdot\mathbf{J}_f(\mathbf{r})}{J_i(\mathbf{r})\cdot J_f(\mathbf{r})}\ . \tag{2.6}$$

The contributions from the regions which are inaccessible to classical trajectories can be included by using the quantal $\chi(\mathbf{r})$.

The physical meaning of Eq.(2.2) is given as follows. $(k_i(\mathbf{r})/k_i)|\chi_i(\mathbf{r})|^2$ is the probability that the incident particle with the flux k_i at infinity can reach the point $\mathbf{r}$ with the flux $k_i(\mathbf{r})$ and $(k_f(\mathbf{r})/k_f)|\chi_f(\mathbf{r})|^2$ is the probability that an outgoing particle arising at the point $\mathbf{r}$ with the flux $k_f(\mathbf{r})$ appears at the infinity with the momentum k_f with the flux k_f. $\left[\partial^2\sigma/\partial\varepsilon_f(\mathbf{r})\partial\Omega_f(\mathbf{r})\right]_{\mathbf{r}}$ is the average cross section for the two-body collision at $\mathbf{r}$ as mentioned above. The effect of the reflection, refraction, and absorption of the distorted waves are taken into account in $\chi(\mathbf{r})$.

3. CALCULATION AND DISCUSSION

3-1. Nonlocality correction factor

The effect of nonlocality in the optical potential can be considered in the manner described in Ref. 12. The relation between the distorting wave function $\chi_{NL}(r)$ for the nonlocal potential and $\chi_L(r)$ for the equivalent local potential $U_L(r)$ is defined in the following analytic expression:

$$\chi_{NL}(r) = F(r)\,\chi_L(r) \tag{3.1}$$

$$F(r) = \left[1 - \frac{\mu\beta^2}{2\hbar^2} U_L(r)\right]^{-1/2} \tag{3.2}$$

where $F(r) \rightarrow 1$ as $r \rightarrow \infty$ and β is the nonlocality range.

The distorting waves $\chi_L(r)$ for projectile and ejectile are calculated using the local potential $U_L(r)$ with global optical potential parameters. Note that the Coulomb potential is regarded as the local one and is excluded from $U_L(r)$ in Eq.(3.2). When the nonlocality is taken into account, the $\chi_{NL}(r)$ is used in place of $\chi_L(r)$ as $\chi_i(r)$ and $\chi_f(r)$ in Eqs. (2.2) and (2.5). If $U_L(r) < 0$, then $F(r) < 1$. This leads to the $\chi_{NL}(r)$ smaller in magnitude than the $\chi_L(r)$ and results in reduction of the absolute value of cross sections.

3-2. Input data of numerical calculations

The input data used in the present calculation are different from those in Ref. 9. The different points are briefly mentioned.

For distorting potentials of protons, two sets of global optical potentials are used according to the incident and outgoing energy region: the global potential of Menet et al.[13] is used for energies up to 80 MeV and that of Schwandt et al.[14] is used for energies between 80 and 200 MeV. Spin-orbit potentials are not taken into account in all cases.

The Fermi distribution form $\rho(r) = \rho_0/[1 + \exp\{(r - R_\rho)/a_\rho\}]$ for the nucleon density using the parameters[15] $R_\rho = r_\rho A^{1/3}$ with $r_\rho = 0.978 + 0.0206\,A^{1/3}$ and $a_\rho = 0.54$ fm. The constant ρ_0 is obtained from the normalization $\rho_0 = \int \rho(r)dr$.

The value of β used in the nonlocality correction in Eq.(3.2) is chosen to be 0.85fm, which was derived from the best fit to the energy dependence of the neutron-nucleus scattering experiments by Perey and Buck[16].

3-3. Comparisons with experimental data on (p,p') scattering

3.3.1. Angular distributions of (p,p') scattering at incident energies below 100 MeV

Figure 1 shows the angular distributions of (p,p') scattering from ^{120}Sn at the incident energy of 62 MeV and the outgoing energies of 40 and 50 MeV. The calculation based on the LK model agrees with the experimental data[17] well in the middle angular region of 30° - 80°, although it gives underestimation at smaller and larger angles. The calculated results of the generalized exciton model (GEM)[18] are also shown by dashed lines. In the GEM calculation, emissions from higher exciton states are also included.

The two models are in qualitative agreement with each other. More detailed comparison between the two models has been discussed in Ref. 9.

Figure 2 shows comparisons of calculated results and experimental angular distributions of protons from proton-induced reactions on ^{209}Bi at 62 MeV. As shown in Fig.1, the calculation reproduces the experimental data[17] well in the middle angular region at a high outgoing energy. Comparisons are also made with the multistep direct reaction (MSDR) model[4]. The two models agree generally well with each other, although there is disagreement at small and large angles.

In Fig.3, calculated angular distributions are compared with recent experimental data[19] on (p,p') scattering from ^{90}Zr at 80 MeV. At Ep'=60MeV, both angular distributions show good agreement in the middle angular region. On the other hand, the agreement becomes worse at lower outgoing energy. This is probably because the contribution of multistep process is not included in the LK model. The dashed lines show the one-step component[19] of the MSD cross sections based on the FKK theory[5]. The two models disagree in the middle angle region at the high exit energy, where the LK model shows better agreement with the experimental data. These two models gives similar angular distributions at lower outgoing energies.

Now we discuss the effect of nonlocality in the optical potential. Figure 4 shows the cross section of (p,p') scattering from ^{120}Sn at 62 MeV calculated with and without nonlocality correction obtained from Eq.(3.2). The cross section without nonlocality correction is larger than that with nonlocality correction by a factor of about two over the whole angular region. The reduction of the cross section due to the nonlocality results in good agreement with the experimental data. The effect of the nonlocality becomes smaller with increase in incident energy as will be shown in Fig. 7-(b).

3.3.2. Angular distributions of (p,p') scattering at incident energies of 100 to 200 MeV

The LK model is applied to (p,p') scattering at higher incident energies of 100-200 MeV. The results are shown together with experimental angular distributions[21,22] in Figs. 5-8 for ^{58}Ni and Fig.9 for ^{197}Au. The calculated results reproduce well in the angular region except very small and large angles as in the case of incident proton energies below 100 MeV in Figs.1-3. Agreement with the experimental data becomes better as the outgoing proton energy increases. The disagreement at large angles may be due to the contribution of multistep processes. The underestimation of the cross section at small angle may be attributable to the use of the degenerate Fermi-gas model, because the N-N scattering inside the nucleus is kinematically forbidden by the Pauli principle at

small angles in the model. More detailed discussion about this problem has been made in Ref. 9.

3.3.3. Angle-integrated (p,p') energy spectra for ^{54}Fe

The angle-integrated energy spectra are also calculated using the LK model and compared with experimental (p,xp) data[17] for ^{54}Fe at three incident energies of 29, 39, and 62 MeV in Fig.10. The calculated spectra show fairly good agreement with the experimental spectra in high outgoing energy range. This may be understood from that the one-step process becomes important in emissions of particles with high energies and the middle angular region where the LK model prediction is very successful has a large contribution in the angle-integration.

The energy spectra calculated using a EXIFON code based on the SMD-SMC model[7] are also plotted by long-dashed and short-dashed lines for the total energy spectra and the one-step component of the MSD cross sections, respectively. The calculation by the EXIFON code underestimates somewhat the cross section in the high energy portion of interest. However, the spectral shape of one-step component for the two models is very resemble in the continuum portion.

4. APPLICATION TO NUCLEAR DATA EVALUATION

In the previous section, the comparisons between the model calculation and several experimental data were shown. Here we discuss the LK model from the viewpoint of the application to high energy nuclear data evaluation.

The LK model does not include any adjustable parameters if the free N-N scattering cross section and the optical potential are used. In addition, the formula is given as a simple closed-form with a three-dimensional integral as in Eq.(2-2). With respect to the three-dimensional integral, we have found it possible to achieve faster calculations by using a certain numerical calculation technique (Legendre-Gauss or Legendre-Laguerre methods). Thus, the LK model has attractive aspects for application to nuclear data evaluation. The present version of the LK model, however, has some problems to be resolved as follows.

One of the problems is the treatment of charge exchange process, such as the (p,n) and (n,p) reactions. The process should not be neglected in the incident energy range of 20- 200 MeV, where the LK model is applicable. However, the LK model can not calculate these processes in the present version. In particular, the (p,n) data are important from the viewpoint of the shielding design of accelerators. Therefore, it will be

necessary to refine the LK model so that the (p,n) and (n,p) reactions can be taken into account.

The present model can not treat the multistep process which becomes important as the outgoing energy decreases. Neglect of this process leads to underestimation of the cross sections at large angles as indicated in the previous section. Recently, the formulation of two-step calculation based on the LK model has been completed by Kawai and Weidenmüller[22]. An extension of the present calculation code is in progress so as to include the two-step process. It is of our particular interest to estimate two step process by using the LK model, because the MSD calculation based on the FKK theory indicates that multistep components become dominant even at forward angles with decrease in the outgoing energy.[19]

Within the framework of the LK model, only the MSD process is treated and the MSC process is not included. Accordingly, the other model is required for calculations of the MSC component. Furthermore, the extension to the MSD process more than three steps is not considered to be adequate in practical because of time-consuming calculations. From a practical viewpoint, therefore, a hybrid-type of model may be proposed as a compromise, in which the LK model is used for the one and two step direct processes and the semiclassical model such as the GEM model[18] or the GDH model[3] is combined for the other multistep processes and compound process. In future, we would like to pursue the application of the LK model to nuclear data evaluation in this direction after the above-mentioned improvements and extensions.

5. SUMMARY

The LK model was applied to the calculation of proton inelastic scattering to the continuum in the incident energy range of 20-200 MeV. It was confirmed that there is large contribution from the one-step direct process in the high energy region of the energy spectrum of emitted protons as the other preequilibrium models have indicated. The model calculation can reproduce very well the experimental angular distributions in the middle angular region with no adjustable parameters. In addition, we have found that the effect of nonlocality correction leads to reduction of the cross section in magnitude and the agreement with the experimental data is improved.

In the application to nuclear data evaluation, some related problems were indicated. In particular, it will be necessary to extend and refine the LK model so as to include the (p,n) reaction and the two-step process. Development and some improvement of the LK model calculation code are now in progress in this direction.

ACKNOWLEDGEMENTS

The author wishes to thank Professor M. Kawai and Dr. Y.L. Luo for their offer of a calculation code PREFS and valuable advice in this work. The computer calculation for this work has been financially supported by Research Center for Nuclear Physics, Osaka University.

REFERENCES

1. P.E. Hodgson, Proceedings of the Int. Conf. on Nuclear Data for Science and Technology, Mito, Japan, Ed. S. Igarashi (SAIKON PUBLISHING Co. Ltd., 1988) p.655.
2. J. Griffin, Phys. Rev. Lett. **17**, 478 (1966); G. Mantzouranis et al., Z. Phys. A **276**, 145 (1976).
3. M. Blann, Annu. Rev. Nucl. Sci. **25**, 123 (1975); M. Blann et al., Phys. Rev. C **30**, 1493 (1984).
4. T. Tamura, T. Udagawa, and H. Lenske, Phys. Rev. C **26**, 379 (1982).
5. H. Feshbach, A. Kerman, and S. Koonin, Ann. Phys. (N.Y.) **125**, 429 (1980).
6. N. Nishioka, H.A. Weidenmüller, and S. Yoshida, Ann. Phys. (N.Y.), **183**, 166 (1988); **193**, 195 (1989).
7. H. Kalka et al., Phys. Rev. C **40**, 1619 (1989).
8. Y.L. Luo and M. Kawai, Phys. Lett. B **235**, 211 (1990).
9. Y.L. Luo and M. Kawai, Phys. Rev. C **43**, 2367 (1991).
10. M.L. Goldberger, Phys. Rev. **74**, 1269 (1948).
11. K. Kikuchi and M. Kawai, *Nuclear Matter and Nuclear Reactions* (North-Holland, Amsterdam, 1968), p.33.
12. N. Austern, *Direct nuclear reaction theories* (John Wiley & Sons, New York, 1970) p.114.
13. J.J.H. Menet et al., Phys. Rev. C **4**, 114 (1971).
14. P. Schwandt et al., Phys. Rev. C **26**, 55 (1982).
15. J.W. Negel, Phys. Rev. C **1**, 1260 (1970).
16. F.G. Perey and B. Buck, Nucl. Phys. **32**, 353 (1962).
17. F.E. Bertrand and R.W. Peele, Phys. Rev. C **8**, 1045 (1973); Oak Ridge National Laboratory Report No. ORNL-4460, 1960; No. ORNL-4471,1970; No. ORNL-4638, 1971.
18. A. Iwamoto and K. Harada, Nucl. Phys. **A419**, 472 (1984).

19. A.A. Cowley et al., Phys. Rev. C **43**, 678 (1991).
20. S.V. Fortsch et al., Phys. Rev. C **43**, 691 (1991).
21. A.A. Cowley et al., Z. Phys. A **336**, 189 (1990).
22. M. Kawai and H.A. Weidenmüller, private communication.

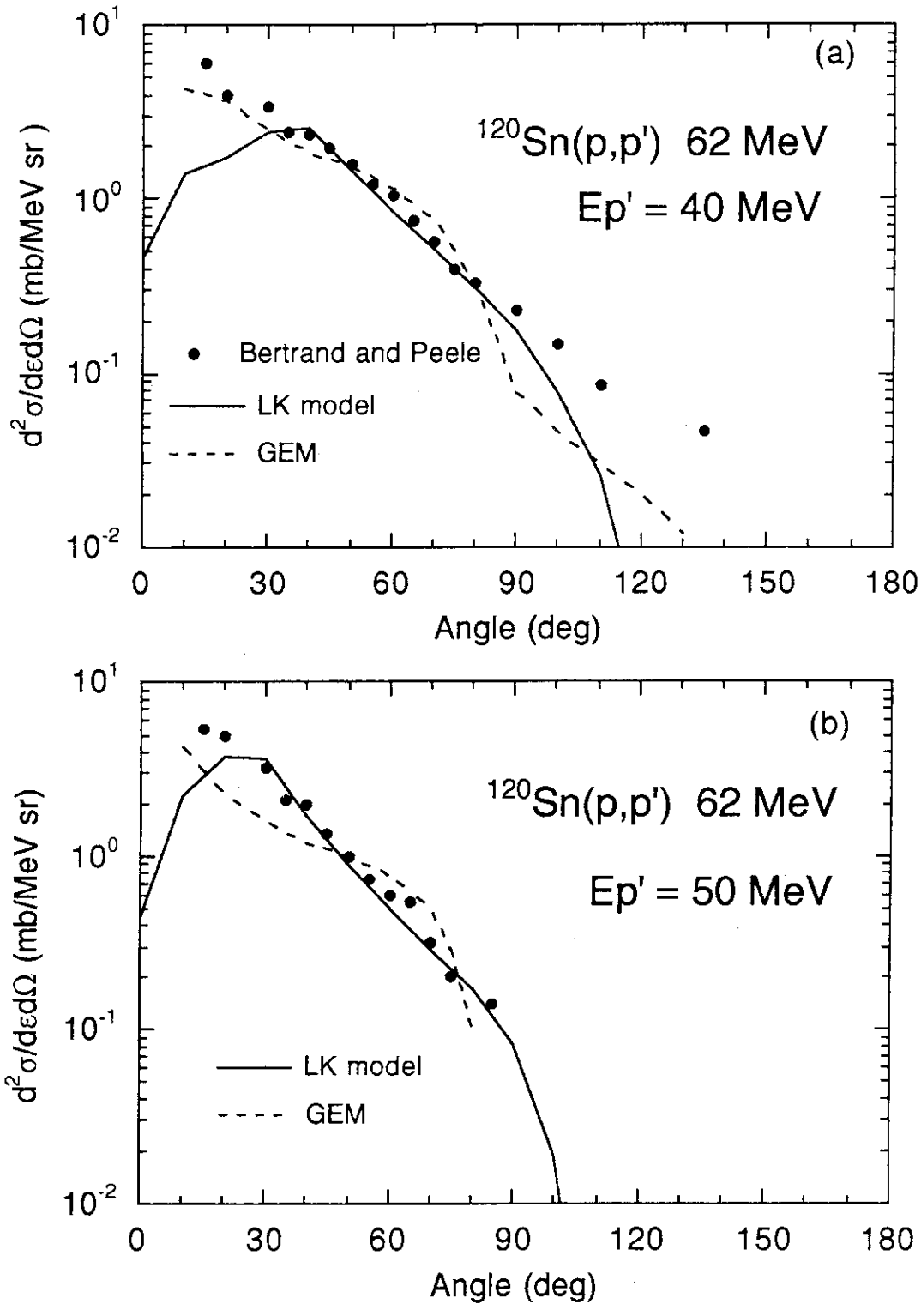

Fig.1 Calculated and experimental angular distributions of ^{120}Sn(p,p') at the incident energy of 62 MeV for two different outgoing energies of (a) 40 MeV and (b) 50 MeV. The solid lines represent the LK model calculation and the dashed lines show the GEM model calculation by Iwamoto and Harada (Ref. 18). The experimental data from Ref. 17 are indicated by the closed circles.

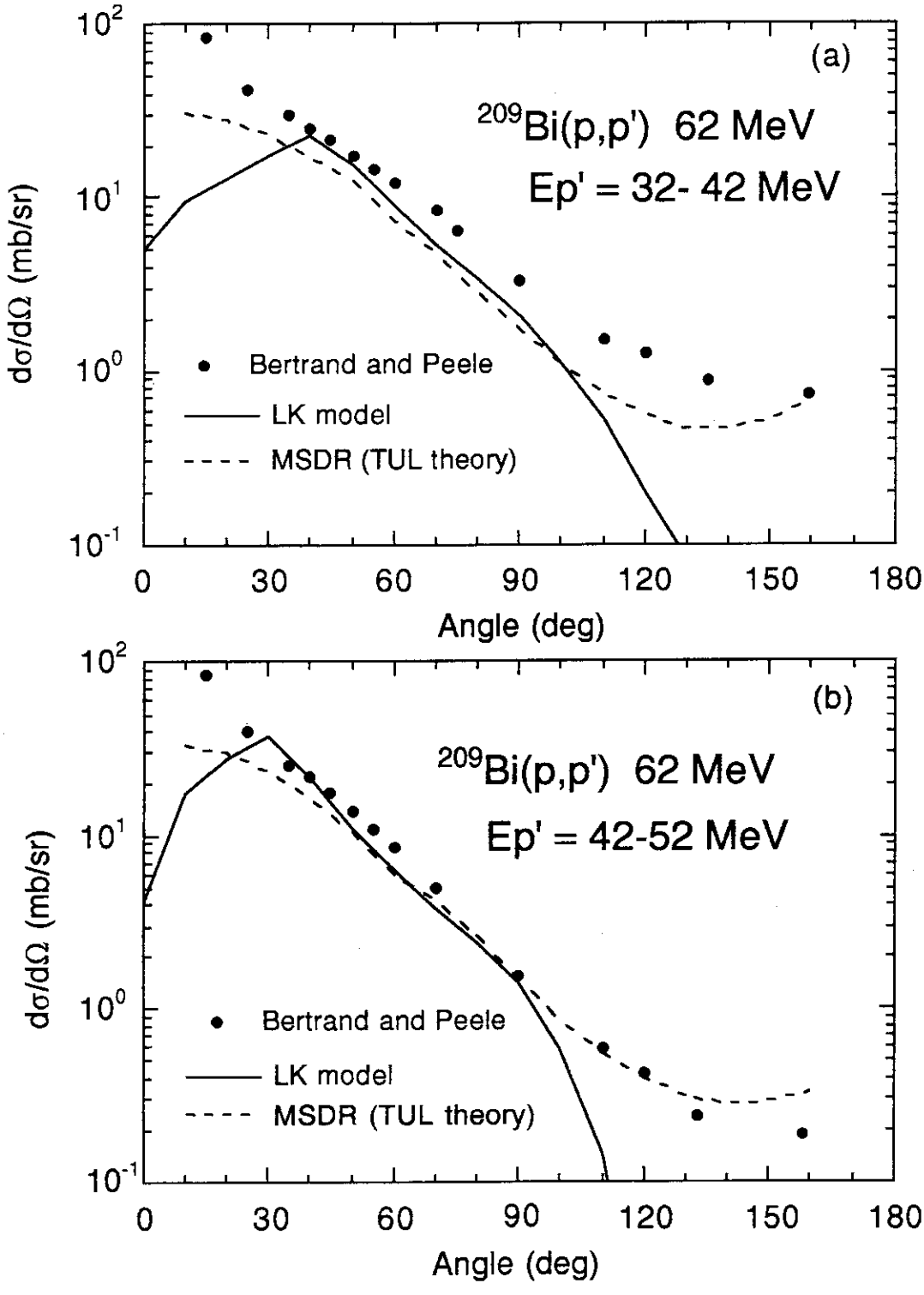

Fig.2 Calculated and experimental angular distributions of the cross sections summed over the 10-MeV energy bins of the emitted particles of ^{209}Bi(p,p') at 62 MeV. The experimental data (closed circles) are taken from Ref. 17. The solid and dashed lines represent the LK model calculation and that by the TUL theory (Ref. 4), respectively.

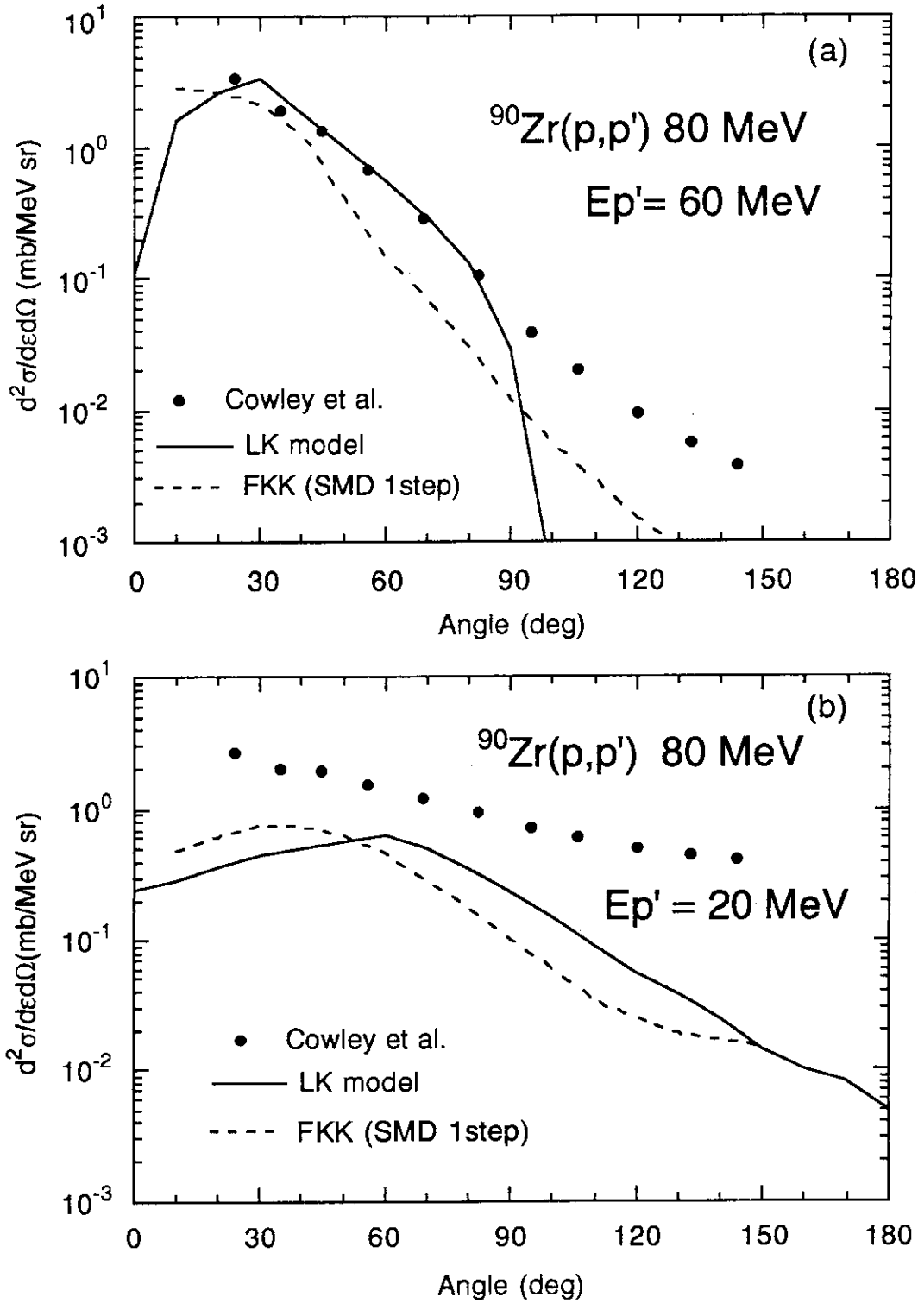

Fig.3 Calculated and experimental angular distributions of ^{90}Zr(p,p') at the incident energy of 80 MeV. The solid lines represent the LK model calculation and the dashed lines denote the one-step component of SMD by the FKK theory (Refs. 5 and 19). The experimental data are from Ref. 19.

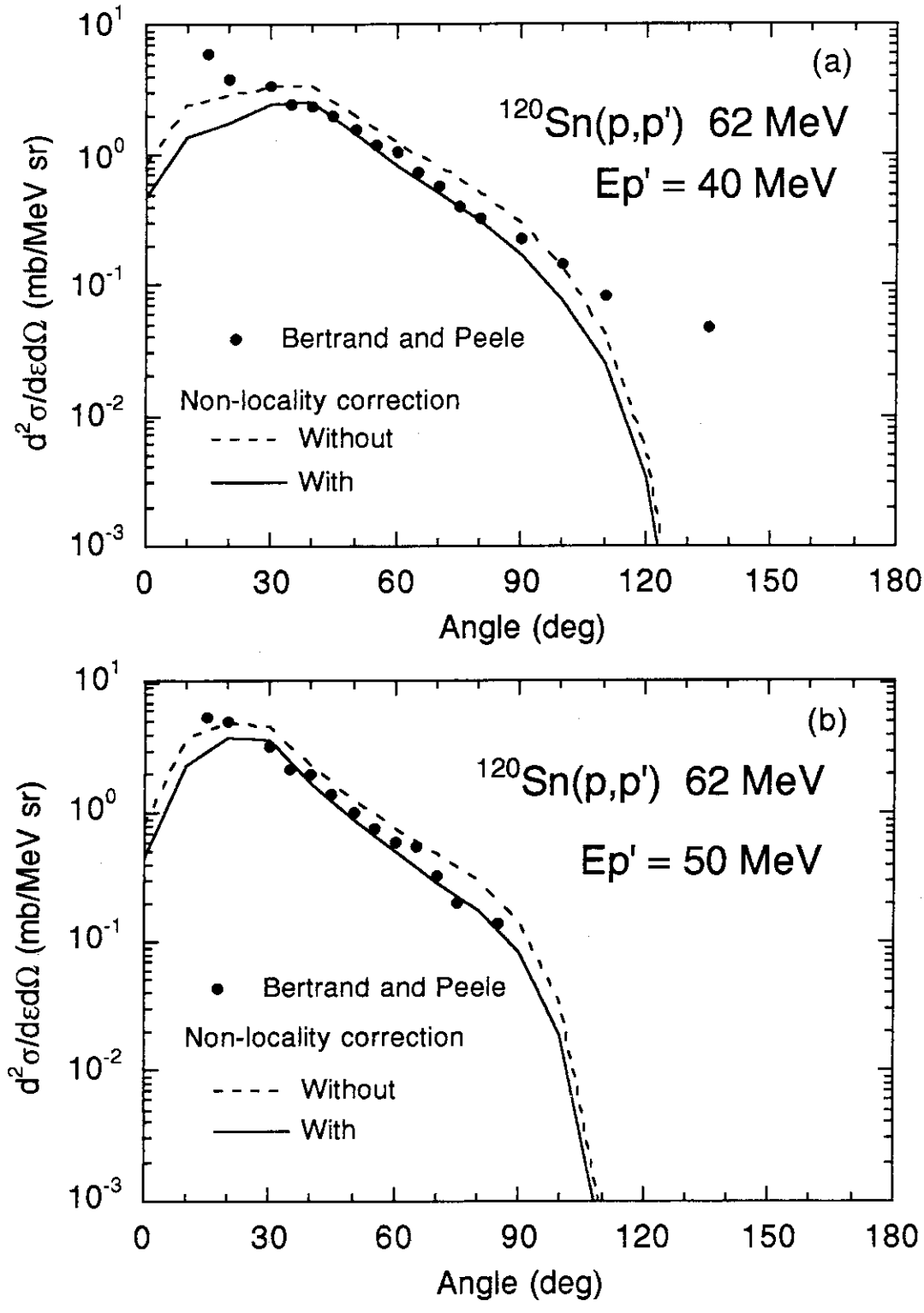

Fig.4 Effect of nonlocality correction on angular distributions of ^{120}Sn(p,p') at 62 MeV. The solid and dashed lines represent the results of the calculations with and without the nonlocality correction, respectively.

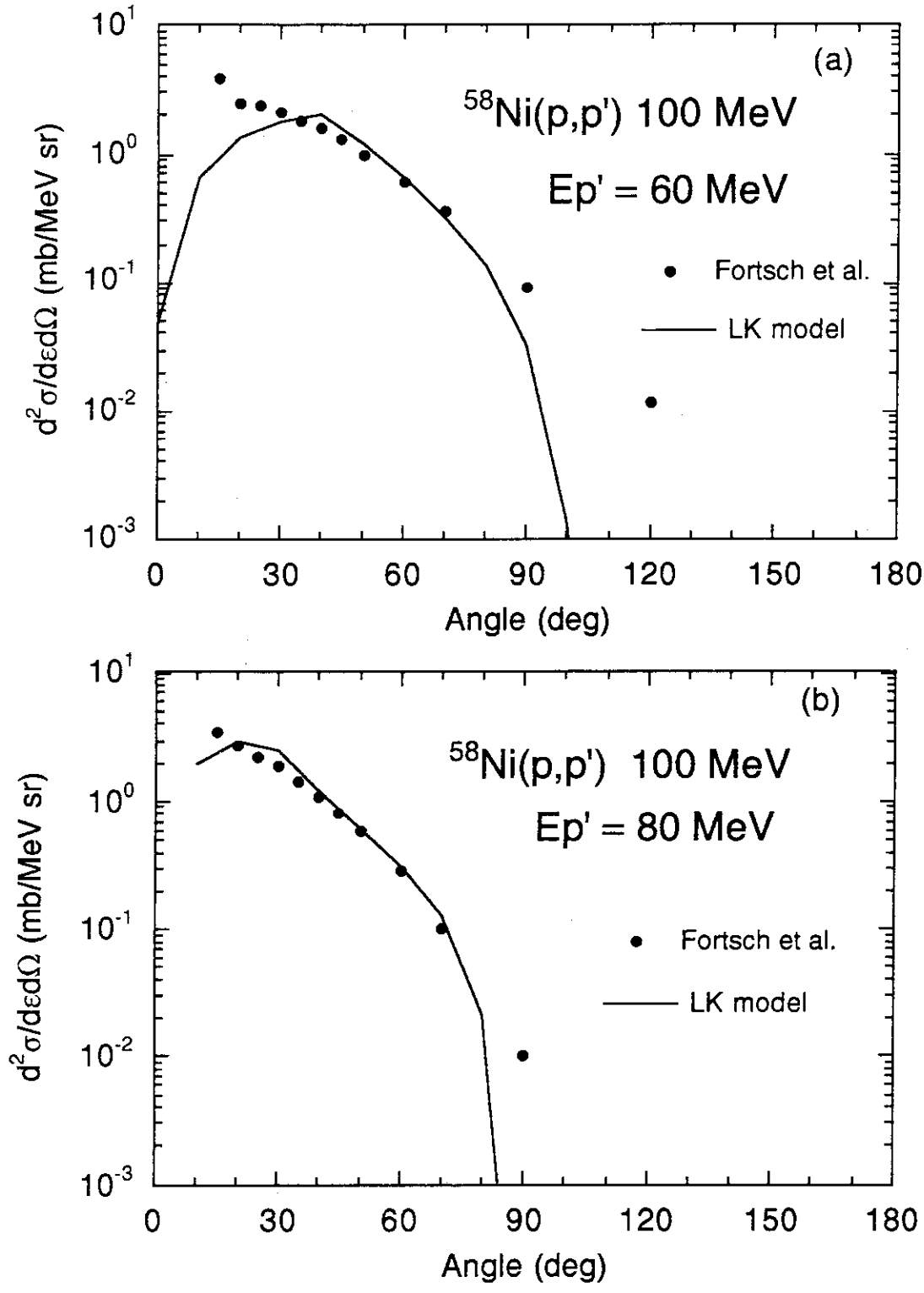

Fig.5 Calculated and experimental angular distributions of ^{58}Ni(p,p') at the incident energy of 100 MeV. The solid lines represent the LK model calculation and the experimental data are from Ref. 20.

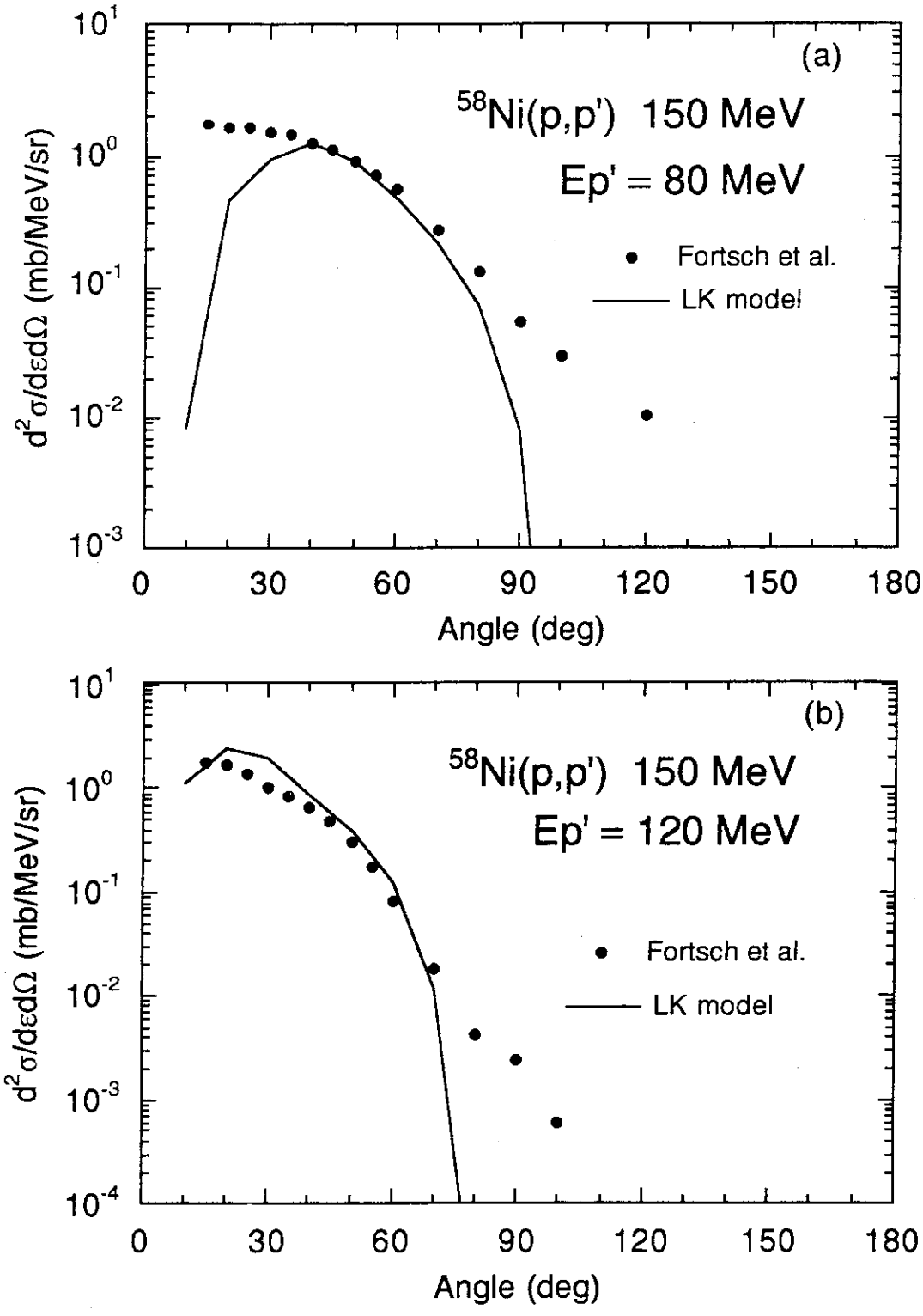

Fig.6 Same as Fig.5, but at the incident energy of 150 MeV

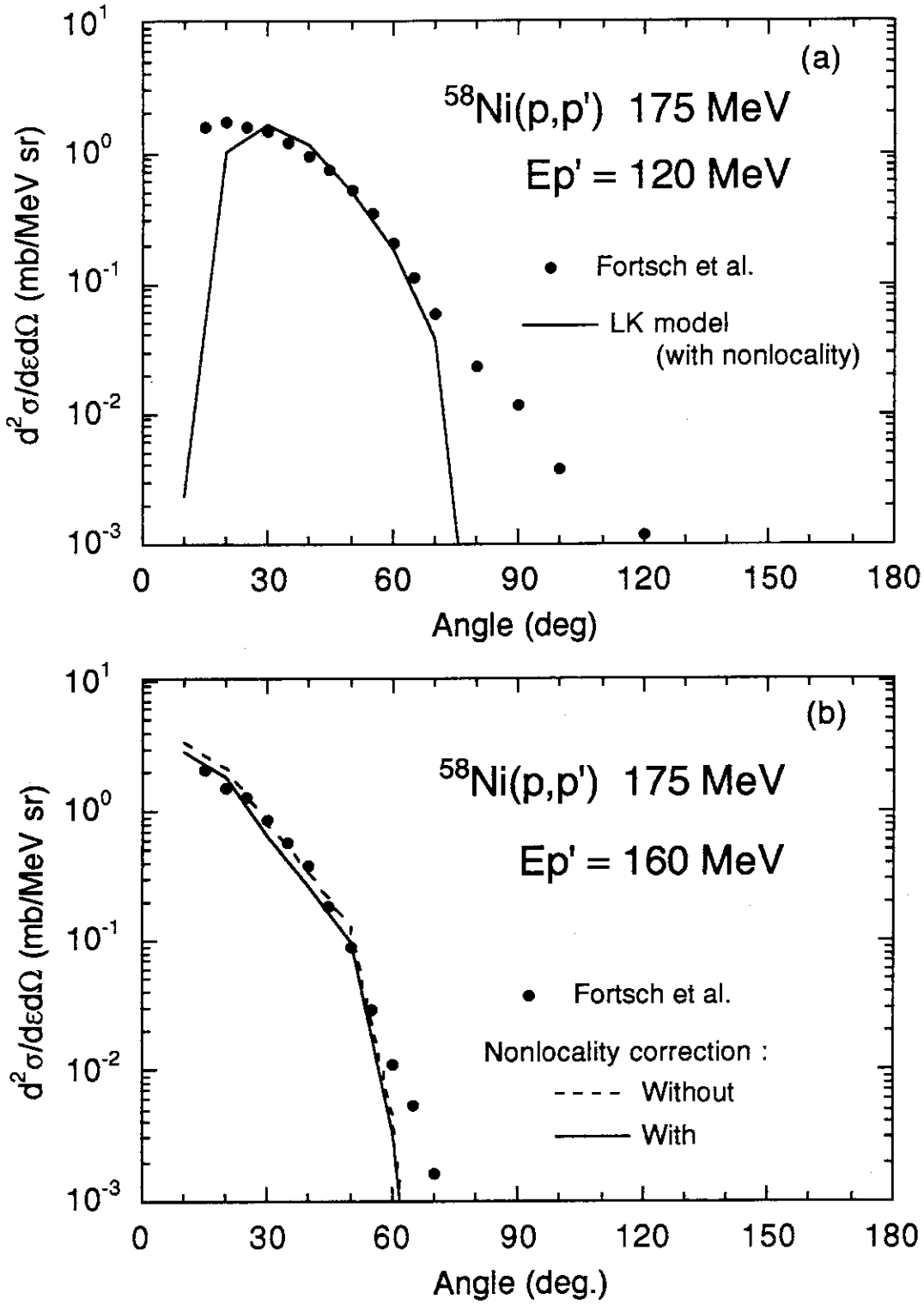

Fig.7 Same as Fig.5, but at the incident energy of 175 MeV. The dashed line represents the result of the calculation without the nonlocality correction.

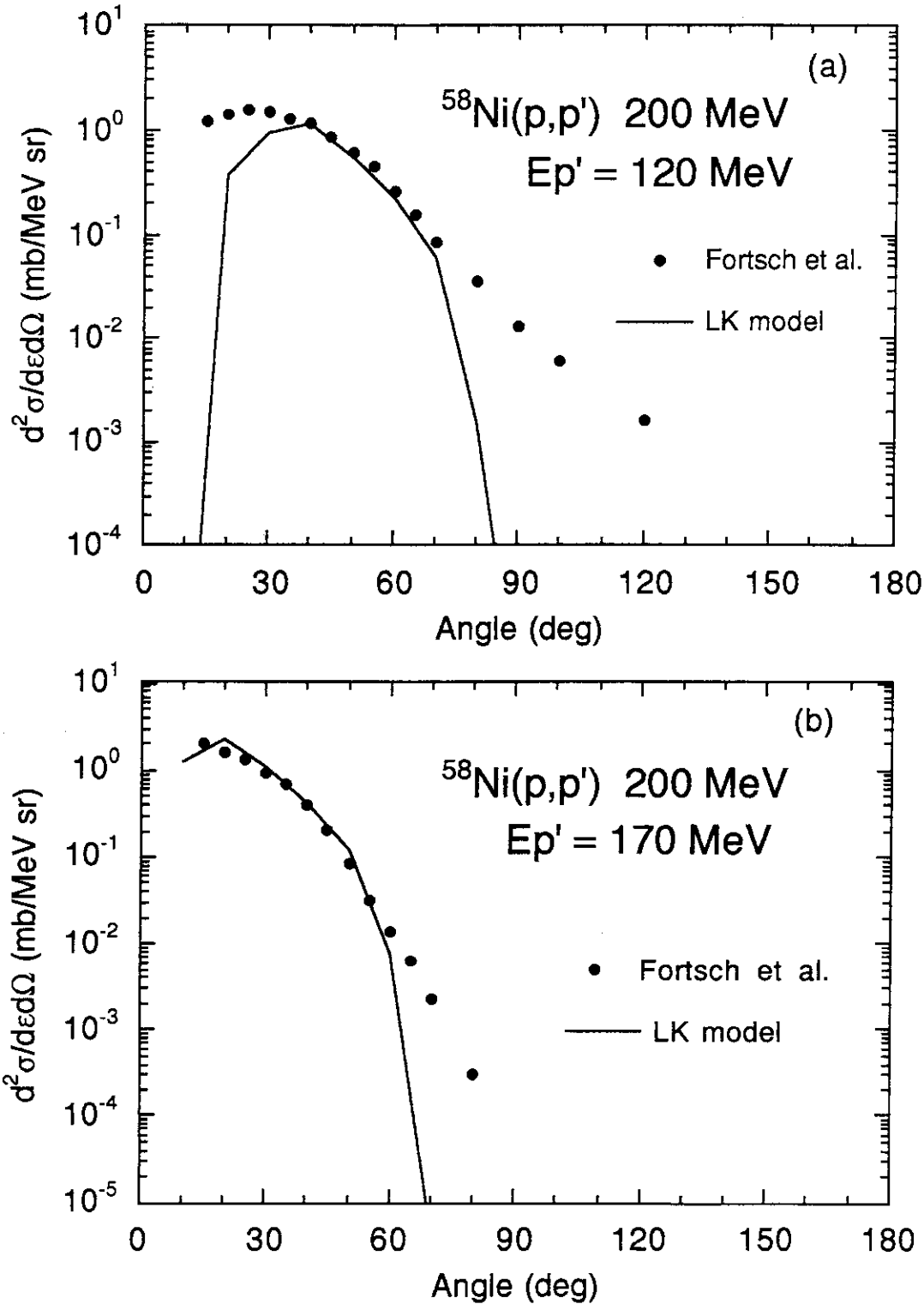

Fig.8 Same as Fig.5, but at the incident energy of 200 MeV

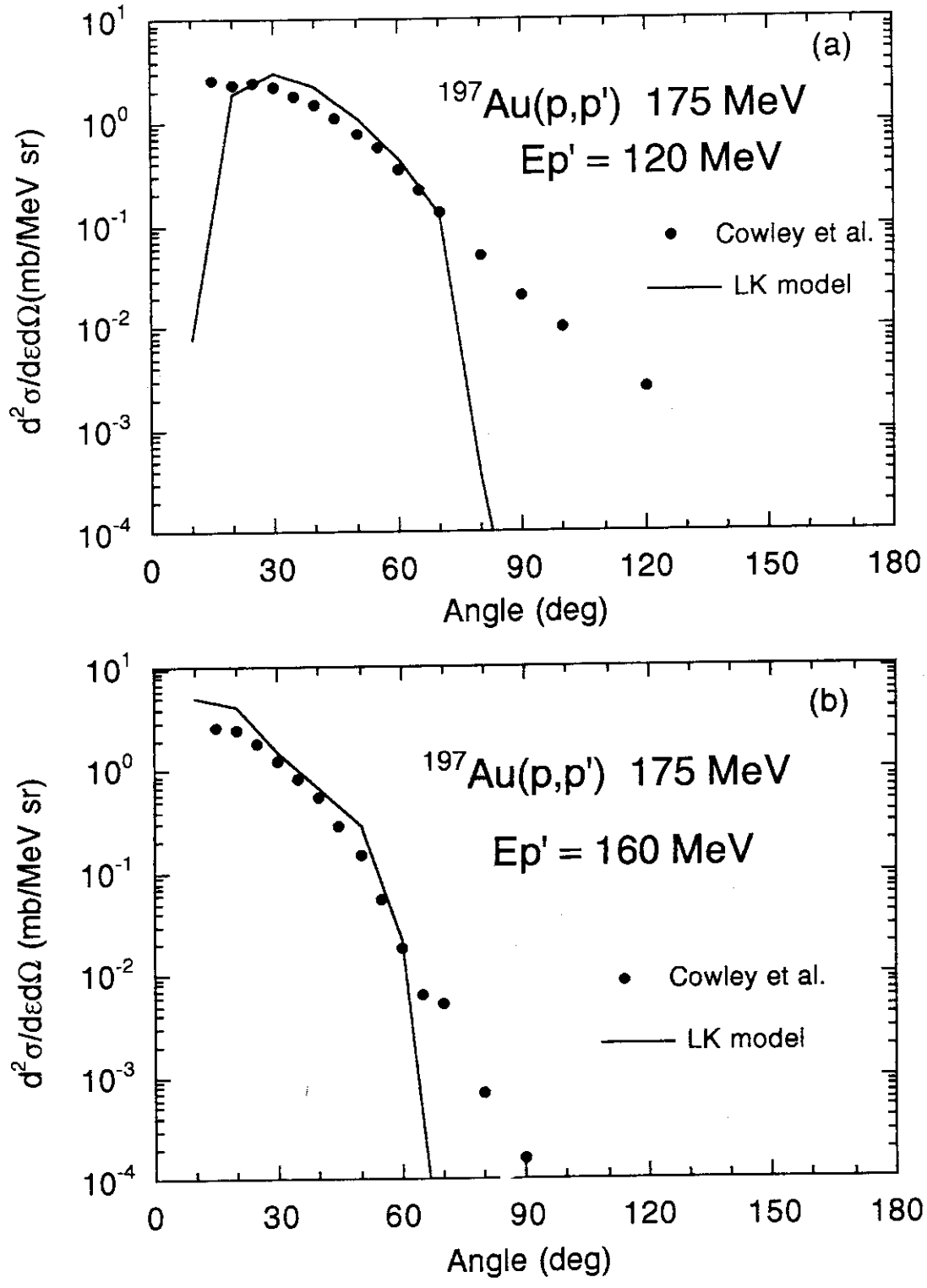

Fig.9 Same as Fig.5, but for ^{197}Au(p,p') at the incident energy of 150 MeV. The experimental data are from Ref. 21.

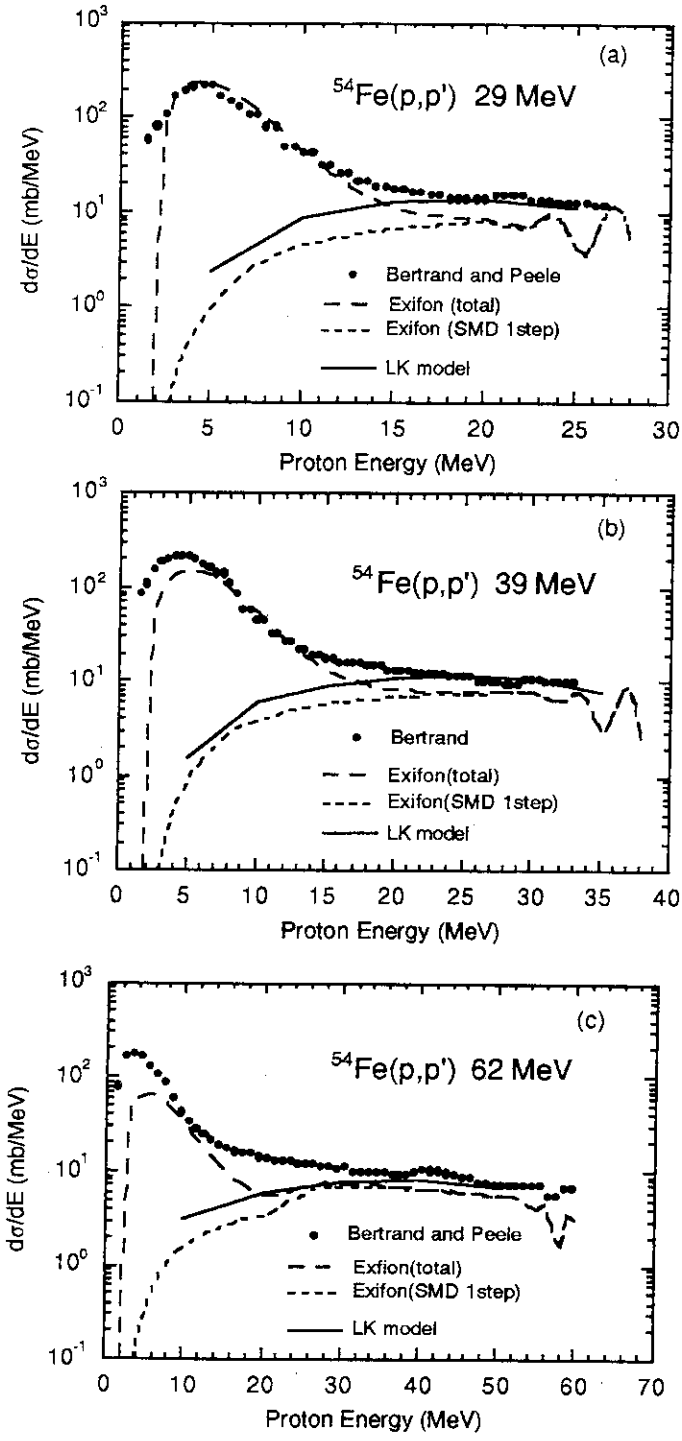

Fig.10 Calculated and experimental proton energy spectra of ^{54}Fe(p,p') at the incident energies of (a) 29 MeV, (b) 39 MeV, and (c) 62 MeV. The experimental data are from Ref. 17. The results of the LK model are indicated by the solid lines. The long-dashed and the short-dashed lines represent the total proton spectra and the one-step direct component of them calculated by a EXIFON code (Ref. 7), respectively.

5.2 Nucleus as a Canonical Ensemble: Level Density

Hiroshi Sato
Radiation Laboratory, RIKEN, Wako, Saitama 351-01, JAPAN

ABSTRACT

The nuclear level density is studied with the temperature dependent antisymmetrized density matrix of many fermions in a harmonic oscillator well. Comparing it with that obtained by the conventional formula, the applicability and limitation of the conventional formula are disscussed. Then extending the method to the deformed nucleus, the Strutinsky type level density distribution is observed at low temperature limit.

1. Introduction

One of the main subject of nuclear physics is to study the behavior of the nuclear matter at various excitation energies and densities in a consistent manner. Thus far, nuclear phenomena at low ecitation energy have been successfully studied by the shell model. And highly excited nuclear states (HX) formed by medium and high energy nuclear collisions have been studied with various thermal models. One of the essential differences between the conventional shell model and thermal models of the HX is that the shell model state is in good quantum state of the energy E and the nucleon number N, while the HX is expressed by the temperature parameter T and the nucleon multiplicity T (or chemical potential μ). In this sense one may quote the microcanonical ensemble of interacting many fermions as the conventional shell model and the canonical ensemble (or grand canonical ensemble) as models of the HX from the statistical mechanical view point. While these ensembles are thermodynamically equivalent, in order to describe the nuclear system both at low and high excitation energies consistently, we must choose either the micrcanonical or canonical (or grand canonical) ensemble as for the total representation of the nuclear system. In the previous works, we have studied the nuclear system both at low and high excitation energies in terms of the canonical ensemble with the employment of the temperature dependent antisymmetrized many particle density matrix in a harmonic oscillator (HO) potential. Then we studied thermodynamical quantities of the nucleus, and show-

ed that this ensemble is equivalent to the ground state of the HO shell model at low temperature limit. We also studied the nuclear level density, and found that characteristic features of the nuclear level density, experimentally observed, can be expressed as the properties of this ensemble[1]. Then we showed that various phenomena observed in medium and high energy nuclear collisions are nicely explainable as the properties of this ensemble at high temperature[2]. In this talk, first we review the theoretical treatment of the canonical ensemble and the level density, and extend the study to the deformed HO case, and mention briefly the relationship between the entropy of this ensemble and the Strutinsky type level density distribution.

2. Nucleus as a Canonical Ensemble

2.1. Density Matrix for the Canonical Ensemble

At temperature T (= 1/β) the unnormalized one particle density matrix in a HO potential with a oscillator constant ω is given by[3,4]

$$\rho^{u,1}(\vec{x},\vec{x}':\beta)=\langle\vec{x}|e^{-\beta h}|\vec{x}'\rangle$$

$$=\left(\frac{m\omega}{2\pi\hbar\sinh 2f_\beta}\right)^{3/2}\exp\left\{-\frac{m\omega}{4\hbar}\left[(\vec{x}+\vec{x}')^2\tanh f_\beta+(\vec{x}-\vec{x}')^2\coth f_\beta\right]\right\},$$

where $f_\beta = \frac{1}{2}\beta\hbar\omega$. The trace Z of this matrix and the normalized one particle density matrix are given, respectively, by

$$Z=Tr(\rho^{u,1})=\int d\vec{x}\,\rho^{u,1}(\vec{x},\vec{x}:\beta)=F_\beta=\left(\frac{1}{2\sinh f_\beta}\right)^3$$

and

$$\rho^1(\vec{x},\vec{x}':\beta)=\frac{1}{Z}\rho^{u,1}(\vec{x},\vec{x}':\beta)\,.$$

The unnormalized density matrix for the system of N fermions in a HO potential is given by

$$\rho^{u,N}(\xi_1..\xi_N,\xi_1'..\xi_N':\beta)=\frac{1}{N!}\sum_P(-1)^P\rho_D^{u,N}(\xi_1..\xi_N,P\xi_1'..P\xi_N':\beta)\,,$$

where $(-1)^P = \begin{cases} 1 & \text{for even permutation} \\ -1 & \text{for odd permutation.} \end{cases}$

The distinguishable density matrix $\rho_D^{u,N}$ is given by

$$\rho_D^{u,N}(\xi_1..\xi_N,\xi_1'..\xi_N':\beta)=\prod_{i=1}^{N}\rho^{u,1}(\xi_i,\xi_i':\beta)\,.$$

Here the coordinate ξ_i represents spatial and spin (also isospin) variable. The trace of the unnormalized density matrix is found to satisfy the following recurrence relation

$$Z_N=Tr(\rho^{u,N})=\frac{1}{N}\sum_{n=1}^{N}(-1)^{n+1}H_{n\beta}Z_{N-n}=Z_N\sum_{n=1}^{N}G^{\beta}(N,n)\,,$$

where $Z_0 = 1$ and $G^{\beta}(N,n) = (-1)^{n+1}H_{n\beta}Z_{N-n}/NZ_N$. The trace of the single particle density matrix is given by $H_{n\beta} = N_g F_{n\beta}$ with $N_g = 2$ for spin formalism and $N_g = 4$ for isospin formalism. The Helmholz free energy F_N, the internal energy U_N, and the entr-opy S_N are given, respectively, as follows

$$F_N=-\frac{1}{\beta}\ln(Z_N)\,,\quad U_N=\frac{d}{d\beta}(\beta F_N)\,,\quad \textit{and}\quad S_N=\beta(U_N-F_N)\,.$$

2.2. Relationship with the Conventional Shell Model

Since, at zero temperature limit, the ensemble has no interaction with the other part of the system (heat bath), the ensemble becomes the ground state of the HO shell model. To examine this matter, we calculate thermodynamical quantities of the canonical ensemble at low temperature and compare the results with those obtained by the HO shell model. Here we employ the spin formalism, and we neglect the spin orbit splitting of the single particle state.

A. The Internal Energy : First, we calculated the internal energy U_N, and found that the U_N obtained approaches the total energy of the ground state of the HO shell model at low temperature limit. Although we are not explicitly treating the system in the orbital angular momentum representation, due to the Pauli exclusion principle, we find the systematics of the orbital angular momentum of the occupied nucleon state (1S, 1P, 2S1D, etc). The particle number N (=A/2) and temperature dependence of the excitation energy E ($U_N(T)-U_N(T=0)$) calculated with the HO constant $\hbar\omega = 41(2N)^{-1/3}$ MeV is summarized in Fig. 1. The closed shell

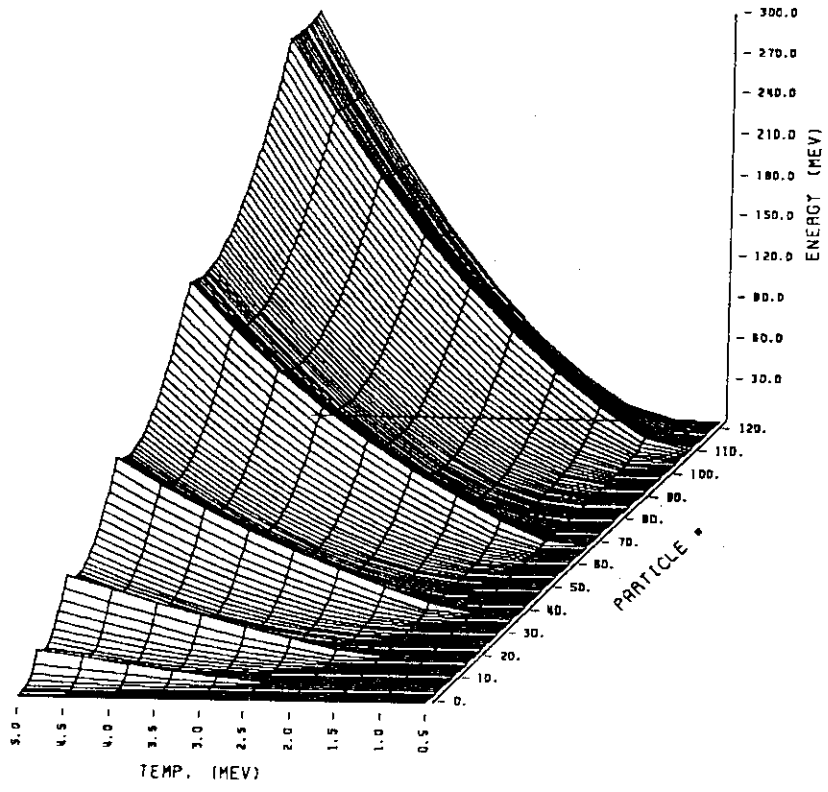

Fig.1. The temperature dependence of the excitation energy E ($U_N(T)-U_N(T=0)$).

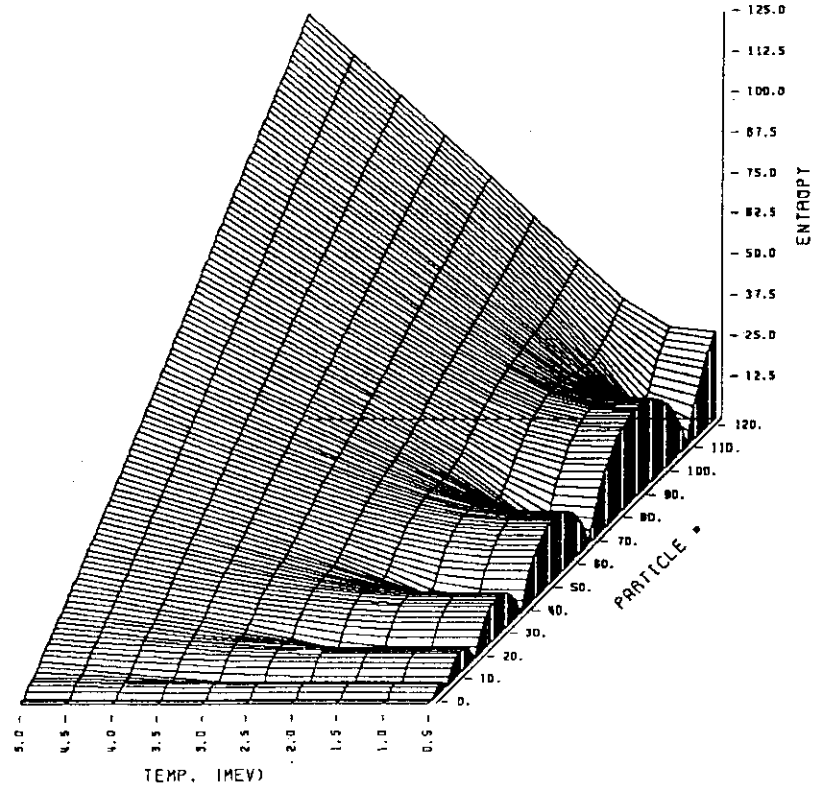

Fig.2. The temperature dependence of the entropy S_N.

effect on the internal energy is clearly seen in Fig.1.
B. The Entropy : Next, we calculated the entropy S_N, and found that the exponential of the S_N, which corresponds to the number of available states of the system, approaches the degree of degeneracy of the ground state of the HO shell model at low temperature limit. The balancing effects between the thermal randomness of the system and the ordering of the closed shell are found in systems near closed shell nuclei. The particle number and temperature dependence of the entropy is calculated and summarized in Fig. 2. The closed shell effect on the entropy is also clearly seen in Fig.2.

2.3. Single Particle Spectra

The single particle emission probability (spectra) from the HX is obtained with the density matrix such that

$$P_1^N(E:\beta)=\sum_{n=1}^{N} G^{\beta}(N,n)P_1^1(E:n\beta)\,,$$

$$P_1^1(E:n\beta) \underset{T\to 0}{\overset{\beta\to\infty}{\longrightarrow}} \frac{1}{N}\left[\frac{\hbar}{\pi m\omega}\right]^{3/2}\exp\left[-(E+v_0)\Big/\left[\frac{\hbar\omega}{2}\right]\right]$$

$$\underset{T\to\infty}{\overset{\beta\to 0}{\longrightarrow}} \frac{1}{N}\left[\frac{n\hbar^2\beta}{2\pi m}\right]^{3/2}\exp[-(E+v_0)n\beta]\,.$$

Here v_0 is the potential depth schematical shown in Fig.3. We found that the particle emitted from the HX shows two typical spectra ; 1) the usual Maxwellian distribution of thermal motion at high temperature limit and 2) the Maxellian distribution with the effective temperature $\hbar\omega/2$ at low temperature limit. The existence of these two slope parameters is consistent with the experimental spectra observed in the medium and high energy nuclear reactions.

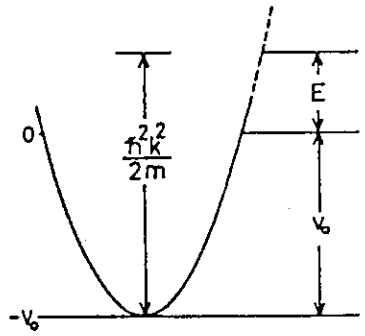

Fig.3. The schematic relationship between the particle emission energy E, the potential depth v_0, and the HO potential.

3. Nuclear Level Density

Since the exponential of the entropy (e^{S_N}) is the number of available states, the nuclear level density is defined by

$$\rho = \frac{de^{S_N}}{dE} = \beta s^{S_N}.$$

On the other hand, a conventional nuclear level density formu-la is given by the microcanonical treatment of the free Fermi gas with the saddle point approximation of the inverse Laplace transformation, as follows

$$\rho(N, E) = \frac{1}{\sqrt{48E}} \exp(2\sqrt{aE}),$$

where E is the excitation energy[5]. The thermodynamic temperature t is given by $t = \sqrt{E/a}$. The theoretical level density parameter a is A/15 for a free Fermi gas and A/10 for a Fermi gas in a harmonic oscillator well, while the parameter extracted from experimental data is approximated by A/8[6]. Therefore, the applicability of the conventional formula to the real nuclear system is not clear. Furthermore, the excitation energy dependence of the parameter a is poorly known compared to its mass number dependence[7].

By equating above two expressions, we studied energy and mass number dependence of the parameter a. The parameter a obtained is small at closed shell nuclei and large in the middle of shell nuclei. The mass number dependence of a becomes A/8 at about 20 MeV excitation energy and A/13 at about 70 MeV excitation energy except at around closed shell nuclei. Then it becomes A/15 at high energy limit. The existence of the excitation energy dependence of the parameter a suggests that (1) the level density formula based on the saddle-point approximation in the inverse Laplace transformation is not adequate to the real nuclear system (*i.e.* nuclear single particle states are not well degenerated in comparison with the usual electron gas in the metal), and (2) we should deal with the entropy itself instead of the level density parameter a.

4. Deformed Nucleus

Since the canonical ensemble becomes the ground state of the shell model at low temperature limit, it can be expected that the many particle system in the Nilsson type potential reveals the systematics of the rotation and deformation and fission phenomena. Here, at the moment, we show

the case of a simple deformed nucleus.

For a spheroidal symmetric HO potential,

$$h=\frac{p^2}{2m}+\frac{m}{2}(\omega_3^2 z^2+\omega_\perp^2(x^2+y^2)),$$

$$\omega_\perp=\omega_0\eta^{1/3},\quad \omega_3=\omega_0\eta^{-2/3}\quad and\quad \eta=\frac{3+\delta}{3-2\delta},$$

where ω is a HO constant for the sherical case, the trace Z of the unnormalized one particle density matrix is given by

$$Z=\frac{1}{2\sinh f_{3\beta}}\left(\frac{1}{2\sinh f_{\perp\beta}}\right)^2\quad with\quad f_{3\beta}=\frac{\beta\hbar\omega_3}{2}\quad and\quad f_{\perp\beta}=\frac{\beta\hbar\omega_\perp}{2}.$$

The other theoretical treatments are identical with those of the spherical case except the density matrix and submatrices.

A. The Internal Energy : We study the deformation and particle number dependence of the internal energy U_N. As an example, we calculate the energy difference Δ ($U_N(\delta)-U_N(\delta=0)$) at temperature T = 0.25 MeV. The energy difference Δ and its negative value $-\Delta$ calculated are summarized in Fig.4. The contour plot of the Δ is also summarized in Fig.5. We find that the energy differences Δ at magic numbers of spherical HO shell model increase with the amount of the deformation, while those in the middle of shell of spherical shell model firstly decrease and then increase with the deformation. However, thus far at present, we cannnot find the favorability of the positive deformation observed by experiments[8]. The deformation dependence of the internal energy U_N is found to be weak with the increase of the temperature T.

B. The Entropy : We also study the deformation and particle number dependence of the entropy S_N. The entropy S_N and its negative value $-S_N$ calculated with temperature T = 0.25 MeV are summarized in Fig.6. The contour plot of the S_N is also shown in Fig.7. We find the peak of the entropy at deformation δ = -0.75, 0.0, and 0.6, which correspond to the simple integer ratios of the HO constants $\omega_\perp$ and ω_3. Since the entropy of S_N = 0 corresponds to the well packed system, we may say that the zero entropy state in this calculation cor-

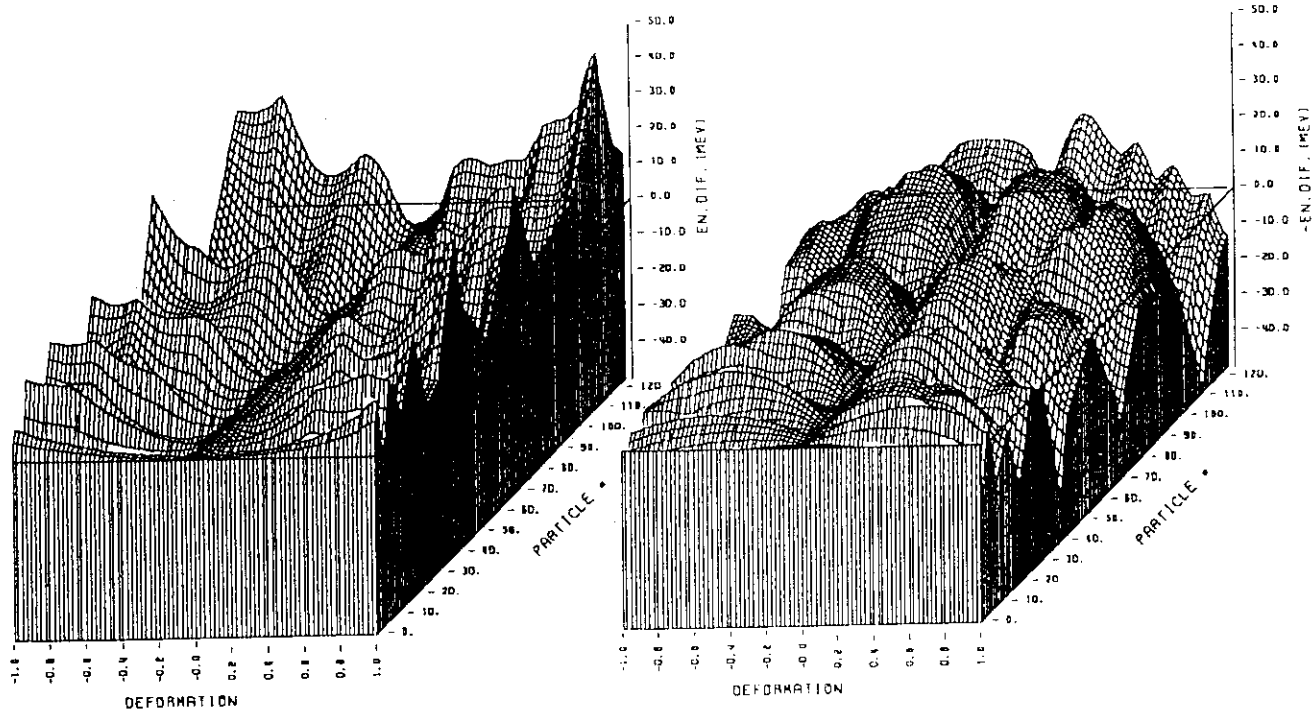

Fig.4. The deformation dependence of the energy difference $\Delta\ (U_N(\delta)-U_N(\delta=0))$.

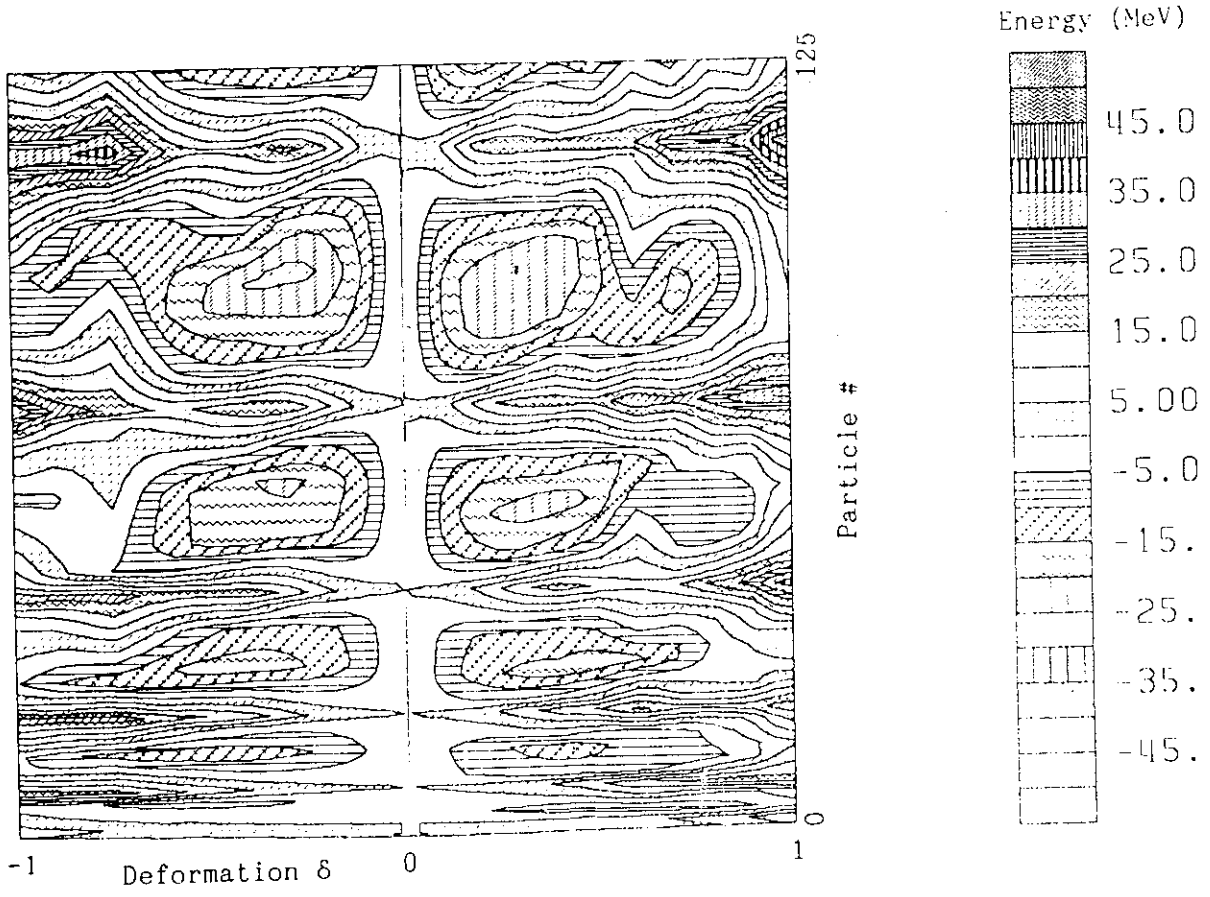

Fig.5. The contour plot of the energy difference $\Delta\ (U_N(\delta)-U_N(\delta=0))$.

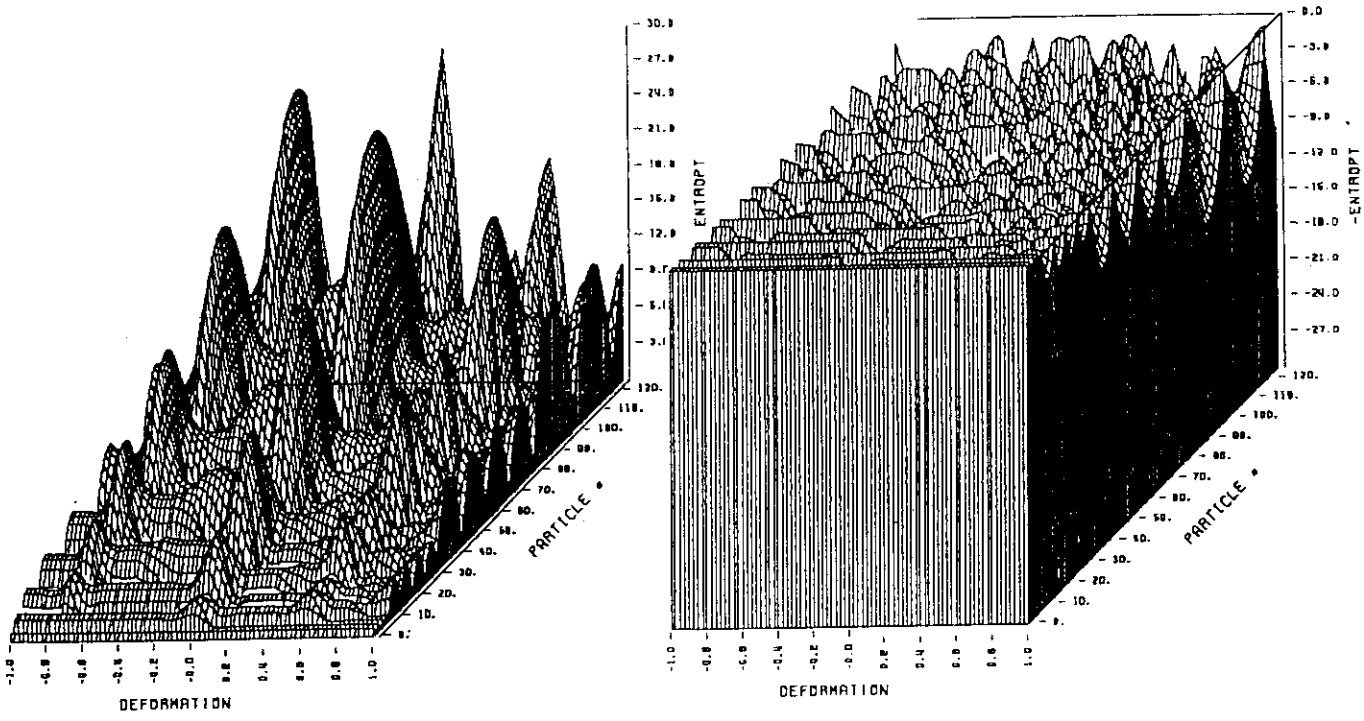

Fig.6. The deformation dependence of the entropy S_N.

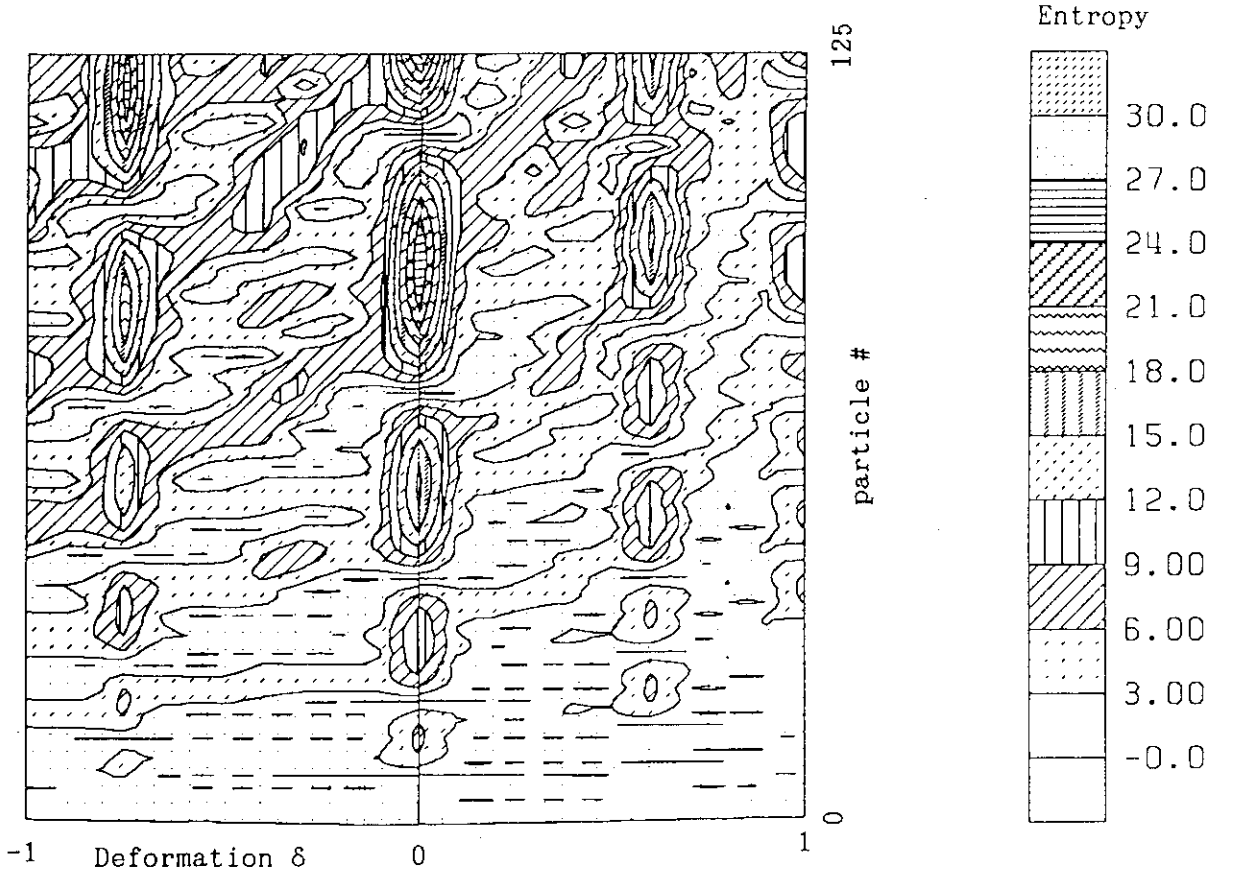

Fig.7. The contour plot of the entropy S_N.

responds to some kind of the closed shell state. Since the entropy relates to the level density of the system, we can say also that Figs. 6 and 7 correspond to the level density distribution discussed by Strutinsky in the study of fission phenomena[9]. This point may be more clearly seen, if we treat the canonical ensemble in a Nilsson type potential. Such kind of study is now in progress.

Here we stress the advantage of this treatment in nuclear physics. We can treat the thermodynamical quantities of the nucleus in addition to the usual shell model calculation of nuclear levels and properties with this method. Also we can discuss both closed shell and middle of shell nuclei in a consistent manner, whilethe treatment by Strutinsky is not consistent in this sense. And then we can discuss the properties of the HX formed by medium and high energy heavy ion collisions.

I would like to express my sincere thanks to Professor M. Ishihara for his encouragement. Computational work has been performed with the FACOM M380 at INS and FACOM M380 at RIKEN.

References:

1. H.Sato, *Phys.Rev.*C36 (1987) 785.
2. H.Sato, *Phys.Rev.*C36 (1987) 794.
3. R.Kubo, H.Ichimura, N.Hashizume, and T.Usui, in *Statistical Machanics* (North-Holland, Amsterdam, 1965), and in *Thermodynamics* (North-Holland, Amsterdam, 1968).
4. R.P.Feynman, in *Statistical Mechanics : A Set of Lectures* (Benjamin, Reading, Mass., 1972).
5. A.Bohr and B.Mottelson, in *Nuclear Structure* Vol.1 (Benjamin, New York, 1969).
6. E. Erba, U. Facchini, and E. Saetta-Menichella, *Nuovo Cimento* 22 (1961) 1237.
7. G. Nebbia et al., *Phys. Lett.* 176B (1986) 20.
8. W.Zickenddraht, *Phys.Rev.Lett.*54 (1985) 1906, and B. Castel, D.J.Rowe and L.Zamick, *Phys.Lett.*B236 (1990) 121.
9. V.M.Strutinsky, *Nucl.Phys.*A122 (1968) 1.

5.3 High Energy Fission

A. Iwamoto
Department of Physics, JAERI

Abstract: Nuclear fission which involves highly excited state of the nucleus is briefly reviewed. A special attention is given to the kinds of fission where the systematic data for the high-energy and high-angular momentum reactions are available.

1 Characteristics of High Energy Fission

We define the term "high-energy fission" as the fission which starts from the highly excited state of the compound nucleus. Highly excited state means not only with respect to energy but also with respect to the angular momentum. Therefore we can say that the characteristics are

- High Excitation Energy
- High angular momentum

The fission width is written as

$$\Gamma_f(w) \sim \frac{ckT}{2\pi} \exp\left(-\frac{B_f(L)}{kT}\right) . \tag{1}$$

The barrier height $B_f(L)$ depends on the angular momentum L in such a way that higher the L value, lower the barrier height becomes. This effect, together with the effect of temperature kT, causes the fission width larger for high energy fission. As a result, we can observe the fission even for the light compound nucleus. Fission barrier heights calculated for the light compound nuclei are shown in Fig.1. ref.[1]. Although no data is shown in this figure, there is evidence that the old liquid-drop model gives a poor result and finite range model gives a better results. For such light compound nuclei, the saddle shape is quite necked-in and for such shape, the surface energy formula of the old liquid-drop mode is not able to give a correct energy.

From microscopic point of view, an interest is how the shell correction energy which plays an important role in low energy fission phenomena changes as a function of the excitation energy. On this problem, a theoretical consideration of the shell correction energy was given ref.[2] long before but the confirmation by data is not well established. This is a very important problem especially for the production of the super-heavy element, because these nuclei are known to be stabilized dominantly by shell effect. By heavy-ion fusion experiment, for example, we start from a hot compound nucleus and the stability of the nucleus is quite sensitive to the temperature dependence of the shell correction energy.

2 High Energy Fission Caused by Various Light-Ion Reactions

Among various kinds of light-ion induced induces nuclear fission, following reactions are related to the term "high energy fission".

2.1 High energy hadron induced fission

There are data for high energy proton-induced fission but they are not enough systematic to be used for the detailed analysis of the basic fission mechanism. Another item is a low energy anti-proton induced fission. In this case, the pair annihilation produces almost 2 GeV of energy in a point in the nucleus with small total momentum. In this respect, it has a different feature compared to the high-energy proton-induced fission. In Fig.2,ref.[3], we show fission probability as a function of the system size parameter for anti-proton and proton-induced reactions. From this figure, the data for anti-proton resemble those of the high energy proton-induced fission as far as the fission probability is concerned.

2.2 Pion induced fission

When the nucleus is hit by the pion, various kinds of nuclear reaction occur. One of the most important reaction is the resonant capture process in which pion and nucleons form a resonant state like Δ particle first and then it interacts with other nucleon to form a system of excited nucleons. Such kind of state can be an initial stage of pion-induced nuclear fission. We have some data for the process but they are not so systematic and the involved reaction mechanism might be rather complicated. Thus it is not easy to discuss the special mechanism of nuclear fission caused by the pion.

2.3 Muon induced fission

There are two important modes in the muon-induced nuclear fission; the prompt fission and the delayed fission. When muon is induced on target nucleus, mu-mesic atom is formed with some probability. Normally, the orbit of the captured muon is in some excited state at the beginning of the reaction. Then the muon makes transition to lower orbits. The excess energy freed by the transition can be balanced by the emission of the γ ray but the energy can also be transferred to the nuclear excitation to cause the nuclear fission. This is the case for the prompt fission caused by the muon-induced fission. Finally, the muon is captured in the lowest orbit, i.e., the ground state orbit of the mu-mesic atom. The next process is the capture of the muon by the nucleus through weak interaction between muon and nucleons. When this reaction happens, some energy is converted to the kinetic energy of the nucleon produced in the process in addition to the emission of the neutrino. One typical process is

$$\mu^- + p \rightarrow n + \nu_\mu \ , \tag{2}$$

where the neutron acquires some kinetic energy which can be converted to the nuclear excitation energy to cause nuclear fission. This type of fission is called as delayed fission.

In Fig.3, we show the time spectrum of the fission phenomena for the mu-mesic atom of ^{238}U ref.[4]. In this figure, the first rapid increase of the yield and related bump correspond to the prompt fission and the following gradual decrease of the yield corresponds to the delayed fission. The decomposition of the components are shown by a solid line and a dashed line. A clear separation of two components is seen in the figure.

In prompt fission experiments, an interesting results is the relative sticking probability of the muon to heavy or light fission fragments after the scission ref.[3]. This probability should reflect the fission reaction mechanism, for example, how rapidly the fission process proceed from saddle to scission. With the comparison to a suitable theoretical model, we may get information for such transient state during the reaction.

3 High Energy Fission Caused by Heavy-Ion Reactions

Among various kinds of heavy-ion induced fission, I will treat two items which are rather closely related to the characteristic of high energy fission

3.1 Fast fission

For the fission following the high energy heavy-ion fusion reaction, some deviation from the low energy fission was observed. First it was pointed out that the fragment mass distribution becomes somewhat broader when the incident energy exceeds a certain value. The value was thought to be related to an angular momentum value above which some deviation from the standard fission model happens. The observed broadening of the mass distribution, however, was not very distinct and we had to wait some other indications. A clearer effect was observed later in the angular distribution data ref.[5]. Following the transient state model of Aage Bohr, the fragment angular distribution is determined by the shape of the nucleus at its saddle point and the temperature. For low energy fission, this model works well. When the projectile is rather heavy in the fusion-fission reaction, however, a deviation of the angular distribution from the transient state model occurs. The deformation of the saddle point obtained by fitting the angular distribution data by the model calculation is much larger than the shape calculated by the finite-range model. Such deviation does not occur when the mass of the projectile is light. Several consideration was given to the reason for it. A convincing argument is that because of the difference of the fusion potential surface and the fission one, a mismatch may happen when the projectile is heavy. In that case, even though the projectile and the target is trapped by the fusion potential barrier, it is outside of the fission saddle point and can be reemitted outside without reaching to the fission barrier. This is a typical model to explain the fast fission but it is not easy to check the validity of the model exclusively.

3.2 Transient effect

For the fission width expression from an excited parent nuclei, the formula given in eq. 1 is usually used. From the similar consideration, we can get a formula for the width of

neutron evaporation Γ_n, with which we can calculate the quantity

$$\frac{\Gamma_n}{\Gamma_f} = \frac{4kTmR^2}{\hbar^2}\exp[(B_f - B_n)/kT] \ , \tag{3}$$

where m is a neutron mass, kT is a temperature and B_n is the neutron separation energy. This eq. 3 gives a rough estimate of the number of neutrons emitted par one fission event, that is, the neutron multiplicity. In the realistic calculation of neutron multiplicity, Monte Carlo method is adopted by using the width expressions given in eq. 1 and eq. 3. Comparison was made between the data and statistical model calculations and some typical difference was observed when the excitation energy of the compound nucleus is increased. It is shown in Fig.4 ref.[6] where the pre-fission neutron multiplicity is plotted as a function of the excitation energy of the compound nucleus. From this figure, it is clear that at higher excitation energy, simple statistical model fails. To understand this anomaly, many theoretical works have been done and a promising idea among them is that it takes some time before the fission width reaches an asymptotic value like the one given in eq .1. This delay time is composed of two components, one is the transient time and the other is the saddle-to-scission time. During this delay time, a fission is suppressed while the neutron emission takes place normally. As a result, the neutron multiplicity increases. The reason why the deviation becomes clear when compound nucleus is highly excited is explained in the following way. The delay time is almost independent of the excitation energy while the average fission life-time decreases rapidly with the excitation energy. Thus at high energy, the delay time becomes comparable to the fission life-time and the effect of the delay becomes visible. On the other hand, at low excitation energy, the fission life-time is too long compared to the delay time and the effect of delay is no more visible. Theoretical works along this line have been done extensively in recent years based on Fokker-Planck equation ref.[7], Langevin equation and other models. Up to now, however, several problems remain in this interpretation and the phenomena is not understood completely. One of the problem is the charged-particle multiplicity data which contradict somewhat with the neutron data ref.[8].

References

[1] A. J. Sierk, Phys. Rev. **C33** (1986), 2039.

[2] A. Bohr and B. R. Mottelson, "Nuclear Structure",vol. 2 (Benjamin, 1975).

[3] S. Polikanov, Nucl. Phys. **A502** (1989), 195c.

[4] D. Chultem et al., Nucl. Phys. **A247** (1975), 452.

[5] B. B. Back et al., Phys. Rev. **C32** (1986), 195.

[6] H. J. Hinde et al., Nucl. Phys. **A452** (1986), 550.

[7] P. Grange et al., Phys. Rev. **C34** (1986), 209.

[8] H. Ikezoe et al., Phys. Rev. **C42** (1990), 342.

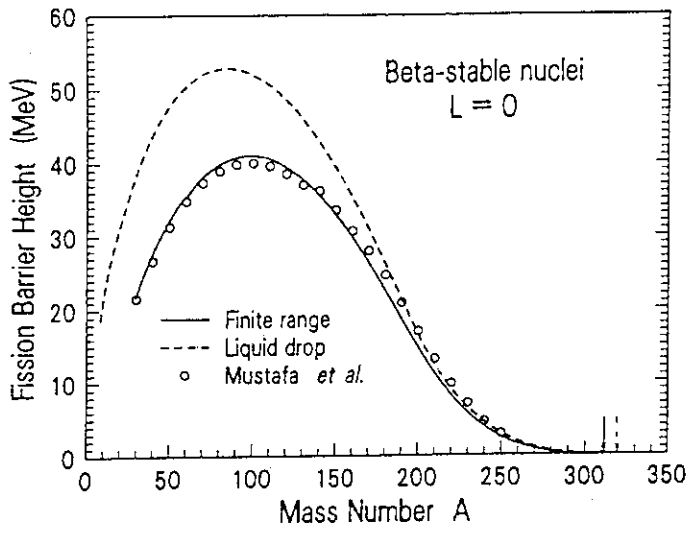

Fig.1 Calculated fission barrier heights as a function of the mass numbers of the compound nucleus, from ref.[1].

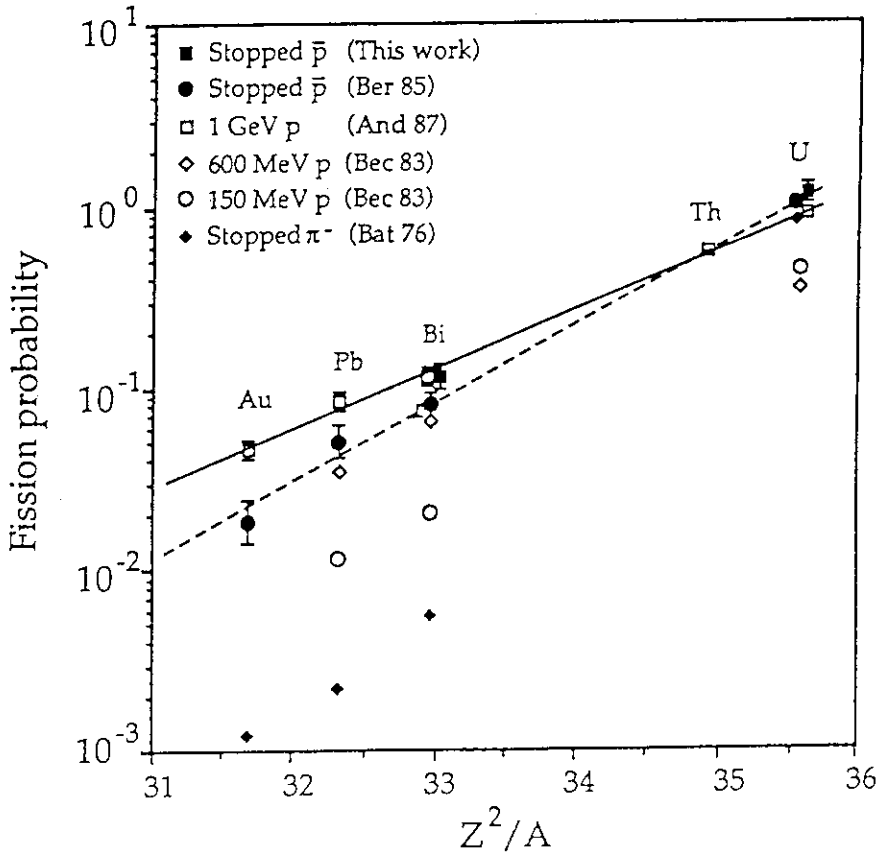

Fig.2 Fission probability as a function of Z_2/A, from ref.[3].

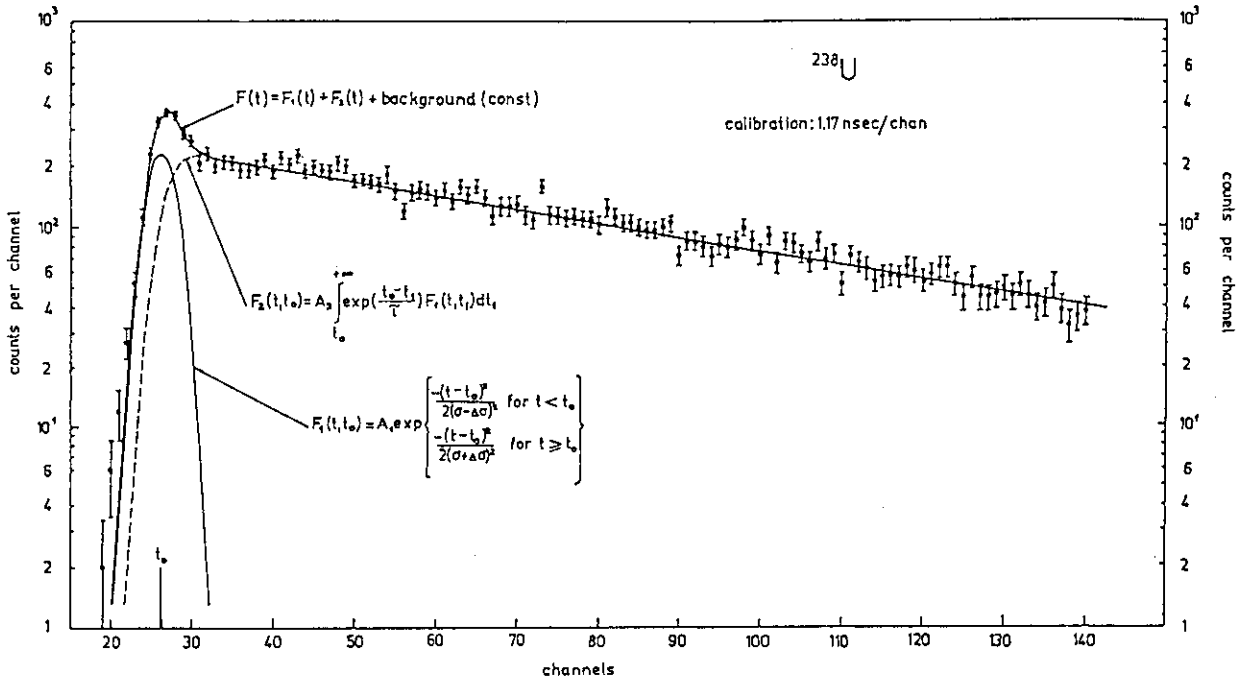

Fig.3 Fission yield from the mu-mesic atom of ^{238}U as a function of time, from ref.[4].

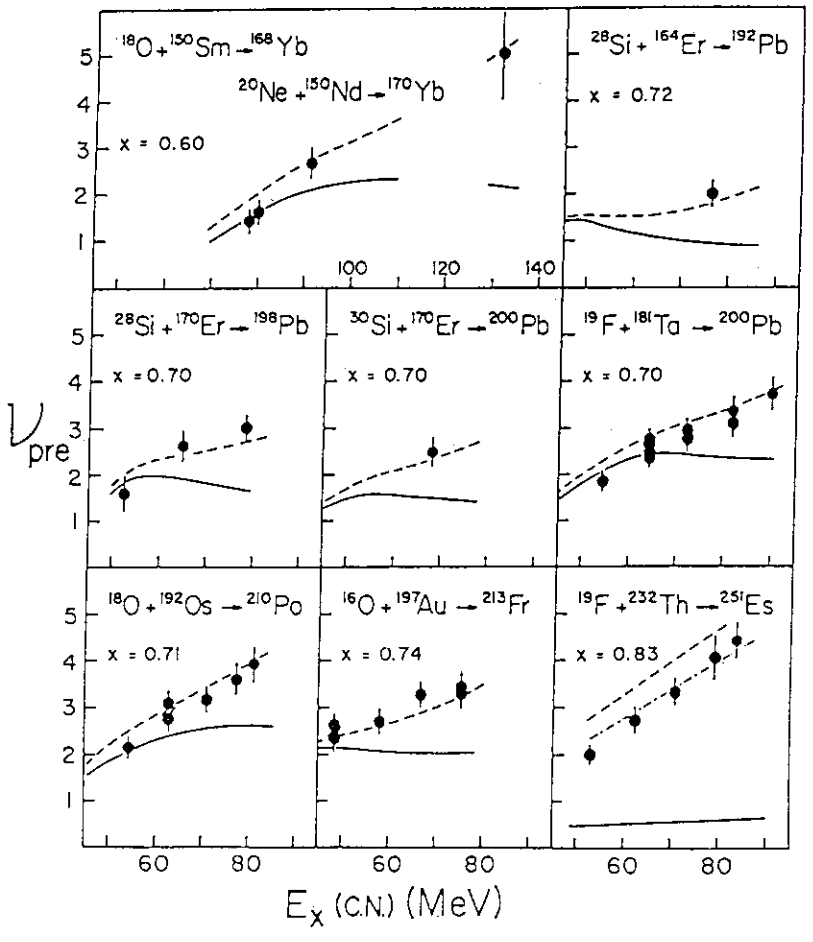

Fig.4 Pre-fission neutron multiplicity as a function of the excitation energy of the compound nucleus, from ref.[6]. Lines are statistical model calculations for different level density parameters.

6.1 Phenomenological Nucleon-Nucleon Potential

S. Morioka
Technology Development Division
CRC Research Institute Inc.
1-3-D17, Nakase, Chiba-shi, Japan 261-01

Abstract: The present situation of the nucleon-nucleon problems and the essential points concerning the one-boson-exchange model and the Paris potential are briefly reviewed. The extension of the nucleon-nucleon potential up to 2.5 GeV is discussed, and our recent phenomenological method for this extension is explained. Some of the successful results obtained by this phenomenological method are also shown.

1. Introduction

The present situation concerning the nucleon-nucleon (NN) problems up to the nucleon kinematic energy in the laboratory system $T_L \sim 1$ GeV is as follows: Below the π-production threshold energy ($T_L \sim 0.3$ GeV), there exist a large amount of experimental data on NN scattering to obtain good phase-shift analyses for both of proton-proton (pp) and neutron-proton (np) scatterings. Thus the NN potentials which accurately describe these data have been nearly established.[1~3] On the other hand above the π-production threshold energy the amount of NN (especially np) experimental data decrease as the energy increases, and theoretical approaches in these energy regions become very complicated since they involve few-body problem[4]. Nevertheless some attempts[5,6] to obtain a practical NN potential which describes some of the NN data in these energy regions were made, but have not completed yet.

In the present note, we would like to explain our recent method[7] to obtain a practical NN potential which is capable to describe the NN data above the π-production threshold energy, and even in the 2π-production energy region, namely up to $T_L \sim 2.5$ GeV. In order to do so let us briefly go through the two standard approaches to get the NN potential, namely the one-boson-exchange model[1,3,8] and the Paris potential[2,9] in the next subsequent sections.

2. The One-Boson-Exchange Model

The one-boson-exchange (OBE) model was originally proposed by the group[8] who calculated the Born terms of the perturbative series (see Fig.1) employing several exchange-bosons. These bosons are π, ρ, ω, a fictitious scalar boson σ, and other heavier bosons. The fictitious σ represents partly the scalar part of the 2π-exchange contribution of the perturbative series.[8]

In general the NN amplitude thus obtained (M_B) is pure real, so that one employs the K-matrix method,

$$S_{lJ} = \frac{1 + i\alpha_{lJ}/2}{1 - i\alpha_{lJ}/2} \tag{1}$$

to evaluate the NN phase shifts δ_{lJ},

$$S_{lJ} = e^{i2\delta_{lJ}}, \tag{2}$$

for uncoupled states (othewise see Ref. 8), where l and J are the angular momentum and the total spin-angular momentum respectively. α_{lJ} are the NN amplitude decomposed by the partial waves.

The NN potential V conventionally expressed by the argument of the internucleon distance $\boldsymbol{r}$ is obtained by the Fourier transformation of the NN amplitude as

$$V(\boldsymbol{r}) = \frac{1}{(2\pi)^3} \int d\boldsymbol{q} e^{i\boldsymbol{q}\cdot\boldsymbol{r}} M_B(\boldsymbol{q}), \tag{3}$$

in the simple case where the NN amplitude has only one variable $\boldsymbol{q}$ (usually the NN relative momentum). The OBE model gives the outline of the NN potential as follows: In the region $r > 2fm$ (R1), the one-pion-exchange contribution dominates. In the region $1fm < r < 2fm$ (R2), the contribution from the fictitious scalar boson is important. In the region $r < 1fm$ (R3), the ω contribution gives the repulsive NN force (see Fig.2).

Introducing phenomenological vertex form-factors for the bosons, and hence with about 10 parameters the model has been improved to highly realistic level[1,3] capable to describe about 3000 experimental pp and np data.

3. The Paris Potential

As mentioned above, the OBE model introduces the fictitious boson σ which partly represents the 2π-exchange contribution. Thus the "2π pseudo" bosons such as ρ and σ may be replaced by evaluating the 2π-exchange diagrams of the perturbative series. The dispersion relation is succesfully applied[9,10] to evaluate the 2π-exchange contribution.

The detailed argument can be found in the adequate literatures, and hence we give here the essence of this approach.

The NN amplitude of the 2π-exchange contribution is basically written in the following form by the dispersion relation:

$$M^{2\pi}(w,t) = \frac{1}{\pi^2} \int_{4m_\pi^2}^{\infty} \frac{dt'}{t'-t-i\epsilon} \int_{4M^2}^{\infty} \frac{dw'}{w'-w-i\epsilon}\, y(w',t'), \tag{4}$$

with

$$y(w,t) = \int ds'ds" F_{kin}(w,t,s',s") f_{\pi N}^{A}(s',t) f_{\pi N}^{A}(s",t), \tag{5}$$

where m_π and M are the masses of π and nucleon respectively. F_{kin} is the function of the kinematics $w = (N_1+N_2)^2, t = (N_1'-N_2)^2$ where N_1 and N_2 are nucleon four-momenta, and s the total energy of the πN channel (see Fig.3). The imaginary part of the πN amplitude is indicated by $f_{\pi N}^{A}$. Therefore by knowing the πN amplitude one can calculate the NN amplitude of the 2π-exchange contribution without any free parameters.

The Paris group estimated the 2π-exchange contribution given by Eq.(4) in addition to the Born terms (M_B) of only π- and ω-exchange contributions. Thus it is sometimes called as the $(\pi + 2\pi + \omega)$ model. Usually the imaginary part of $M^{2\pi}$ is ignored, and hence the total amplitude of the $(\pi + 2\pi + \omega)$ model is pure real. The conventional NN potential $V(\boldsymbol{r})$ is then similarly obtained by Eq.(3) replaced by $M_B \rightarrow M_B + M^{2\pi}$. In this way the original Paris potential[9] was obtained numerically, and later it was parametrized by superposing the Yukawa-type potentials as

$$V(r) = \sum_{j=1}^{n} g_j F(m_j r) \frac{e^{-m_j r}}{m_j r}, \tag{6}$$

where $F(m_j r) = 1, n = 24$ for central potential (otherwise see Ref.2), and g_j and m_j are free parameters. These parameters (about 300) are determined by χ^2 search examing about 3150 experimental pp and np data, but not to deviate from the original Paris potential in the regions of R1 and R2.

4. The Optical Potential

Above the π-production threshold energy, the NN potential must be complex,

$$V = V_R + iV_I, \tag{7}$$

where V_R and V_I are real, so that the inelastic NN processes can be described. Thus V_I must be zero below the π-production threshold energy. As for V_R we may employ the established NN potentials such as the OBE model[1] or the Paris potential[2]. On the other hand we do not have any established ones for V_I. We would like to mention about the atempt[6] of the Paris group to obtain V_I, on which our method is mainly based.

Recalling the dispersion relation (4), the NN amplitude of 2π-exchange contribution is decomposed into real and imaginary parts:

$$M^{2\pi}(w,t) = M_R^{2\pi}(w,t) + iM_I^{2\pi}(w,t). \tag{8}$$

As mentioned previously, the imaginary part $M_I^{2\pi}$ has been ignored in the $(\pi + 2\pi + \omega)$ model. Here we regard this $M_I^{2\pi}$ to contribute to V_I instead. Employing the K-matrix method with the total NN amplitude whose real and imaginary parts are calculated respectively by the Paris potential and by $M_I^{2\pi}$ given by Eq.(8), the Paris group evaluated NN inelasticity parameters, and pp and np inelastic cross sections. They found that the 1-blob and 2-blob diagrams as shown by Fig.3 contribute dominantly to describe the inelastic cross sections in the regions $T_L = 0.4 \sim 1$ GeV and $1 \sim 2.5$ GeV respectively. In fact the $N\Delta$ [the 33 resonance $(J = I = 3/2)$] and $\Delta\Delta$ intermediate states enhance in the calculations of the 1-blob and 2-blob diagrams respectively. The $\Delta\Delta$ intermediate state contributes to the $I = 0$ states, so that the calculation predicts a clear structure in the np inelastic cross sections caused by the $N\Delta$ and $\Delta\Delta$ intermediate states (see Fig.4).

Now the next task is to obtain a parametrization of $M_I^{2\pi}$ by superposing the Yukawa-type potentials in the similar way previously mentioned. This procedure is very difficult since $M_I^{2\pi}$ is highly energy dependent so that the parameters g_j should involve energy arguments. We recently presented[7] a phenomenological method to parametrize both of the real and imaginary parts of the NN total amplitude associated with the resonance behaviour caused by the $N\Delta$ intermediate state as

$$\alpha_{lJ}^{ph} = N(E)\sum_{l'}(g_{lJ}\frac{E-E_\pi}{E+E_\pi})^{l'+1/2}\frac{\{\xi_{lJ}(E-E_\Delta)+i\Gamma_{lJ}/2\}M}{(E-E_\Delta)^2+\Gamma_{lJ}^2/4}\,Q_l(x), \tag{9}$$

$$x = 1 + \mu^2/2p^2, \tag{10}$$

where $N(E)$ is a trivial kinematical factor $(E+M)^2/2pE$, E and p are the incident nucleon energy and momentum respectively, E_π and E_Δ the threshold energies of π and Δ productions respectively. Q_l is the Legendre function of the second kind. g_{lJ}, ξ_{lJ} and Γ_{lJ} are our parameters to seek by χ^2 fitting to the empirical phase and inelasticity parameters[11].

l' are possible angular momenta[12] of the $N\Delta$ system which is described by 2π-exchange diagram. We take thus $\mu = 2m_\pi$. The threshold behaviour of Eq.(9) is required of a quasi two-body channel. Employing the obtained parameters given in the Tables 1 and 2, some of our obtained results[7] are shown in Figs. 5 and 6. The detail of this method and the results can be found in Ref. 7

5. Summary

Let us summarize our procedure to obtain the phenomenological NN potential up to $T_L \sim 2.5$ GeV as follows: Firstly in the K-matrix method, we seek parameters in our phenomenological amplitudes given by Eq.(9) by examing the empirical phase and inelasticity parameters in the π production energy region, and further by examing the theoretical results[6] obtained by the Paris group for the energy region of 2π productions. Then solving the Thompson equation[13] (a relativistic integral equation), we refine the parameters, which leads to a NN phenomenological potential in momentum representation.

From our phenomenological potential thus obtained, we can evaluate the following NN physical observables up to $T_L \sim 2.5$ GeV:

1. The scattering differential cross sections,
2. The inelastic differential cross sections,
3. The total scattering cross sections,
4. The total inelastic cross sections,
5. The total cross sections,

and furthermore various nuclear phenomena which essentially require NN potentials.

Acknowledgement

The author would like to appreciate useful discussions with Dr. T. Ueda, Dr. H. Kadotani and the Paris-potential research group at l'IPN d'Orsay.

References

1. T. Ueda, F.E. Riewe and A.E.S. Green, Phys. Rev. **C17** 1763 (1978).
   T. Ueda and A.E.S. Green, Phys. Rev. **C18** 337 (1978).
2. M. Lacombe, B. Loiseau, J.M. Richard, R. Vinh Mau, J. Côté, P.Pirès and R. de Tourreil, Phys. Rev. **C21** 861(1980).
3. R. Machleidt, K. Holinde and Ch. Elstern, Phys. Rep. **149** 1 (1987).
4. T. Ueda, Nucl. Phys. **A463** 69c (1987), and references cited therein.
5. T. Ueda, M.L. Nack and A.E.S. Green, Phys. Rev. **C8** 2061 (1973).
6. M. Lacombe, B. Loiseau, S. Morioka and R. Vinh Mau, in Book of Abstracts Vol.1 of Int. Conf. on Particles and Nuclei, 1984, Heidelberg, Germany (Edited by F. Güttner et al.), p.C10, Springer-Verlag.
   B. Loiseau, Journal de Physique, Colloque C2, supplément au n°2, Tome 46, février (1985) p.C2-339.
7. S. Morioka, T. Ueda and H. Kadotani, to be published in the Proceedings on Nuclear Data for Science and Technology at Jülich, Germany in May 1991.
8. S. Sawada, T. Ueda, W. Watari and M. Yonezawa, Prog. Theor. Phys. **28** 991 (1962); **32** 380 (1964), S. Ogawa et al., Prog. Theor. Phys. Supple, No.39, 140 (1967).
9. W.N. Cottingham, M. Lacombe, B. Loiseau, J.M. Richard and R. Vinh Mau, Phys. Rev. **D8** 800 (1973).
10. S. Furuich, Prog. Theor. Phys. Supple, No.39, 190 (1967).
11. R. A. Arndt, J.S. Hyslop III and L. David Roper, Phys. Rev. **D35** 128 (1987).
12. S. Mandelstam, Proc. Roy. Soc. (London) **A244** 491 (1958).
13. R.H. Thompson, Phys. Rev. **D1** 110 (1970).
14. J. Bystricky and F. Lehar, Physics Data 11-1, Karlsruhe (1978).
    F. Shimizu, Y. Kubota, H. Koiso, F. Sai, S. Sakamoto and S.S. Yamamoto, Nucl. Phys. **A386** 571 (1982).

Table 1 OBEM parameters.

Boson	Mass (MeV)		Coupling constant	Damping factor Ω(MeV) Ref.1
π	138.7		13.8	x
ρ	759.1		0.82	3250
		(f/g)	-2.40	
ω	782.8		9.00	3250
		(f/g)	0.11	
s	591.0		9.80	x

Table 2 Parameters for phenomenological amplitudes.

State	ξ	g	Γ(MeV)
$^3P_0$	0	17.7	722.1
$^3P_1$	0	0.12	92.6
$^3P_2$	0	6.60	276.1
$^1D_2$	-1.60	3.38	150.5
$^1G_4$	1.85	7.96	691.7
$^1I_6$	0.75	8.14	131.1
$^3F_2$	-9.60	0.51	174.0
$^3F_3$	-0.45	7.61	87.4
$^3F_4$	-0.43	5.25	128.3
$^3H_4$	0	0	x
$^3H_5$	1.51	8.78	334.1
$^3H_6$	0.30	7.55	69.2

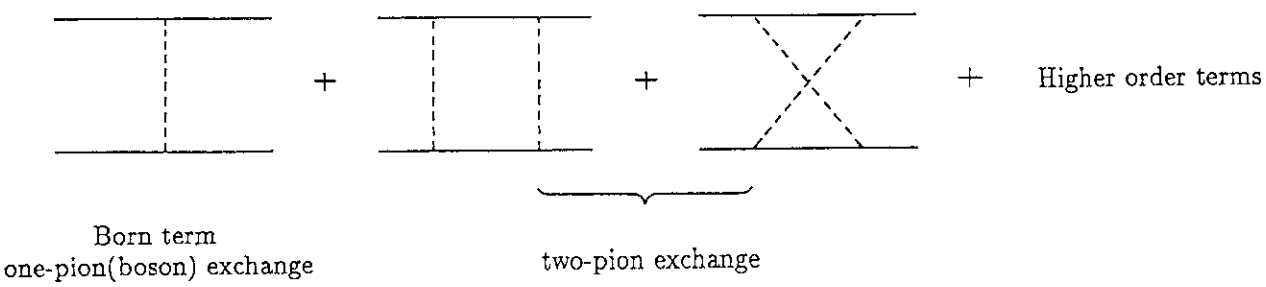

Fig.1 Perturbative series.

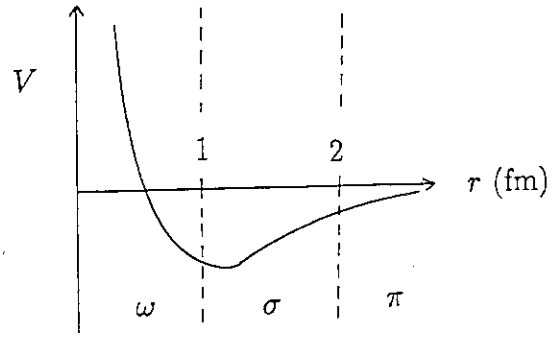

Fig.2 NN potential for $^1S_0$ state.

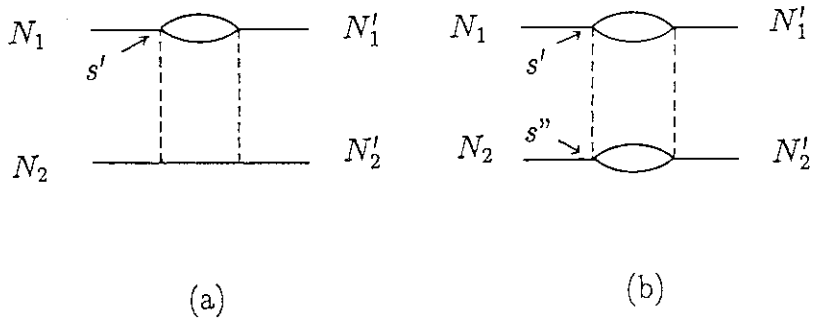

Fig.3 2π-exchange diagrams with πN blobs.
(a) 1-blob diagram. (b) 2-blob diagrams. The blobs represent the πN interaction without the nucleon-pole contribution. s' and $s"$ are the integral variables in the πN amplitude (see Eq.(5)).

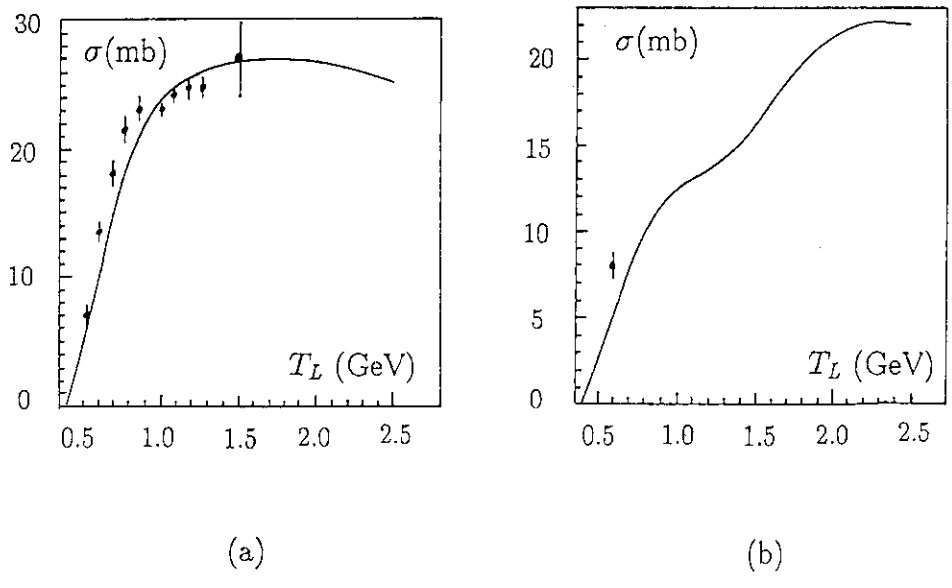

Fig.4 Numerical results[6] obtained by the Paris group.
(a) Inelastic pp cross sections. (b) Inelastic np cross sections. The broken curves correspond to 1-blob contribution, and the solid to the sum of 1- and 2-blob contributions. The experimental data are taken from Ref.14.

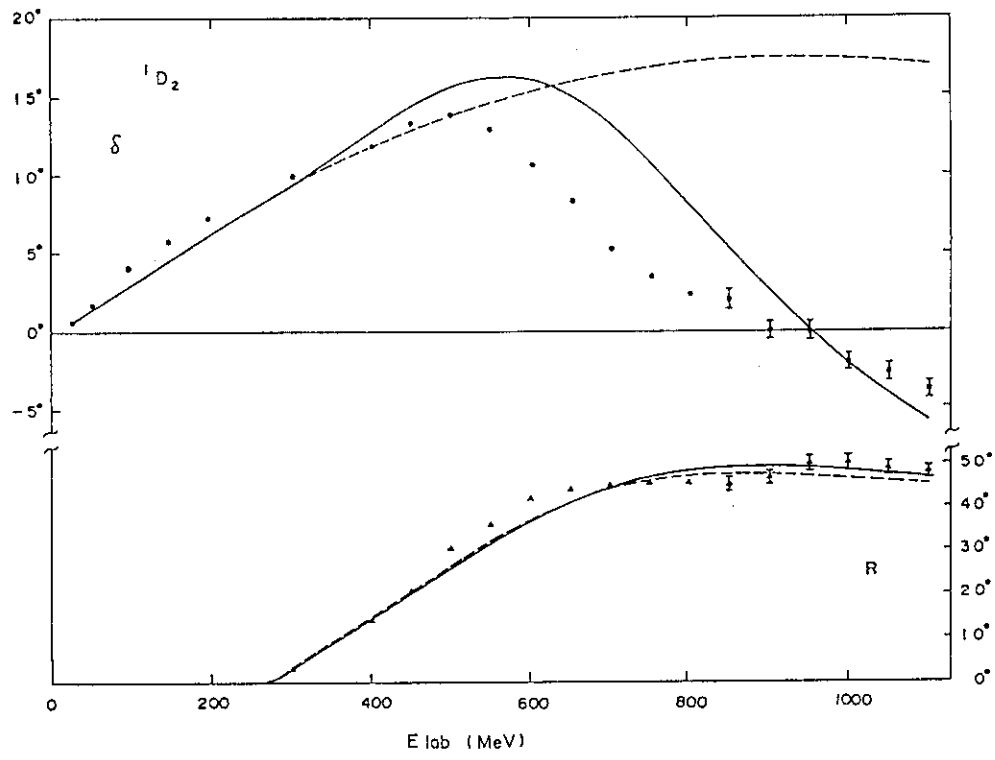

Fig.5 Phase (δ) and inelasticity ($R = cos^{-1}\eta$) parameters for $^1D_2$. Circles indicate the empirical ones[11]. Broken curves represent the contribution from the phenomenological amplitudes without the real part. Solid curves correspond to the total contributions.

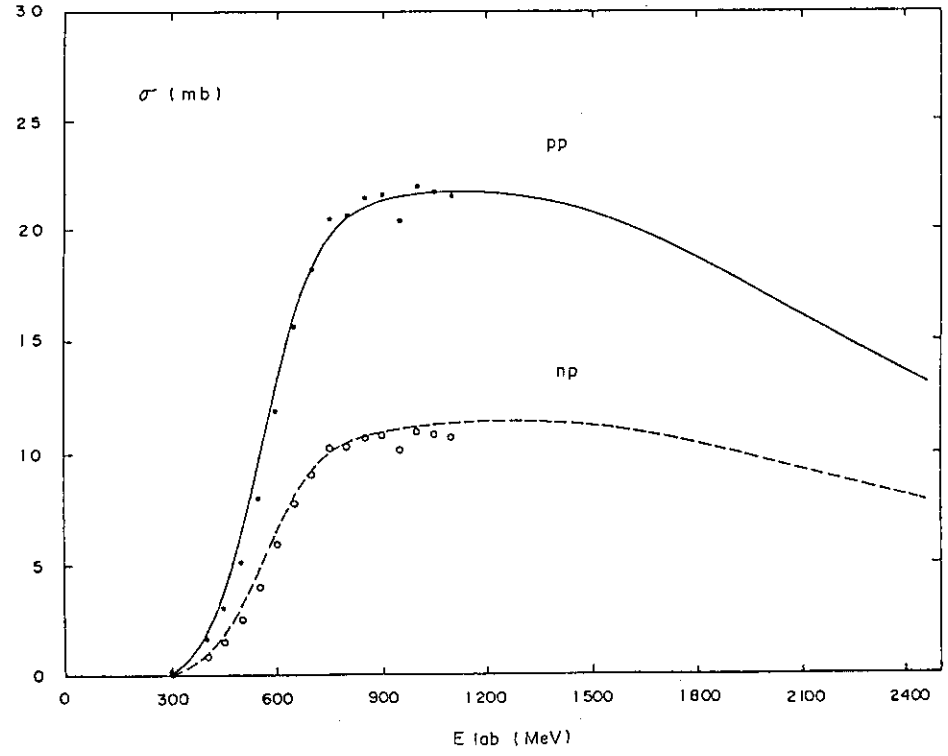

Fig.6 The inelastic total cross sections. Circles indicate the empirical ones[11]. Solid curves correspond to the present results.

6.2 Dynamical Simulation of Heavy Ion Collisions; VUU and QMD Method

KOJI NIITA

Department of Physics, JAERI

We review two simulation methods based on the Vlasov–Uehling–Uhlenbeck (VUU) equation and Quantum Molecular Dynamics (QMD), which are the most widely accepted theoretical framework for the description of intermediate–energy heavy–ion reactions. We show some results of the calculations and compare them with the experimental data.

1. Introduction

During the past decade a great development in heavy–ion collisions has been done both in experiments and in theory. One of the major aims of heavy–ion collisions in the energy regime from 20MeV/u to 2GeV/u is to obtain information about the nuclear equation of state (EOS) and strong interaction vertices at high nuclear density and/or high temperature far from the ground state [1–4]. Since the nuclear matter under such extreme conditions created during heavy–ion collisions is unstable and not uniform in time and space, the EOS cannot directly be extracted from experimental data. We thus need microscopic phase–space simulation to keep track of the nonequilibrium dynamics and the nucleon–nucleon collisional history, which determine the degree of thermalization.

In this report we review two simulation methods based on the Vlasov–Uehling–Uhlenbeck (VUU) equation [4–6] and Quantum Molecular Dynamics (QMD) [7,8], which are the most widely accepted theoretical framework nowaday for the description of intermediate–energy heavy–ion reactions. A lot of work has been done by these simulations up to now, and we will show some results of the calculations and compare them with the experimental data. We also discuss the limitation and applicability of these simulations, and what kind of observables can be described by VUU and QMD.

2. VUU and QMD Method

The most simple dynamical model for heavy–ion collisions is the cascade model, which describes intermediate–energy heavy–ion reactions by superposition of sequential incoherent nucleon–nucleon collisions. In the low energy regime, the mean field description like TDHF (Time–dependent Hartree–Fock) is effective, since

explicit nucleon–nucleon two–body collisions are suppressed very much by the Pauli principle. However, as energy increases, the effects of nucleon–nucleon collisions become important more and more. Thus the cascade model neglects the mean field contribution (some versions of the cascade code take into account the effect of the mean field phenomenologically in order to bound the nucleons into nucleus before two nuclei collide). Though the cascade model could reproduce a lot of experimental data, the systematic comparison with experimental data led to a new aspect of the transport theory for heavy–ion collisions.

Stock et al. [9] measured the multiplicity of π^- in the energy regime from 360 MeV/u to 1.8 GeV/u and compared them with the results of the cascade calculation done by Cugnon et al. [10]. They found the results of the cascade model always overestimate the experimental data, and conected the systematic deviation from the data to intrinsic compression energy which is not taken into account by the cascade model. Although this estimation depends on the model, it was the first time that the EOS of the nuclear matter at high density is extracted from the experimental data of heavy–ion collisions. After this analysis, the dynamical simulation including the mean field effect like VUU and QMD is widely used for the description of heavy–ion collisons.

2.1. VUU (Vlasov–Uehling–Uhlenbeck) equation

The most reliable theoretical framework nowadays for the description of intermediate energy heavy–ion reactions is based on the Vlasov–Uehling–Uhlenbeck (VUU) equation for the one–body phase–space distribution. This equation has originally been proposed by Nordheim in 1928 and later on by Uehling and Uhlenbeck for weakly interacting Fermion systems as an extension of the Boltzmann equation. While its derivation has commonly been based on perturbative arguments or 'plausibility' [4], it has been shown by Botermans and Malfliet [11] and Cassing et al. [12], that it may consistently be derived also in a nonperturbative framework.

VUU equation is given by

$$\left[\frac{\partial}{\partial t} + \frac{\mathbf{p}_1}{m} \frac{\partial}{\partial \mathbf{r}} - \frac{\partial}{\partial \mathbf{r}} U(\mathbf{r};t) \frac{\partial}{\partial \mathbf{p}_1} \right] f(\mathbf{r},\mathbf{p}_1;t) = \left[\frac{\partial f}{\partial t} \right]_{coll}$$

$$= \frac{4}{(2\pi)^3} \int\int d^3p_2\, d^3p_3 \int d\Omega\, |v_{12}| \frac{d\sigma}{d\Omega}(p_2-p_4)\, \delta(p_1+p_2-p_3-p_4)$$

$$\{f(\mathbf{r},\mathbf{p}_3;t)\, f(\mathbf{r},\mathbf{p}_4;t)\, [1-f(\mathbf{r},\mathbf{p}_1;t)]\, [1-f(\mathbf{r},\mathbf{p}_2;t)]$$

$$-f(\mathbf{r},\mathbf{p}_1;t)\, f(\mathbf{r},\mathbf{p}_2;t)\, [1-f(\mathbf{r},\mathbf{p}_3;t)]\, [1-f(\mathbf{r},\mathbf{p}_4;t)]\} \qquad (1)$$

where $U(r;t)$ is the time–dependent mean field and $d\sigma/d\Omega$ denotes the nucleon–nucleon cross section in medium, while $|v_{12}|$ is the relative velocity of the colliding nucleons. This equation describes the time evolution of the one–body distribution function $f(r,p;t)$ in the phase–space. The left hand side of eq.(1) is called Vlasov term, which determines the time evolution under the self–consistent mean field $U(r;t)$, while the right hand side is called the collision term, which describes the incoherent on–shell NN collisions taking into account the final–state Pauli–blocking factors. If the righ–hand side equals to zero, the Vlasov term just corresponds to a classical limit of the TDHF equation. The physical quantities which determine the dynamics in the VUU equation are thus the time–dependent mean field $U(r;t)$ and NN cross section in medium $d\sigma/d\Omega$. Usually these two quantities are independently parametrized, while on the level of a more fundamental transport theory they are related to each other and can, in principle, both be extracted from the bare NN interaction within the framework of many–body theory.

In the time–dependent G–matrix theory (TDGMT) [12], these two quantities are given in terms of the G–matrix,

$$U(r,t) = \int d^3r' \; \mathrm{Re}\{G_a(r-r')\} \; \rho(r',t), \tag{2}$$

$$\frac{d\sigma}{d\Omega}(q) = \frac{m^2}{16\pi^2\hbar^4} \; G(q) \; G_a^{\dagger}(q). \tag{3}$$

where $\rho(r,t)$ denotes the local density summed over spin and isospin, and q the momentum transfer in the nucleon–nucleon collision. In eq.(2) and (3), the suffix "a" denotes that antisymmetrization effects are already included in G_a. G–matrix is given by

$$G(E) = v + v \; g_{12}(E) \; Q_{12} \; G(E), \tag{4}$$

where v is the bare interaction, g_{12} is the in–medium two–nucleon propagator and Q_{12} denotes the Pauli–blocking operator for intermediate states, while E is the energy of two nucleons in the medium. If we solve the VUU equation (1) coupled with G–matrix equation (4) for each configuration in phase space determined by VUU, one could get a complete transpot theory without any parameters except for the bare NN interaction. It is, however, still out of scope even in the fastest computer. Moreover, our knowledge about the G–matrix for the high temperature and/or high density nuclear matter is too poor to handle. Therefore we have employed a local density–dependent parametrization for G as a first step of the consistet treatment of VUU in terms of G–matrix, and analized the deeply inelastic heavy–ion collisions

[13] and high energy photon production [14].

We solve the VUU equation (1) by means of the test–particle method [4,5], where the smooth and continued phase–space function f(r,p;t) is evaluated by the sum of the finite number of the delta–function or gaussian wave packet as in the following,

$$f(\mathbf{r},\mathbf{p};t) = \frac{1}{N}\sum_{i=1}^{NA} \frac{1}{(\Delta_r\Delta_p)^3} \exp\left[-\frac{1}{2}\left\{ \left(\frac{\mathbf{r}-\mathbf{r}_i}{\Delta_r}\right)^2 + \left(\frac{\mathbf{p}-\mathbf{p}_i}{\Delta_p}\right)^2 \right\} \right] \tag{5}$$

where A is the total mass number and N denotes the number of test particle per nucleon.

The test particle propagates classically between collisions according to Hamilton's equation,

$$\dot{\mathbf{p}}_i = -\nabla_r U(\mathbf{r}_i;t), \qquad \dot{\mathbf{r}}_i = \mathbf{p}_i / (m_i^2 + \mathbf{p}_i^2)^{1/2} \tag{6}$$

where $\mathbf{r}_i$ and $\mathbf{p}_i$ are the centroidal values of the coordinate and momentum of the individual test particles. The collision criterion for test particles within same ensemble is close to that used in cascade simulations and is based on the minimum–distance concept, which states that two nucleons can collide only if their distance fulfills the relation

$$|\mathbf{r}_1-\mathbf{r}_2|_{min} \le (\sigma_{NN}(\sqrt{s}) / \pi)^{1/2} \tag{7}$$

Furthermore, a collision actually takes place only if the final–state phase–space factor fulfills the following condition

$$\{1-f(\mathbf{r},\mathbf{p}_3;t)\}\{1-f(\mathbf{r},\mathbf{p}_4;t)\} \ge x \tag{8}$$

where x is a random number in the interval between 0 to 1. More detail about the numerical realization as well as about the cross sections can be found in refs. [4,5].

Here we discuss some features of the VUU simulation and what kind of observables can be treated by VUU. In general, an important point of the analysis by making use of the transport theory like VUU is how to extract the basic physical quantities from the actual numerical simulation. If there are a lot of input parameters, it is very difficult to get a definite physical conclusion from the numerical simulations. Sometimes the experimental data, particularly inclusive data, can be reproduced by different models based on very different assumptions. Since the VUU equation has following features compared to the other kinetic models, it is the most reliable theoretical framework nowadays for the description of intermediate energy heavy–ion reactions. First, the VUU type equation has been derived within a nunperturbative framework. Therefore the physical meanings of the input quantities are very clear, and one can avoid double counting of interactions. Second, the assumptions and

approximations introduced in the derivation of VUU type equation have been checked in detail [12,14]. Third, all ingredients of VUU are consistently characterized by the basic quantity in nuclear physics i.e. G–matrix. On the other hand, one of the week point of VUU type equation is that it is limited to the described one–body observables only. This means that VUU approach cannot address the multifragmentation, since the fragmentation process involves many–body correlations. As a N–body daynamics, "Quantum Molecular Dynamics" [7], therefore, has been proposed in order to describe the maltifragmentation and some observables concerning to the fluctuations, which also cannot be addressed by VUU.

2.2. QMD (Quantum Molecular Dynamics)

A large number of models has been introduced to describe the mass distribution of the fragmentation. Most of these model assume statistical feature in the fragment formation process, thus neglecting completely the dynamical evolution of the collisions. Other approaches use a simplified model for the dynamics of the expansion. They cannot treat the early stage of the reaction and start from assumptions about the configuration at the state of highest density. Some of them emphasize the role of the fluctuations for fragment formation. As mentioned before, VUU is not able to treat the fragmentation.

Aichelin and Stocker [7] thus proposed a novel N–body approach to discribe heavy ion collision based on the classical "molecular dynamics" (MD). They combined the advantages of the classical molecular dynamics approach (explicit two–body interaction) with the important quantum features, which are essential to describe the reaction dynamics properly as well known in the VUU calculations. In their model each nucleon is represented by a gaussian Wigner density in momentum and coordinate space, and propagates accordingly to Hamilton's equation of motion with finite range nucleon–nucleon potential, which are adjusted to give reasonable NN scattering cross sections and nuclear binding properties. The effective interactions actually used in QMD calculations so far are almost same as that employed in VUU simulations, e.g. Skyrme type interaction. The collision criterion for test particles (gaussian wave packets in this case) is same as in VUU, and the final blocking factors are also checked by (1–f)(1–f). This is a reason that they dubbed this approach "quantum molecular dynamics", QMD, to distinguish it from the purely classical "molecular dynamics" methods well known in the literature.

In the QMD approach, the phase space factor f(r,p;t) is calculated by the same expression as eq.(5) in the VUU approach except for the number of the test particle per nucleon N, which is just one in this case. Therefore, roughly speaking, VUU

approach with one test particle per nucleon leads to QMD model in a sense of the actual calculations. However these two models are quite different each other in the theoretical framework on which they are standing. VUU approach is essentially one–body theory with taking the effects of the incoherent two–body collisions, while QMD is a N–body approach. Thus QMD can treat N–body correlations and the fluctuations caused by the two–body collisions, which are washed out by the mean field description in VUU. Due to the large fluctuation it was difficult to construct numerically the stable ground state. Recently Ohnishi et al. [15] resolved this problem by introducing a cooling method for construction of the initial ground state. So far a lot of phenomena of the intermediate heavy ion collisions has been analyzed by QMD simulations, e.g. fragmentation, particle production and sideward flow [7,8,15].

3. Comparison of theory and experiment

3.1. p–like cross section and transverse flow

So far several groups have developed transport models of VUU and QMD type. While most of these transport models can fit the final baryon distribution e.g. p–like cross section and flow (transverse momentum as a function of the rapidity), the form of U or the effective interaction that leads to the best fit of the data differs substantially from one model to the next. These differences are due to differences in the dynamical implimentation of Pauli blocking and binding effects, the momentum dependence of U, and differences between numerical techniques. In order to clear this situation, Aichelin et al. [16] compared these models on the data of inclusive p–like cross section.

Fig.1 [16] shows the inclusive p–like data at laboratory angles 20, 40, and 60 on La+La at 800MeV/u [17] compared with the various calculations. The full line and dotted line denote momentum–independent VUU [18] and QMD [7,8] with incompressibility module K=380 MeV, which is an important quantity for the nuclear equation of motion. The dashed line shows the momentum–dependent BUU [19] with K=210MeV, while dot–dashed line is the relativistic RVU [20]. We can see from this figure the remarkable insensitivity of the results to variations in the nuclear equation of state (the values of the incompressibility modulus which varies by a factor 2 between the various medels) and to the details of the trasport models. In fact VUU, BUU, QMD, and RVU give results within 20% of the Cugnon cascade calculation [10]. However all models fail to reproduce the low–cross section yields at 20. This discrepancy may indicate the medium effects in high density nuclear matter, which have been not taken into account yet by these models.

Another baryon observable which is expected to be sensitive to the nuclear eqation of state is the transverse momentum as a function of the rapidity (flow). Aichelin also compared the transverse momentum calculated by the various models [21]. Fig.2 [21] shows the average transverse momentum as a function of the center of mass rapidity for different theories for the reactions 400 MeV/n Nb+Nb b=3fm. We see a striking similarity of the results of the one–body theories (VUU, BUU). This shows that the results are independent of the quite different numerical methods employed to solve this complicated VUU–type equation. The results of the QMD calculations agrees with that of the one body theories at central rapidity but are smaller around the beam rapidity. He pointed out that in this rapidity region there are very few nucleons, most of them bound in clusters, and the fluctuations are most important which are not treated correctly in the BUU/VUU model. The transverse flow was discussed as a good observable sensitive to the nuclear equation of motion. However, it has been shown that not only the incompressibility (EOS) but also the change of the NN cross section in medium affects the flow, furthermore the momentum dependence of the potential also change the flow. Therefore one needs to treat these input quantities (potential (EOS) and the NN cross section in medium) consistently in order to subtract the physical information from the flow observables.

3.2. Production of energetic particles

Average properties like deflection angles or transverse flow provide only integrated information about the reaction dynamics. On the other hand, light particle spectra for neutrons, protons, deutrons etc. carry information about the time evolution of the heavy–ion reaction. The "fastest" particles in central collisions are emitted from the early nonequilibrium stage of the reaction while "slow" nucleons are evaporated from the excited fragments during much longer time scales and provide some idea about the temperature of the exicited residual nuclei. In order to obtain a more precise clock of the reaction dynamics we need probes that are sensitive to the early stages of the reaction and not affected by the final (equilibrium) expansion phase. Such a clock may be provided by the emission of particles, which are not available as real particles in nuclei, and are strongly suppressed in the final stage of the reaction. One of the most promissing candidates for these probes are hard photons since they couple perturbatively to the nuclear current, are emitted with the velocity of light and experience little rescattering due to the weak electromagnetic interaction with protons. We have analyzed the hard photon production [5,14] and the dilepton production [22] in heavy ion collisions based on a transport equation of the VUU type.

Here we show another probes, which are sensitive to a specific phase space during the collisions, i.e. the subthreshold meson production [5,23]. In heavy ion collisions the meson production (π, η, K^+,...) are observed even far below the free nucleon–nucleon threshold. ("subthreshold" means the situation where the beam energy per nucleon is smaller than the free NN threshold to produce the mesons) One hopes to learn either about cooperative (coherent plus incoherent) nuclear phenomena or about high momentum components of the nuclear many–body wave function. By varying mesonic probes (π, η, K^+,...), one can study such problems in different energy regimes of heavy–ion collisions. For instance, subthreshold heavy meson (η, K^+) production provides knowledge on the production mechanism and also detailed information on the phase–space distribution of the collisions from 500 MeV/u to 1 GeV/u.

The simplest production mechanism of the mesons in subthreshold region is the Fermi motion in nucleus. If the beam momentum of colliding nucleons plus twice of the Fermi momentum is lager than the corresponding threshold momentum, the first chance NN collisions can produce the mesons. However, in more extreme low energy case where the first chance NN collisions cannot produce the mesons energetically, anather mechanisms are expected, collective phenomena or thermalization of the nuclear matter. To clear this situation we have studied the subthreshold η production base on a VUU simulation for the evolution of the nuclear phase space distribution and an incoherent production mechanism with free production rates [5,23].

Fig.3 shows the number of produced pions and η's at the two bombarding energies of 500 and 1000 MeV/u as a function of the total number of collisions n_1+n_2 that both participating nucleons have suffered before the production process. It is seen that at 500 MeV/u most of the nucleons that produce the η's have on average undergone a total number of 6–7 collisions prior to the actual particle production. Since about 3 collisions per nucleon are sufficient to establish thermal equilibrium for this energy regime, the η's are at this bombarding energy predominantly produced in a hot, thermalized collision zone. This is more clearly demonstrated in fig.4, where the source distribution in momentum space for η production is shown for the same system at 600 MeV/u. In contrast, the pions are still mainly created in the first NN collisions. We, furthermore, find that the η production rate closely tracks the density compression (ρ/ρ_0=2.5~3 at this energy). This makes subthreshold η's, produced at bombarding energis from about 500 to 800 MeV/u, an ideal probe for highly compressed, equilibrated nuclear matter, in contrast, for example, to pions, most of which are created in the first collisions when target and projectile nucleons are still well separated in momentum space. As new data of the subthreshold η production are

coming up in SIS–GSI, the detail comparison between our predictions and the experimental results will be soonly appeared.

We have also studied K^+ production in proton–nucleus and nucleus–nucleus collisions. We found [23] an excellent agreement with the data for p+A reaction (Fig.5). It indicates that kaons are produced by the secondary pion–nucleon inelastic scattering below 1 GeV. In nucleus–nucleus reactions, however, secondary $\pi N \rightarrow K^+ + \Lambda$ production plays a minor role and the K^+–yield is dominated by baryon–baryon production processes in the entire energy range. This shows that multiple nucleon–nucleon collisions, which equilibrate and broaden the momentum distribution, are the dominant dynamical effect for subthreshold K^+–production in nucleus–nucleus reactions. On the other hand, in the p–nucleus case, the high momentum components in the ground state and the secondary π–nucleon process become visible due to the lack of Fermi motion in the projectile and the smaller number of NN collisions in contrast.

For subthreshold pion production in the energy regime from 40 MeV/u to 200 MeV/u, the main dynamical difference as compared to the heavy mesons production, other than the difference of the meson–nucleon interaction, is the effect of the Pauli–blocking of the final states of nucleons after producing the pions. Below 80 MeV/u, initially the two boosted Fermi spheres of the ground state nuclei overlap in momentum space even before the two nuclei touch each other. If one employs the simple Fermi gas model and an incoherent production mechanism, the subthreshold π–yield is underestimated by loughly one–order of magnitude due to storong Pauli blocking effects. Therefore, the collective model and cooperative model have been proposed. However, as well known from TDHF calculations and kinetic simulations like VUU, the phase space distribution is drastically changed by dynamical effects in the first stage of the reacton. The main change is the appearance of an open phase space (so–called Pauli pocket) at the middle of phase space, which is very important for the final–state blocking in the case of particle production [5]. This open phase space, however, is rapidly filled by nucleon–nucleon collisions. This is one of the reason why the contributions from secondary and further multiple NN collisions to subthreshold pion production and hard–photon production are strongly supressed in this energy regime contrary to subthreshold heavy meson production mentioned above.

In fig.6 we compare the results of our calculation to the experimental π^0 data for the system $^{12}C+^{12}C$ at the incident beam energies of 60, 74 and 84 MeV/u [24] and for $^{40}Ar+^{40}Ca$ at 84 MeV/u [25]. For the latter case, the experimental data and our result are converted into the sytem $^{12}C+^{12}C$ using $(A_t A_p)^{2/3}$ scaling law for the

total cross section. In fig.6 the angle integrated cross section $d\sigma/dE$ is plotted as a function of the kinetic energy of the pion in the laboratory frame. The experimental data are represented by histgrams, and the full lines are the results of our calculation. One can find a remarkable agreement with the data in the total cross section and also in the energy spectra for the entire energy region down to 44 MeV/u.

4. Summary

We have briefly introduced the VUU and QMD methods which are the most widely used theoretical framework for the description of the intermediate heavy–ion collisions. A lot of developments have been done in these simulations up to now. The most important feature of them is that they can describe on the same framework a variety of phenomena of heavy–ion collisons in the quite large energy range loughly from 10 MeV/u to 2 GeV/u. In this energy regime, the effects of the mean–field as well as the individual NN collisions (elastic and inelastic) are essential to describe the whole dynamical evolution of the reactions.

In this report we have shown only a part of the results of these simulations and compared with the experimental data. Particulaly we have not shown the results of the multi–fragmentation nor the deep inelastic collisons. For these phenomena we refer the reader to refs. [13, 21]. Though there are some aspects to improve in these simulation methods, we hope that these simulation shall contribute very much not only to the heavy–ion nuclear physics but also to the construction of the high–energy nuclear data table in future.

REFERENCES

[1] S. Nagamiya and M. Gyulassy, Advances in Nuclear Physics, Vol. 13 (1984) 201

[2] R. Stock, Phys. Rep. 135 (1986) 259

[3] H. Stocker and W. Greiner, Phys. Rep. 137 (1986) 277

[4] G.F. Bertsch and S. Das Gupta, Phys. Rep. 160 (1988) 189

[5] W. Cassing, V. Metag, U. Mosel and K. Niita, Phys. Rep. 188 (1990) 363

[6] C. Gregoire, B. Remaud, F. Sebille, L. Vinet and Y. Raffray, Nucl. Phys. A465 (1987) 317

[7] J. Aichelin and H. Stocker, Phys. Lett. 176B (1986) 14

[8] J. Aichelin, G. Peilert, A. Bohnet, A. Rosenhauser, H. Stocker and W. Greiner, Phys. Rev. C37 (1988) 2451

[9] R. Stock et al., Phys. Rev. Lett. 49 (1982) 1236

[10] J. Cugnon et al., Nucl. Phys. A352 (1981) 505 and A372 (1982) 553

[11] W. Botermans and R. Malfliet, Phys. Rep. 198 (1990) 115

[12] W. Cassing, K. Niita and S.J. Wang, Z. Phys. A331 (1988) 439

[13] S. Hannuschke, W. Cassing, U. Mosel, and K. Niita, Nucl. Phys. A (1991) in press

[14] K. Niita, W. Cassing and U. Mosel, Nucl. Phys. A504 (1989) 391

[15] A. Ohnishi, T. Maruyama and H. Horiuchi, preprint KUNS–1021

[16] J. Aichelin et al., Phys. Rev. Lett. 62 (1989) 1461

[17] S. Hayashi et al., Phys. Rev. C38 (1988) 1229

[18] H. Kruse, B.V. Jacak and H. Stocker, Phys. Rev. Lett. (1985) 289; J.J. Molitoris and H. Stocker, Phys. Rev. C32 (1985) 346; Phys. Lett. 162B (1985) 47; J.J. Molitoris, H. Stocker and B.L. Winer, Phys. Rev. C36 (1987) 220

[19] G.M. Welke, M. Prakash, T.T.S. Kuo, S. Das Gupta and C. Gale, Phys. Rev. C38 (1988) 2101

[20] C.M. Ko and and Q. Li, Phys. Rev. C37 (1988) 2270; Q. Li, J.Q. Wu and C.M. Ko, Phys. Rev. C39 (1989) 849

[21] J. Aichelin, to be published

[22] Gy. Wolf, G. Batko, W. Cassing, U. Mosel, K. Niita, and M. Schaffer, Nucl. Phys. A517 (1990) 615

[23] A.L.De Paoli, K. Niita, W. Cassing, U. Mosel, and C.M. Ko, Phys. Lett. 219B (1989) 194; W. Cassing, G. Batko, U. Mosel, K. Niita, O. Schult, and Gy. Wolf, Phys. Lett. B238 (1990) 363

[24] H. Noll et al., Phys. Rev. Lett. 52 (1984) 1284

[25] H. Heckwolf et al., Z. Phys. A315 (1984) 243

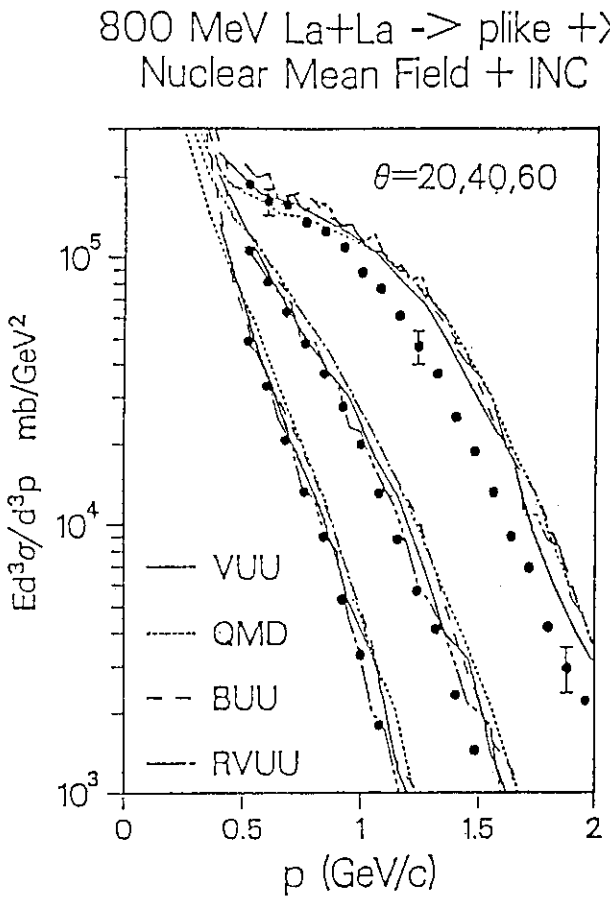

Fig.1

Comparison of nuclear transport calculations to data (ref. 17). The full line and dotted line denote momentum-independent VUU [18] and QMD [7,8] with incompressibility module K=380 MeV. The dashed line shows the momentum-dependent BUU [19] with K=210 MeV, while dot-dashed line is the relativistic RVU [20].

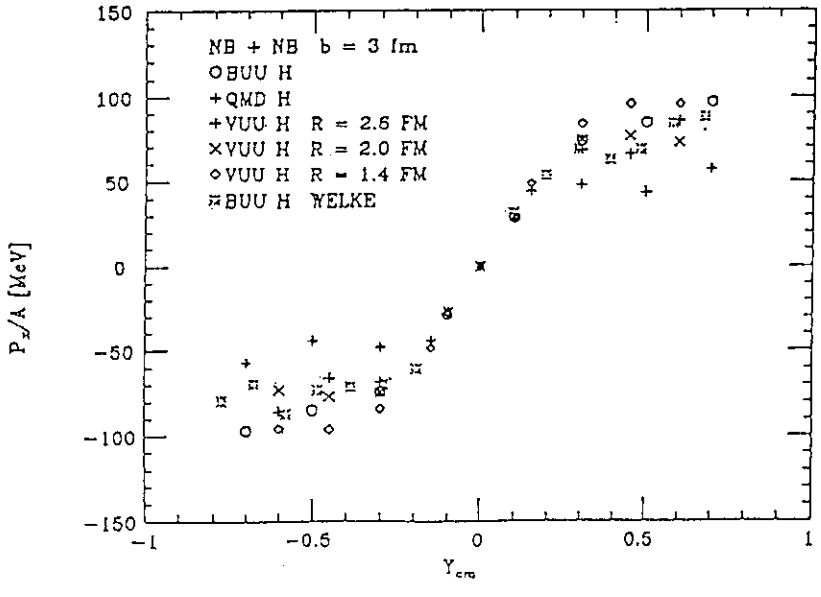

Fig.2

Average transverse momentum as a function of the center of mass rapidity for different theories for the reactions Nb+Nb b=3fm.

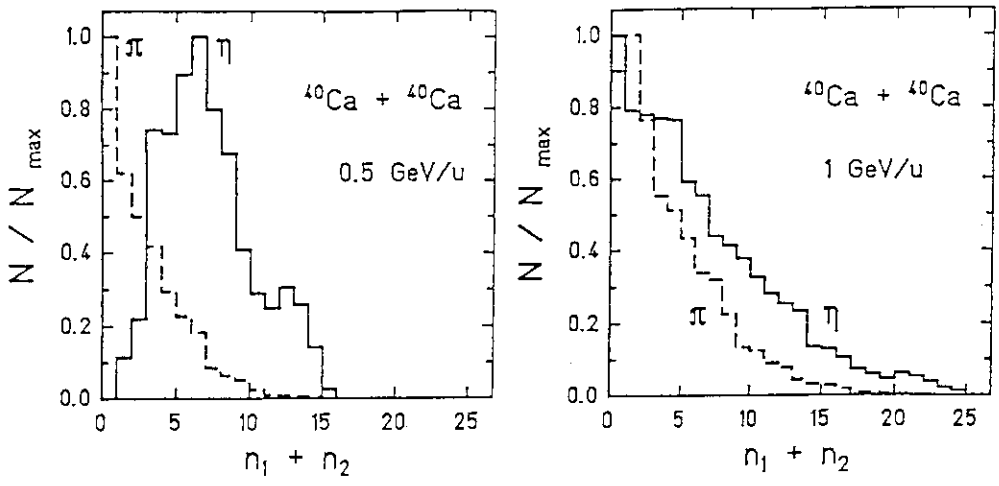

Fig.3

Number of produced pions and η's as a function of the total number n_1+n_2 of collisions that the participating nucleons have undergone before the production takes place, at 0.5 GeV/u and 1 GeV/u. The curves are normalized so that their maxima coincide.

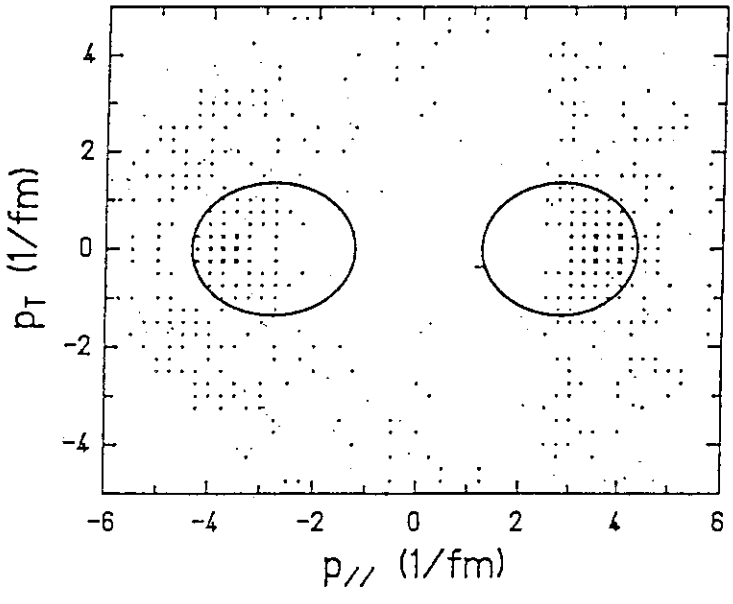

Fig.4

Distribution of nucleons in momentum space which prouce a eta meson in a central collision of ^{40}Ca + ^{40}Ca at 600 MeV/u.

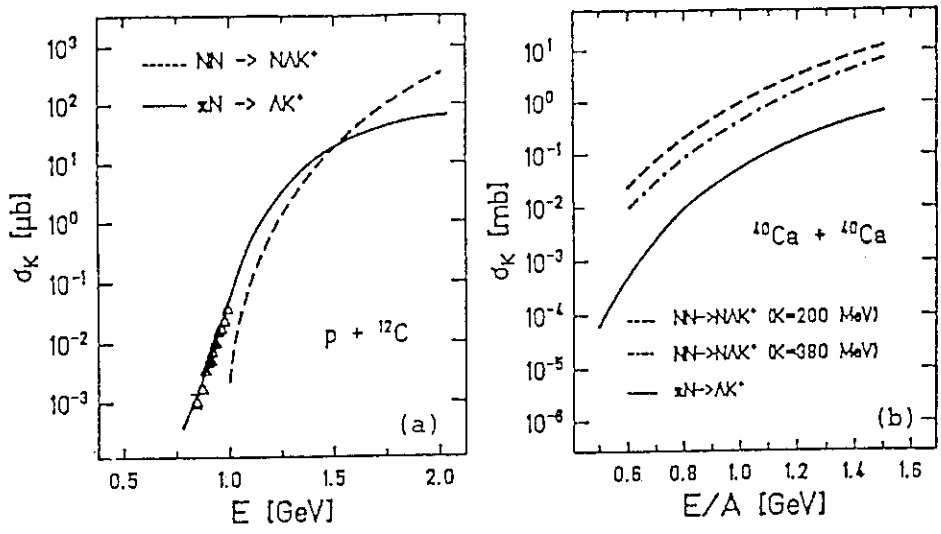

Fig.5

Calculated cross section for K^+–production as a function of the bombarding energy per nucleon for the system p + ^{12}C (a) and ^{40}Ca + ^{40}Ca (b). The contribution of $\pi N \rightarrow K^+\Lambda$ processes is denoted by the solid lines while the dotted and dash–dotted curves indicate contributions emerging from $BB \rightarrow BK^+\Lambda$ process for nuclear compressibility of K=200 MeV and 380 MeV, respectively. The experimental data are given by the triangles.

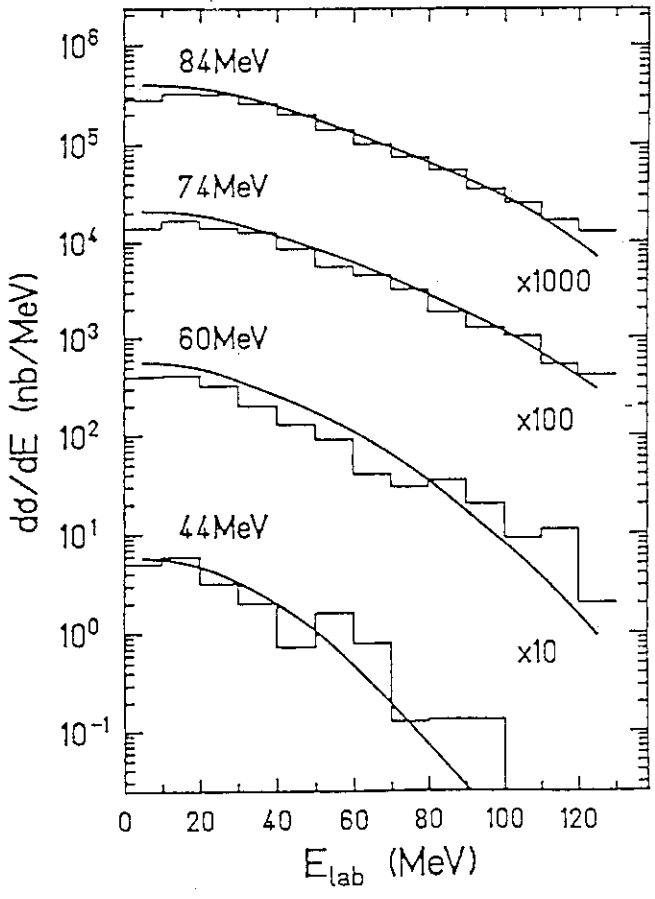

Fig.6

Energy spectra of π^0 from collisions of ^{12}C + ^{12}C at beam energies of 60, 74, and 84 MeV/u, and ^{40}Ar + ^{40}Ca at 44 MeV/u. The full lines are the results of our calculations and the histgrams represent the data taken from refs. [24,25]

6.3 Pion Nucleus Interaction*

Hiroshi Toki, Department of Physics, Tokyo Metropolitan University
Hachiohji, Tokyo 192 and Riken, Wako, Saitama 351, Japan

We discuss the pion nucleus interaction. In the delta region, the delta isobar plays an important role as a doorway to various channels. In the GeV region, the interaction of pion with nucleon becomes weaker and the description of the interaction in terms of the Glauber theory becomes feasible.

Pion interacts strongly with nucleon. The pion mass is small; m=140MeV, which is much smaller than the nucleon mass(M=939MeV). Pion is an isovector and pseudoscalar meson; T=1 and $J^{\pi}=0^{-}$. Pions are produced easily when a hadron interacts with another hadron above a sufficient energy as 1GeV. It is therefore very important to understand the interactions of a pion with nucleus for any phenomena, once a large energy is brought into a nuclear system.

The pion nucleon interaction in the low energy region is dominated by the delta isobar, whose mass is M_{Δ}=1232MeV. Delta has isospin and spin of T=3/2 and S=3/2 and, hence, called often 3-3 resonance. We have to describe the pion nucleon interaction in terms of delta dynamics for pion energy below 500MeV. For GeV pion; above 500MeV, the interaction becomes reasonably small. Various resonances contribute to the pion nucleon interaction. Hence, microscopic theory would have to deal with many baryon resonances, whose interactions with pion are to be determined. At the present, it would be economical to describe pion-nucleus interaction using the experimental pion-nucleon scattering amplitudes. As a reference, we show in Fig.1 the pion nucleon total cross section as a function of pion momentum.

In this paper, we discuss only pion absorption in the delta region and elastic scattering in the GeV region.

Pion Absorption

Pion absorption is the most important process for pion in the delta region. We discuss first pion absorption in light nuclei as d, ^{3}He, ^{4}He. The important finding on pion absorption by these light nuclei is the dominance of pion absorption by a T=0 nucleon pair. The pion absorption cross sections by a T=0 nucleon pair is by two orders of magnitude larger than those by a T=1 nucleon pair. This preference of T=0 pion absorption is understood by the delta mechanism. One can easily convince oneself that the delta mechanism is Pauli forbidden for the T=1 nucleon pair. For a T=1 pair, L=0 and S=0 initially for these light nuclei, which lead to a $J^{\pi}=1^{+}$ and T=1 nucleon pair after absorption of l_{π}=1 pion for excitation of a delta state. This final nucleon state is Pauli forbidden. A result of a simple estimate together with experiment for the ratio of absorption cross sections for T=0 against T=1 as a function of the pion momentum

is shown in Fig.2[1]. Restricting to only l_π=1 pion partial wave, the ratio can be written as the ratio of the direct delta propagator and the crossed delta propagator, which is depicted by dashed curve. Including all the partial waves, the ratio comes down to about 30 at the resonance. The experimental data are shown by the vertical bars.

This preference of pion absorption by T=0 nucleon pairs is gone for pion absorption in heavy nuclei, since the initial nucleon pairs are not only in the zero angular momentum states but also in higher angular momentum states. In order to work out pion absorption systematically for heavy nuclei, it would be most economical to calculate pion absorption rates in infinite matter. We find it not sufficient to consider the two nucleon mechanism, where a pion is absorbed by a nucleon to become a delta and then the delta interacts with another nucleon to go back to nucleon as shown in Fig.3(a). We need to consider multi-nucleon absorption processes. They are called three body (b) and four body (c) processes. These cross sections are worked out in ref.2, for which essentially all the input values are fixed by pion absorption in deuteron. We then use the local density approximation for pion absorption by a finite nucleus. The numerical results are shown in Figs.4 and 5[2]. In fig.4, shown are the absorption cross sections in ^{12}C as a function of the pion kinetic energy. Numerical results with and without the medium corrections on the delta propagator and the interaction are depicted by solid and dashed curves, respectively. The solid curve goes through the experimental values denoted by vertical bars. The mass dependences of absorption cross sections at various pion energies are also shown in Fig.5 together with experimental data. We show in Fig.6 the contribution of the two body process against all as a function of the pion kinetic energy. At low energy, the two body process dominates but above T_π~200MeV it comes down to about 50 %. The rest is due to the three body process and the four body process is negligibly small in this energy range.

Pion scattering

Pion nucleon interaction becomes small above the delta resonance region (GeV pion region). Due to this fact, it becomes easier to describe the pion nucleus interactions in the GeV region. We have elastic an inelastic pion scattering data at P=0.8GeV/c. The interest here is if such data can be described by the Glauber theory, which totally fails for pion nucleus scattering in the delta region. We show in Fig.7 the results of the Glauber calculations as dashed curves in comparison with experiment[3]. The agreement is satisfactory. This fact indicates that the pion nucleus interactions are described well by simply applying the multiple scattering theory.

We see however a slight difference in the angular distributions. This difference may be considered as a medium effect on the pion nucleon interaction. Hence, one might try to extract a modified pion nucleon scattering amplitude from the elastic scattering data. The results of such analyses are shown as solid curves also in Fig.7. The modification on the scattering amplitude is not large and the origin of this modification is being studied microscopically. The use of the modified scattering amplitudes on inelastic scattering is performed and the results are

shown in Fig.8. The inelastic scattering cross sections are also reproduced very nicely with the use of the modified scattering amplitudes. Here, the forward deviations are probably due to the experimental contamination. This fact indicates that the GeV pion can be extremely a good spectroscopic tool for extraction of the nuclear structure informations.

There are a lot of works being published on pion nucleus interactions. We could have covered only a few subjects in this paper. As a review of this subject, we refer two review articles[4,5].

* An invited talk at a Symposium on the high energy nuclear interactions in Tokai-mura in 1991.

1. H. Toki and H. Sarafian; Phys. Lett. B119 (1982) 285
2. E. Oset, Y. Futami and H. Toki; Nucl. Phys. A488 (1986) 597
3. M. Mizoguchi and H. Toki; Nucl. Phys. A513 (1990) 685
4. E. Oset, H. Toki and W. Weise, Phys. Report 83 (1982) 281
5. T.E.O. Ericson and W. Weise, a book "pions and nuclei" published by Oxford University Press (1988)

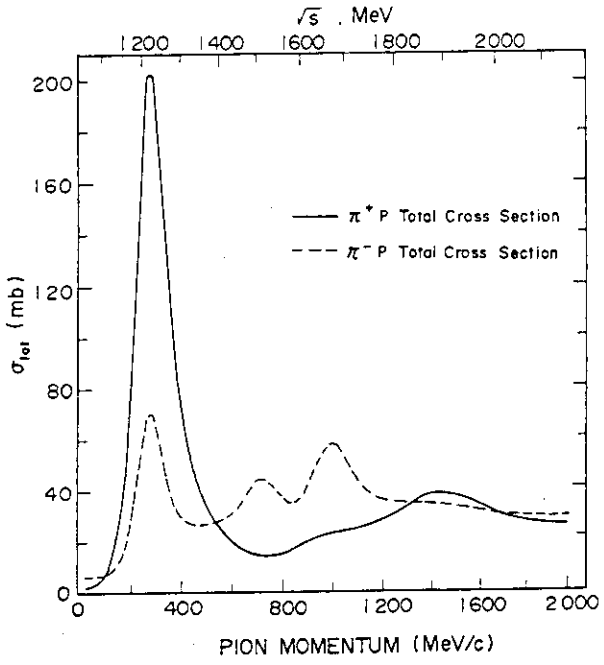

Fig.1 Pion nucleon total cross sections as a function of pion momentum. The above scale is $s^{1/2}$.

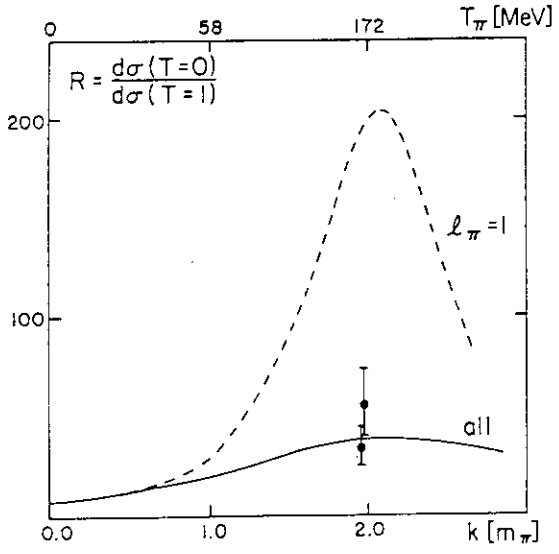

Fig.2 Ratios of pion absorption cross sections for T=0 against T=1 nucleon pairs as a function of the incident pion momentum and in the above scale the pion kinetic energy. The calculated results with only l_π=1 and with all the pion partial waves are depicted by dashed and solid curves. The experimental values are shown by vertical bars.

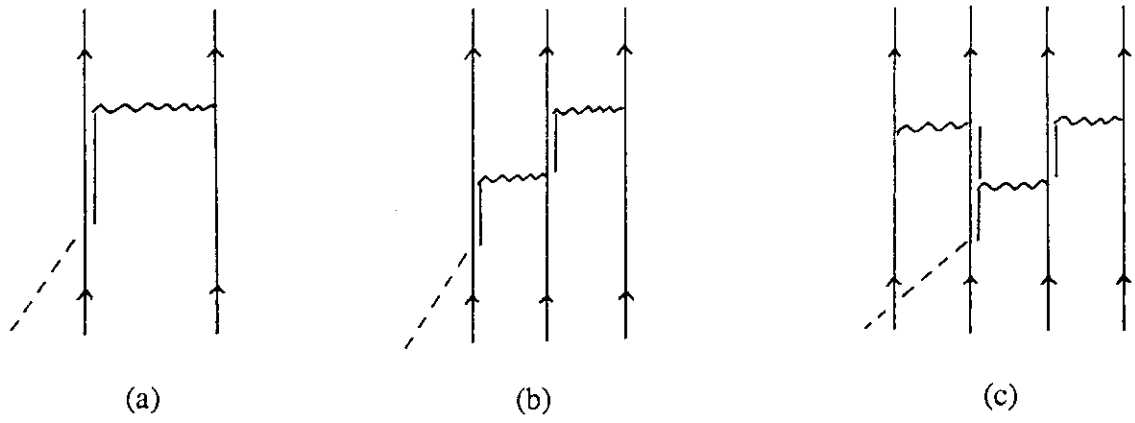

Fig.3 Pion absorption mechanisms; (a) two nucleon process, (b) three nucleon process and (c) four nucleon process.

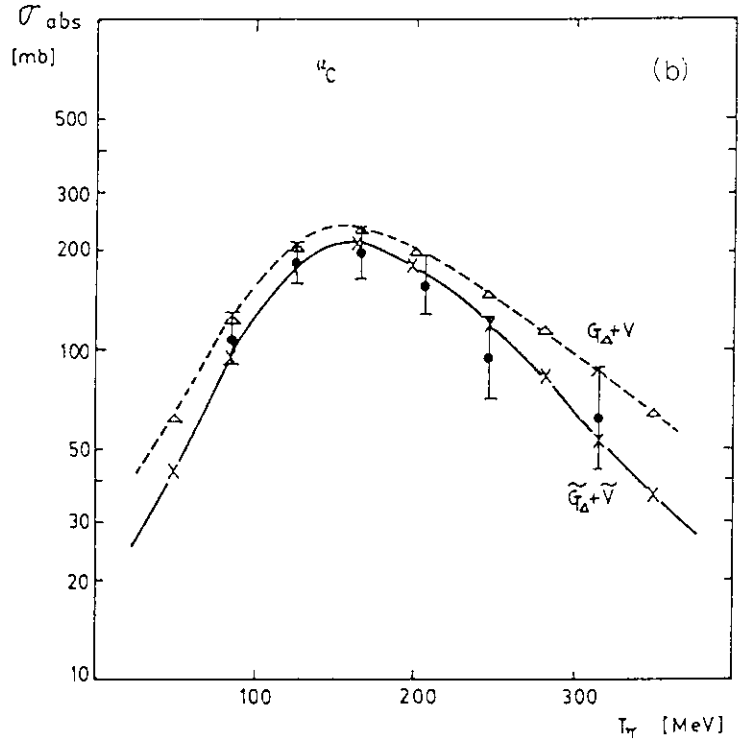

Fig.4 Pion absorption cross sections in ^{12}C as a function of the pion kinetic energy. Numerical results with and without the medium modification on the delta propagator and the interaction are depicted by solid and dashed curves. The experimental values are shown by vertical bars.

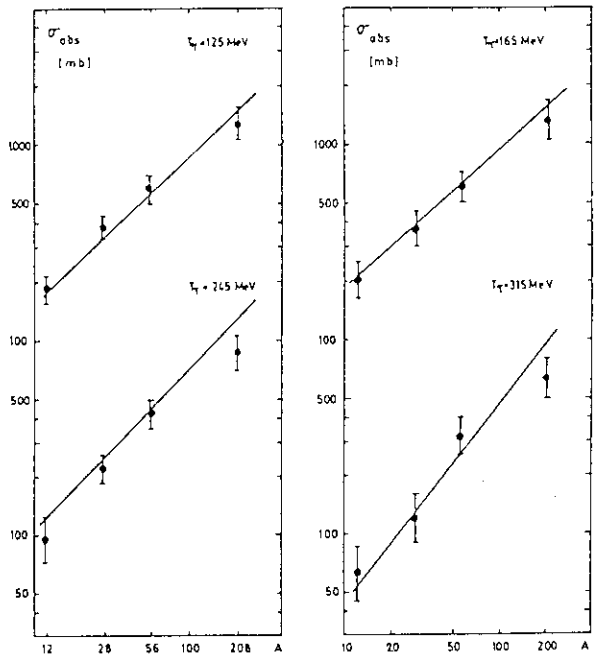

Fig.5 Pion absorption cross sections at various pion energies as a function of the nuclear mass number A.

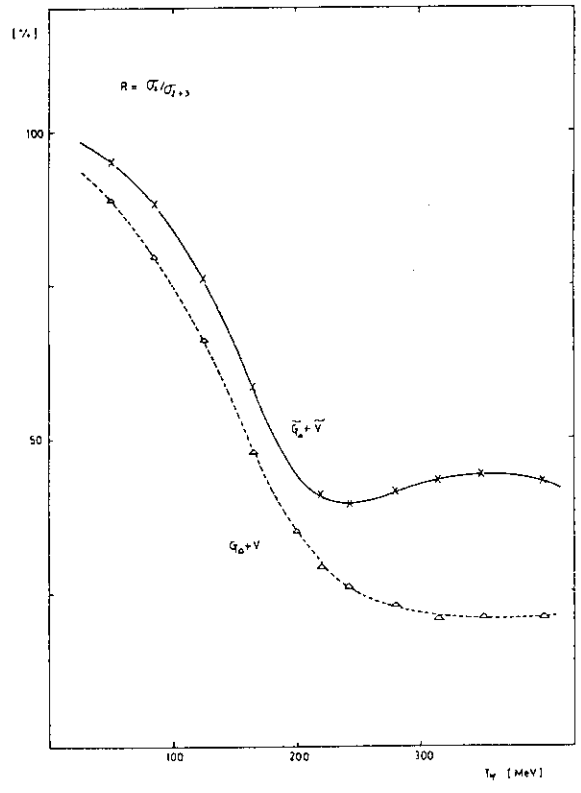

Fig.6 The ratio of the two body pion absorption process against all as a function of the incident pion kinetic energy. The numerical results with and without the medium modifications on the delta propagator and the interaction are depicted by solid and dashed curves.

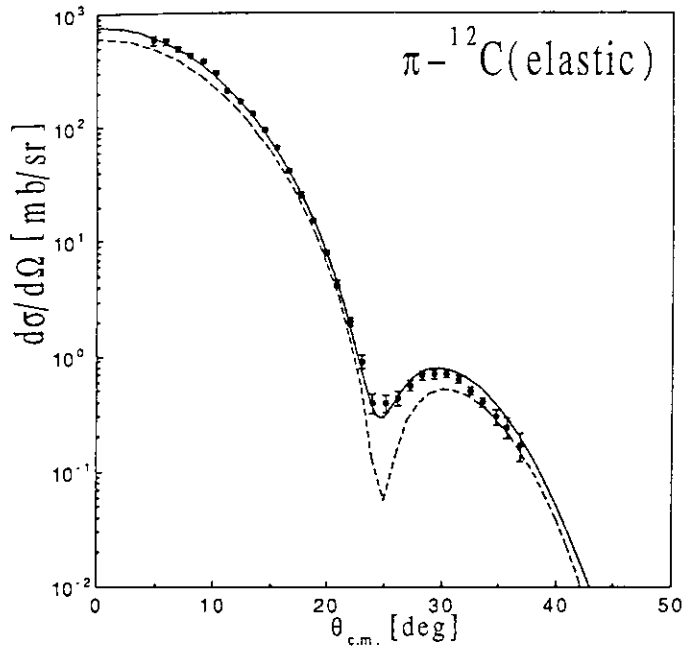

Fig.7 Pion elastic scattering cross sections on ^{12}C as a function of c.m angle at the incident pion momentum of 0.8GeV/c. The Glauber results with and without the modification of the pion nucleon scattering amplitude are depicted by solid and dashed curves together with experimental data points.

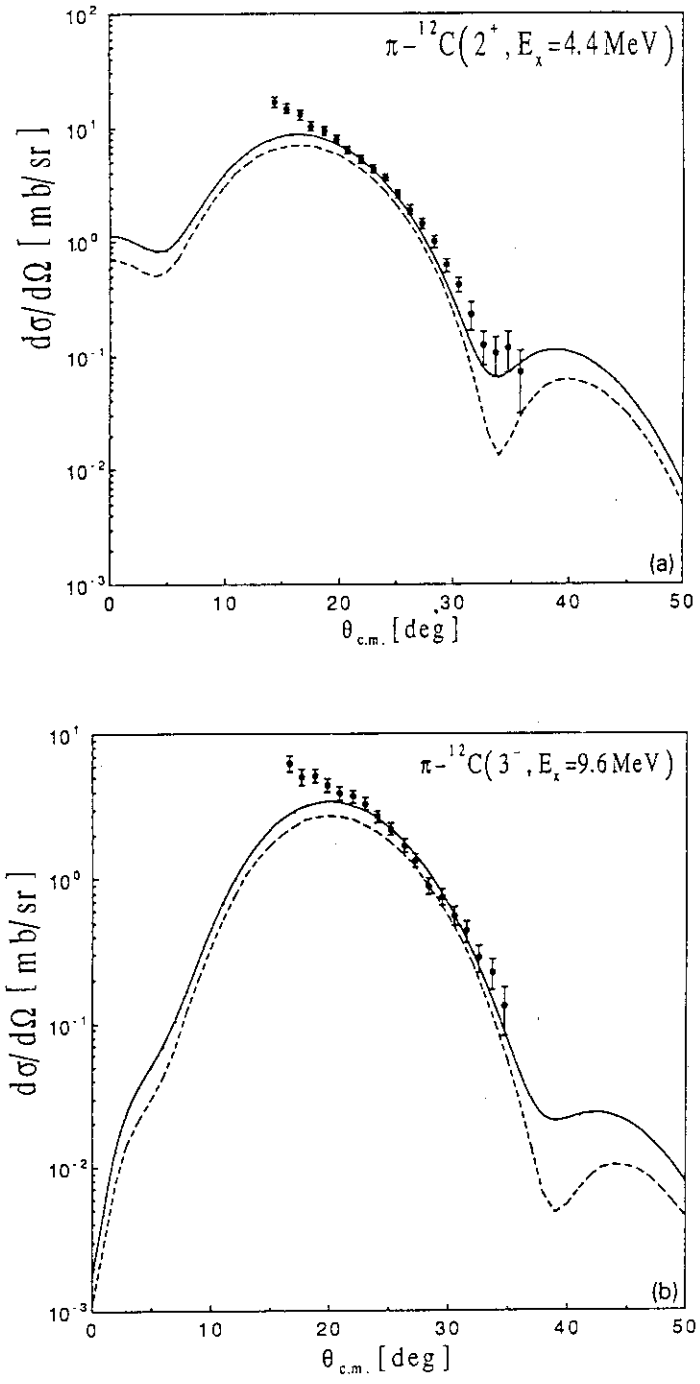

Fig.8 Pion inelastic scattering cross sections leading to 2^+ and 3^- sates in ^{12}C as a function of c.m. angle at the incident pion momentum of 0.8GeV/c. The Glauber results with and without the modification of the pion nucleon scattering amplitude, whose modification is fixed by the elastic scattering data are shown by solid and dashed curves together with experimental data points.

Appendix I The Program of the Specialists' Meeting on High Energy Nuclear Data

October 3 (Thursday)

10:00-10:05

I. Opening Address — M.ISHII(JAERI)

10:05-12:05

II. Experiments — Chairman: M.MIZUMOTO(JAERI)

1. Measurement of Radioactive Nuclides Produced by Spallation Neutrons
   H.Takada(JAERI)
2. Thick Target Neutron Yield for Charged Particles
   K.SHIN(Kyoto Univ.)
3. Measurement of Neutron Activation and Photoneutron Cross Sections
   T.NAKAMURA(Tohoku Univ.)

12:05-13:10 Lunch

13:10-14:55

III. Topics 1 — Chairman: T.NAKAMURA(Tohoku Univ.)

4. Japanese Hadron Project and Shielding Calculation
   Y.UWAMINO(Univ. of Tokyo)
5. High Intensity Proton Linear Accelerator Development Plan and Accelerator-based Nuclear Waste Transmutation
   M.MIZUMOTO(JAERI)
6. Acceleration of Proton Beams with RIKEN Ring Cyclotron
   A.GOTO(RIKEN)

14:55-15:15 Coffee Break

15:15-17:15

IV. Topics 2 — Chairman: N.KISHIDA(CRC)

7. High Energy Electron-Photon Transport Calculation by Monte Calro Method
   H.HIRAYAMA(KEK)

8. Recent Topics on Heavy-Ion Nuclear Reaction in Tandem Energy Region

Y.SUGIYAMA(JAERI)

9. The Database Activity of Charged-Particle Nuclear Reaction Data Group

M.CHIBA(Sapporo Gakuin Univ.)

18:00-20:00 Reception at Akogigaura Club

October 4 (Friday)

9:00-10:10

V. Evaluations Chairman: Y.NAKAHARA(JAERI)

10. Systematics of Neutron-Production Cross Section for Proton-Induced Spallation Reactions

K.ISHIBASHI(Kyushu Univ.)

11. ALICE-F Calculation of Nuclear Data up to 1 GeV

T.FUKAHORI(JAERI)

12. Comparison between Calculated Cross Sections by MCEXCITON and ALICE-P for Medium-Energy Nucleon Induced Reactions on ^{208}Pb and ^{209}Bi

N.KISHIDA(CRC)

10:10-12:10

VI. Theories 1 Chairman: H.KITAZAWA(TIT)

13. Luo-Kawai Model and its Application to Nuclear Data Evaluation

Y.WATANABE(Kyushu Univ.)

14. Nucleus as a Canonical Ensemble: Level Density

H.SATO(RIKEN)

15. Review of High Energy Fission

A.IWAMOTO(JAERI)

12:10-13:10 Lunch

13:10-15:40

VII. Theories 2 Chairman: H.SATO(RIKEN)

16. Phenomenological Nucleon-Nucleon Potential
S.MORIOKA(CRC)

17. Review of Theory Applied to π-Nucleus Reaction
H.TOKI(Tokyo Metropolitan Univ.)

18. Dynamical Simulation of Heavy Ion Collisions: VUU and QMD Method
K.NIITA(JAERI)

15:40-16:00 Coffee Break

16:00-16:45

VIII. Discussion Chairman: Y.KIKUCHI(JAERI)

高エネルギー核データ専門家会議プログラム

１０月３日（木）　　発表時間　分（討論）

Ⅰ．開会の辞　10:00 ～ 10:05　　石井　三彦　　（司会：中村尚司）

Ⅱ．実験 10:05 ～ 12:05　　（座長：水本元治）
1. 高田　弘（原研）　スポレーション中性子による核種生成量の測定　30(10)
2. 秦　和夫（京大）　重イオン反応からの中性子放出　30(10)
3. 中村尚司（東北大）放射化及び光核反応断面積の測定　30(10)

昼食 12:05 ～ 13:10

Ⅲ．トピックス１ 13:10 ～ 14:55　　（座長：中村尚司）
4. 上蓑義朋（核研）　大型ハドロン計画と遮蔽計算　30(10)
5. 水本元治（原研）　大強度陽子リニアック計画と消滅処理　30(10)
6. 後藤　彰（理研）　理研リングサイクロトロンの陽子ビーム加速　20(5)

コーヒーブレーク 14:55 ～ 15:15

Ⅳ．トピックス２ 15:15 ～ 17:15　　（座長：岸田則生）
7. 平山英夫（高エネ研）　高エネルギー電子および光子の輸送計算　30(10)
8. 杉山康治（原研）　タンデム領域での重イオン反応研究の最近の話題　30(10)
9. 千葉正喜（札幌学大）　荷電粒子実験データベース　30(10)

懇親会（アコギクラブ　ＢＣルーム）18:00 ～ 20:00

１０月４日（金）

Ⅴ．評価　9:00 ～ 10:10　　（座長：中原康明）
10. 石橋健二（九大）　スポレーション計算と核データ評価　30(10)
11. 深堀智生（原研）　ALICE-F による 1GeV までの計算　10(5)
12. 岸田則生（CRC総研）MCEXCITON による 1GeV までの計算　10(5)

Ⅵ．理論１　10:10 ～ 12:10　　（座長：北沢日出男）
13. 渡辺幸信（九大）　Luo-Kawai の理論と核データ評価への適用　30(10)
14. 佐藤　弘（理研）　原子核の準位密度について　30(10)
15. 岩本　昭（原研）　高エネルギー核分裂について　30(10)

昼食 12:10 ～ 13:10

Ⅶ．理論２　13:10 ～ 15:40　　（座長：佐藤　弘）
16. 森岡信一（CRC総研）核子-核子現象論的ポテンシャル　40(10)
17. 土岐　博（都立大）π中間子-原子核反応について　40(10)
18. 仁井田浩二（原研）VUU および QMD 理論のレビュー　40(10)

コーヒーブレーク 15:40 ～ 16:00

Ⅷ．討論　16:00 ～ 16:45　　（司会：菊池康之）

Appendix II List of Participants for the Specialists' Meeting on High Energy Nuclear Data

Participant		Affiliation
Mamoru	BABA	Tohoku University
Masaki	CHIBA	Sapporo Gakuin University
Satoshi	CHIBA	Japan Atomic Energy Research Institute
Tokio	FUKAHORI	Japan Atomic Energy Research Institute
Akira	GOTO	The Institute of Physical and Chemical Research
Masanori	HACHIYA	Data Engineering Inc.
Akira	HASEGAWA	Japan Atomic Energy Research Institute
Kazuo	HASEGAWA	Japan Atomic Energy Research Institute
Yoshiko	HARIMA	Tokyo Institute of Technology
Hideo	HIRAYAMA	National Laboratory of High Energy Physics
Sin-iti	IGARASI	Nuclear Energy Data Center
Masayuki	IGASHIRA	Tokyo Institute of Technology
Kenji	ISHIBASHI	Kyushu University
Mitsuhiko	ISHII	Japan Atomic Energy Research Institute
Satoshi	IWAI	Mitsubishi Atomic Power Industries Inc.
Akira	IWAMOTO	Japan Atomic Energy Research Institute
Yukinori	KANDA	Kyushu University
Masayoshi	KAWAI	Toshiba Corp.
Toshihiko	KAWANO	Kyushu University
Yuuki	KAWARASAKI	Japan Atomic Energy Research Institute
Yasuyuki	KIKUCHI	Japan Atomic Energy Research Institute
Norio	KISHIDA	CRC Research Institute Inc.
Hideo	KITAZAWA	Tokyo Institute of Technology

Participant	Affiliation
Norihiko KOORI	Tokushima University
Kazuaki KOSAKO	Japan Atomic Energy Research Institute
Fujio MAEKAWA	Japan Atomic Energy Research Institute
Hiroshi MAEKAWA	Japan Atomic Energy Research Institute
Hiroyuki MATSUNOBU	Sumitomo Atomic Energy Industries Ltd.
Motoharu MIZUMOTO	Japan Atomic Energy Research Institute
Shin-ichi MORIOKA	CRC Research Institute Inc.
Tsuneo NAKAGAWA	Japan Atomic Energy Research Institute
Yasuaki NAKAHARA	Japan Atomic Energy Research Institute
Ryuzo NAKAJIMA	Hosei University
Takashi NAKAMURA	Tohoku University
Tsutomu NARITA	Japan Atomic Energy Research Institute
Koji NIITA	Japan Atomic Energy Research Institute
Takahiko NISHIDA	Japan Atomic Energy Research Institute
Yukio OYAMA	Japan Atomic Energy Research Institute
Hiroshi SATO	The Institute of Physical and Chemical Research
Tetsuo SAWADA	Tokyo Institute of Technology
Kazuo SHIN	Kyoto University
Yasuharu SUGIYAMA	Japan Atomic Energy Research Institute
Hiroshi TAKADA	Japan Atomic Energy Research Institute
Hiroshi TOKI	Tokyo Metropolitan University
Yoshitomo UWAMINO	University of Tokyo
Yukinobu WATANABE	Kyushu University
Naoki YAMANO	Sumitomo Atomic Energy Industries Ltd.
Yoshimaro YAMANOUCHI	Japan Atomic Energy Research Institute
Yoshiaki YOSHIZAWA	Mitsubishi Research Institute Inc.